Titre: Title:	Functional Connectivity of the Rodent Brain Using Optical Imaging
Auteur: Author:	Edgar Guevara Codina
Date:	2013
Type:	Mémoire ou thèse / Dissertation or Thesis
Référence: Citation:	Guevara Codina, E. (2013). Functional Connectivity of the Rodent Brain Using Optical Imaging [Thèse de doctorat, École Polytechnique de Montréal]. PolyPublie. https://publications.polymtl.ca/1269/

UNIVERSITÉ DE MONTRÉAL

FUNCTIONAL CONNECTIVITY OF THE RODENT BRAIN USING OPTICAL IMAGING

EDGAR GUEVARA CODINA

INSTITUT DE GÉNIE BIOMÉDICAL

ÉCOLE POLYTECHNIQUE DE MONTRÉAL

THÈSE PRÉSENTÉE EN VUE DE L'OBTENTION

DU DIPLÔME DE PHILOSOPHIÆ DOCTOR

(GÉNIE BIOMÉDICAL)

NOVEMBRE 2013

UNIVERSITÉ DE MONTRÉAL

ÉCOLE POLYTECHNIQUE DE MONTRÉAL

Cette thèse intitulée:

FUNCTIONAL CONNECTIVITY OF THE RODENT BRAIN USING OPTICAL IMAGING

présentée par : GUEVARA CODINA Edgar

en vue de l'obtention du diplôme de : Philosophiæ Doctor

a été dûment acceptée par le jury d'examen constitué de :

M. COHEN-ADAD Julien, Ph. D., président

M. LESAGE Frédéric, Ph. D., membre et directeur de recherche

M. BEAUMONT Eric, Ph. D., membre et codirecteur de recherche

M. COMTOIS Philippe, Ph. D., membre

M. WHITTINGSTALL Kevin, Ph. D., membre

DEDICATION

A Santiago

ACKNOWLEDGMENTS

I express my gratitude to my supervisor Professor Frédéric Lesage for the opportunity he gave me to be part of his research group, and mostly for his constant guidance, supervision and support. His confidence in my work and prompt corrections contributed enormously to the bringing up of this thesis.

My sincere appreciation to all the co-authors Philippe Pouliot, Hélène Girouard, Eric Beaumont, Dang Khoa Nguyen, Nataliya Sadekova, Simon Dubeau, Nicolas Ouakli, Maxime Abran and Samuel Bélanger and for all the contributions to our joint publications. A special acknowledgement goes to Romain Berti, Irene Londono, Carl Matteau-Pelletier, Ningshi Xie and Grégory Lodygensky for their tireless efforts towards the experiments with photoacoustics. Many thanks to Pierre Bellec for the fruitful discussion about functional connectivity. I would also like to acknowledge the support of Caroline Boudoux for the use of her laboratory facilities, as well as Edward Baraghis, Kathy Beaudette and Simon Lemire-Renaud for their invaluable help with the OCT system.

I would like to sincerely thank all the staff of the Montreal Heart Institute animal facility, in particular Marc-Antoine Gillis, Natacha Duquette, Vanessa Durocher-Granger and Karine Nadeau. Their invaluable technical assistance in animal preparation, animal monitoring and administrative help undoubtedly facilitated my research. I am also grateful to past and current members of LIOM who provided much help through my studies and shared many pleasant moments: Abas Sabouni, Alexandre Castonguay, Alexis Machado, Azadeh Naderiyanha, Benoit Hamelin, Clément Bonnery, Émilie Beaulieu-Ouellet, Joël Lefebvre, Karim Zerouali-Boukhal, Léonie Rouleau, Li Baoqiang, Mahnoush Amiri, Michèle Desjardins, Peng Ke, Simon Archambault, Tri Truong Van, Zhang Cong.

I gratefully acknowledge the Mexican National Science and Technology Council (CONACYT) through scholarship No. 304501 and the Ministry of Public Education (SEP) for providing me with financial support throughout most of my doctorate; I would also like to thank my advisor's financial assistance. Many thanks to my mother and my aunt who have always supported me to achieve my goals, even in the distance. I would like to express my endless thankfulness to my wonderful wife Jenny, who left everything behind to accompany me on this journey; without her encouragement and love this task would not have been possible at all.

RÉSUMÉ

L'objectif de cette thèse de doctorat est d'appliquer la connectivité fonctionnelle dans une variété de modèles animaux, à l'aide de plusieurs techniques d'imagerie optique. Le cerveau, même au repos, montre une activité métabolique élevée : la corrélation des fluctuations spontanées lentes permet d'identifier des régions cérébrales distantes mais connectées; d'où le terme connectivité fonctionnelle. Les changements dans l'activité spontanée peuvent donner un aperçu des processus neuronaux qui comprennent la majorité de l'activité métabolique du cerveau, et constituent en conséquent une vaste source de changements reliés aux maladies.

L'hémodynamique du cerveau peut être modifiée grâce à des affections neurovasculaires et avoir un effet sur l'activité au repos. Cette thèse vise la compréhension des changements de connectivité fonctionnelle induits par des maladies, à l'aide de l'imagerie optique fonctionnelle.

Les techniques d'imagerie explorées dans les deux premières contributions de cette thèse sont l'Imagerie Optique Intrinsèque et l'Imagerie par Granularité Laser. Ensemble, elles peuvent estimer les changements de consommation d'oxygène, étroitement liés à l'activité neuronale. Ces techniques possèdent des résolutions temporelles et spatiales adéquates et bien adaptées pour imager la convexité du cortex cérébral. Dans le dernier article, une modalité d'imagerie en profondeur, la Tomographie Photoacoustique a été utilisée chez le rat nouveau-né. La Tomographie par Cohérence Optique et la Tomographie Laminaire Optique font également partie de la gamme des techniques d'imagerie développées et appliquées dans d'autres collaborations.

La première partie des résultats mesure les changements de connectivité fonctionnelle dans un modèle d'activité épileptiforme aiguë chez le rongeur. Il y a des augmentations ainsi que des diminutions entre les corrélations homologues, avec une faible dépendance aux crises épileptiques. Ces changements suggèrent un découplage potentiel entre les paramètres hémodynamiques dans les réseaux au repos, en soulignant l'importance d'investiguer les réseaux épileptiques à l'aide de plusieurs mesures hémodynamiques indépendantes.

La deuxième partie des travaux étudie un nouveau modèle de rigidité artérielle chez la souris : la calcification unilatérale de la carotide droite. L'analyse de connectivité basé sur les régions d'intérêt montre une tendance décroissante de corrélation homologue dans les cortex moteur et cingulum. L'analyse de graphes montre une randomisation des réseaux corticaux, ce qui suggère une perte de connectivité; plus spécifiquement, dans le cortex moteur ipsilateral à la carotide

traitée. Néanmoins, ces changements ne se reflètent pas dans un métabolisme différencié. Ils restent toujours des facteurs confondants dûs au fait que la calcification de la carotide induit un déclin neuronal dans l'hippocampe ainsi qu'une altération unilatérale de la pulsatilité vasculaire. Cependant, les résultats appuient la nécessite d'observer plusieurs paramètres hémodynamiques lorsqu'on image le cerveau suite à la remodélisation artérielle.

La troisième partie des travaux étudie un modèle de lésion inflammatoire chez le rat nouveau-né. La saturation d'oxygène et la connectivité fonctionnelle ont été mesurées avec la Tomographie Photoacoustique. La saturation d'oxygène a diminué dans le site de la lésion et dans le cortex ipsilateral à la lésion, toutefois cette diminution n'a pas été complètement expliquée par l'hypovascularisation révélée par l'histologie. Une analyse de connectivité des régions d'intérêt a montré que la connectivité intra-hémisphères n'est pas modifiée par la lésion inflammatoire.

ABSTRACT

The aim of this thesis is to apply functional connectivity in a variety of animal models, using several optical imaging modalities. Even at rest, the brain shows high metabolic activity: the correlation in slow spontaneous fluctuations identifies remotely connected areas of the brain; hence the term “functional connectivity”. Ongoing changes in spontaneous activity may provide insight into the neural processing that takes most of the brain metabolic activity, and so may provide a vast source of disease related changes.

Brain hemodynamics may be modified during disease and affect resting-state activity. The thesis aims to better understand these changes in functional connectivity due to disease, using functional optical imaging.

The optical imaging techniques explored in the first two contributions of this thesis are Optical Imaging of Intrinsic Signals and Laser Speckle Contrast Imaging, together they can estimate the metabolic rate of oxygen consumption, that closely parallels neural activity. They both have adequate spatial and temporal resolution and are well adapted to image the convexity of the mouse cortex. In the last article, a depth-sensitive modality called photoacoustic tomography was used in the newborn rat. Optical coherence tomography and laminar optical tomography were also part of the array of imaging techniques developed and applied in other collaborations.

The first article of this work shows the changes in functional connectivity in an acute murine model of epileptiform activity. Homologous correlations are both increased and decreased with a small dependence on seizure duration. These changes suggest a potential decoupling between the hemodynamic parameters in resting-state networks, underlining the importance to investigate epileptic networks with several independent hemodynamic measures.

The second study examines a novel murine model of arterial stiffness: the unilateral calcification of the right carotid. Seed-based connectivity analysis showed a decreasing trend of homologous correlation in the motor and cingulate cortices. Graph analyses showed a randomization of the cortex functional networks, suggesting a loss of connectivity, more specifically in the motor cortex ipsilateral to the treated carotid; however these changes are not reflected in differentiated metabolic estimates. Confounds remain due to the fact that carotid rigidification gives rise to neural decline in the hippocampus as well as unilateral alteration of vascular pulsatility; however

the results support the need to look at several hemodynamic parameters when imaging the brain after arterial remodeling.

The third article of this thesis studies a model of inflammatory injury on the newborn rat. Oxygen saturation and functional connectivity were assessed with photoacoustic tomography. Oxygen saturation was decreased in the site of the lesion and on the cortex ipsilateral to the injury; however this decrease is not fully explained by hypovascularization revealed by histology. Seed-based functional connectivity analysis showed that inter-hemispheric connectivity is not affected by inflammatory injury.

TABLE OF CONTENTS

LIST OF TABLES

LIST OF FIGURES

LIST OF ACRONYMS AND ABBREVIATIONS

This list presents in alphabetical order the abbreviations and acronyms used in the thesis as well as their meanings.

4-AP	4-Aminopyridine
ADC	Analog to Digital Conversion
AL	Aiming Laser
BOLD	Blood Oxygenation Level Dependent
BPD	Balanced Photodetector
CBF	Cerebral Blood Flow
CBV	Cerebral Blood Volume
CHD	Coronary Heart Diseases
CIR	Circulator
$CMRO_2$	Cerebral Metabolic Rate of Oxygen consumption
CNR	Contrast-to-Noise Ratio
COL	Collimator
CVD	Cardiovascular disease
DAQ	Data Acquisition board
DCB	Dispersion Compensation Block
DFT	Discrete Fourier Transform
EEG	Electroencephalography
fc	Functional Connectivity
FC	Fiber Coupler
fcEEG	Electroencephalography Functional Connectivity
fcOIS	Functional Connectivity Optical Intrinsic Signal Imaging

FDG	Fluorodeoxyglucose
FD-OCT	Fourier-Domain Optical Coherence Tomography
fMRI	Functional Magnetic Resonance Imaging
fNIRS	Functional Near-Infrared Spectroscopy
FOV	Field of View
FPGA	Field-Programmable Gate Array
f_s	Sampling Frequency
FWHM	Full Width at Half Maximum
HbO_2	Oxyhemoglobin
HbR	Deoxyhemoglobin
HbT	Total hemoglobin
ICA	Independent Component Analysis
LFP	Local Field Potential
LOT	Laminar Optical Tomography
LPS	Lipopolysaccharide
LSCI	Laser Speckle Contrast Imaging
LSF	Line Spread Function
M	Mirror
Mbps	Megabits per second
MRI	Magnetic Resonance Imaging
NA	Numerical Aperture
NDF	Neutral Density Filter
NIRS	Near-Infrared Spectroscopy
OCT	Optical Coherence Tomography

OD	Optical Density
OIS	Optical Imaging of Intrinsic Signals
PAT	Photoacoustic Tomography
PC	Polarization Controller
PCA	Principal Component Analysis
PET	Positron Emission Tomography
PSF	Point-Spread Function
PVL	Periventricular Leukomalacia
RCCA	Right Common Carotid Artery
rsMRI	Resting-State Functional Magnetic Resonance Imaging
RSN	Resting-State Network
RTE	Radiative Transfer Equation
SCI	Spinal Cord Injury
SNR	Signal-to-Noise Ratio
SO_2	Oxygen Saturation
SPD	Short-Pass Dichroic
SS-OCT	Swept Source Optical Coherence Tomography
SVD	Singular Value Decomposition
TCO	Telecentric Objective
TD-OCT	Time-Domain Optical Coherence Tomography

INTRODUCTION

Brain function has been traditionally studied in terms of physiological responses to the administration of external stimuli or tasks. From early physiology work (Hubel & Wiesel, 1962) to cognitive activation paradigms in humans (Raichle, 1998), this approach has been very valuable in linking brain topography with function; this perspective considers the brain to be mainly driven by external inputs, ignoring the fact that human brain consumes 20% of the body energy at rest, even though it accounts for less than 2% of total body mass (Raichle, 1998, 2010).

A variety of functional imaging techniques have been developed to indirectly record the metabolic traces of neural activity in the central nervous system. About 23 years ago, one of the most promising modalities appeared, called functional magnetic resonance imaging (fMRI). fMRI uses a non-invasive method that relies on Blood Oxygenation Level Dependent (BOLD) contrast, due to the paramagnetic properties of HbR (Ogawa, Lee, Kay, & Tank, 1990).

The empirical motivation for studying spontaneous neural activity arose from the first observation of spatially coherent activity in the fMRI BOLD signal (B. Biswal, Yetkin, Haughton, & Hyde, 1995). In their seminal paper, Biswal and colleagues observed spontaneous fluctuations on the right motor cortex that were correlated with spontaneous fluctuations in its contralateral homologue, even during the absence of an overt motor task. This finding has been replicated by several groups since then, extending the studies from the motor cortex to the visual, auditory, and language processing regions (Cordes et al., 2001; De Luca, Beckmann, De Stefano, Matthews, & Smith, 2006; Fox, Snyder, Zacks, & Raichle, 2006; Greicius, Krasnow, Reiss, & Menon, 2003; Lowe, Dzemidzic, Lurito, Mathews, & Phillips, 2000). Brain regions that showed greater BOLD signal during rest than during task performance have also received attention; these regions that routinely exhibit decreased activity during experimental tasks have been labeled the default-mode network (Raichle et al., 2001). Functional connectivity is a method that describes the correlation of spatially remote areas in the temporal domain (Karl J Friston, 2011) and the regions of coherent activity found with functional connectivity methods have been termed resting-state networks (RSNs) (Fox & Raichle, 2007; la Iglesia-Vaya, Molina-Mateo, Jose, S., & Marti-Bonmati, 2013). Far from being pretty noise, spontaneous fluctuations are correlated within functionally related brain zones (Deco & Corbetta, 2011). While extensively used in humans, the application of fMRI in mice remains difficult, as the small size of murine brain

needs exceptionally good signal-to-noise ratio (SNR) and spatial resolution (Benveniste & Blackband, 2002; Jonckers, Van Audekerke, De Visscher, Van der Linden, & Verhoye, 2011); making it challenging to relate human studies to mouse models of disease, where molecular and genetic mechanisms are well-established. Although BOLD fMRI is widely used in functional imaging, it is subject to confounds due to the competing effects of changes in blood flow and oxygen metabolism. An attractive alternative to work around the limitations of fMRI is to use optical imaging in the small animal. First, it may be possible to reveal functional networks consistently identified in the resting-state. Second, using multiple wavelengths a complete set of hemodynamic parameters may be obtained and then be used to disambiguate the confounds present in the BOLD signal. Finally, translating the advances of functional connectivity fMRI to optical techniques in disease murine models would enable new studies on a multitude of cost-effective and efficient animal models, with high genetic similarity (European Commission Workshop, 2010). Therefore, the goal of this thesis is to combine a variety of optical imaging modalities with resting-state functional connectivity mapping.

The studies presented in this work aim to establish the utility of different optical imaging techniques such as multi-spectral intrinsic optical imaging, laser speckle imaging and photoacoustic tomography (PAT) to assess resting-state connectivity in various murine models. Using multiple illumination wavelengths, relative changes in HbO_2 and HbR can be estimated, while speckle imaging gives access to relative cerebral blood flow (CBF). This then enables estimations of $CMRO_2$, a measurement more closely related to neural activity than hemoglobin concentrations alone (Brieu, Beaumont, Dubeau, Cohen-Adad, & Lesage, 2010; Zappe, Uludag, Oeltermann, Ugurbil, & Logothetis, 2008). Hence, due to access to distinct hemodynamic components, functional connectivity based on optical imaging of intrinsic signals (fcOIS) may provide additional information that complements resting-state studies with fMRI in the context of neurological and vascular disease. PAT is a technique that combines the intrinsic contrast capabilities of optical imaging with the advantage of high spatial resolution of ultrasound (L. V. Wang & Hu, 2012). A short laser pulse is absorbed by molecules in living tissue, generating an ultrasonic pressure wave, which is detected by an ultrasound transducer to form images (X. Wang et al., 2003). Its non-invasive nature lends itself to application in newborn models and it also provides access to deeper layers of the brain.

The techniques presented in this thesis are an attempt to unravel the functional correlates of several disease models, leading to a better understanding of connectivity changes in rodent models.

Brief literature review

Proxy measures of neural activity

Brain imaging depends largely on evoked hemodynamic signals. In 1878, Mosso tested the hypothesis that blood flow is related to brain activity, recording changes in brain volume related to cerebral blood flow (CBF) on the exposed dura mater in the frontal region of a 37-year old subject (Mosso, 1884; Sandrone et al., 2013; Yu, Schummers, & Sur, 2010; Zago, Lorusso, Ferrucci, & Priori, 2012). He observed that pulsations in the frontal cortex increased during the performance of a computation task. Although modern imaging techniques are not based on the same principles as Mosso's, his idea of indirect measurements of neural activity may be considered the precursor to modern functional neuroimaging.

When a neuron depolarizes, there is a localized oxygen consumption indicated by an initial increase in deoxyhemoglobin (HbR). A few seconds later (1–2 s), there is a large increase in CBF and cerebral blood volume (CBV) as a compensation mechanism to the initial oxygen utilization. This large mismatch between oxygen supply and consumption leads to a delayed augmentation in oxyhemoglobin (HbO_2) concentration and the consequent dilution of HbR (Malonek & Grinvald, 1996). These responses have a temporal width of 4–6 s to even a very brief stimulus; this delay depends on the metabolic filter of each brain region, the choice of estimator and the duration of the stimulus (ON) period (C. H. Liao et al., 2002; Saad, DeYoe, & Ropella, 2003). Thus, activity of the neurons can be indirectly localized and quantified by measuring the hemodynamic changes following electrical activation: the so called hemodynamic response (HDR).

However, the relationship between neural activation and HDR remains complex, even non-linear (Devor et al., 2003). This non-linearity is more pronounced when comparing the HDR to a wide range of stimuli (Richard B. Buxton, Uludag, Dubowitz, & Liu, 2004). Another finding that is still subject to controversy in the literature (Chen & Pike, 2009) is the so-called "initial dip": a decrease in HDR signal (from a HbR increase) lasting 1–2 s before the standard augmentation in HbO_2; this initial dip has been reported in optical imaging (Malonek & Grinvald, 1996) but the

effect is small and not always present (R B Buxton, 2001); in some studies it has been shown that this initial augmentation of HbR is counterbalanced by an equal diminution in HbO_2 (Devor et al., 2003).

It is commonly accepted that precise regulation of blood flow involves the dilation of arterioles (Cox, Woolsey, & Rovainen, 1993), but it is not clear how the signal transfers from neurons to surrounding vasculature. One hypothesis claims that the activation of specific subsets of vasomotor interneurons can directly evoke dilation or constriction of adjacent vessels, transmuting neuronal signals into vascular responses (Cauli et al., 2004). Another hypothesis states that glutamate released from firing neurons initiates calcium waves in astrocytes; this post-synaptic calcium in turn induces the release of several vasoactive agents that are central to CBF increase (Iadecola, 2004). Furthermore, there is a growing body of evidence suggesting that astrocytes may be responsible for a critical component of neurovascular coupling and the HDR (Petzold & Murthy, 2011; Yu et al., 2010).

This complex neurovascular coupling makes the interpretation of optical imaging difficult. Nonetheless, neural activity is undoubtedly reflected in hemodynamic changes, which are detectable by the optical imaging techniques utilized in this work.

Functional connectivity

The term functional connectivity (fc) is applied to a variety of studies that examine coherent inter-regional correlations of neuronal activity during both cognitive tasks and rest (Fox & Raichle, 2007). In the present work, functional connectivity is explored in the absence of external stimuli. It is a technique sensitive to spatial and temporal synchronicity of fluctuations in neural activity from different brain areas, that may be spatially remote (Waites, Briellmann, Saling, Abbott, & Jackson, 2006). In the context of functional neuroimaging, fc is used to describe the relationship between the neurovascular activation patterns of anatomically separated regions. Synchronization has been measured by several methods, ranging from direct measures of neural activity such as local field potential (LFP) (Bressler, Ding, & Yang, 1999; Ding, Bressler, Yang, & Liang, 2000; Magill et al., 2006; Nir et al., 2008; Shmuel, Augath, Oeltermann, & Logothetis, 2006), electro-encephalography (EEG) (Aarabi, Wallois, & Grebe, 2008; Green, Sora, Bialy, Ricamato, & Thatcher, 1998; Mormann et al., 2003; C. J. Stam, Jones, Nolte, Breakspear, & Scheltens, 2007; Thatcher RW, Krause PJ, & Hrybyk M., 1986) and magnetoencephalography

(MEG) (Brookes et al., 2011; L Douw et al., 2013; Linda Douw et al., 2010; Z. Liu, Fukunaga, de Zwart, & Duyn, 2010; Pasquale et al., 2010), to indirect measures of neural-related fluctuations such as functional magnetic resonance imagining (fMRI) (Beckmann, DeLuca, Devlin, & Smith, 2005; B. Biswal et al., 1995; Damoiseaux et al., 2006; De Luca et al., 2006; Fox & Raichle, 2007; Greicius et al., 2003) and a variety of optical imaging techniques: near-infrared spectroscopy (NIRS) (Lu et al., 2010; Mesquita, Franceschini, & Boas, 2010; Sasai, Homae, Watanabe, & Taga, 2011; Wolf et al., 2011; H. Zhang et al., 2010), diffuse optical tomography (DOT) (S. M. Liao et al., 2012; Niu et al., 2011; Brian R. White et al., 2009; Brian R White, Liao, Ferradal, Inder, & Culver, 2012), optical imaging of intrinsic signals (OIS) (Bero et al., 2012; Li, Zhou, Luo, & Li, 2012; Brian R White et al., 2011) and photoacoustic tomography (PAT) (Xiang et al., 2012). The application of the aforementioned techniques will be described in the following sub-section.

Imaging techniques

EEG & MEG in humans

EEG is a technique which uses electrodes to record the spontaneous electrical activity of the brain (Gibbs, Gibbs, & Lennox, 1937). Functional connectivity between networks of neurons can be inferred from the synchronization of their respective activities (Thatcher RW et al., 1986) and has been widely studied with EEG measures in several studies, ranging from Alzheimer's disease (C. J. Stam et al., 2007), to spinal cord injury (Green et al., 1998) to epilepsy (Aarabi et al., 2008; Mormann et al., 2003; Ponten, Bartolomei, & Stam, 2007; Schindler, Leung, Elger, & Lehnertz, 2007; Wendling, Hernandez, Bellanger, Chauvel, & Bartolomei, 2005). Although invasive LFP recordings have been used to investigate task-related connectivity in the macaque cortex (Bressler et al., 1999; Ding et al., 2000; Shmuel et al., 2006; Stevenson & Körding, 2010), and the rodent brain (Magill et al., 2006), its application to human studies remains limited only to conditions where surgery management is needed, e.g. in epilepsy cases (B. J. He, Snyder, Zempel, Smyth, & Raichle, 2008; Nir et al., 2008). MEG is a non-invasive technology in which the magnetic fields induced by neuronal current flow in the brain are measured above the scalp (Cohen, 1972). Functional connectivity explored with MEG has added weight to the neural basis of fMRI (Z. Liu et al., 2010); this technique has been applied to the healthy brain (Brookes et al.,

2011; Pasquale et al., 2010), the epileptic brain (L Douw et al., 2013; Horstmann et al., 2010) and schizophrenic disease (Hinkley et al., 2010).

fMRI in humans

Several studies have shown that fMRI could use blood as a proxy for measuring the response of the neurons to sensory stimulation (Kwong et al., 1992; Ogawa et al., 1992). A similar technique using MRI to map the human visual cortex had appeared a few months earlier (Belliveau et al., 1991), with the inconvenience that a contrast agent had to be injected. fMRI is a safer and more comfortable alternative to positron emission tomography (PET), which uses a radioactive modified glucose called fluorodeoxyglucose (FDG); it is traced as it flows through the human body and its consumption will indicate the particular areas of the brain with a higher metabolism, indicating a higher neural activity (Alavi et al., 1986). PET has been widely used in both health and disease (K J Friston, Frith, Liddle, & Frackowiak, 1993), despite its poor spatial resolution, which is a limitation to human brain imaging (Dharmarajan & Schuster, 2012).

Functional connectivity was first demonstrated by fMRI detecting low-frequency variations (<0.1Hz) in the motor cortex without any external stimuli, i.e. during resting-state (B. Biswal et al., 1995). The original validation of Biswal and colleagues was that left and right hemispheric regions of the primary motor region are not silent, but show a high correlation between their BOLD time-series; the resulting spatial correlations correspond with the brain's functional activation maps as elicited by task-evoked responses.

Functional communication between separate brain regions plays an important role in complex processes; these correlations yield detailed maps of complex neural systems (B. B. Biswal et al., 2010). The observed RSNs could be consistently identified across subjects and within groups (Damoiseaux et al., 2006; De Luca et al., 2006). Therefore, the examination of functional connectivity might be of high importance because it could provide insights into the intrinsic brain organization and reorganization with cognitive processes, pathology and drug effects (Gusnard, Raichle, & Raichle, 2001; Raichle, 2011; Raichle et al., 2001; van den Heuvel & Hulshoff Pol, 2010). Several interesting studies have sprung up from these observations, assessing possible impaired functional connectivity in aging (Damoiseaux et al., 2008; J. Sun, Tong, & Yang, 2011), dementia (Gili et al., 2011; Greicius, Srivastava, Reiss, & Menon, 2004; Y. He, Chen, Gong, & Evans, 2009; Rombouts et al., 2009; Sanz-Arigita et al., 2010), epilepsy (W. Liao et al.,

2011; C. Luo et al., 2012; Mankinen et al., 2012; Waites et al., 2006; Z. Wang et al., 2011; Z. Zhang et al., 2009), cardiovascular disease (Cheng et al., 2012; Y. Sun et al., 2011; van Norden et al., 2011), schizophrenia (Lawrie et al., 2002; Y. Liu et al., 2008; Whitfield-Gabrieli et al., 2009) and depression (Greicius et al., 2007).

The discovery of functional connectivity MRI has led to a wide application in neuroimaging research (B. B. Biswal et al., 2010; Fox & Raichle, 2007; van den Heuvel & Hulshoff Pol, 2010), including insights into infant brain development (Fair et al., 2007, 2008; Fransson et al., 2007), the preterm infant (Damaraju et al., 2010; Doria et al., 2010; W.-C. Liu, Flax, Guise, Sukul, & Benasich, 2008; Smyser et al., 2010) and pediatric Tourette syndrome (Church et al., 2009).

Optical imaging in humans

Optical imaging has strong clinical potential, because it has the ability to monitor brain function in longitudinal, non-invasive way, not unlike fMRI, while providing better temporal resolution and sensitivity to two distinct endogenous contrasts HBO_2 and HbR. The translation of resting state fMRI to optical techniques, such as NIRS has enabled new developmental studies. Yet, its application poses significant challenges due to the influence of systemic physiology and superficial signals. Spontaneous low frequency fluctuations of brain hemodynamics have been investigated by NIRS (Elwell, Springett, Hillman, & Delpy, 1999; Mesquita et al., 2010; Obrig et al., 2000). Temporal correlations using NIRS have been found in resting-state adults (Toronov et al., 2000; Wolf et al., 2011), in elderly subjects (Schroeter, Schmiedel, & von Cramon, 2004) and in sleeping infants (Taga et al., 2000). The aforementioned findings have motivated several studies using NIRS that have successfully demonstrated functional connectivity (Lu et al., 2010; H. Zhang et al., 2010), outlining frequency-specific characteristics, dependent on the studied brain regions (Sasai et al., 2011). While such studies have shown interesting results, they suffer from performance limitations, such as low spatial resolution (~3cm, barely sufficient to resolve the spatial extent of the BOLD response ~$4cm^3$ (Saad, Ropella, DeYoe, & Bandettini, 2003)) that may average spatial correlations and the need of a large FOV to cover both correlated and uncorrelated regions (Brian Richard White, 2012). These limitations have prompted the use of DOT systems with high-density of sources and detectors; this approach has the capability to yield three-dimensional reconstructions of hemoglobin maps through the resolution of the inverse problem. Resting-state functional connectivity has been since revealed by DOT in both in the

adult brain (Niu et al., 2011; Brian R. White et al., 2009) and the neonatal brain (Brian R White et al., 2012).

fMRI in animals

The application of fMRI in the animal brain has remained scarce, because a high intensity magnetic field is required in order to obtain sufficient SNR and spatial resolution for small animal imaging (Benveniste & Blackband, 2002; Jonckers et al., 2011); until recent demonstrations, functional connectivity-MRI (fcMRI) has been limited to either the rat brain (Bifone, Gozzi, & Schwarz, 2010; B. B. Biswal & Kannurpatti, 2009; Hutchison, Mirsattari, Jones, Gati, & Leung, 2010; Kalthoff, Seehafer, Po, Wiedermann, & Hoehn, 2011; Kannurpatti, Biswal, Kim, & Rosen, 2008; Magnuson, Majeed, & Keilholz, 2010; Pawela et al., 2008, 2009, 2010; van Meer, van der Marel, Otte, Berkelbach van der Sprenkel, & Dijkhuizen, 2010; F. Zhao, Zhao, Zhou, Wu, & Hu, 2008) or the monkey brain (Moeller, Nallasamy, Tsao, & Freiwald, 2009; Shmuel & Leopold, 2008; Teichert, Grinband, Hirsch, & Ferrera, 2010; Vincent et al., 2007). Extending these studies to a well-established and widely used species in clinical research, such as the mouse, would permit the use of this tool in multiple robust disease models. In this context, a recent effort was made to establish a comparison of resting-state functional maps between the mouse and the rat (Jonckers et al., 2011).

Optical imaging in animals

Despite many advantages offered by the non-invasive nature of fMRI, there has been intense debate on the origin of the measured signal, especially because the measured BOLD effect is the combination of several metabolic byproducts: HbR concentration, CBF and CBV within a voxel on the order of the cubic millimeter and within a temporal resolution (repetition time, TR) around 2 – 3 seconds, for a typical fMRI acquisition (De Luca et al., 2006). Therefore, independent measures of HbR, HbO_2, CBV and CBF with high spatial (~50μm) and temporal resolution (~5 Hz) is a key to better characterize vascular dynamics at the cortex level.

Optical imaging of intrinsic signals (OIS) is a technique that can be used to compute measurements of blood oxygenation, based on the distinct absorption spectra of HbO_2 and HbR. The setup is relatively simple: light at the appropriate wavelengths is shone upon the exposed nervous tissue and images are then captured with a CCD camera. The neuronal activity changes the local concentration in HbO_2 and HbR. Consequently, the light absorption properties of

nervous tissue are modified due to fluctuations in these components, meaning that the amount of reflected light will also change. OIS has been applied in neuroscience research (Frostig, Lieke, Ts'o, & Grinvald, 1990; Grinvald, Lieke, Frostig, Gilbert, & Wiesel, 1986; Ts'o, Frostig, Lieke, & Grinvald, 1990) and has been since a well-established method to image neural activity in the exposed cortex of the animal (Cang, Kalatsky, Löwel, & Stryker, 2005; Dunn, Devor, Dale, & Boas, 2005; W. Luo, Li, Chen, Zeng, & Luo, 2007).

Whereas OIS provides measurements of blood oxygenation, it does not explicitly measure blood flow. Laser speckle contrast imaging (LSCI) is used to provide relative variations in CBF. LSCI uses a similar setup to OIS, but the light is replaced with a diverging laser diode (E. M. C. Hillman, 2007). When this coherent light is incident upon a turbid medium, such as biological tissue, it scatters producing an interference pattern called speckle (Boas & Dunn, 2010). Speckle contrast is quantified from the blurred images at each time point (the ratio of standard deviation to mean intensity). If there are moving scatterers in tissue, such as blood cells, each speckle will be fluctuating in intensity. These fluctuations cause a blurring of the speckle, leading to a reduction in the speckle contrast. Therefore blood flow variations can be determined from speckle contrast variations (Boas & Dunn, 2010; Dunn, Bolay, Moskowitz, & Boas, 2001).

$CMRO_2$ can be estimated from blood flow and blood volume measurements (Dunn et al., 2005; M. Jones, Berwick, Johnston, & Mayhew, 2001; Mayhew et al., 2000). Assuming that changes in CBV are proportional to changes in HbT, the Grubb equation can be used to explore the relationship between HbT and CBF (Grubb, Raichle, Eichling, & Ter-Pogossian, 1974). The simultaneous measurement of multiple hemodynamic parameters has provided a more complete picture of the hemodynamic response to functional activation (Dunn et al., 2005). This technique has assessed lesions in the spinal cord (Brieu et al., 2010) as well as effects of cerebral ischemia on the cerebral cortex (P. B. Jones et al., 2008; Luckl et al., 2010).

Photoacoustic tomography in animals

Photoacoustic tomography (PAT) is a non-invasive technique that combines the intrinsic contrast capabilities of optical imaging with the advantage of high spatial resolution of ultrasound (L. V. Wang & Hu, 2012). A short laser pulse is absorbed by molecules in living tissue, generating an ultrasonic pressure wave, which is detected by an ultrasound transducer to form images (X. Wang et al., 2003). Application of PAT imaging to study functional connectivity is uncommon. An

application was recently showed (Xiang et al., 2012) where epileptic brain networks were analyzed through the Granger causality method (Granger, 1969).

Objectives

O1: The first aim of this thesis was to develop tools for the analysis of functional connectivity using optical imaging. These tools were then validated in an acute murine model of epilepsy. For this aim the following hypotheses were tested:

> **H1.1:** Regional bilateral functional connectivity is disrupted after the injection of a focal epileptogenic agent.
>
> **H1.2:** Changes in functional connectivity correlate with seizure duration.

The article related to this objective is:

Guevara, E., Pouliot, P., Nguyen, D. K., & Lesage, F. (2013). Optical imaging of acute epileptic networks in mice. *Journal of Biomedical Optics*, *18*(7), 076021–076021. doi:10.1117/1.JBO.18.7.076021.

O_2**:** The second objective was to use functional connectivity methods to investigate changes in a novel carotid stiffness murine model, testing the following hypothesis:

> **H2.1:** Uncoupling is shown between hemodynamic measures and metabolic activity in bilateral functional correlations.
>
> **H2.2:** Resting state functional networks derived from hemodynamic signals are disrupted following a unilateral carotid artery calcification.

The paper where this objective is pursued is:

Guevara, E., Sadekova, N., Girouard, H., & Lesage, F. (2013). Optical imaging of resting-state functional connectivity in a novel arterial stiffness model. *Submitted to Biomedical Optics Express*.

O3: Finally, the third aim was to use photoacoustic tomography (PAT) imaging resting-state to assess the impact of an acute inflammatory injury in the neonatal rat brain. The following hypothesis was put under test:

H3.1: Local SO_2 values are significantly lower in the injured group, as compared to sham controls.

H3.2: Bilateral functional connectivity decreases significantly in pups with inflammatory brain injury.

The article related to this objective is:

Guevara, E., Berti, R., Londono, I., Xie, N., Bellec, P., Lesage, F., & Lodygensky, G. A. (2013). Imaging of periventricular leukomalacia in the newborn rat brain with photoacoustic tomography. *Submitted to PLOS ONE*.

Other contributions

Within the work performed for this thesis, preliminary and sometimes complementary results were obtained separately; these efforts are described in the following publications:

In the exploration of optical imaging in the spinal cord, I was able to contribute to the following articles:

Ouakli, N., Guevara, E., Dubeau, S., Beaumont, E., & Lesage, F. (2010). Laminar optical tomography of the hemodynamic response in the lumbar spinal cord of rats. *Optics Express*, *18*(10), 10068–10077. doi:10.1364/OE.18.010068

Beaumont, E., Guevara, E., Dubeau, S., Lesage, F., Nagai, M., & Popovic, M. R. (2013). Functional electrical stimulation post spinal cord injury improves locomotion and increases afferent input into the central nervous system in rats. *Journal of Spinal Cord Medicine*. doi: http://dx.doi.org/10.1179/2045772313Y.0000000117

And the following conferences:

Beaumont, E., Guevara, E., Nagai, M., Lesage, F., & Popovic, M. R. (2010). Optimizing the spinal cord neuronal circuitry to restore locomotion after a spinal cord injury by using functional electrical stimulation. In *Neuroscience 2010* (Vol. 40, p. 259.28). Presented at the Neuroscience 2010, San Diego, CA, USA: Society for Neuroscience. Retrieved from http://books.google.ca/books?id=JF6Q0ajTk44C&pg=PT709&lpg=PT709&dq=%22Optimizing+

the+spinal+cord+neuronal+circuitry+to+restore+locomotion+after+a+spinal+cord+injury+by+using+functional+electrical+stimulation%22&source=bl&ots=cJYtrgWvV9&sig=GTeDym6DTe0kjjKtiEFAiaw9Y_U&hl=en&sa=X&ei=5r0SUdCeMIT9ygGXvIGADA&ved=0CCwQ6AEwAA

Guevara, E., Abran, M., Belanger, S., Ouakli, N., & Lesage, F. (2010). Comparison of the performance of two depth-resolved optical imaging systems: laminar optical tomography and spatially modulated imaging. In A. P. Wax & V. Backman (Eds.), *Biomedical Applications of Light Scattering IV* (Vol. 7573, pp. 757317–10). Presented at the Biomedical Applications of Light Scattering IV, San Francisco, California, USA: SPIE. doi:10.1117/12.841886

Guevara, E., Ouakli, N., Dubeau, S., Beaumont, E., & Lesage, F. (2010a). Hemodynamic response revealed by laminar optical tomography in rat lumbar cord. In *GRSTB 2010 Student Poster Day*. Presented at the GRSTB 2010 Student Poster Day, University of Montreal.

Guevara, E., Ouakli, N., Dubeau, S., Beaumont, E., & Lesage, F. (2010b). Réponse hémodynamique dans la moelle épinière du rat mesurée à l'aide de la tomographie laminaire optique. In *78ième congrès de l'ACFAS*. Presented at the 78ième congrès de l'ACFAS, Université de Montréal. Retrieved from http://www.acfas.net/programme/c_78_219.html#

Guevara, E., Beaumont, E., & Lesage, F. (2011). Imaginología óptica en la médula espinal. In *18ª. Semana de La Ciencia y Tecnología*. Presented at the 18ª. Semana de La Ciencia y Tecnología, Universidad Tecnológica de Tula–Tepeji, México.

As part of the applications of optical coherence tomography I collaborated in this article:

Sadekova, N., Vallerand, D., Guevara, E., Lesage, F., & Girouard, H. (2013). Carotid calcification in mice: a new model to study the effects of arterial stiffness on the brain. *Journal of the American Heart Association*, *2*(3), e000224. doi:10.1161/JAHA.113.000224

And the following conferences:

Guevara, E. (2012a, April 27). *Optical Coherence Tomography*. Presented at the First Mexican-Canadian Biomedical Imaging Meeting, Coordinación para la Innovación y la Aplicación de la Ciencia y Tecnología de la UASLP.

Guevara, E. (2012b, May 16). *Tomografía por Coherencia Óptica*. Invited conference, Instituto Tecnológico Superior de San Luis Potosí.

Sadekova, N., Vallerand, D., Guevara, E., Lesage, F., & Girouard, H. (2013). La calcification des carotides altère l'homéostasie cérébrale chez la souris. In *21e Réunion Scientifique Annuelle*. Presented at the Congrès de la Société Québécoise d'Hypertension Artérielle, Montreal (Canada). Retrieved from http://www.hypertension.qc.ca/gestion/pdf/2013-Sciences-fondamentales.pdf

Finally, the preliminary results contributing to the objective O3 of this thesis were presented in the conference:

Berti, R., Matteau-Pelletier, C., Guevara, E., Londono, I., Lesage, F., & Lodygensky, G. A. (2013). Locoregional Cortical Oxygen Saturation and Resting State Assessment by Photoacoustic Imaging Following an Inflammatory Injury in the Neonatal Rat Brain. In *Pediatric Academic Societies Annual Meeting*. Presented at the 2013 PAS Annual Meeting, Washington, DC.

CHAPTER 1 OPTICAL IMAGING OF INTRINSIC SIGNALS

Optical methods, such as intrinsic and speckle imaging have proved being useful to study neural function in the small animal. These optical techniques can distinguish distinct hemoglobin types (HbO_2 and HbR) and CBF, providing a whole set of hemodynamic parameters to assess neural activity. Both these techniques have been successfully applied to imaging neural activity on the exposed cortex of the small animal (Dunn et al., 2003, 2005; M. Jones et al., 2001).

1.1 Optical Intrinsic Signals (OIS) system description

Optical images based on intrinsic signals (OIS) were acquired with a 12-bit CCD camera (Pantera 1M60, DS-21-01M60-12E, Teledyne Dalsa, Waterloo, ON) with a pixel size of 12µm and full resolution of 1024×1024 pixels. The setup used in this work is depicted in Figure 1-1A:

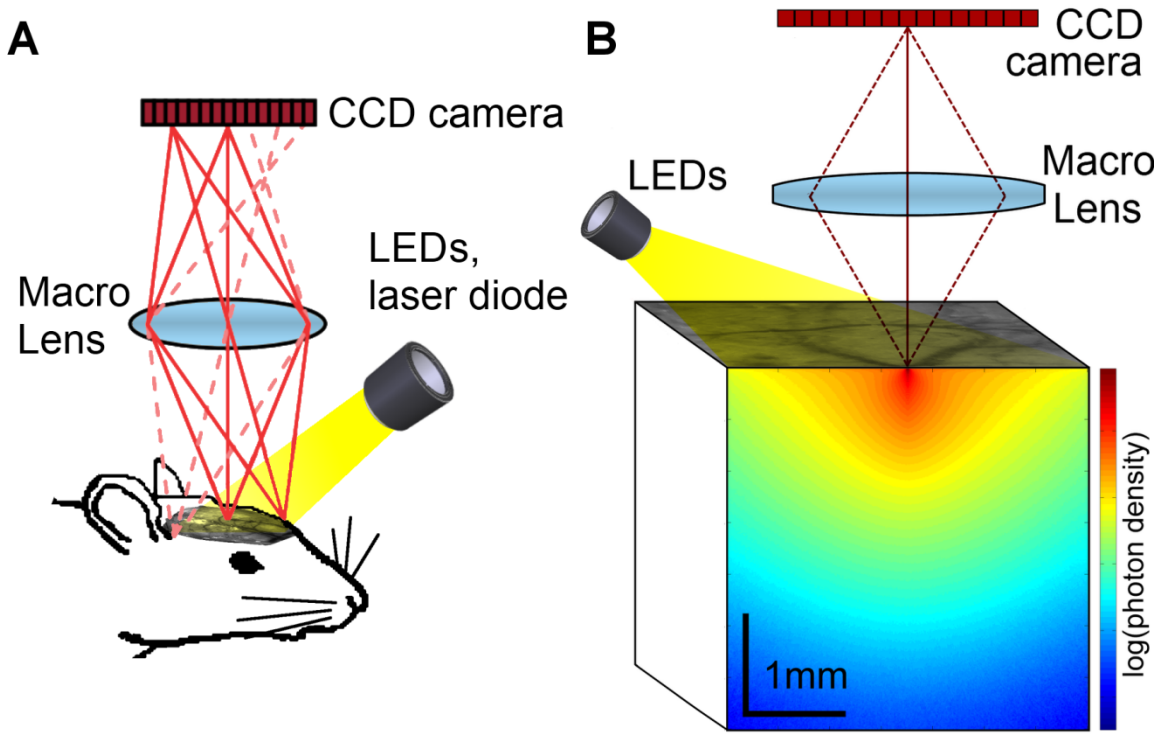

Figure 1-1: (A) Overview of the intrinsic signal optical imaging system. (B) Sensitivity profile of optical imaging of intrinsic signals (λ=625nm).

A custom-made interface programmed in LabView controls the camera, grabs images and physiological signs, while synchronizing acquisition and illumination. A Macro Lens (105mm f/2.8max, Sigma Corp., Ronkonkoma, NY) with small focal depth (350 µm) is used. Reflectance

images of the brain cortex are recorded with time-multiplexed illumination (525, 590, 625 nm) produced by 10W LEDs (LZ4-00MA00, Led Engin, San Diego, CA). Illumination for speckle imaging was provided by 90 mW, 785 nm laser diode (L785P090, Thorlabs, Newton, NJ) and aperture was adjusted to f/8, so that the pixel size and speckle size are matched (Briers, 2001). Aperture adjustment is important to ensure proper sampling of the speckle pattern: the size of a single speckle should be equal to the width of the diffraction-limited spot size and is given by $2.44\lambda(f/\#)$, where λ is the wavelength and *f/#* is the f-number of the system (Dunn et al., 2001). The four illumination diodes are interleaved, which yields a full-frame rate of 5 Hz for each wavelength. A 2×2 binning on camera is performed to allow continuous data streaming to hard drive. Illumination is usually adjusted so that no part of the brain is under- or over-saturated by any of the wavelengths. The exposure time of the camera is set to 10 ms. The whole optical setup is mounted on an optic table with tuned damping (RS 2000, Newport, Irvine, CA) to avoid spurious signals from vibrations.

1.2 OIS theory

Brain optical absorption in the visible spectrum originates primarily from the two types of hemoglobin: HbO_2 and HbR. Knowing their molar extinction coefficients $\epsilon_i(\lambda)$, their differential path length factor D(λ) and assuming a baseline molar concentration C_i, changes in hemoglobin concentration can then be estimated with optical measurements at two different wavelengths, at least. Figure 1-2 shows the molar extinction coefficients of both types of hemoglobin as a function of wavelength, along with the spectral profile of the LEDs used in the OIS setup.

The analysis of spectroscopic images was based on previously published work (Dubeau, Ferland, Gaudreau, Beaumont, & Lesage, 2011; Dunn et al., 2003). In short reflectance images from each LED wavelength were recorded with the CCD camera and interpreted as changes in attenuation (optical density) $\Delta OD = \log(I_0/I)$, where I is the reflected light intensity and I_0 the incident light intensity. Relative changes in oxy- and deoxyhemoglobin were found using the modified Beer-Lambert law (Delpy et al., 1988) and a Moore-Penrose pseudoinverse:

$$\Delta OD(\lambda, t) = \sum_i \epsilon_i(\lambda)\, C_i(t) D(\lambda) \tag{1.1}$$

D(λ) was taken from (Dunn et al., 2005) and values out of the 560-610 nm range were extrapolated from (Kohl et al., 2000). Total hemoglobin baseline concentration of 100 μM with 60% oxygen saturation was assumed (Dunn et al., 2005) for the spectroscopic analysis. These hemoglobin values were estimated for the whole rat brain in the study by (Mayhew et al., 2000). The hemoglobin molar extinction coefficients $\epsilon_i(\lambda)$ (see Figure 1-2) were obtained from (Prahl, 1999); $\epsilon_i(\lambda)$ describes the probability of photon interaction (absorption or scattering) with the medium per unit path-length and per molar concentration (L. V. Wang & Wu, 2007, p. 6). Reflectance values were corrected for the spectral response of the CCD camera and convolved with the LEDs spectral power distribution (Brieu et al., 2010).

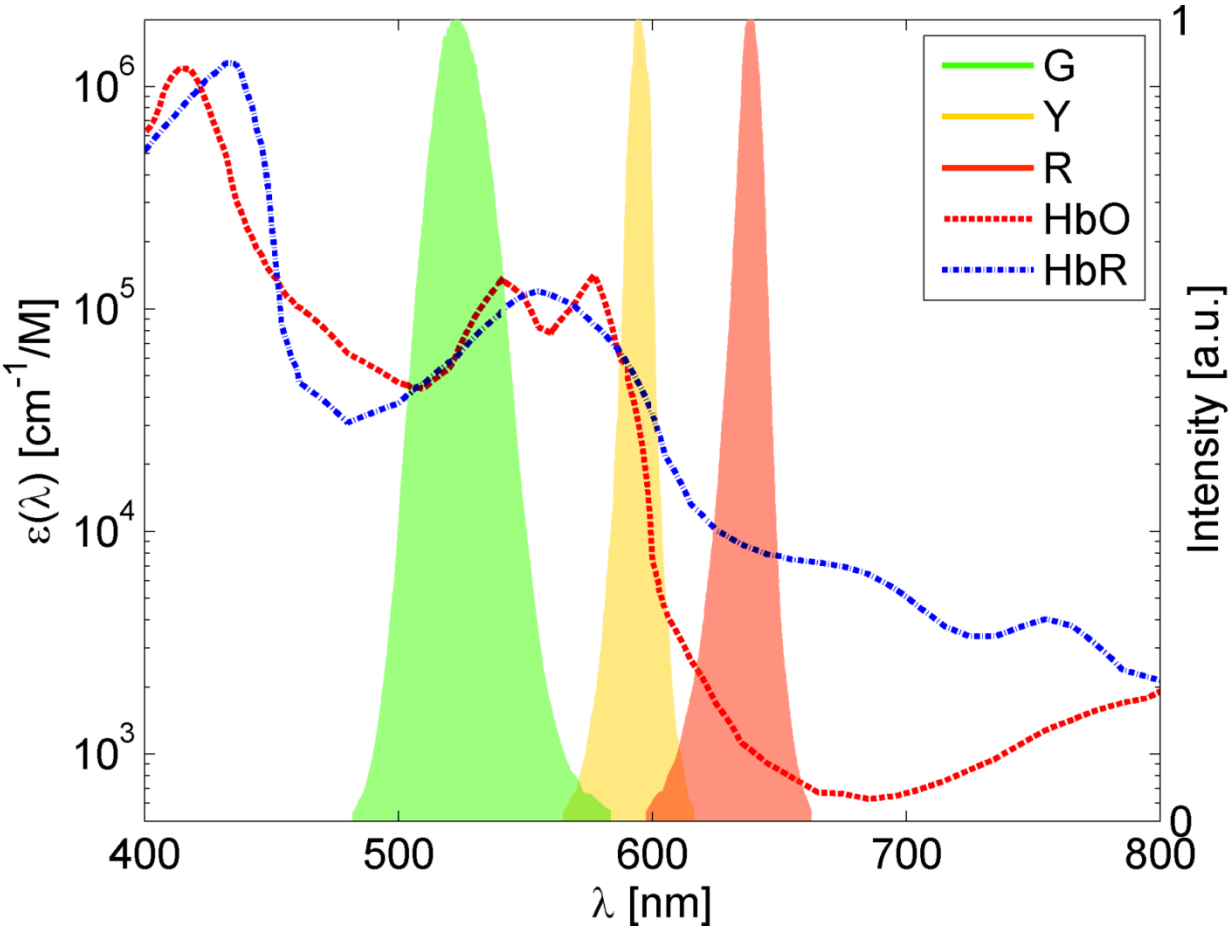

Figure 1-2: Optical absorption of oxy- and deoxy-hemoglobin (HbO_2 and HbR) and measured spectra of the LEDs (Green, Yellow and Red) used on the OIS imaging system.

In the computation of hemoglobin concentrations light absorption was assumed to be uniform all over the imaged FOV. Since penetration depth in tissue depends on the wavelength, some

wavelengths are more sensitive to deeper changes in absorption. This is not taken into account in equation (1.1); a Monte Carlo simulation of a sensitivity profile for measurements taken at λ=625nm is shown in Figure 1-1B, indicating that OIS is most sensitive up to depths of ~500µm.

1.3 OIS system characterization

SNR and resolution were estimated with a negative USAF 1951 microscope target (R3L3S1N, Thorlabs, Newton NJ), acquiring images at a single wavelength (λ=525nm) and with the same parameters (camera mode, aperture, integration time, binning and gain) as in the animal experiments. The metric considered was differential SNR, given by equation(1.2); SNR_{diff} was obtained by taking the difference in intensity values between the target f_t and the background f_b integrated over the area A of the target, and by dividing it by the standard deviation σ_b of image intensity values over the area A of the background (Prince & Links, 2005, p. 89). The computed SNR_{diff} was approximately equal to 112:1 (41 dB).

$$SNR_{diff} = \frac{A(f_t - f_b)}{\sigma_b(A)} \tag{1.2}$$

Resolution was defined as the full-width at half maximum (FWHM) of the smallest distinguishable element, in this case it corresponds to element 3 from group 3 (10.10 lines pairs/mm) and the measured FWHM was ~60µm, as shown on Figure 1-3:

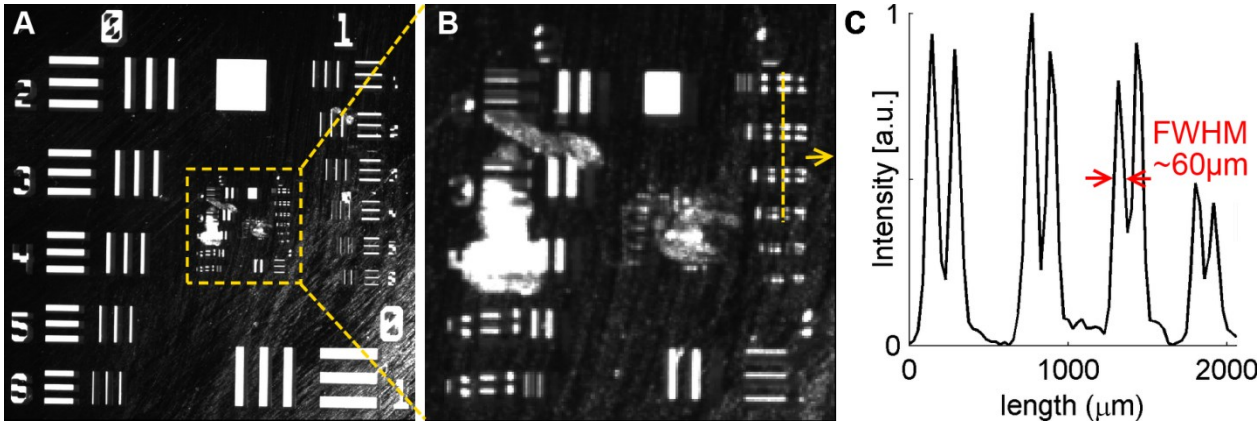

Figure 1-3: (A) Full FOV of the resolution target (20×20mm^2). (B) Zoom on the dotted square in A; the vertical dotted line is 2mm long and it is placed over the smallest resolvable features. (C) Intensity profile along the dotted line in B.

1.4 Laser speckle contrast imaging

In addition to imaging changes in hemoglobin concentrations, changes in cerebral blood flow (CBF) were also computed by LSCI. Speckle originates from the random interference of multiple backscattered coherent light. In the presence of moving scatterers the interference field fluctuates, creating intensity variations, known as speckle patterns (Boas & Dunn, 2010; Dunn et al., 2001, 2005). When integrated over the exposure time of the camera, the speckle pattern becomes blurred in areas of increased blood flow. Images of blood flow were obtained by measuring the spatial contrast of the speckle *C*, defined as the ratio of the standard deviation to the average intensity $\sigma/\langle I\rangle$. The contrast is a function of the CCD camera exposure time *T* and it is related to the correlation time τ_C of the speckle, which is assumed to be inversely proportional to the speed of the scattering particles (Briers & Webster, 1995; Briers, 2001).

A sliding window of 5×5 pixels was used to compute the speckle contrast images in order to balance the tradeoff between adequate estimates of the speckle contrast and spatial resolution. Assuming a Lorentzian distribution of the scatterers, speckle contrast was calculated with the equation (1.3), a plot of this equation is presented in Figure 1-4.

$$C = \frac{\sigma}{\langle I\rangle} = \sqrt{\left(\frac{\tau_c}{2T}\right)\left(1 - e^{\frac{-2T}{\tau_c}}\right)} \tag{1.3}$$

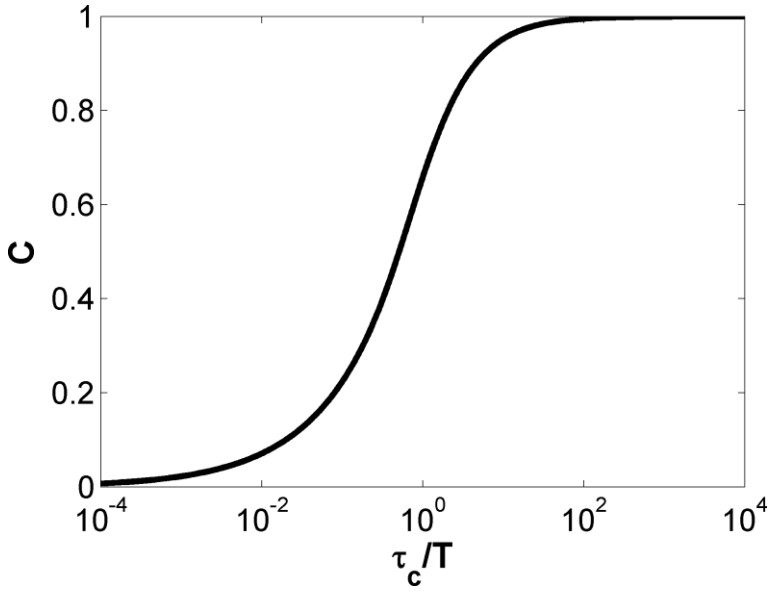

Figure 1-4: Variation of the speckle contrast C with the ratio correlation time to exposure time τ_c/T.

When the integration time T is much greater than the speckle correlation time τ_C, we are at the asymptotic regime (Duncan & Kirkpatrick, 2008), therefore equation (1.3) can be simplified into equation (1.4). Although relative variation of the scatterers velocity $\Delta v/v_0$ is not directly related to CBF, laser speckle imaging underestimates CBF by less than 5% (Luckl et al., 2010), so both quantities were assumed to be equal in this work. Relative changes in blood flow were obtained via the following formula:

$$-\frac{2\Delta C}{C_0} \approx \frac{\Delta v}{v_0} \approx \frac{\Delta CBF}{CBF_0} \tag{1.4}$$

Note the minus sign in equation (1.4) due to the conversion of speckle contrast values to intensity autocorrelation decay time, which is inversely proportional to blood flow (Bonner & Nossal, 1981).

1.5 Cerebral metabolic rate of oxygen

Measured changes in CBF, total hemoglobin (HbT) and HbR are combined in a steady state mathematical model (1.5) to estimate changes in the cerebral metabolic rate of oxygen consumption ($CMRO_2$) (M. Jones et al., 2001; Mayhew et al., 2000):

$$\frac{\Delta CMRO_2}{CMRO_{2,0}} = \frac{\left(1+\frac{\Delta CBF}{CBF_0}\right)\left(1+\gamma_R\frac{\Delta HbR}{HbR_0}\right)}{\left(1+\gamma_T\frac{\Delta HbT}{HbT_0}\right)} - 1 \tag{1.5}$$

RSNs are identified from data band-pass filtered (0.009-0.08 Hz); these low frequency fluctuations are considered to agree with the central hypothesis of the aforementioned model, which states its validity in the absence of transients of hemodynamic components. The constants γ_R and γ_T are chosen within a physiologically plausible range (0.75–1.25)(M. Jones et al., 2001); usually their value is set to 1.

1.6 Conclusions

In this chapter I have shown how OIS and LSCI allow us to obtain HbO_2, HbR and CBF images. These three hemodynamic measures can then be used in physiological models to characterize the hemodynamic response via the relative changes in metabolism. All these measures were used in the identification of resting-state networks.

CHAPTER 2 LAMINAR OPTICAL TOMOGRAPHY

Optical imaging of intrinsic signals and laser speckle imaging have been proved to be useful to image the neural activity in the cortex (Dunn et al., 2005; M. Jones et al., 2001; W. Luo et al., 2007), nevertheless their application in the spinal cord is not common (Beaumont et al., 2013; Beaumont, Brieu, Dubeau, & Lesage, 2008a, 2008b; Brieu et al., 2010; Brieu, Beaumont, & Lesage, 2008; Lesage, Brieu, Dubeau, & Beaumont, 2009; Sasaki et al., 2002; Sasaki, Sato, Shinomiya, & Momose-Sato, 2003) because of multiple difficulties including animal preparation, minimization of thoracic movements and above all, the deeper localization of the interneurons (1-1.5 mm in the adult rat) due to white matter surrounding the gray matter. An optical technology that can quantify light absorption changes at a deep of 1~2 mm will allow to observe the hemodynamic activity of the embedded gray matter, thus providing complementary information to the well established techniques. Such technique is described in the present chapter.

Laminar Optical Tomography (LOT) is a recently developed three-dimensional optical imaging technique in turbid media, sensitive to relative changes in light absorption, mainly from the chromophores oxy- and deoxy-hemoglobin (E. M. C. Hillman, Boas, Dale, & Dunn, 2004). In LOT, light is injected serially into the sample by scanning the surface imaged with a light source with two galvanometer mirrors. This technique utilizes different source-detector separations to collect light emerging at different distances from the source position. The wider the distance between the source position and the detector position, the deeper on average the detected light has traveled. This results in a dataset containing rich information about the depth-resolved properties of the tissue(E. M. C. Hillman & Burgess, 2008). Figure 2-2 shows the schematic of the imaging system developed in the laboratory.

2.1 LOT theory

In order to obtain full 3D images from LOT measurements one needs an *a priori* knowledge of light propagation. A model of light propagation in turbid media, such as biological tissue is described by the radiative transfer equation (RTE) (Arridge & Hebden, 1997),

$$\frac{1}{c}\frac{\partial I}{\partial t} + \hat{s}\cdot\nabla I(r,t,\hat{s}) + (\mu_a+\mu_s)I(r,t,\hat{s}) - \mu_s\int_{S^2} f(\hat{s},\hat{s}')I(r,t,\hat{s}')d^2\hat{s}' = q(r,t,\hat{s}') \qquad (2.1)$$

where the parameters μ_a and μ_s are the absorption and scattering coefficients respectively, c is the speed of light in the medium, I is the radiance (also called specific intensity) at a position r in a direction $\hat{s}$. The first term $\frac{1}{c}\frac{\partial I}{\partial t}$ is the change of the radiance within the solid angle element; the term $\hat{s}\cdot\nabla I(r,t,\hat{s})$ is a loss due to divergence, independently of the optical properties of the diffusing medium D; $(\mu_a+\mu_s)I(r,t,\hat{s})$ represents the probability of photon extinction, by either absorption or scattering; the function $f(\hat{s},\hat{s}')$ represents the probability of light with propagation direction $\hat{s}'$ being scattered into the differential solid angle element $d^2\hat{s}'$ around direction $\hat{s}$ and the right-hand side of (2.1) is the contribution from the light source q. Although the formulation of (2.1) ignores polarization and considers only elastic collisions, it is sufficient to describe light-tissue interaction in the optical imaging modalities described here. Inelastic collisions are neglected because they represent only a small fraction (about 1 in 10 million) of the scattered photons (Le, Yue, & Cheng, 2010) and the optical imaging techniques used in this work do not have the means to discriminate them.

The system described below utilize a constant-power continuous wave light beam, thus a time-independent response is measured and the first term of eq. (2.1) becomes zero, yielding the time invariant form of the RTE:

$$\hat{s}\cdot\nabla I(r,\hat{s}) + (\mu_a+\mu_s)I(r,\hat{s}) - \mu_s\int_{S^2} f(\hat{s},\hat{s}')\,I(r,\hat{s}')d^2\hat{s}' = q(r,\hat{s}') \tag{2.2}$$

To completely define the problem in a domain D bounded by the surface ∂D, boundary conditions are prescribed by:

$$I(r,\hat{s}) = 0 \qquad r\in\partial D \qquad \hat{s}\cdot\hat{n}(r) < 0 \tag{2.3}$$

With the convention that $\hat{n}(r)$ is the outward normal to boundary surface ∂D. Physically, (2.3) means that no photons travel in an inward direction at the boundary, except those due to the source q. When the source q is a diffuse point source $q(r,\hat{s})=\delta(r-r')\delta(\hat{s}-\hat{s}')$ subject the boundary conditions (2.3) the solution to (2.2) is the Green function $G(r,\hat{s};r',\hat{s}')$ so that:

$$I(r,\hat{s}) = \iint_{DS^2} G(r,\hat{s};r',\hat{s}')q(r',\hat{s}')d^2\hat{s}'d^3r' \tag{2.4}$$

In neuronal applications of LOT, the measured local changes in absorption reflect the hemodynamic response. To model those changes, the inhomogeneous absorption coefficient $\mu_a(r)$, can be decomposed into a homogenous part μ_{a0} and a spatially varying part $\delta\mu_a(r)$:

$$\mu_a(r) = \mu_{a0} + \delta\mu_a(r) \tag{2.5}$$

Substituting (2.5) into (2.2), one arrives at:

$$\hat{s} \cdot \nabla I(r,\hat{s}) + (\mu_{a0} + \mu_s) I(r,\hat{s}) - \mu_s \int_{S^2} f(\hat{s},\hat{s}')\, I(r,\hat{s}') d^2\hat{s}' = q(r,\hat{s}) - \delta\mu_a I(r,\hat{s}) \tag{2.6}$$

and according to (2.4) the solution to (2.6) is:

$$I(r,\hat{s}) = \iint_{DS^2} G_0(r,\hat{s};r',\hat{s}') q(r',\hat{s}') d^2\hat{s}' d^3r' - \iint_{DS^2} G_0(r,\hat{s};r',\hat{s}') \delta\mu_a(r') I(r',\hat{s}') d^2\hat{s}' d^3r' \tag{2.7}$$

where I is expressed as the sum of I_i, the incident radiance, and I_s, interpreted as the scattered radiance; which may be interpreted as the propagation of a secondary source of the form $q(r,\hat{s})=-\delta\mu a(r) I(r,\hat{s})$, which is the RTE equivalent of the Huygens's principle (Kim & Schotland, 2006). G_0 is the Green function in a spatially homogeneous medium. Substituting $q(r,\hat{s})=\delta(r-r')\delta(\hat{s}-\hat{s}')$ into (2.7) and using the first order Born approximation, I obtain:

$$G(r,\hat{s};r',\hat{s}') = G_0(r,\hat{s};r',\hat{s}') - \iint_{DS^2} G_0(r,\hat{s};r'',\hat{s}'') \delta\mu_a(r'') G_0(r'',s'';r',\hat{s}') d^2\hat{s}'' d^3r'' \tag{2.8}$$

Here $(r,\hat{s})$ can be denoted as $\mathbf{r}_s$, which is the source location at the boundary of the medium; and $(r',\hat{s}')$ can be represented by $\mathbf{r}_d$, where a detector is located; $(r'',\hat{s}'')$ are replaced by $\mathbf{r}$, by carrying out the angular integration over S^2 in (2.8). Finally, the following equation for every source-detector pair is obtained:

$$G(r_s,r_d) - G_0(r_s,r_d) = -\int_D G_0(r_s,r) \delta\mu_a(r) G_0(r,r_d) d^3r \tag{2.9}$$

Three-dimensional images of the spatially varying absorption coefficient $\delta\mu_a(\mathbf{r})$ can then be reconstructed given measurements of the $G(\mathbf{r}_s,\mathbf{r}_d)$ and $G_0(\mathbf{r}_s,\mathbf{r}_d)$, from the perturbed and

unperturbed states, respectively. Calculating $G_0(\mathbf{r}_s,\mathbf{r})$ and $G_0(\mathbf{r},\mathbf{r}_d)$, the Green functions for the source and the detector, which are known from the background optical properties and inverting the discretized form of (2.9) to find $\delta\mu_a(\boldsymbol{r})$ completes the reconstruction procedure. The discretized form of the integral equation (2.9) can be expressed as:

$$\Delta M_{s,d} = A_{s,d}(r)\Delta\mu_a(r) \tag{2.10}$$

Eq. (2.10) states that a small change in the absorption coefficient $\Delta\mu_a(\boldsymbol{r})$ will result in a change in the measurement $\Delta M_{s,d}$ between source position s and detector position d measured at the surface of the sample(E. M. C. Hillman & Burgess, 2008). These changes are related by the spatial sensitivity matrix $A_{s,d}$ (also known as the weight function or photon measurement density function), which is derived from the source detector Green functions. Practical calculations of the Green functions derived from the RTE involve modeling individual photon interactions governed by local optical properties and this photon migration can be simulated numerically by the Monte Carlo method, mainly because analytic Green functions for the RTE are known only for relatively simple geometries (Kim & Schotland, 2006). An accurate Monte Carlo model is used to generate source-detector Green functions (Boas, Culver, Stott, & Dunn, 2002). The practical implementation of (2.10) requires normalizing the measurements by M_0, representing the unperturbed signal. The right hand side of (2.10) must be similarly divided by I_0, representing the simulated signal that would be detected from the sample in the absence of an inclusion:

$$\frac{\Delta M_{s,d}}{M_{0s,d}} = \frac{A_{s,d}(r)}{I_{0s,d}}\Delta\mu_a(r) \tag{2.11}$$

Once the propagation model is obtained, image reconstruction is performed by solving the equation system, however A, i.e. the sensitivity matrix calculated from $A_{s,d}$, is a nonsquare matrix and cannot be directly inverted. In order to find its Moore-Penrose generalized pseudoinverse $A^{\dagger}$, both sides of Eq. (2.2) are multiplied by its conjugate transpose A^H to create a square matrix that can then be inverted:

$$\begin{aligned} A^H\Delta M &= A^H A\Delta\mu_a \\ (A^H A)^{-1}A^H\Delta M &= \Delta\mu_a \\ A^T\Delta M &= \Delta\mu_a \end{aligned} \tag{2.12}$$

This reconstruction process is ill-posed (Vogel, 2002) in the sense that noise in data ΔM may give rise to significant errors in the estimated absorption coefficients μ_a. Simple regularization techniques are used below to deal with ill-posedness. The regularization technique employed was based on the truncated singular value decomposition of the sensitivity matrix A, where any singular value less than a certain tolerance value is treated as zero. The tolerance limit was set empirically to give the maximum contrast. This Moore-Penrose pseudoinverse has a very high computational cost, and this regularization technique is feasible for spatially modulated imaging (Belanger, Abran, Intes, Casanova, & Lesage, 2010; Guevara, Abran, Belanger, Ouakli, & Lesage, 2010). However, LOT generates more measurements for a 3D reconstruction, hence the need for another regularization technique less computationally expensive. The inversion method described in references (E. M. C. Hillman et al., 2004; E. M. C. Hillman & Burgess, 2008) is then used where a Tikhonov regularization was used to find the solution to this underdetermined problem:

$$\Delta\mu_a = A^T(AA^T + \alpha I)^{-1}\Delta M \tag{2.13}$$

where α is the regularization parameter and I is the identity matrix. Finding a suitable regularization parameter is a challenge faced by all forms of optical tomography. There exist several methods that allow the selection of a regularization parameter α so that the corresponding regularized solution $\Delta\mu_a$ minimizes some measure of the size of the solution error. One of these methods is the L-curve method; to implement it, one plots the log of the regularized solution against the squared norm of the regularized residual for a range of values of the regularization parameter α. This curve is given in Figure 2-1. The criterion for α selection is to pick the parameter corresponding to the corner of this curve (Vogel, 2002), which minimizes the error norm. All reconstructions were carried out with the same regularization method, i.e. Tikhonov regularization.

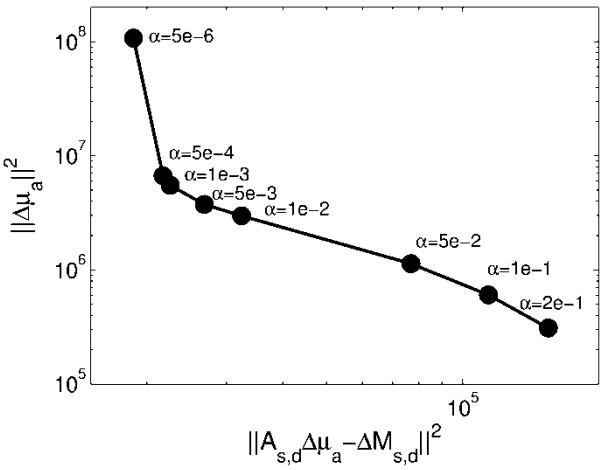

Figure 2-1: L-curve analysis from a LOT reconstruction with SNR=60dB. The parameter that minimizes the error corresponds to the point of maximum curvature of this curve. In this case a value α=5e-4 was chosen.

2.2 LOT system description

The experimental setup used in this study has been described in detail in other papers (Burgess, Baohong, Radosevich, Bouchard, & Hillman, 2007; E. M. C. Hillman & Burgess, 2008; E. M. C. Hillman et al., 2007, 2004; E. M. C. Hillman, Bouchard, Devor, Crespigny, & Boas, 2006; Elizabeth M. C. Hillman, 2006; B. Yuan et al., 2009), but the main features of the system are briefly mentioned here. The system is illuminated by one laser diode (HL6738, Opnext Inc.), which outputs a beam at 35 mW, although it may differ from the effective power used for imaging, as it is diminished by the system's optical components. The laser beam is collimated, linearly polarized and then sent into the beamsplitter (50:50, 25.4mm diameter, Y43736 Edmund Optics). The beam emerging from the beam splitter is incident into the scanning system. The scanning system consists of two scanning mirrors, and the electronics to drive and monitor the mirrors. In order to achieve a high frame rate and an adequate number of pixels in the digitized images, the scanning device must operate at several kHz. One scanner that meets our requirements is a resonant scanner (SC-10 with driver PLD-XYG, Electro-Optical Products Corp.) that oscillates sinusoidally at a pre-set resonant frequency of 1.5 kHz. The resulting delay varies sinusoidally, thus distorting the image along the rapid axis. A software implementation was developed to correct for this nonlinearity. The second scanner controlled by that same driver is a galvanometer mirror (6810P, Cambridge Technology, Inc.) operating at 15 Hz to provide a

linear frame-scan with an effective frame rate of 7.5 frames/s. The magnitudes of the scanning angles of the mirrors can be adjusted through two knobs on the panel of the driver box, adjusting in turn the field of view (FOV) of the system. The beam reflects from the galvanometer mirror and is focused by a scan lens (f_{scan}=25.4 mm, 25.4mm diameter, LB1761-B, Thorlabs, Newton NJ) on an intermediate focal plane. This plane is then imaged directly into the sample by an objective lens ($f_{objective}$=50mm, 25.4mm diameter, LB1471-B, Thorlabs, Newton NJ). Light re-emitted from the imaged object passes back up through the objective, through the scan lens and onto the scanning system, where it is de-scanned. It passes then into the beam splitter, where it is reflected towards the detection plane. This returning light is composed from specularly reflected light from the sample and the optical components and from backscattered light from the sample. Another polarizer is placed before the fiber array to reduce the effect of specular reflections, which retain its original polarization(E. M. C. Hillman et al., 2006). The image is produced by a $f_{imaging}$=100mm focal length lens (LB1676-B, Thorlabs, Newton NJ) whose focal plane is located at the scan lens. An 4×8 avalanche photodiode detector (APD) array (S8550, Hamamatsu Photonics K.K., Japan) is positioned in this plane, capturing light at different radial positions relative to the center of the scanning spot, which is focused on the first element. At the present moment only one line of 7 elements is used. The first element which is aligned with the optical axis of the system was not employed for acquiring data, because the signal contained some specular reflection even though crossed-polarizers were used. The formed images are equivalent to tomographic reflectance measurements from 192×80 = 15,360 source positions (over a $(5.5mm)^2$ FOV) and 192×80×7 = 107,520 detector positions, even though these acquired images are later downsampled to a smaller grid to perform 3-D reconstruction. The size of the detecting spot a_{det} is determined by the APD detection area and the system magnification m, in our case,

$$\mathrm{m} = \frac{f_{imaging}}{f_{scan}} = \frac{100mm}{25mm} = 4 \tag{2.14}$$

Therefore the detecting spot area a_{det} currently achieved can be calculated as the ratio of the effective detection area a_{eff} and the magnification m:

$$a_{det} = \frac{a_{eff}}{m} = \frac{2.56mm^2}{4} = 0.64mm^2 \tag{2.15}$$

The scanning spot radius was measured to be approximately equal to 100μm, yielding thus a source on the sample with an area of 0.0314 mm^2. The detectors distances are also determined by the ratio of the distance between the APD elements and the magnification m; currently the maximum and minimal source-detector distances, r_{sd_min} and r_{sd_max}, are respectively:

$$r_{sd\_min} = \frac{2.3mm}{4} = 0.575mm, \qquad r_{sd\_max} = \frac{16.1mm}{4} = 4.025mm, \tag{2.16}$$

Each APD element is read by an analog input channel in the data acquisition card (16 bit, 8 channels, 250kS/s per channel, PCI-6143, National Instruments, Austin TX). Data acquisition is synchronized with the galvanometers movement with a custom made graphical user interface developed in LabView™ (National Instruments, Austin TX).

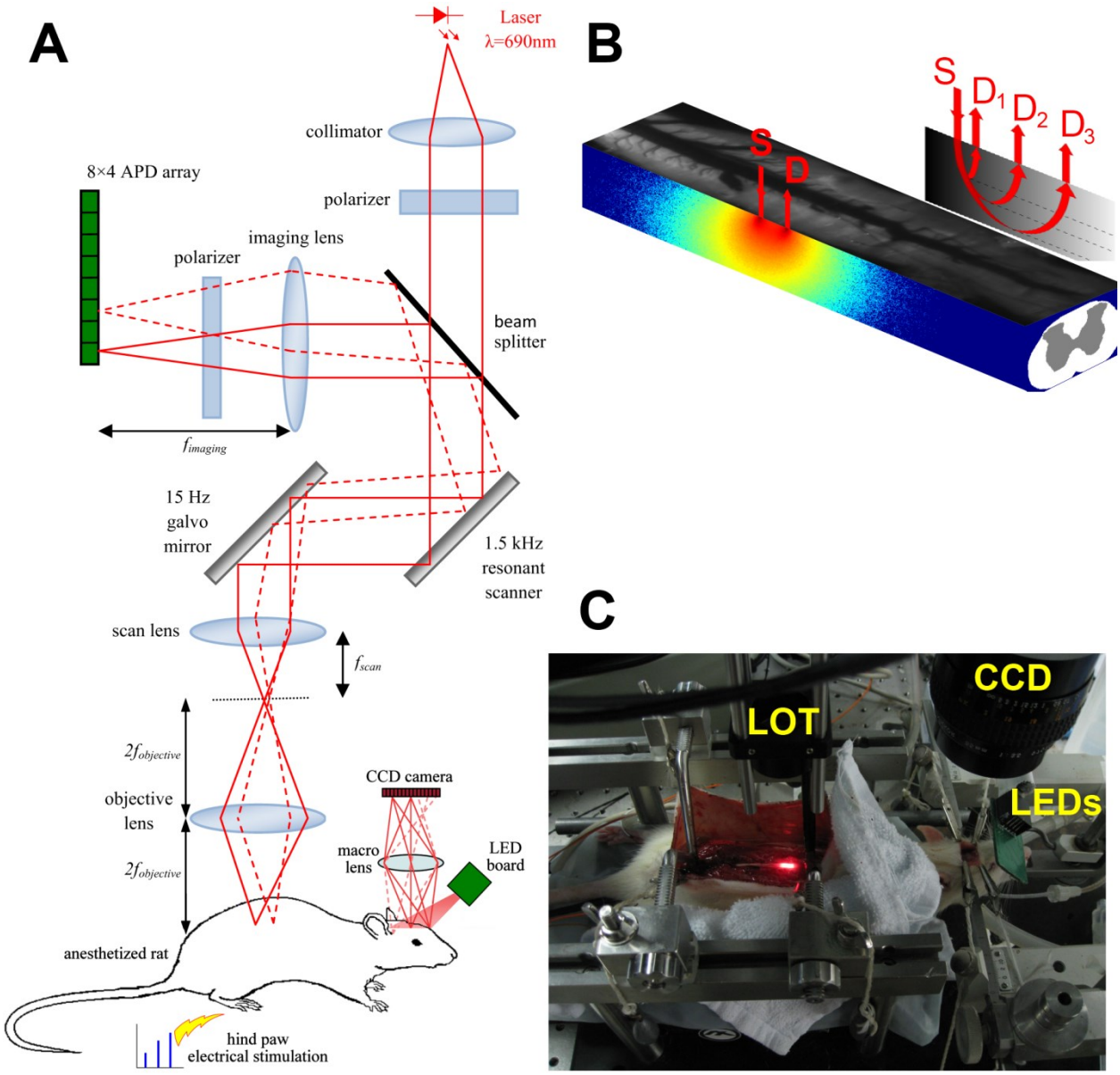

Figure 2-2: (A) Schematic illustration of multi-modal imaging system, showing LOT system design and CCD based intrinsic imager. (B) Depiction of the sensitivity matrix for a given source-detector pair. (C) Multi-modal imaging system experimental setup.

2.3 Simulation results

To validate the LOT image reconstruction process, a simulation framework with identical source-detector geometry as the experimental system was used. A series of numerical simulations of several computer-generated phantoms with different noise levels was performed to find the optimal regularization parameter that would yield the most accurate reconstruction (at the

expense of image resolution). The simulation background parameters were μ_a=0.01mm^{-1}, μ_s=10mm^{-1} and g=0.9, chosen to mimic cortex gray matter (Bevilacqua et al., 1999). The Monte Carlo model was used to simulate light transport in a homogenous volume of 10×10×2.5 mm (64×64×16 voxels) with 10^6 photons propagated within approximately one hour of computation time on a Xeon E5440 2.83 GHz dual CPU, with 32 GB of RAM.

Figure 2-3 A depicts the simulation results for tomographic reconstruction of a simple numerical phantom consisting of an absorbing stick of 150μm diameter immersed in a homogenous scattering medium; this simple phantom was used to find the line-spread function (LSF) of the system. Broadening and degradation of the tomographic reconstruction appears as the signal-to-noise ratio decreases and the depth of inclusion increases. The full width at half maximum (FWHM) is established as one criterion for a conservative estimation of the optical resolution. Panel C from Figure 2-3 illustrates the effect of the target depth in the reconstruction; the normalized cross-sections of the line object are wider and with lesser amplitude as the target goes deeper.

Another criterion is contrast to noise ratio (CNR), where contrast is defined as peak $\Delta\mu_a$ of the reconstructed volume, while noise is defined as the distribution of voxels $<\Delta\mu_a^2>^{1/2}$ (Culver et al., 2003). This measure was also considered to evaluate the quality of the reconstructed volume in the experimental phase. The effect of noise is more important when the object of interest is not deeper than 1 mm. After this depth the reconstructions yielded similar CNR regardless of the SNR, demonstrating the adverse effect of depth in the quality of the reconstruction. Figure 2-3 B shows that CNR decreases with depth, while LOT FWHM increases with depth as illustrated in Figure 2-3 D. The measured resolution of the system was within the range of 0.5 to 1mm depending on the depth of the object of interest.

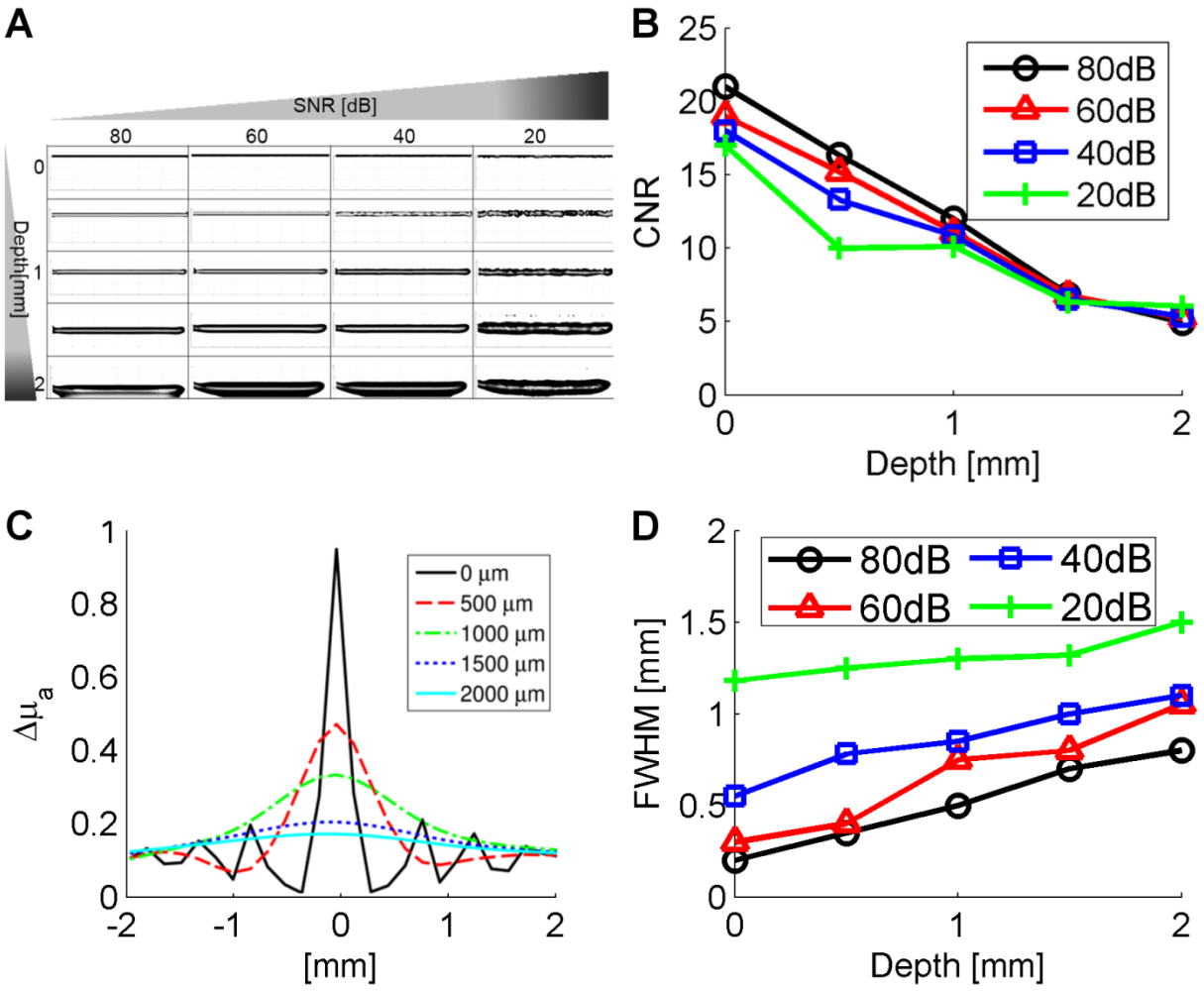

Figure 2-3: Regularized solutions and figures of merit for an absorbing stick at different depths and several signal to noise ratios.

A complex numerical phantom was also simulated in the turbid media at different depths. Figure 2-4 shows the simulation of a complex phantom located at 1mm depth. To generate realistic measures, Monte-Carlo simulations were used and 1 percent noise was added corresponding to the level of noise obtained in experiments (SNR=40dB). To avoid inverse-crime issues, the sensitivity matrix for the inverse problem was generated with Monte-Carlo simulations at a different spatial resolution than that used for the forward problem. A Tikhonov regularization scheme was used and the regularization parameter was chosen by using a L-curve technique. Results of these simulations are provided in Figure 2-4.

This simulation framework with identical source-detector geometry as the experimental setup allowed us to validate the LOT reconstruction process.

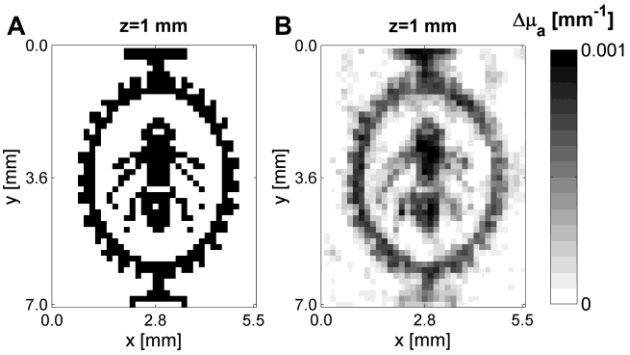

Figure 2-4: Representative slices from the volume at 1 mm (A) Numerical complex phantom with 100% contrast, (B) reconstruction from simulated data.

2.4 Experimental results

In this sub-section LOT outcome is presented for the phantom experiments as well as the in vivo proof of concept, where the spinal cord was imaged on a wild type rat.

2.4.1 Phantom imaging

In order to validate the measurement capabilities of the LOT system it is important to characterize the reconstructed images obtained for different target depths. Our target consisted of a strong absorbing wire (150 μm in diameter) placed at different depths in an intralipid-india ink dilution (μ_a=0.1mm^{-1}, μ_s=10mm^{-1} at 680nm) whose optical properties resemble those of gray matter (Yaroslavsky et al., 2002). The scanned field of view (FOV) was the same size as the simulated FOV (5.5×7 mm). Figure 2-5A displays the sensitivity functions for different source-detector separations in the left most column and the measurements obtained when the absorbing wire was at different depths; panel B of the same Figure 2-5 shows a representative slice of the tomographic reconstruction at a target depth of 1mm. The absorbing wire appears on the image when the source is positioned over it, while the shadows appear when the detector is placed over the absorbing wire. The distance between the wire and its shadow indicate the source-detector distance. The imaging target was successfully reconstructed up to 1.5mm deep, establishing the limit for later in vivo reconstructions.

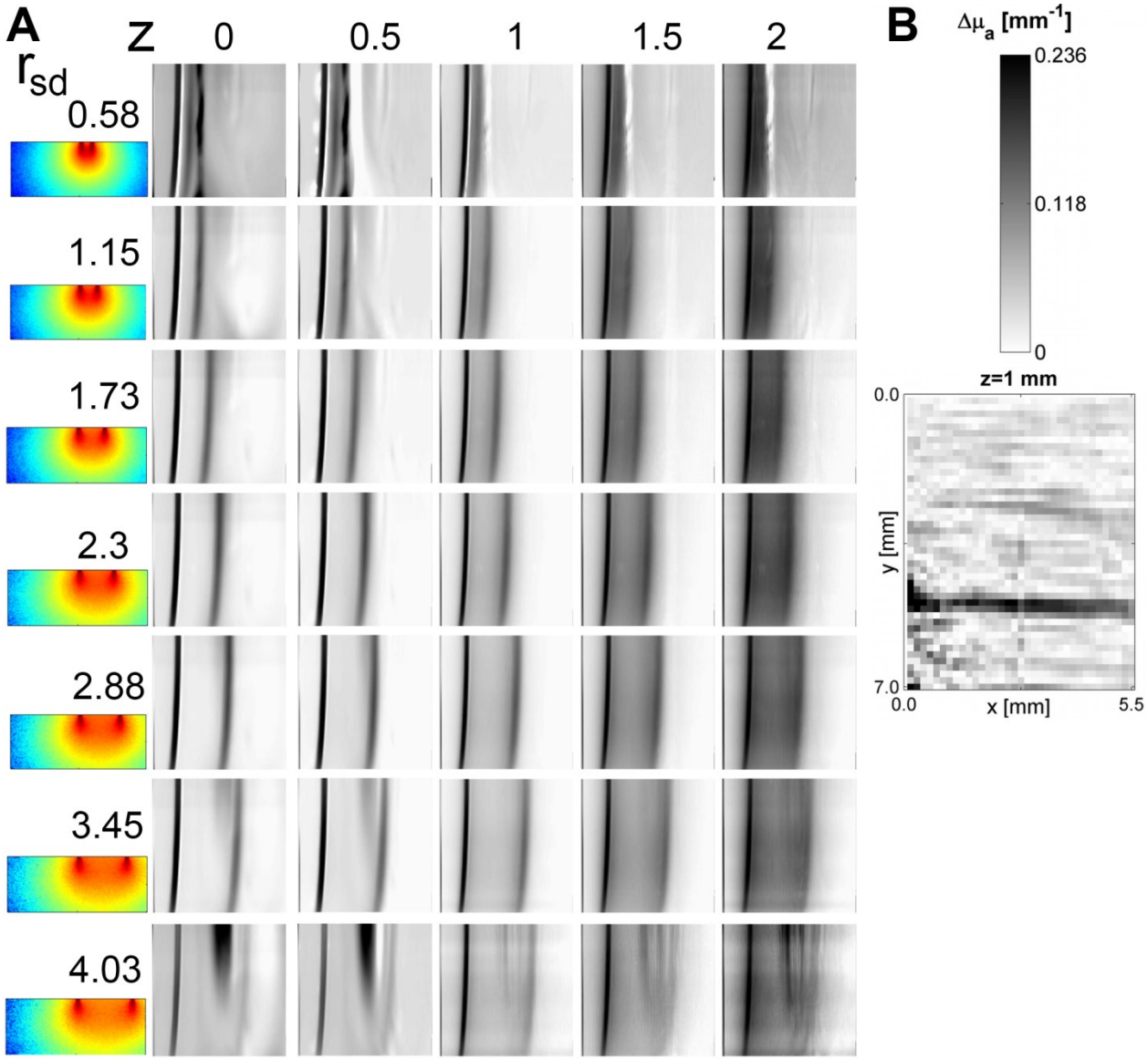

Figure 2-5: (A) LOT measurements from an ink-filled tube immersed in an intralipid-ink dilution (μ_a=0.1mm^{-1}, μ_s=10mm^{-1} at 680nm). Each column of data shows the tube at increasing depths z. Sensitivity functions for all source-detector separations $r_{s,d}$ shown on left. All units in mm. (B) representative slice of the reconstructed volume, the absorbing wire is placed along x axis at 1 mm depth. Some heterogeneity is observed near x=0, because the tube is slightly curved at the edge of the container.

2.4.2 In vivo imaging

In our proof of concept work two animals were used to test LOT imaging in the spinal cord (Ouakli, Guevara, Dubeau, Beaumont, & Lesage, 2010). Animals were anesthetized with

isoflurane (5%), and body temperature was maintained at 37°C with a feedback controlled heating blanket. Both heart rate and expired CO_2 level were monitored. In addition to isoflurane and before surgery the animals were anesthetized with 50 mg/kg bolus of alpha-chloralose (Bonvento et al., 1994). A tracheotomy was performed, and the rats were artificially ventilated with ambient air. Their breathing rate was maintained between 60 and 80 cycles/min, with approximately 2-ml tidal volume and set to obtain an end tidal expired CO_2 concentration of 3%. The rats were then positioned on a custom-made stereotaxic apparatus to immobilize the spinal cord and minimize movement artifacts due to both respiration and hind paw stimulation. Lumbar spinal cord segments from the thoracic (T10) to the sacral (S1) area are exposed by laminectomy and covered with mineral oil to prevent drying. Isoflurane administration was stopped after surgery and alpha-chloralose was administered at a rate of 40 mg/kg/h. Thirty minutes were allowed for animal stabilization. Then the spinal cord was firmly fastened by 2 sets of clamps to impede any longitudinal spinal cord movement induced by breathing. The skull was thinned to around 100 µm over the somatosensory cortex and blood was removed with a cotton swab moistened with saline solution. The skull was also covered with mineral oil before performing simultaneous intrinsic imaging.

The recordings were performed in sessions of 40 minutes. Each stimulation block consisted of 1-second duration with a randomized inter-stimulus interval of at least 20 seconds. The acquired measurements were then block averaged. The stimulus consisted of 3-ms current pulses at a 3 Hz repetition rate. Muscular movement threshold determined the three different stimulation intensities (0.9×, 1.2× and 1.5×), which were interlaced. Imaging protocol was made up of LOT recordings of the exposed spinal cord with simultaneous intrinsic imaging of the brain.

The source-detectors were lined parallel to the rostrocaudal axis (Figure 2-6B), imaging a FOV of 2.5×7.5mm of the lumbar area (L3 – L5 segments). Block averaged time course of the ipsilateral ROI (Figure 2-6A) revealed higher amplitudes with regard to contralateral ROI (Figure 2-6C); stimuli indicated with vertical blue lines. Contralateral activation also showed greater variance, displayed as gray shadows around the mean time trace. The amplitude of activation was proportional to stimuli intensity in both sides of the spinal cord. The blood is drained through the dorsal vein approximately one second after ipsilateral activation peak, as shown in the lower part of Figure 2-6B.

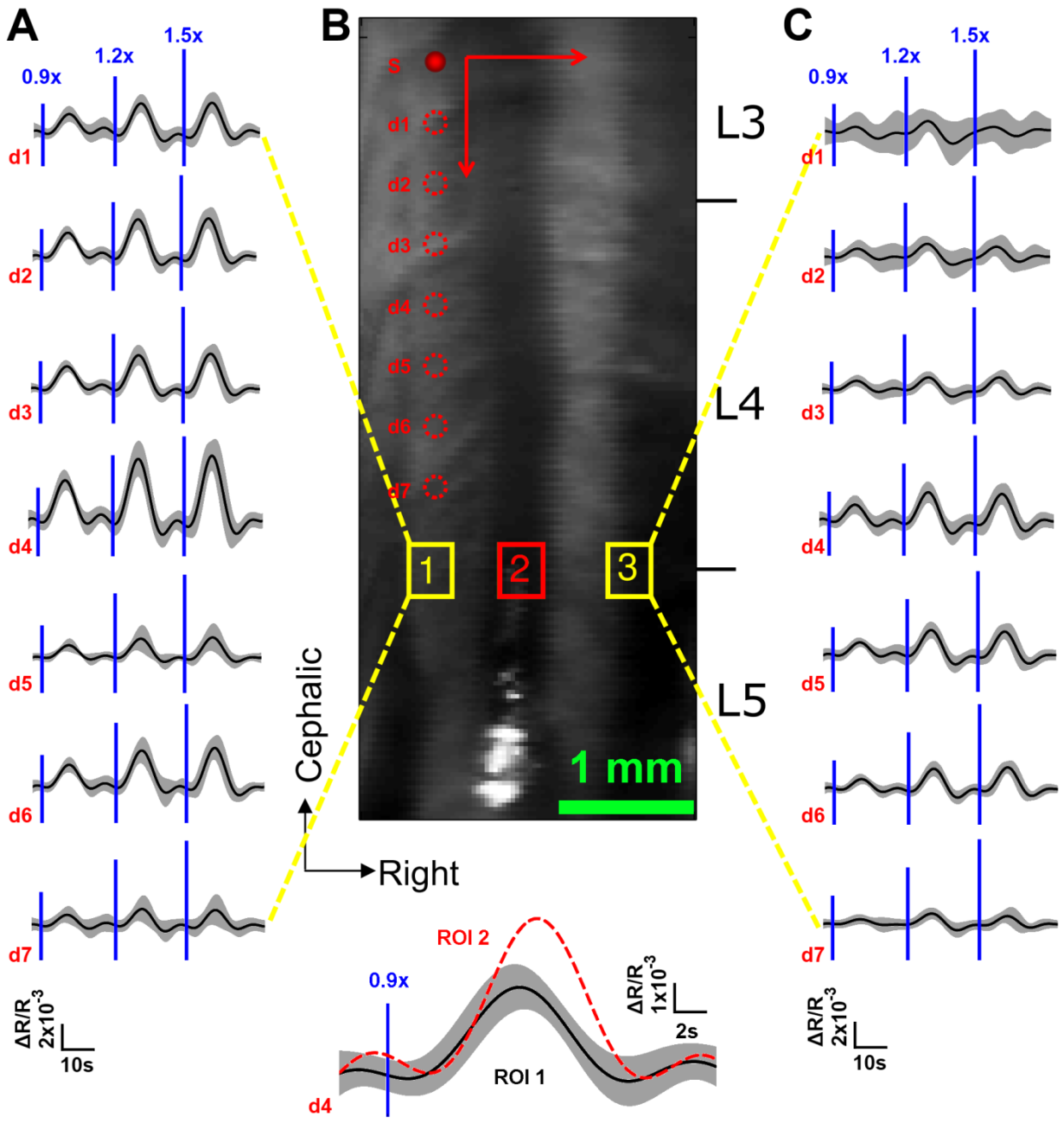

Figure 2-6: LOT hemodynamic response evoked by left hind paw stimulus intensity at 0.9× , 1.2× and 1.5× muscle threshold in normal rat. (A) ROI 1 averaged time traces for all detectors, ipsilateral to stimuli. (B) Top: Image of the exposed spinal cord. Bottom: ROI 2 averaged time course showing delay with regard to ipsilateral activation. (C) ROI 3 averaged time traces for all detectors, contralateral to stimuli.

The feasibility of concurrent OIS imaging was also investigated. Figure 2-7 depicts simultaneous imaging in the cortex and spinal cord. The behavior described previously by the curves in Figure

2-6 could be localized spatially. In panel A, an initial slight dip was localized on the dorsal vein at ~3.6s, then the activation increased on the left side of the spinal cord at ~7.20s, followed by blood drained through the dorsal vein at ~10.8s. In contrast to the spinal cord, where the hemodynamic response was ipsilateral to stimuli, the somatosensory cortex response was contralateral, as shown on Figure 2-7B, confirming the expectations. Note a blob of what appears to be ipsilateral activation on the left side of the cortex; this can be explained by the fact that an arbitrary threshold was chosen and no correction for false positives was done in the activation maps.

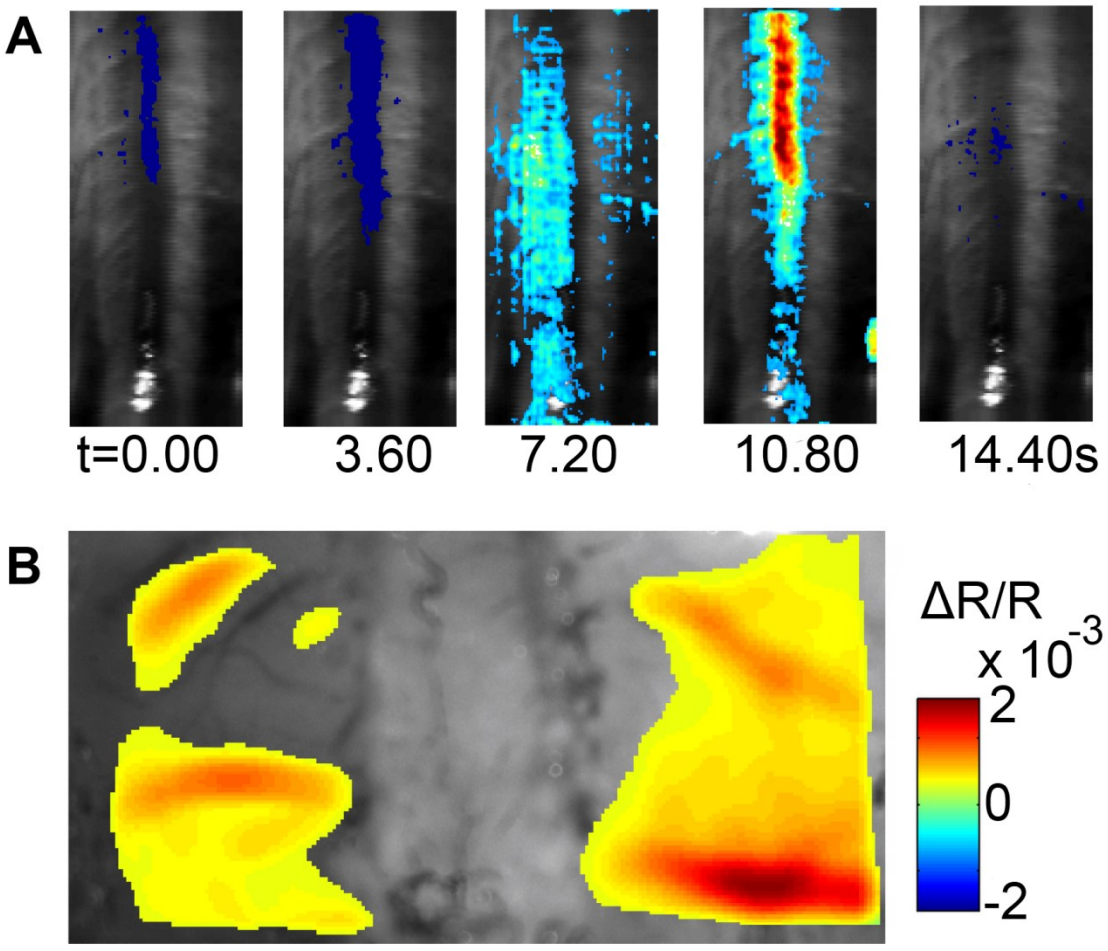

Figure 2-7: (A) Time course of LOT signals evoked by left hind paw stimulation collected at detector 1 over 15s at 0.9× muscular threshold. (B) Maximum intrinsic optical signal measured simultaneously on the somatosensory cortex.

The LOT data on each source-detector pair was integrated between 4.5 and 9 s post-stimulation (at 0.9× muscular threshold) to generate measurements for the inverse problem at activation peak.

Monte Carlo simulations (Boas et al., 2002) were used to model light propagation in the spinal cord using atlas-based anatomical information (Figure 2-8 B). A sensitivity matrix was generated to relate absorption changes to the measured data by using the first Born approximation (Kim & Schotland, 2006). A 3D map of neural activation evoked by hind limb stimulation was recovered by solving the inverse problem, with Tikhonov regularization, choosing the optimal regularization parameter value, found in the previous liquid phantoms reconstructions.

The reconstruction results are shown in panels A and C in Figure 2-8. The signal from the dorsal half of the spinal cord at z=0.4mm was representative of interneuron activation (Willis & Coggeshall, 1991), and in accordance with anatomical expectations for afferents from the sciatic nerve. Deeper in the gray matter the signal is more diffuse and contralateral activation is observed, that may originate from interneuron connections.

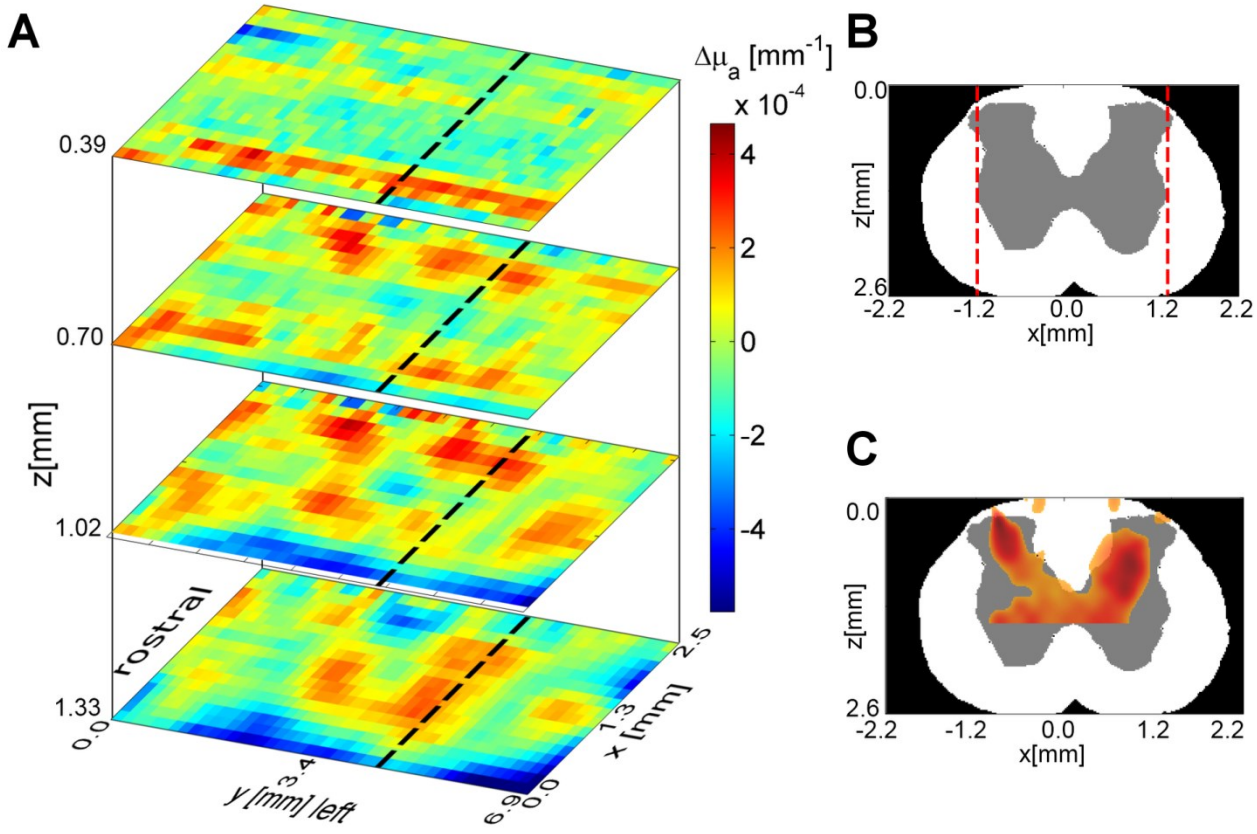

Figure 2-8: (A) 3D map of neural activation in the spinal cord induced by left hind paw stimulation at the 0.9× muscle threshold. Ipsilateral activation around z = 0.4 mm is consistent with interneuron activation. (B) Histology based segmented model of lumbar spinal cord of the rat, used for Monte Carlo simulation of light propagation. Dotted red lines indicate the extent of

field of view (C) Reconstruction viewed across the segmented volume along the dotted line in (A).

The proof of concept provided here demonstrates the concurrent use of LOT and OIS to image the spinal cord and the cortex respectively. This multimodal setup may pave the way to investigate neural plasticity after a spinal cord injury (SCI) and the adaptation of the cortex to this reorganization. Nevertheless depth limitations and lack of repeatable results due to poor SNR remain an issue. Another shortcoming of LOT is the reconstruction process involving an atlas template cord model for light propagation. Although spinal cord dimensions remain very similar for a given species at a certain age, the procedure is not optimal for generalized results. The ideal forward model would be produced from an anatomical MRI scan of each subject, which is expensive or spinal-cord histology along the imaged FOV, which is time-consuming.

To test the effect of errors in anatomical priors several models were constructed where the gray matter was displaced ±20% both horizontally and vertically, as shown on Figure 2-9. L2 metric was chosen to quantify errors in the reconstruction. Small errors (±20%) in the anatomical priors yield considerable errors in the reconstruction: ~80-100% greater than the reconstruction using the anatomically correct model. These results suggest that L-curve tuned Tikhonov regularization is highly sensitive to the *a priori* model for photon propagation and more robust techniques such as Bayesian reconstruction (Abdelnour, Genovese, & Huppert, 2010) should be investigated in future works.

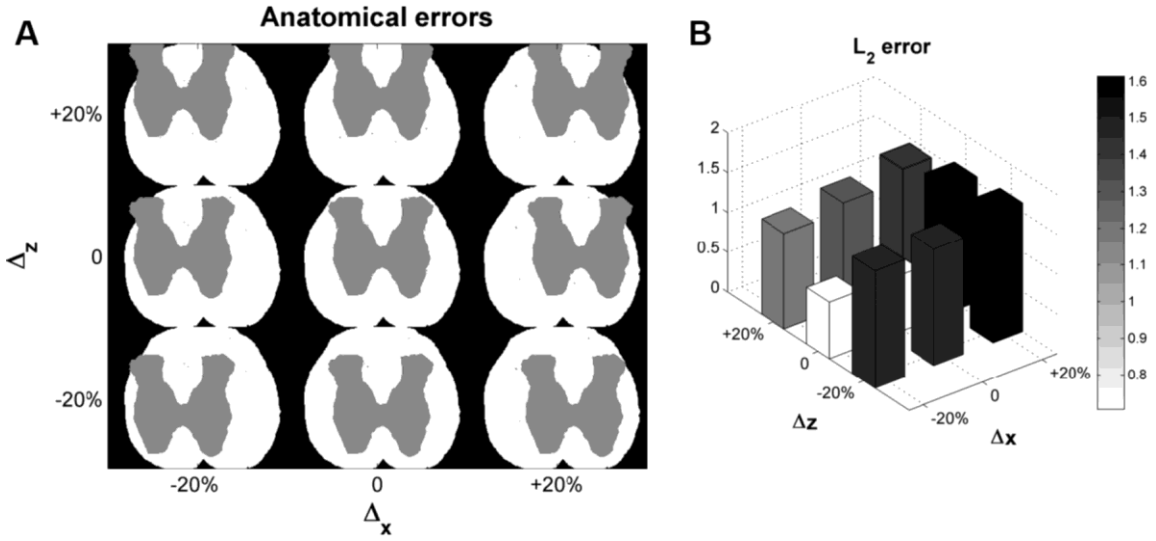

Figure 2-9: (A) Light propagation models with the gray matter positioned in different places. (B) L2 reconstruction error resulting from incorrect anatomical priors.

2.5 Conclusions

In this proof of concept work, LOT has proved to be able to map hemodynamic response in three dimensions, proving sensitivity up to 1.5 mm in the rat spinal cord; however the SNR of the system did not allow imaging the responses of every specimen in a repeatable fashion.

I believe this could be alleviated with a redesign of the optical setup, placing a low-magnification objective with a higher NA and upgrading the rest of the optics to 2" pieces to gather more backscattered photons. Another aspect to improve is the resolution of the inverse problem; more robust techniques, such as Bayesian reconstructions could be applied instead of Tikhonov regularization, which is very sensitive to errors in the anatomical priors used as the propagation medium in the forward model.

Our initial aim was to observe the depth-resolved hemodynamic response in the spinal cord and the brain. Despite achieving a modest success, the technique is ill-posed and less suitable to unraveling resting-state networks. Therefore, the efforts of this thesis were channeled to alternative techniques, better adapted to the study of resting-state functional connectivity.

CHAPTER 3 OPTICAL COHERENCE TOMOGRAPHY

Optical Coherence Tomography (OCT) was applied to characterize the effects of a novel carotid stiffness model (Sadekova, Vallerand, Guevara, Lesage, & Girouard, 2013) in the mouse brain; more specifically, OCT was used to measure blood flow pulsatility in arteries pertaining to different areas of the mouse brain. The data acquired with OCT was a prelude to our resting state study, I thus describe here this imaging technique. This chapter will cover the technical aspects pertaining to the optical, mechanical and electronic design of the apparatus. The Figure 3-4 offers a schematic representation of the different system components.

OCT is a novel biomedical imaging technique. It fills the void between confocal microscopy and high-resolution ultrasound in terms of resolution and penetration depth (Figure 3-1A). Standard clinical ultrasound can image deep structures with limited resolution. Higher frequencies yield finer resolution, but ultrasonic attenuation is increased, thus limiting image penetration. The axial image resolution in OCT ranges from 1–15 μm and is determined by the properties of the light source. The lateral resolution is determined by the objective used to image the sample. In most biological tissues, the imaging depth is limited to 2–3mm due to optical scattering. Confocal microscopy has better resolution (<1 μm), but the imaging depth is limited to a few hundred micrometers in most tissues, because of scattering.

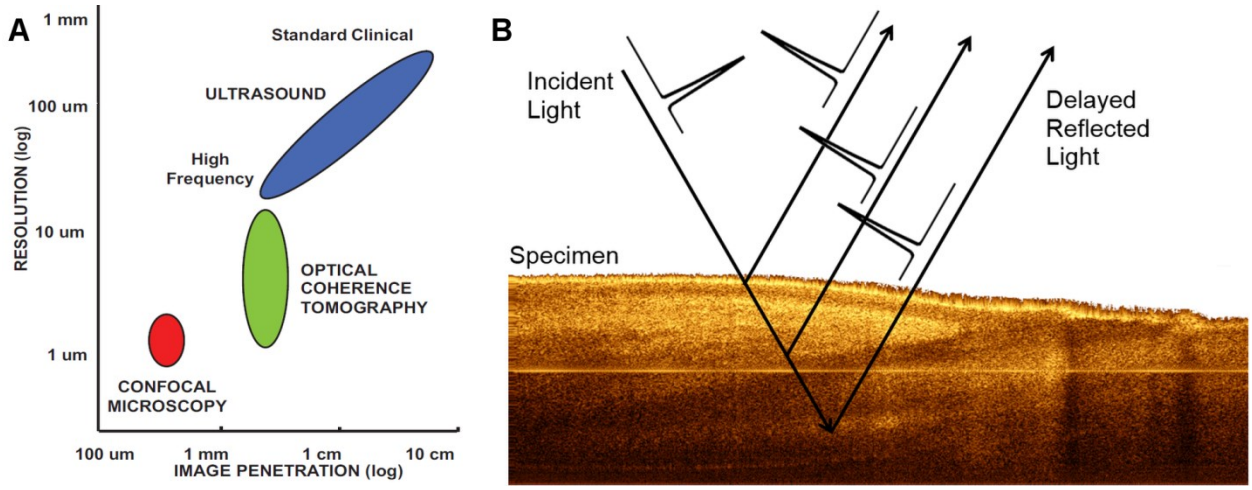

Figure 3-1: (A) OCT resolution compared to other imaging modalities. Reproduced from (Drexler & Fujimoto, 2008). (B) Echoes of light.

OCT is based on a backscattering technique developed during the 1980's in the telecommunications field, called Optical Frequency Domain Reflectometry (OFDR), which was used for the purpose of fault detection in fiber optics (Ghafoori-Shiraz & Okoshi, 1985, 1986). A pulse of light was sent into the fiber and if its return were detected, it usually meant that a fault was sending a reflection of the light pulse.

The concept of optical ranging was first applied to biological tissue imaging in 1991 by James Fujimoto at the Massachusetts Institute of Technology, performing in vitro imaging of the peripapillary area of the human retina and of the coronary artery (Huang et al., 1991). OCT imaging is performed by directing an optical beam at the object to be imaged, and the echo delay of backscattered light is measured. In contrast to ultrasound, because the velocity of light is extremely high, the echo time delay of reflected light (Figure 3-1B) cannot be measured directly and interferometric detection techniques must be used.

The first use of OCT was ophthalmology and, still is to date, the leading area for clinical application of OCT (Fujimoto, Pitris, Boppart, & Brezinski, 2000). In the late nineties OCT was adapted to an endoscope, referred as "optical biopsy" and used to visualize tissue in a living animal (Tearney et al., 1997).

In the first years of the new millennium there was a shift in the way OCT was performed, from a time-domain (TD-OCT) to a frequency-domain detection (FD-OCT), resulting in the improvement of signal-to-noise ratio (SNR) and scanning speed (Leitgeb et al., 2000). The earlier-mentioned method was first presented in 1995 by (Fercher, Hitzenberger, Kamp, & El-Zaiat, 1995) and the first in vivo tomograms were presented in 2002(Wojtkowski, Leitgeb, Kowalczyk, Bajraszewski, & Fercher, 2002).

3.1 OCT theory

In the OCT basic setup shown in Figure 3-2, the raw output of the detected signal is the Fourier transform of the depth reflectance profile. The output of the source is split into a reference arm, which shines light on a stationary mirror and a sample arm which illuminate and receive the light reflected from within the sample. Reflectance measures of tissue at each depth are recorded simultaneously.

The light from the sample is interfered with light coming back from the mirror; interference can occur only when the optical path lengths of the two arms match to within the coherence length of the source. The detector current is defined by (3.1),

$$i_{det}(t) = \frac{\eta q}{h\nu}\left(P_r + P_o \int r^2(z)dz + 2\sqrt{P_r P_o} \int r(z)\Gamma(z)\cos\big(2k(t)z + \phi(z)\big)\,dz\right) \tag{3.1}$$

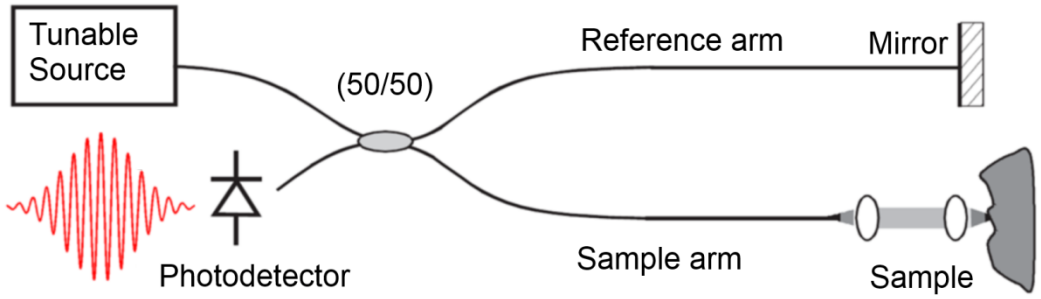

Figure 3-2: Basic configuration of a swept-source OCT. Modified from (Bouma, Tearney, Vakoc, & Yun, 2008).

Where η is the photodetector sensitivity, q is the elementary charge and $h\nu$ is the energy of a single photon. The first term P_r is the optical power reflected from the reference arm. The second term depends on the optical power illuminating the sample P_o. $\Gamma(z)$ is the coherence function of the instantaneous laser output and $k(t)$ is the wavenumber, which is linearly swept by the laser source. The third term represents the interferometric signal, which is related to the sample reflection profile via the Fourier transform relation. In practice, the detected signal is digitized and a FFT is performed to obtain an axial scan, called an A-line (Figure 3-3A). Cross-sectional images are generated by performing a series of axial scans at different transverse positions to generate a two-dimensional data set (B-scan), which is displayed as a grey scale or false color image (Figure 3-3B). Three-dimensional data sets (3D-OCT) can be generated by raster scanning a series of two-dimensional B-scans (Figure 3-3C).

3.2 OCT system overview

The OCT setup is based on a Michelson interferometer with additional components that allow for raster scanning of the light and data acquisition. The first stage of the design is to choose both the electronic and the optical components to create and detect an interference pattern and to raster

scan the beam of light over the sample. Choosing the adequate opto-mechanical components ensures the stability of the setup and allows a rapid and precise adjustment of the optical parts. The OCT system is depicted in Figure 3-4:

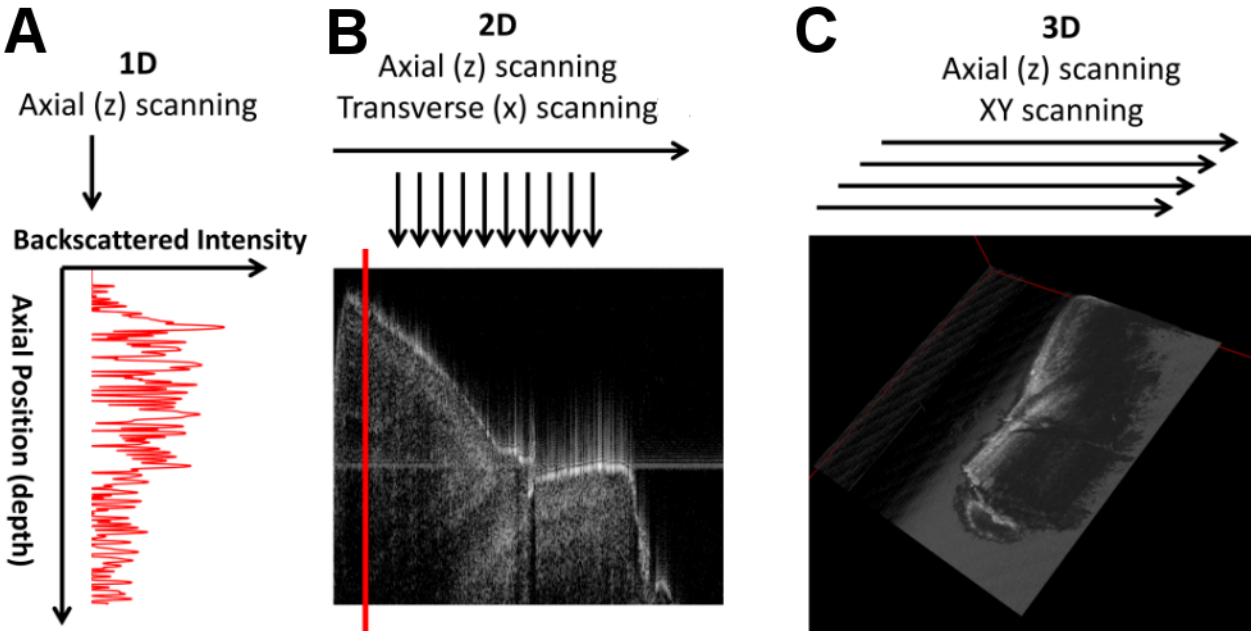

Figure 3-3: OCT scanning modes. (A) A-line. (B) B-scan. (C) Volumetric OCT.

The OCT system developed in this thesis uses a swept-source laser (Axsun, 1310 Swept Source Engine) which has a central wavelength of λ_0=1310nm with a tuning bandwidth $\Delta\lambda$=100nm (Figure 3-5A). The average power was measured to be ~18mW at the laser output. Light intensity across the bandwidth, distributed in high peak powers at each discrete wavelength allows greater sensitivity with little risk of optical damage (B. Liu & Brezinski, 2007), while a 50 kHz sweeping rate enables high-speed imaging. The core of the imaging system is a Michelson-type interferometer built with two fiber couplers and two circulators. The incoming light from the swept-source, passes through a broadband 90/10 fused fiber optic coupler (Thorlabs, FC1310-70-10-APC). The 90% portion goes into a circulator (Thorlabs, CIR-1310-50-APC) that sends light to the sample arm and collects the backscattered light from the sample. The 10% portion is passed into another circulator that sends to and collects light from the reference arm. Backscattered light from both the sample and reference arms are combined in the 50/50 fused fiber optic coupler (Thorlabs, FC1310-70-50-APC), producing the interference pattern that goes

to the inputs of the balanced photodetector (Thorlabs, PDB120C). The polarization controller (Thorlabs, PLC-900) is used to optimize the contrast of the interference pattern.

All fibers are single-mode, 125µm cladding, terminated with FC/APC (8° angle physical contact) connectors that minimize back-reflections in the OCT system.

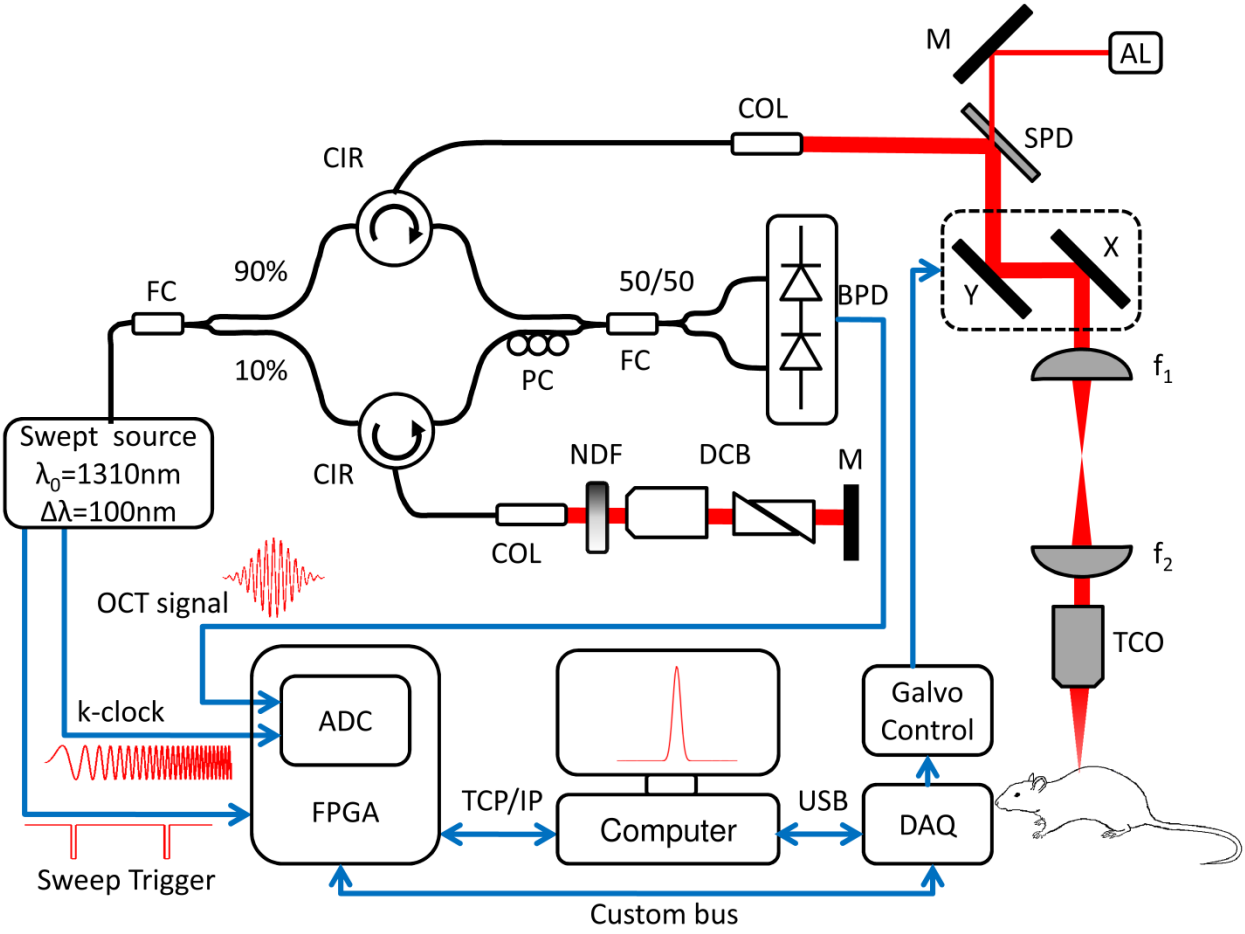

Figure 3-4: OCT system setup. ADC: Analog to Digital Conversion, AL: Aiming Laser, BPD: Balanced Photodetector, CIR: Circulator, COL: Collimator, DAQ: Data Acquisition board, DCB: Dispersion Compensation Block+Prisms, f1 and f2: Unitary relay, FC: Fiber Couplers, FPGA: Field-Programmable Gate Array, M: Mirror, NDF: Neutral Density Filter, PC: Polarization Controller, SPD: Short-pass dichroic, TCO: Telecentric Objective, X and Y: Galvo mirrors.

3.2.1 Sample Arm

The sample arm allows raster scanning of the laser beam along the tissue surface, to obtain cross sectional or full three-dimensional images of the sample under examination. Figure 3-5B displays

the schematic of the sample arm. To propagate the beam from the optical fiber a collimator (Thorlabs, F280APC-C) is plugged to the FC/APC connector, providing a collimated beam with a ~3.27mm diameter. In order to provide a visual guide of the scanning FOV an aiming laser (Thorlabs, LP660-SF40) is incorporated in the sample arm. Collimation of the aiming laser is achieved with an uncoated plano-convex lens (Thorlabs, LA1951). A silver-coated mirror (Thorlabs, PF10-03-P01) mounted on a kinematic stage allows precise steering of the aiming laser. Both the imaging and the aiming beams are coupled with a shortpass dichroic mirror (Thorlabs, DMSP1000, 50% at λ=1000nm) where they are centered and aligned to the optical axis. The beams are then redirected to a pair of galvanometer mirrors (Thorlabs, GVSM002/M) mounted on a cage (GCM002/M). After the galvanometer mirrors there is a unitary telescope or relay consisting of two identical lenses arranged in an afocal (infinite focus) assembly (Thorlabs, LA1131-C , $f_1 = f_2 = 50$mm, $1050 < \lambda < 1620$ nm). This optical relay is used to image the mirrors pivot point at a distance of ~18.9 mm from the telecentric scan lens (Thorlabs, LSM04) mounting plate. This lens is advantageous in our application because it allows a flat image plane when the laser is scanned across the sample. In addition, the spot size is uniform over the entire FOV, keeping the lateral resolution constant. On the return path, the light backscattered by the specimen is collected by the Telecentric scan lens, passes through the optical relay, then again deflected by the oscillating mirrors and sent to the fiber collimator. All chosen lenses and collimators are made from N-BK7 common optical glass and they have a coating deposited on both sides that minimizes reflection in the 1050 – 1620 nm range.

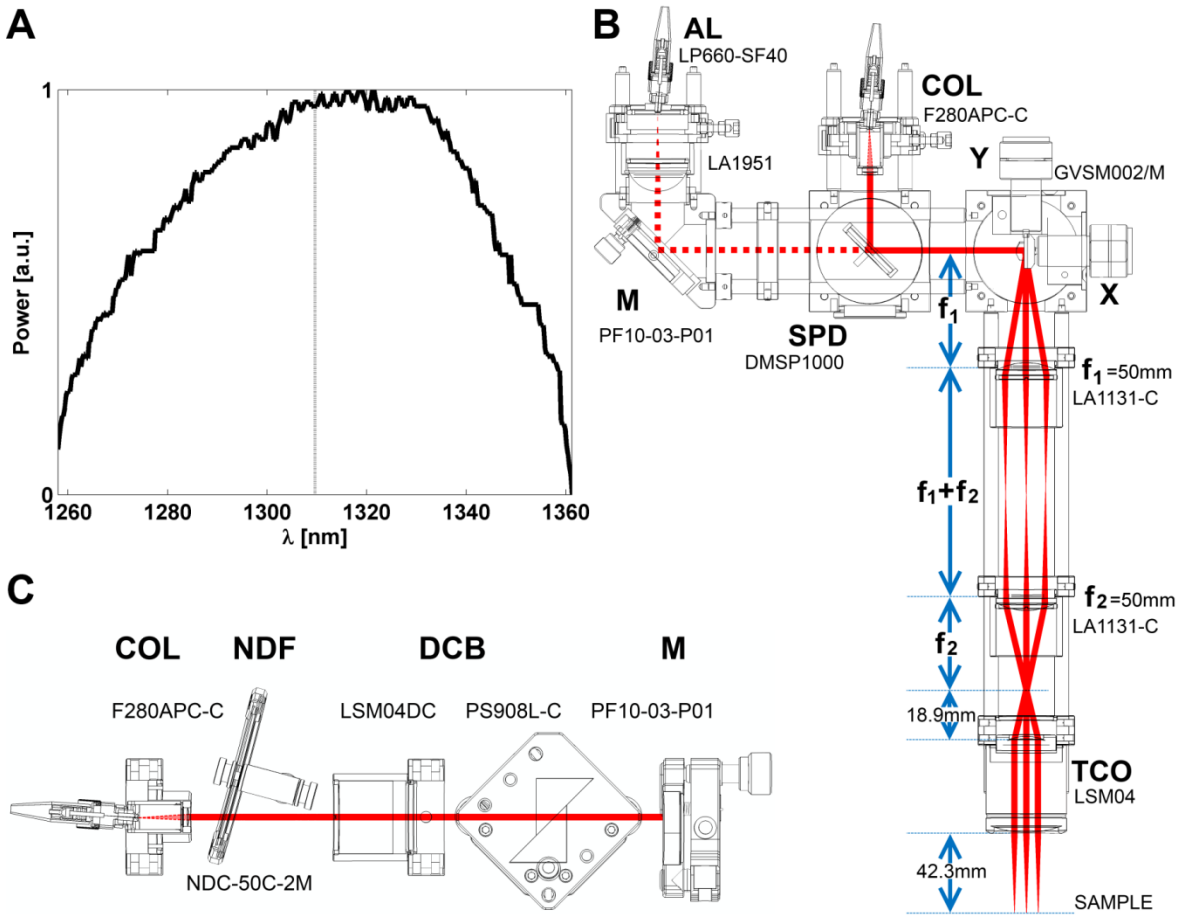

Figure 3-5: (A) Swept source laser spectrum. Average from three scans grabbed by the oscilloscope. (B) Schematic of the sample arm. (C) Schematic of the reference arm. For details refer to Figure 3-4 caption.

3.2.2 Reference arm

The reference arm (Figure 3-5C) is the optical equivalent of the sample arm: it has the same optical path length and the same amount of glass-induced dispersion. Besides, it permits to adjust the intensity of the light with an adjustable neutral density filter (Thorlabs, NDC-50C-2M), that goes from 0 to 2 OD, i.e. transmission levels from 10^{0} to 10^{-2}. Since this filter is reflective one has to be careful of reflected light that could go back into the fiber collimator, so the adjustable neutral density filter has to be placed slightly off-axis to prevent spurious interference patterns in our OCT signal. First, the optical path length must equal that of the sample arm. This distance must have a coarse adjustment to obtain an interference pattern, which is done by sliding the silver coated mirror (Thorlabs, PF10-03-P01) on a dovetail rail. Once the coarse adjustment is

set, there has to be a fine adjustment to place the sample at the correct depth. This is achieved by a micrometric stage where the dovetail rail is mounted. Second, because of the large bandwidth of the swept source different wavelengths will travel at different speeds when propagating through dispersive media such as the glass in the fiber optics and the lenses. A dispersion mismatch between the interferometer arms will affect the axial resolution of the system. Therefore, it is necessary to balance dispersion mismatch between the sample and the reference arms to achieve the optimal resolution. In the reference arm I place the same amount of glass that exists in the sample arm. The telecentric objective glass is easily compensated by a dispersion compensation block (Thorlabs, LSM04DC) and the glass of the optical relay is compensated by a prism pair (Thorlabs, PS908L-C), which are coupled with refractive index matching oil for BK7 glass (Cargille, BK-7 Matching Liquid 11510).

3.3 Acquisition software

The balanced detector output signal is digitized by the ADC board (Altera, Data Conversion HSMC Daughter Board). Briefly, the ADC values are stored on the external memory of the Field-Programmable Gate Array (Terasic, DE4 board), then when the memory buffer is full, data is sent to the PC via TCP/IP for image reconstruction and saving to disk. Control of the scanning galvo mirrors and synchronization signals are handled via another data acquisition board (National Instruments, USB-6351). The measured transfer rate was ~110Mbps, which is insufficient to provide real time imaging at the required 878Mbps (~20 Mb per A-line at a rate of 45Khz).

3.4 System characterization

In this section a characterization of the aforementioned OCT setup is presented. As this system can be used in a variety of applications its full characterization becomes important. Quantitative measurements are required to asess the performance of this system.

3.4.1 Resolution

Multiple scattering affects OCT images in an adverse fashion. The ratio of multiple scattering versus single scattering increases as a function of depth. This increase in multiple scattering results in a broadening of the PSF of the system, i.e. a decrease of axial resolution as a function

of increasing depth. In OCT axial and lateral resolutions are decoupled. Axial resolution depends on the coherence length of the source while lateral resolution is determined by the focusing conditions: optics and the lateral scan step size.

3.4.1.1 Axial resolution

The axial resolution is determined by the coherence light of the source (Lexer, Hitzenberger, Fercher, & Kulhavy, 1997). The coherence length is the spatial width of the field autocorrelation produced by the interferometer and it is given by:

$$\Delta z = \frac{2\,ln\,2}{\pi}\frac{\lambda_0^2}{\Delta\lambda} \tag{3.2}$$

Its theoretical value is Δz=7.33µm, however the measured PSF of the system was ~17µm. This discrepancy is due mainly to two reasons: first, the use of a Hanning window to compute the FFT of a single backscatterer (mirror) widens the FWHM, second and most important, the data was acquired at a fixed sampling frequency due to hardware limitations, then interpolated to *k* space, resulting in degraded resolution. This can be alleviated by using the k-clock from the laser source as an external sampling clock on a suitable acquisition board. This issue was confirmed by measuring the PSF with a 500 MS/s, 12 bit PCI Express Digitizer (ATS9350, Alazar Technologies Inc., Canada), capable of external clock sampling; its FWHM was ~13µm.

3.4.1.2 Dispersion compensation

In order to achieve optimal resolution it is necessary to carefully match dispersion between the two paths of the interferometer, this is partially achieved by the use of glass prisms on the reference arm, as described in section 3.2.2. An algorithm of dispersion compensation to the second and third order has to be implemented according to the procedure described in (Wojtkowski et al., 2004). This compensation is performed in order to minimize imbalance in the interferometere arms. The optimization criterion was set to increase image contrast by maximizing a metric of image quality, in this case the axial PSF of the system (defined as the FWHM of a single backscatterer). PSF at different depths are shown before (Figure 3-6A) and after (Figure 3-6B) the implementation of the dispersion compensation algorithm. Notice in Figure 3-6C how the algorithm improves the image quality at all depths, although there is a degradation of image quality with increased depth.

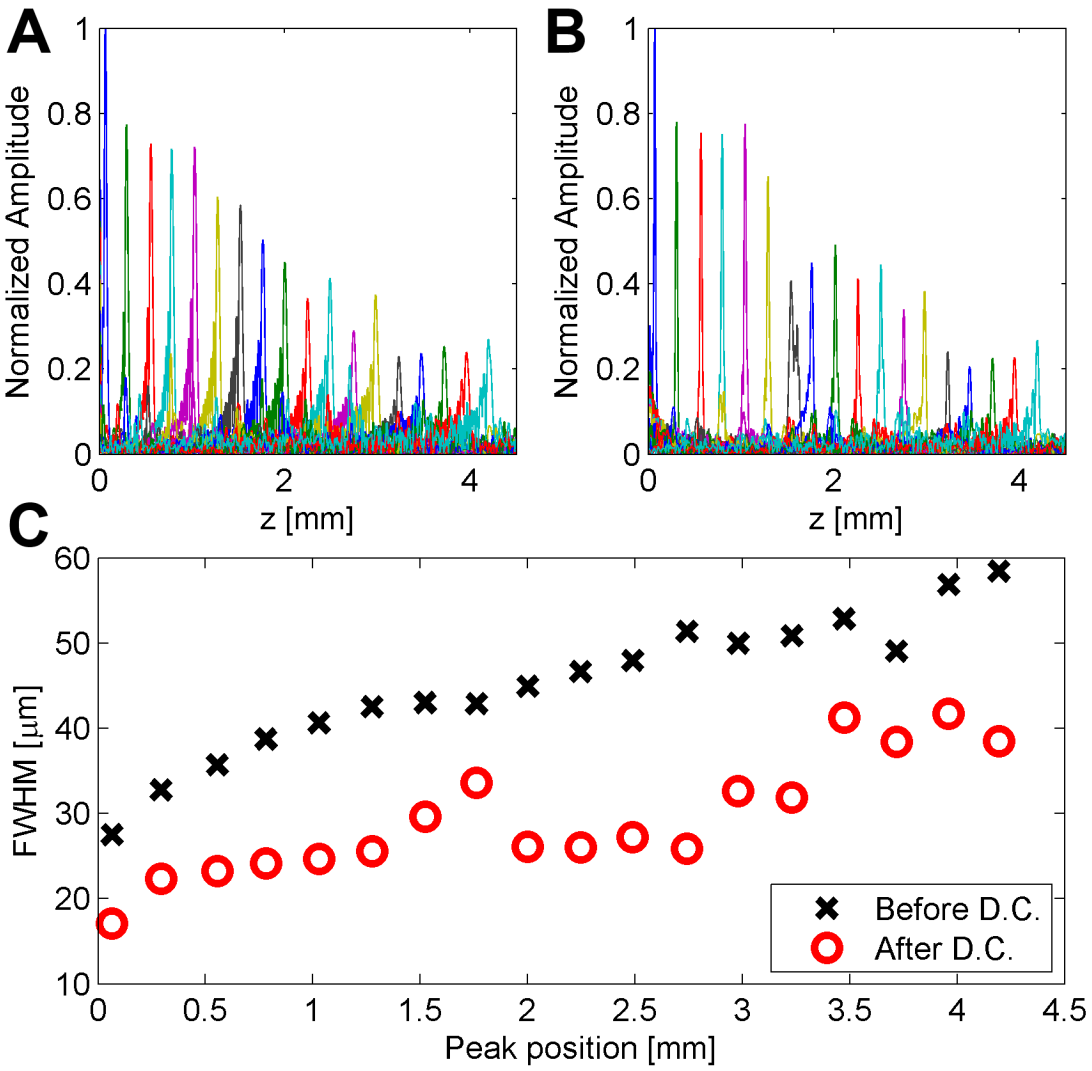

Figure 3-6: Dispersion compensation. (A) Axial PSF measured at different depths before dispersion compensation (D.C.). (B) Axial PSF measured at different depths after D.C. (C) FWHM as a function of depth.

3.4.1.3 Lateral resolution

The depth of focus defines the depth range within which the lateral resolution is approximately maintained. There exists a tradeoff between the focal diameter and the focal zone of the sample beam, the smaller the beam diameter, the shorter the focal zone. A high NA lens is used only in C-scan imaging (*en face*), however in depth-sensitive applications a large FOV is desired (14×14mm); therefore a telecentric lens with feeble NA=0.09 is employed. The theoretical lateral resolution (given by (3.3)) is Δr=26.5μm, and the focal zone is Δf_r=0.84mm.

$$\Delta r = \frac{2\lambda_0}{\pi}\frac{1}{NA}, \qquad \Delta f_r = \frac{\pi \Delta r^2}{2\lambda_0} \tag{3.3}$$

3.4.2 Penetration depth, sensitivity and dynamic range

In swept-source (SS-OCT) the range where an image can be formed is given by the maximum path difference ΔZ_{Nq}, determined by the Nyquist condition (Häusler & Lindner, 1998). The penetration depth thus depends on the number of samples taken every laser sweep Ns = 1152. Assuming a refraction index n = 1.38 and given the swept-source characteristics: center wavelength λ_0 = 1310nm and optical bandwidth $\Delta\lambda$ = 100nm, there is a maximum path difference ΔZ_{Nq} = 3.58 mm in tissue and ΔZ_{Nq} = 4.94 mm in the air.

$$\Delta Z_{Nq} = \frac{N_s \lambda_0^2}{4n\Delta\lambda} \tag{3.4}$$

However, the penetration on turbid media is smaller. On a scattering phantom with a polyethylene tubing (0.28mm inner diameter, 0.61mm outer diameter, BD Intramedic #PE-10-100) the maximum attainable distance is about 3 mm (Figure 3-7A). The penetration depth *in vivo* is even smaller, 1mm on a human fingertip (Figure 3-7B). Notice the presence of a solid horizontal line around ~1mm depth. This artifact is due to the presence of parasitic modulation in the source spectrum (Gelikonov, Kasatkina, & Shilyagin, 2010).

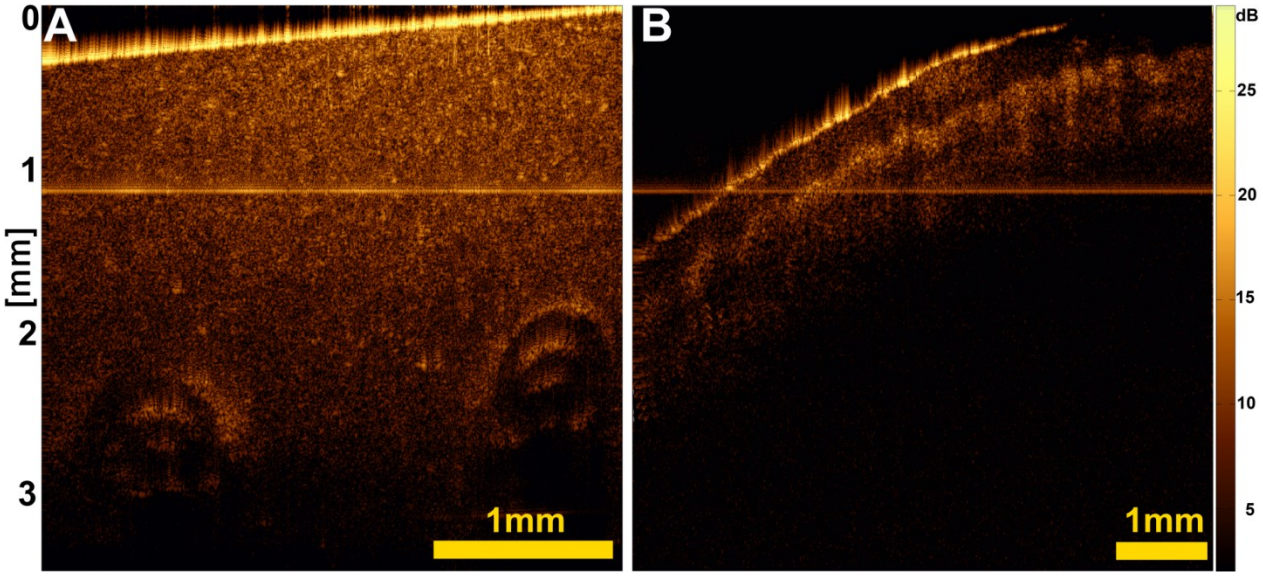

Figure 3-7: (A) Scattering phantom made of resin with two polyethylene tubes. The maximum attainable depth is about 3 mm. (B) Image of a human fingertip, in this case the signal drops at depths >1mm.

The sensitivity is defined as the minimum detectable signal required to produce the same amount of output as random fluctuations (Brezinski, 2006). A mirror is placed as the input signal and it is aligned in order to get the maximum amount of light back into the optic fiber. This intensity will saturate the detector. Then neutral optical density filters are placed on the sample arm in order to reduce the beam intensity. With every added filter, the prisms of the dispersion compensation block on the reference arm are adjusted to have the same path difference as before. More filters are added until the mirror is no longer discernible. The sensitivity of the systems equals twice the total attenuation because the beam travels twice the sample arm. A value of ~114 dB was measured with this method.

The dynamic range is defined as the ratio of the maximum and minimum recordable signals. Ideally this is limited by the capacity of the acquisition board with a 14-bit ADC i.e. ~84 dB. The same setup aforementioned is employed. The necessary attenuation to have a non-saturated image was determined to be 40 dB, which corresponds to a dynamic range of ~74 dB.

3.5 Doppler OCT

A key aspect of OCT imaging is the capability to measure the speed of moving particles thanks to the Doppler effect. The Doppler effect is the change in frequency of a wave due to

relative motion of the source and the receiver; moving particles play the role of the receiver in this case. The observed frequency of the light backscattered by the particle will differ from the source frequency in a fashion proportional to its velocity. The Doppler frequency f_D is the difference between the observed frequency and the source frequency. Several techniques exist to measure the Doppler frequency and this work uses a moving-scatterer-sensitive technique adapted from (Ren, Sun, MacDonald, Cobb, & Li, 2006; Srinivasan et al., 2010). Briefly, let the complex signal of the Fourier-transformed jth A-line be $\Gamma_j(z)$, as a function of depth z, then the difference between two adjacent A-lines $M_j(z)$ is computed:

$$M_j(z) = \Gamma_{j+1}(z) - \Gamma_j(z) \tag{3.5}$$

A region of interest (ROI) is defined as the intersection of N lines and K rows, and the signal $A_j(z)$ is averaged over this ROI:

$$A_j(z) = \sum_{z=m}^{m+K} \sum_{j=n}^{n+N} M_j(z) M_{j+1}^*(z) \tag{3.6}$$

Then the average local Doppler frequency is computed from $A_j(z)$:

$$f_D^j(z) = \frac{1}{2\pi\tau} \tan^{-1} \left\{ \frac{\Im[A_j(z)]}{\Re[A_j(z)]} \right\} \tag{3.7}$$

Where τ is the acquisition period of a single A-line. The advantage of the moving-scatterer-sensitive method is that allows changing the averaging zone. If the ROI is large, the technique is less sensitive to small velocities, but it is also less affected by Doppler noise coming from static scatterers.

3.6 Experimental methods

Hardening of the arteries has been shown to be a predictor of cognitive decline and dementia (Pase, Herbert, Grima, Pipingas, & O'Rourke, 2012), yet there is no specific model of arterial stiffness. A novel model of unilateral carotid calcification was recently developed (Sadekova et al., 2013), and OCT was used to assess the impact of carotid calcification on the brain, measuring blood flow pulsatility over a cardiac cycle. The pulsatility measurements are shown on Figure

3-8. Since the system described in this chapter was not fully functional at the moment of *in vivo* experiments, another OCT, developed in the laboratory was used instead (Baraghis et al., 2011).

In our work, a frequency domain Optical Coherence Tomography (FD-OCT) was used to perform imaging. The details of the system are described in (Baraghis et al., 2011). Briefly, the system is based on a 870 nm LED (Exalos EXS8710-2411, Langhorne, PA), with 65nm of yielding 2.5mW of power on the sample through an infinite corrected 10x objective (Olympus UMPLFLN 10XW, Markham, Ontario). The axial and lateral resolution are 5 and 10um respectively. The detection is done with a custom made spectrometer using a 2048 pixel line camera (Basler Sprint spL2048 -140k, Exton, PA). The A-line rate was limited to 15 kHz due to data streaming to the hard drive. The maximum detectable Doppler blood flow speed was 3mm/s without phase-unwrapping. A series of acquisitions were performed on each mouse with dimensions of 200-800 um, depending of the size of the observed arteries. Light attenuation permitted imaging of vessels as deep as 500 um. Between 4 and 6 distinct arteries were measured per animal.

Images were reconstructed offline using custom software written in Matlab (The MathWorks, Natick, MA). Dispersion compensation was implemented according to the procedure described in (Wojtkowski et al., 2004). Doppler blood flow was computed using a moving-scatterer-sensitive technique adapted from (Ren et al., 2006; Srinivasan et al., 2010). Data was high-pass filtered to remove the stationary scattering components from the image.

In order to obtain the blood speed profile during a cardiac cycle a B-scan (each one consisting of 840 A-lines) has to be performed several times (400 in these experiments) in the same place. The ECG signal is simultaneously acquired during this imaging protocol, allowing reconstructing the evolution of the blood speed during a cardiac cycle. The QRS peaks are detected on the ECG signal, then the time elapsed from the QRS peak is assigned to every single A-line (cardiac cycle time). Typically ~8 images were acquired per cardiac cycle. Each A-line is placed on a 3D matrix with respect to position and cardiac cycle time, allowing to obtain the blood speed profile from any pixel during the whole cardiac cycle.

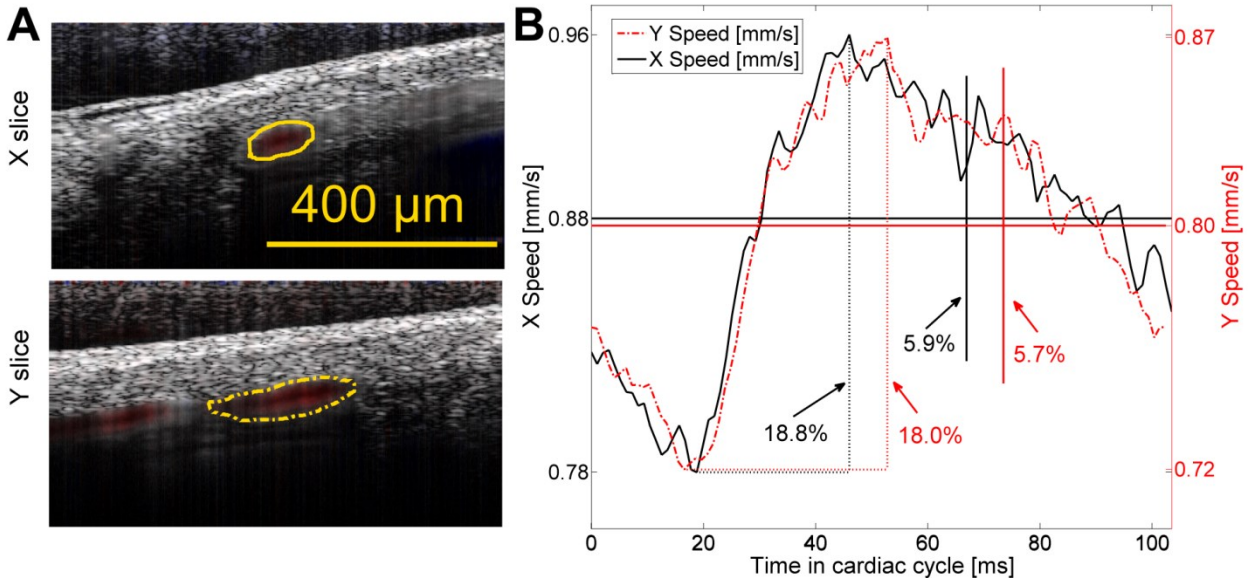

Figure 3-8: Example of blood flow pulsatility in a single artery of a control mouse: (A) Two slices at 90º are measured. The average flow (red-blue) during a cardiac cycle is overlaid onto the structural image (grayscale). (B) The average speed is 0.88 mm/s for the X slice (solid black line) and 0.80 mm/s for the Y-slice (red dash-dot line) due to different size of the ROIs (yellow lines). The speed profile is very similar in both slices confirming that variation is due to heart beat. Variation between the maximum and the minimum speed are calculated (dotted lines). Variability (solid vertical lines) is defined as the standard deviation divided by the mean.

3.7 Experimental results

The impact of the arterial stiffness model on cerebral blood flow pulsatility was asessesed by OCT imaging. In the group with $CaCl_2$ treated arteries, blood flow pulsatility increased significantly both in medium and large sized (>95µm) arteries, with respect to the control group. Furthermore, this increase was significant only on the right side of the cortex, which is unilateral to the $CaCl_2$ treated carotid. Regarding specific regions of the brain the pulsatility was significantly increased in the middle cerebral artery region, however the somatosensory cortex showed no significant differences. These results suggest that carotid-stiffness induced pulsatility depends on the localization of arterial segments.

3.8 Conclusions

In this chapter the application of FD-OCT to evaluate cerebral blood flow pulsatility was demonstrated. The full implementation of the designed SS-OCT system was not carried out due mainly to hardware limitations; however, updating the acquisition board to a high-speed digitizer, capable of linear sampling in *k* domain, would allow real-time imaging. This update would not require any major modifications to the existing optics and should not be cumbersome.

CHAPTER 4 FUNCTIONAL CONNECTIVITY

The term functional connectivity (fc) has been defined the as the assessment of temporal correlation between spatially remote neurophysiological events (K J Friston et al., 1993). This applies both to task-based studies and resting-state paradigms, the work presented here is limited to the latter type of studies.

In this chapter I describe the algorithms used to extract fc information from optical measures. The work presented in the articles was done primarily with seed-based fc and graph theoretical measures. For OIS and PAT data analysis, we have developed in MATLAB two SPM compatible toolboxes with a graphical interface for batch processing, screenshots are presented in the ANNEX , and copies of the program are available upon request from Prof. Lesage's laboratory. Some other techniques including singular value decomposition and hierarchical clustering were also explored, although not fully implemented for a group-level analysis. Some other methods, such as structural equation models (Gonçalves & Hall, 2003), mutual information tools (Salvador et al., 2007) or self-organizing maps (Peltier, Polk, & Noll, 2003) are beyond the scope of this thesis.

4.1 Algorithms description

4.1.1 Seed-based functional connectivity

The first (B. Biswal et al., 1995) and one of the most widely used techniques to identify spatial patterns of coherent brain activity is seed-based analysis. This method entails the extraction of the OIS time course from a region of interest, called a seed region, and then compute the temporal correlation between this extracted signal and the time course from all the pixels belonging to the brain. This analysis can also be limited to seed-to-seed temporal correlation.

The recording sessions of 15 minutes are carried out in resting-state conditions. Time courses of every pixel are temporally band-pass filtered (zero phase-shift fourth-order Butterworth filter) at 0.009-0.08 Hz, according to previous fc studies (Bero et al., 2012; Brian R White et al., 2011). A Butterworth design was chosen because of the flat response in the pass-band; zero-phase filtering was achieved by processing the data in both the forward and reverse directions, using MATLAB

function `filtfilt` (Oppenheim, Schafer, & Buck, 1999, pp. 336–337). After temporal filtering, each pixel time trace is downsampled from 5 Hz to 1 Hz.

A global brain signal is created from the average of all the pixels time traces. In order to account for coherent variability common to all pixels, this global brain signal is then regressed from each pixel time course, using a General Linear Model (GLM) from the package Statistical Parametrical Mapping (Karl J. Friston, Ashburner, Kiebel, Nichols, & Penny, 2006)(SPM8, www.fil.ion.ucl.ac.uk/spm) running on MATLAB ver. 7.10.0.499 (R2010a) (The MathWorks, Natick, MA). This procedure is used in fc-MRI to enhance the quality of the measures, removing spontaneous BOLD fluctuations common to all brain voxels (Fox, Zhang, Snyder, & Raichle, 2009).

Let the OIS data be represented as the $n \times m$ matrix, y, where n is the number of temporal points (frames) and m is the number of pixels. The global brain signal g is defined as the mean time course of all pixels marked as belonging to the brain cortex. This global brain signal g is an $n \times 1$ column vector. Pixelwise regression of the OIS data y on g yields:

$$\beta_g = g^+ y \tag{4.1}$$

where g^+ (a $1 \times n$ row vector) is the pseudoinverse of g, i.e. $g^+ = [g^T g]^{-1} g^T$ and $g^+ g = 1$. Now β_g is a 1×m row vector (image). Removing the global signal from OIS data y generates the new image time series:

$$y' = y - g\beta_g \tag{4.2}$$

This residual image time-series y' is then used to generate seed-based correlation maps.

Global brain regression causes the distribution of correlations to be centered around a value of zero (uncorrelated), thus forcing the existence of negative correlations (anti-correlations). Therefore one must be cautious when interpreting anti-correlations issued from this processing step.

All seeds are manually placed a priori using the coordinates corresponding to left and right frontal, cingulate, motor, somatosensory, cingulate and visual cortices (Brian R White et al.,

2011). Seed time-courses are computed as the mean time course of the pixels within a 7 pixel radius from the seed locus.

The principle of seed-based fc is illustrated with an example in Figure 4-1:

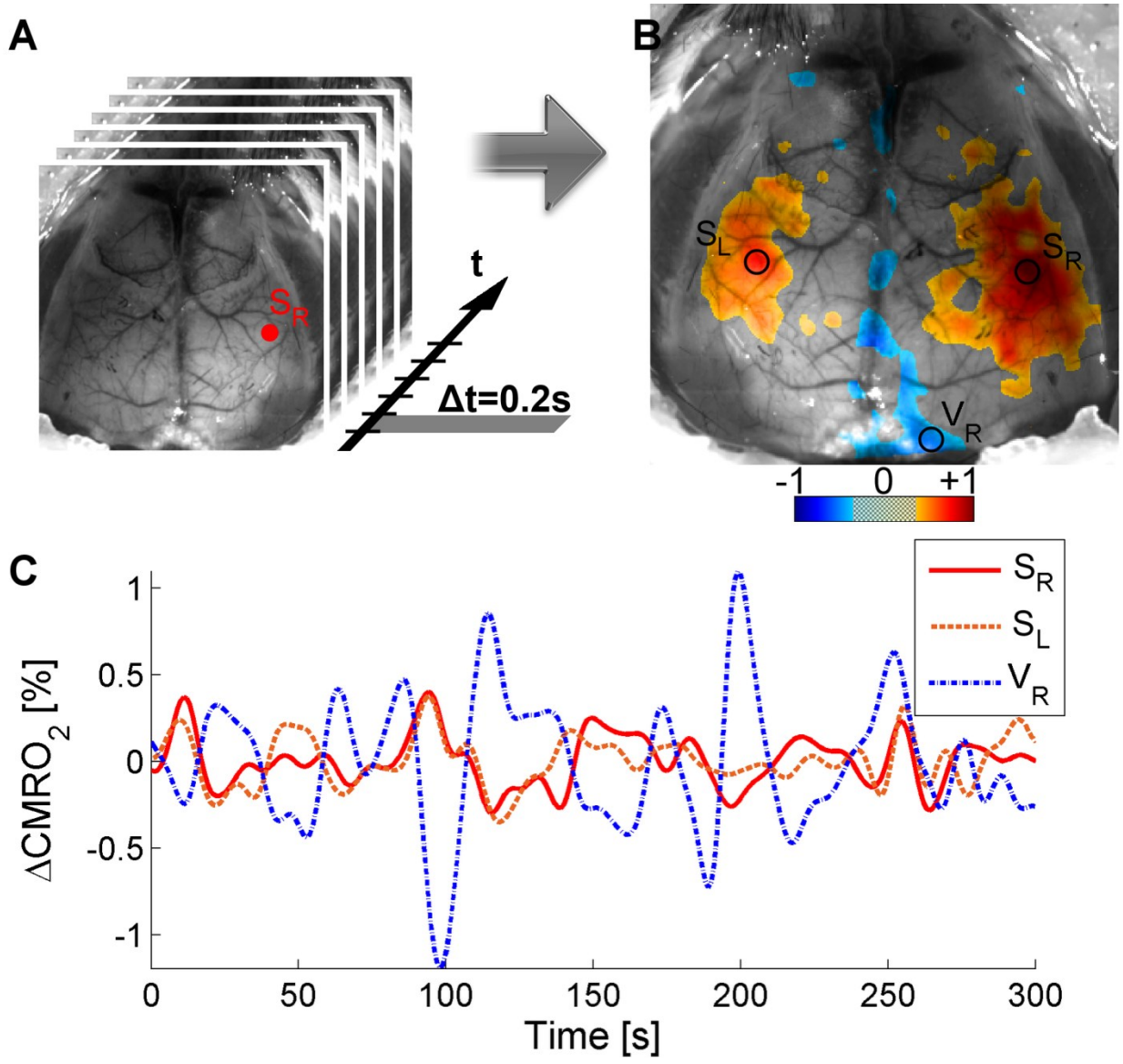

Figure 4-1: Principle of seed-based functional connectivity. (A) The $\Delta CMRO_2$ time course is extracted from a specific region, e.g. the right somatosensory cortex S_R. (B) Correlation coefficients are computed between S_R seed and all other pixels in the brain. The spatial distribution shows both correlations (negative values) and anticorrelations (negative values), thresholded at an arbitrary value of $|r| = 0.35$. (C) The time course is shown for the seed region (S_R red), a seed positively correlated with this seed region in the contralateral somatosensory

cortex (S_L, orange, r = +0.6160) and a region negatively correlated with the seed region in the right visual cortex (V_R, blue, r = −0.5570).

When the animal model implies a unilateral modification, we expect to see differences in the regions and their contralateral homologues, so the metric used to evaluate fc was a regional bilateral functional correlation; defined as the correlation between each seed time-course and its contralateral homologue, yielding six values for each mouse. The Pearson's coefficient r-values were converted to Fisher Z measures using $Z(r) = \frac{1}{2}\ln[(1+r)/(1-r)]$ before performing the random effect rank sum tests. P values were corrected for multiple comparisons using false discovery rate (FDR) adjustment. Adjusted values were considered significant at $p<0.05$.

This approach is widely used in functional neuroimaging because of its simplicity, high sensitivity and easy interpretation (Cordes et al., 2001; Fox & Raichle, 2007; Greicius et al., 2003). Nevertheless this technique has some limitations: a map should be generated for each selected seed region, and a single or several seed maps cannot give a full view of all interactions among ROIs. The information of a seed-based fc map is limited to the functional connections of the selected seed region, making it difficult to examine functional connections patterns on a whole-brain scale. Also, the results depend on the *a priori* information of a seed placement (Fox & Raichle, 2007).

4.1.2 Independent component analysis (ICA)

This approach is probably the second most employed technique for analyzing fc (Fox & Raichle, 2007). ICA minimizes statistical dependence among its components. Each component is associated with a spatial map, some maps reflect neuro-functional systems and some other maps reflect noise components. This technique does not require a priori placement of seed regions, however it does require the user to manually determine which components are the most important and resemble neuro-functional systems and which components reflect noise. It is a promising technique because of the data-driven approach and its use is increasing. Nevertheless, there are still drawbacks. First, results are highly dependent on the number of components the user asks the algorithm to produce. Second, the aforementioned manual separation of noise and physiological

maps. Finally, there has been a debate of temporal versus spatial independence (McKeown, Hansen, & Sejnowsk, 2003).

In this work an alternative to ICA was explored: principal component analysis (PCA) and its equivalent tool, singular value decomposition (SVD) (Worsley, Chen, Lerch, & Evans, 2005). PCA is similar to ICA in terms of results and interpretation, but assumes that the sources of resulting features are merely uncorrelated, not statistically independent. The goal of PCA is to minimize the retroprojection error from compressed data (Draper, Baek, Bartlett, & Beveridge, 2003). Let the OIS data be represented by the spatio-temporal matrix X_{nt} where $n = 1,2, \dots, N$, being N the number of pixels; and $t = 1,2, \dots, T$ where T is the number of time points. The time traces in every pixel were correlated against every other pixel to create the auto-correlation matrix:

$$R_{XX}(i,j) = corr\big(X(i,t), X(j,t)\big), \quad i,j \in N \tag{4.3}$$

Storing into memory this auto-correlation matrix, also known as connectivity matrix, can be forbidding, since R_{XX} size is $N \times N$, hence the need to resort to more sophisticated storage methods such as memory-mapping. Furthermore R_{XX} is can be approximated with:

$$R_{XX} = \sum_{k=1}^{K} U_{nk}\ \Lambda_{kk} V_{nk} \tag{4.4}$$

Where U and V are orthogonal matrices that are best understood as basis of correlation modes, each one representing a spatial connectivity pattern, and Λ is a diagonal matrix of component weights. The singular values indicate the contribution of each particular vector to the total variance in the data. Therefore, the first singular vectors represent the most dominant connectivity patterns, as shown on Figure 4-2.

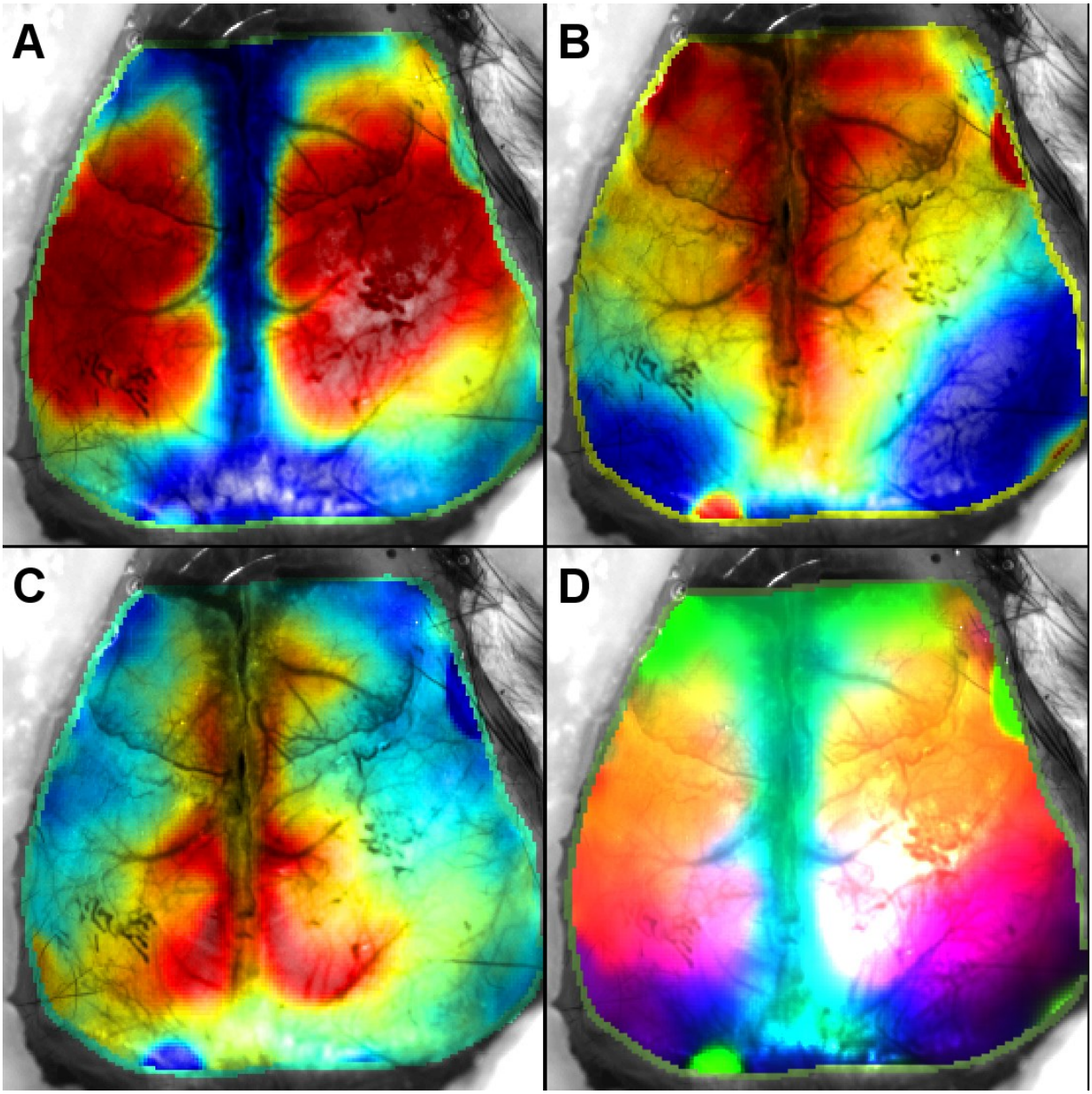

Figure 4-2: Singular value decomposition of the correlation matrix of $CMRO_2$ estimates is shown. The first three singular values validate the seed-based correlation analysis. (A) A very strong sensori-motor network (B) Cingulate-Frontal network that anti-correlates with visual cortex (C) Retrosplenial-cingulate network (D) The first three orthogonal components visualized as red-green-blue (RGB) merged image. All images are overlaid on the anatomical image of the cortex acquired at λ=525nm.

4.1.3 Hierarchical clustering

Hierarchical clustering attempts to agglomerate pixels whose behavior over time is similar (Cordes, Haughton, Carew, Arfanakis, & Maravilla, 2002). In similar fashion to PCA, an auto-correlation matrix is constructed from all the pixels time course. A clustering algorithm is then applied to cluster together all pixels whose similarity exceeds a certain threshold value. Methods differ from one another in how they measure the similarity between clusters; in this example shortest-distance method was used. This information allows building a hierarchical tree or dendrogram, useful to envisage the relationships among several regions. This technique was no further explored in depth due to the limitation imposed by the need of an a priori definition of a maximum number of clusters, as there is no single measure of the optimal number of clusters in which to partition the data (Margulies et al., 2010).

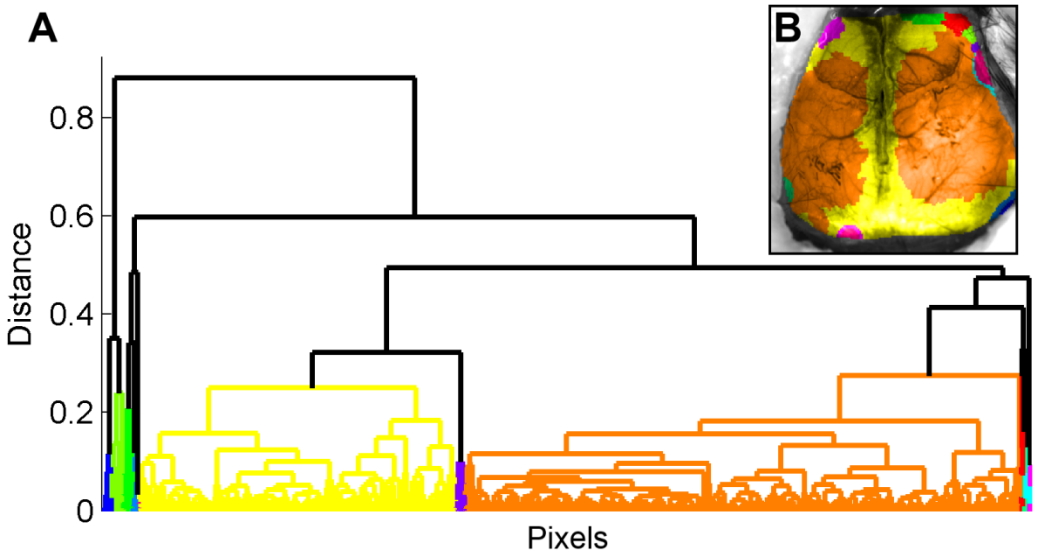

Figure 4-3: Hierarchical clustering of $CMRO_2$ measures ($N_{clusters}$ = 12). (A) Dendogram showing clustering of pixels timecourses according to their correlation. (B) We see a clear delineation of somatosensory-motor network in orange and a large network encompassing cingulate, retrosplenial and visual cortices in yellow. Clusters are overlaid on the anatomical image of the cortex acquired at λ=525nm.

4.1.4 Graph theory

All kinds of complex system can be represented as a network, a collection of elements linked together by connections (Petrella, 2011). Graph theory is a branch of mathematics that deals with

the characteristics of the networks; its origin is often attributed to Euler, who in the XVIII century, solved the problem of the bridges of Königsberg (Euler, 1741). The problem consisted of finding a walk through the city traversing the bridges exactly once and returning to the starting point. Euler demonstrated its impossibility by representing the problem as an abstract network: a graph (Cornelis J. Stam & Reijneveld, 2007). All kinds of interacting elements ranging from social connections, the Internet, power supply grids, public transportation systems, genes, to proteins and neurons can be viewed as networks (Bassett & Bullmore, 2006). The seed-driven technique previously explained predominantly focuses on mapping the spatial extent of the networks, while graph theory, in opposition, provides the complementary methods to characterize several properties of brain organization as a network.

In a graph *G*, i.e. the mathematical representation of a network, vertices (nodes *N*) correspond to elements of the system and lines (edges *K*) connecting each vertex symbolize the interactions between them (Latora & Marchiori, 2001). Thus, the brain cortex can be modeled as a graph where the nodes are associated with seeds and edges are associated with the amplitude of functional connectivity *z(r)* among these seeds. Following the computation of seed-to-seed connectivity matrix, a threshold is generally applied to define the adjacency matrix characterizing the graph G. An appropriate cost threshold level is chosen so that the network exhibits small-world properties, characteristic of brain functional networks (Achard & Bullmore, 2007; Bassett & Bullmore, 2006).

A graph *G* consisting of a set of nodes (vertices) *N* and a set of edges (connections) *K* can be characterized by several measures at seed level (Bassett & Bullmore, 2006; Whitfield-Gabrieli & Nieto-Castanon, 2012). *G* can be represented by its adjacency (or connection) matrix, i.e. the $N \times N$ matrix whose entry $a_{mn}(G)$ indicates the presence of an edge connecting node *m* to node *n*. One of the most elementary measures is the degree, simply defined as the number of edges that connect to a certain node *n*, and it is usually indicated as $k_n(G)$. Another important metric of each node *n* is cost $C_n(G)$, defined as its proportion of connected neighbors. $d_{nm}(G)$ represents the shortest-path between nodes *n* and *m* in graph *G*, and is defined as the path between them with the minimum number of edges. The average path length $L_n(G)$ is defined as the average shortest-path distance from a node *n* to all other nodes in the graph. Related to the former measure is that of global efficiency $E_n^{global}(G)$, which is the average inverse shortest-path

distance from node *n* to all other vertices in the graph. $E_n^{global}(G)$ is sometimes thought as a measure of the relative importance of a given node within a graph. A measure of the robustness of the graph is the clustering coefficient $CC_n(G)$, defined as the probability that the neighbors of this node are also connected to each other; in other words it equals the number of connections between the *n* node neighbors $e_n(G)$, divided by the maximum possible number of connections. Proportional to the clustering coefficient is the local efficiency $E_n^{local}(G)$, defined as the average global efficiency across all neighbors of node *n*. Finally, the betweenness centrality $CB_n(G)$ of a particular node *n* is the number of all shortest-paths in a network that pass through this node $\sigma_{jm}(n)$ divided by the total number of shortest paths in the network $\sigma_{jm}(G)$ (Anthonisse, 1971; Freeman, 1977). It is a measure of the node's importance in the graph.

The measures that reflect the level of global integration in the network were generated by averaging seed-level measures across all nodes of a network (Table 4.1). These summary network-level measures were entered in a second-level general linear model to compare fc patterns between groups.

Table 4.1: Definition of graph theoretical measures

	ROI level measures	Network level measures
Global efficiency	$E_n^{global} = \frac{1}{N-1} \cdot \sum_{m \neq n \in G} \frac{1}{d_{nm}(G)}$	$E^{global} = \frac{1}{N} \cdot \sum_{n \in G} E_n^{global}(G)$
Local efficiency	$E_n^{local} = E^{global}(G_n)$	$E^{local} = \frac{1}{N} \cdot \sum_{n \in G} E_n^{local}(G)$
Betweenness centrality	$CB_n(G) = \sum_{j \neq n \neq m \in G} \frac{\sigma_{jm}(n)}{\sigma_{jm}(G)}$	$CB(G) = \frac{1}{N} \cdot \sum_{n \in G} CB_n(G)$
Cost	$C_n(G) = \frac{1}{N-1} \cdot k_n(G)$	$C(G) = \frac{1}{N} \cdot \sum_{n \in G} C_n(G)$
Average path length	$L_n(G) = \frac{1}{N-1} \cdot \sum_{m \neq n \in G} d_{nm}(G)$	$L(G) = \frac{1}{N} \cdot \sum_{n \in G} L_n(G)$
Clustering coefficient	$CC_n(G) = \frac{2 \cdot e_n(G)}{k_n(G) \cdot (k_n(G)-1)}$	$CC(G) = \frac{1}{N} \cdot \sum_{n \in G} CC_n(G)$
Degree	$k_n(G) = \sum_{m \in G} a_{mn}(G)$	$k(G) = \frac{1}{N} \cdot \sum_{n \in G} k_n(G)$

Statistical significance is determined by a Student's unpaired t-test ($p<0.05$) with false discovery rate (FDR) correction (Benjamini & Hochberg, 1995). Briefly, FDR procedure is defined as:

$$P_{(i)} \leq \frac{i}{m} q^* \tag{4.5}$$

Where $P_{(i)}$ are the ordered p-values, $H_{(i)}$ the null hypothesis corresponding to $P_{(i)}$, and q^* is the significance level of test. Let k is the largest i for which the inequality (4.5) is met, then we reject all $H_{(i)} = 1,2,\ldots,k$ and the FDR is controlled. It provides a less severe control than simple Bonferroni's method, increasing statistical power at the expense of increasing false positive errors.

Graph theory takes advantage of the tools developed on this mathematical field over the years and provides the tools to apply the theory to brain imaging, characterizing brain organization as a network. An important issue is the seeds placement; since the seeds have to be defined a priori, this technique suffers from the same limitations as the seed-based approach outlined earlier.

CHAPTER 5 ARTICLE 1: OPTICAL IMAGING OF ACUTE EPILEPTIC NETWORKS IN MICE

Edgar Guevara[1,2], Philippe Pouliot[1,2], Dang Khoa Nguyen[3], Frédéric Lesage[1,2]

5.1 Presentation of the article

This article (Guevara, Pouliot, Nguyen, & Lesage, 2013) was published in the Journal of Biomedical Optics.

The main purpose of the article was to investigate the potential of OIS as a tool to study resting-state brain networks during epileptiform activity. The neurotoxin 4-Aminopyridine (4-AP) was used in live mice to model epileptiform activity. The identified resting-state networks before and after the onset of seizure-like activity showed both increased and decreased homologous correlations for different ROIs of the cerebral cortex. These changes were not uniform across the different hemodynamic measures (HbO_2, HbR, CBF and $CMRO_2$), thus suggesting a potential decoupling between blood circulation and metabolism in the resting-state networks. These findings support the need to include independent hemodynamic measures in a more extensive investigation of epileptic networks.

5.2 Abstract

In this paper we investigate the potential of intrinsic optical imaging and resting state analysis under anesthetized conditions as a tool to study brain networks associated with epileptic seizures. Using an acute model of epileptiform activity, the 4-Aminopyridine (4-AP) model in live mice, we observe changes in resting state networks with the onset of seizure activity and in conditions of spiking activity. Resting state networks identified before and after the onset of epileptiform activity show both decreased and increased homologous correlations, with a small dependence on seizure intensity. The observed changes were not uniform across the different hemodynamic

---

[1] Department of Electrical Engineering, École Polytechnique de Montréal, Canada

[2] Montreal Heart Institute, Montréal, Canada

[3] Department of Medicine, Université de Montréal, Montréal, Canada

measures, suggesting a potential decoupling between blood flow and metabolism in the low frequency networks. This study supports the need for a more extensive investigation of epileptic networks including more than one independent hemodynamic measurement.

5.2.1 Key Words

Functional connectivity, resting state, biomedical imaging, optical intrinsic signals, laser speckle contrast, 4-aminopyridine, animal models of epilepsy.

5.3 Introduction

Epilepsy is a group of neurological disorders where the abnormal synchrony of discharge in large ensembles of neurons results in an epileptic seizure (ictus), which over time may have serious consequences (Kandel, Schwartz, & Jessell, 1991). Epilepsy is one of the most common major neurological disorders, affecting 0.4 to 0.8% of the population (World Health Organization, 2006). The current method to visualize abnormal epileptiform discharges in patients with epilepsy is to perform an electroencephalogram (EEG), a technique which uses electrodes to record the spontaneous electrical activity of the brain (Gibbs et al., 1937). Epileptiform abnormalities are usually divided into a) 'interictal' discharges which are brief (milliseconds) asymptomatic paroxysmal EEG transients clearly distinguished from background; and b) 'ictal' discharges which are sudden focal rhythmic activity with characteristic patterns of evolution (with respect to amplitude, frequency and spatial distribution) lasting at least several seconds. These ictal discharges are generally associated with clinical seizure manifestations.

Functional imaging based on cerebral perfusion such as combined functional MRI - electroencephalography (fMRI-EEG) (Gotman et al., 2005) and functional near-infrared spectroscopy (fNIRS –EEG) (Gallagher et al., 2008) have recently been explored for their potential at identifying the epileptic focus as well as study the coupling between brain regions involved in the epileptic network. While hemodynamic changes triggered by epileptic events have potential for localization, neuroimaging observations in patients remain confounded in several ways. An overarching reason is that the hemodynamic response is often not restricted to the epileptogenic focus but spreads across a distributed network of brain structures, with complicated dynamics (Nguyen et al., 2012; M. Zhao et al., 2007). For example, the presence of mirror activation (Morrell & deToledo-Morrell, 1999) sometimes makes lateralization difficult.

Even when there is a clear localized focus, the temporal aspects between oxyhemoglobin (HbO_2), deoxyhemoglobin (HbR), cerebral blood flow (CBF), volume, and oxygen metabolism are still very intricate. Interictal discharges, and seizures even more so, are large neuronal discharges requiring an increased metabolic consumption (Bruehl, Hagemann, & Witte, 1998) and thus accompanied by a large increase of perfusion, rendering the interpretation of fMRI and fNIRS data difficult, given the complicated relationship between the various quantities of interest.

The term functional connectivity is applied to a variety of studies that examine coherent inter-regional correlations of neuronal activity during both cognitive tasks and rest (Fox & Raichle, 2007). It is a technique sensitive to spatial and temporal synchronicity of fluctuations in neural activity (Waites et al., 2006). This technique has been widely used with EEG measures in several studies that found changes in synchronicity before and after the seizure(Aarabi et al., 2008; Mormann et al., 2003; Ponten et al., 2007; Schindler et al., 2007; Wendling et al., 2005). Interictal determination of EEG functional connectivity (fcEEG) has been reported in patients with mesial temporal lobe epilepsy (Bettus et al., 2008), as well as in epileptic children (Righi, Barcaro, Starita, Karakonstantaki, & Micheloyannis, 2008). Furthermore, fcEEG has been shown to be a predictor of epilepsy diagnosis (Linda Douw et al., 2010). The application of functional connectivity using hemodynamic measurements to epilepsy is motivated both by observations of a distributed network of activations during epileptic events and by recent studies with resting-state functional magnetic resonance imaging (C. Luo et al., 2012; Mankinen et al., 2012; Waites et al., 2006; Z. Wang et al., 2011), that have documented an altered functional connectivity in several functional networks in epileptic patients. In the first of these studies, investigations in patients with left temporal lobe epilepsy has reported a significant decrease of connectivity in language-related areas during resting-state when compared to controls (Waites et al., 2006). Separate studies of epileptic networks documented a decrease of functional connectivity in the self-referential, somatosensory, visual, and auditory networks (Z. Wang et al., 2011), as well as in the default mode network (Frings, Schulze-Bonhage, Spreer, & Wagner, 2009; W. Liao et al., 2011; C. Luo et al., 2012) and in the dorsal attention network (Z. Zhang et al., 2009). The distributed nature of activation during epileptic seizures, the heterogeneity within the patient population and non-linear coupling (Pouliot et al., 2012; Voges et al., 2012) between vascular components during large neuronal discharges support investigating these phenomena in controlled animal models to better characterize network changes with epileptic events.

We adapted in this work a recently developed technique that combines functional connectivity mapping with optical intrinsic signal imaging (fcOIS) (Bero et al., 2012; Brian R White et al., 2011). This allowed measuring the magnitude of bilateral functional connectivity after the induction of focal seizures in the somatosensory cortex, using a seed region-based cross-correlation analysis. Since all procedures were carried out under anesthetized condition, the resting anesthetized state is simply referred as resting state, for the sake of simplicity and clarity. In addition to the oxyhemoglobin contrast previously used in (Bero et al., 2012; Brian R White et al., 2011), we examined deoxyhemoglobin and also blood flow measured simultaneously with laser speckle imaging to provide an extended set of measures characterizing hemodynamic changes during large neuronal discharges. This multimodal approach with optical and electrical recordings provides a comprehensive depiction of the resting-state activity, before and after the injection of the neurotoxin. Optical imaging based on intrinsic signals (OIS) and laser speckle blood flow imaging map hemodynamic variables all over the convexity of the cortex and electrophysiology recordings give a precise measurement of local field potential (LFP) in the area surrounding the epileptic focus. Injection of the neurotoxin 4-Aminopyridine (4-AP) in the left somatosensory cortex was used to produce seizure-like epileptiform discharges (later simply referred to as seizures) resulting from neuronal hyperactivity in cortical neurons (Fabene et al., 2006; M. Zhao et al., 2011; M. Zhao, Ma, Suh, & Schwartz, 2009). This model offers the possibility to make a comparison of the healthy cortex and the epileptic cortex on the same experimental animal. Motivations for the current study are two-fold: (1) understanding the modulation of brain networks at an early stage in ictogenesis is important to gain a better understanding of the pathophysiology of the disease (Bettus et al., 2011; C. Luo et al., 2012; Mankinen et al., 2012) and may help uncover the mechanisms by which these brain networks are altered. (2) A long-term motivation is to evaluate the usefulness of resting state analyses to support epileptic focus localization or seizure detection. Our aim in this work was to provide a proof-of-principle study using intrinsic optical imaging on acute epileptiform events, with a perspective of translating these techniques to a more chronic animal model of epilepsy and in conditions where anesthesia is not required.

5.4 Methods

5.4.1 Animal preparation

All surgical procedures, performed according to the recommendations of the Canadian Council on Animal Care, were approved by the Animal Research Ethics Committee of the Montreal Heart Institute. Nine male C57BL/6 mice (8.9 ± 0.2 weeks old, 23.3 ± 2.3 g weight, Charles River, Wilmington, MA) were anesthetized via intraperitoneal injections of urethane (2mg/g body weight) in a 10% (wt/vol) saline solution. Body temperature was maintained at 37°C with a feedback controlled heating blanket (MouseSTAT, Kent Scientific, Torrington, CT).

A tracheotomy was done in order to avoid respiratory distress (Moldestad, Karlsen, Molden, & Storm, 2009). Scalp was carefully removed and a stereotaxically guided burr-hole was made over the left somatosensory cortex (coordinates 1 mm lateral to midline, 1mm caudal to bregma Figure 5-1B) for injection of 4-AP and electrophysiological monitoring, using a #22 gauge needle.

Mice were placed on a stereotaxic apparatus and subcutaneous electrocardiogram was recorded with a single lead ECG amplifier (amp-b01, emka TECHNOLOGIES, Paris). The amplified (1000× gain) and filtered signal (0.2-500 Hz) was sampled at 1 kHz. All vital signals were digitized by a data acquisition card (NI-USB 6353, National Instruments, Austin, TX) controlled by a custom made graphical user interface developed in LabView (National Instruments), which also controlled the image acquisition. To prevent drying of the exposed skull a custom chamber made of bone wax was adhered to the skull with ultrasound gel and filled with mineral oil, after positioning the microelectrode.

5.4.2 Epilepsy model and electrophysiology

Epileptiform activity was achieved according to the procedures described by (M. Zhao et al., 2011, 2009), briefly described below. Focal seizures were induced by injection of 500nL of the K+ channel blocking agent 4-AP (A78403, Sigma-Aldrich, St. Louis, MO) solution at 15mM, through a glass micropipette with a micro-syringe pump controller (uMC4, World Precision Instruments, Sarasota FL). The volume was injected at a rate of 50nL/min. The borosilicate glass pipette (1mm outer diameter, 0.7mm inner diameter, 75mm long, World Precision Instruments,

New Haven, CT) was horizontally pulled on a programmable pipette puller (P-2000, Sutter Instruments, Novato, CA).

Following injection, the glass pipette was removed and then a tungsten microelectrode (0.5 to 2MΩ) was placed at a depth of ~500 μm into the cortex, in order to record extracellular LFP at the injection site. The signal was filtered between 10-5000 Hz, amplified 1000 times with a microelectrode AC amplifier (model 1800, A-M systems, Sequim, WA), and then digitized at 10 kHz. LFP data was further filtered between 0.2 and 130 Hz using an order 4 Butterworth digital filter in post-processing. An example of typical epileptiform activity is shown in Figure 5-1C.

5.4.3 Optical recording system

Optical images based on intrinsic signals (OIS) were acquired with a 12-bit CCD camera (Pantera 1M60, DS-21-01M60-12E, Teledyne Dalsa, Waterloo, ON) with a physical pixel size on chip of 12μm and full resolution of 1024×1024 pixels. The setup used in this work is depicted in Figure 5-1A.

A custom-made interface controls the camera, records images and vital signs, while synchronizing acquisition and illumination. A Macro Lens (105mm f/2.8max, Sigma Corp., Ronkonkoma, NY) with small focal depth (350 μm) was used. Reflectance images of the brain cortex were recorded with time-multiplexed illumination (525, 590, 625 nm) produced by 10W LEDs (LZ4-00MA00, Led Engin, San Diego, CA). Illumination for speckle imaging was provided by 90 mW, 785 nm laser diode (L785P090, Thorlabs, Newton, NJ) and aperture was adjusted to f/8, so that the pixel size and speckle size were matched. The four temporally multiplexed wavelengths led to a full-frame rate of 5 Hz. A 2×2 binning on camera was performed to allow continuous data streaming to hard drive. Illumination was further adjusted so that no part of the brain was under- or over-saturated by any of the wavelengths. The exposure time of the camera was set to 10 msec. The setup was mounted on an optic table with tuned damping (RS 2000, Newport, Irvine, CA) to avoid spurious signals from vibrations.

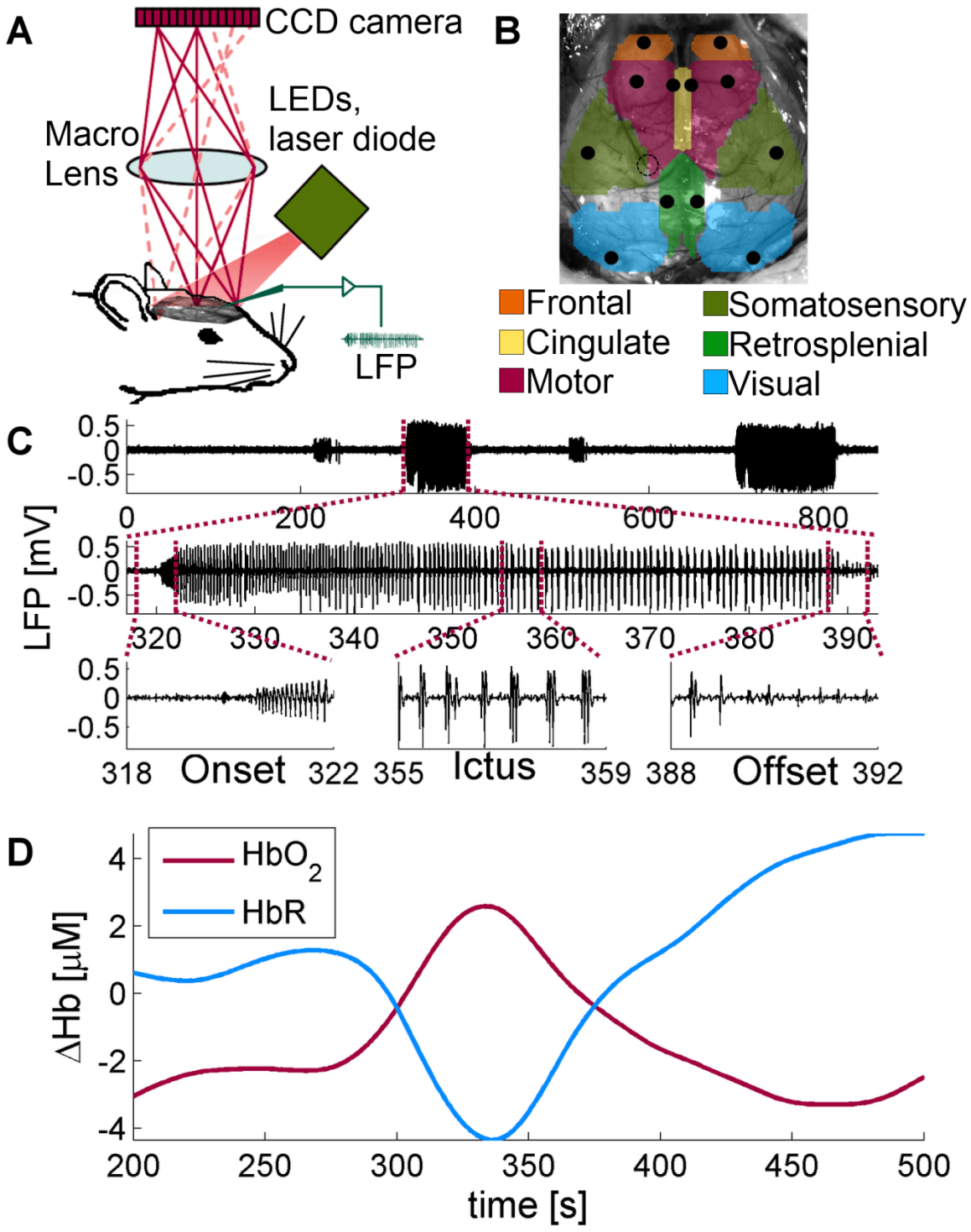

Figure 5-1: (A) Overview of the intrinsic signal optical imaging system. LEDs and laser diode are time-multiplexed and synchronized to the acquisition system. A tungsten electrode is used to record LFP on the left somatosensory cortex. (B) Functional regions on the mouse cortex and seed placement and size, manually constructed from the work of (Bero et al., 2012). Dotted circle

shows the placement of the LFP electrode. (C) Electrophysiology of 4-AP induced seizure. Top: Example showing some ictal discharges after an injection. 4-AP injection was finished at time 0. Middle: Zoom on a single ictal discharge. Bottom: Expanded view showing the onset of the discharge, the intermediate phase and the offset. (D) Filtered time traces of HbO_2 and HbR at the epileptic focus (dotted circle in B), during the seizure.

5.4.4 Optical imaging of intrinsic signals (OIS)

The analysis of spectroscopic images was based on previously published work (Dubeau et al., 2011; Dunn et al., 2003). In short, reflectance images from each LED wavelength were recorded with the CCD camera and interpreted as changes in attenuation (optical density) $\Delta \mathrm{OD} = \log(\frac{I_0}{I})$, where I is the reflected light intensity and I_0 the incident light intensity. Relative changes in HbO_2 and HbR were found using the modified Beer-Lambert law (Delpy et al., 1988) and a Moore-Penrose pseudoinverse:

$$\Delta OD(\lambda, t) = \sum_i \epsilon_i(\lambda)\, C_i(t) D(\lambda) \tag{5.1}$$

The differential path length factor, D(λ), was taken from (Dunn et al., 2005) and values out of the 560-610 nm range were extrapolated from (Kohl et al., 2000). Total hemoglobin baseline concentration of 100 μM with 60% oxygen saturation was assumed (Dunn et al., 2005) for the spectroscopic analysis. The hemoglobin extinction coefficients were obtained from (Prahl, 1999) and the reflectance values were corrected for the spectral response of the CCD camera and convolved with the LEDs spectral power distribution (Brieu et al., 2010).

Images of each chromophore (HbO_2, HbR) were spatially smoothed with a Gaussian kernel of 11×11 pixels (0.6×0.6mm) with a 5 pixel standard deviation (0.3mm). An anatomical image was recorded with illumination at 525 nm, and then the region corresponding to brain was manually selected using a closed spline curve to create a brain mask. All further processing was performed only on those pixels belonging to the brain mask.

5.4.5 Speckle contrast imaging

In addition to imaging changes in hemoglobin concentrations, changes in cerebral blood flow (CBF) were also computed by laser speckle contrast imaging. Speckle originates from the

random interference of multiple backscattered coherent light. In the presence of moving scatterers the interference field fluctuates, creating intensity variations, known as speckle patterns (Boas & Dunn, 2010; Dunn et al., 2001, 2005). When integrated over the exposure time of the camera, the speckle pattern becomes blurred in areas of increased blood flow. Images of blood flow were obtained by measuring the spatial contrast of the speckle *C*, defined as the ratio of the standard deviation to the average intensity $\sigma/\langle I\rangle$. The contrast is a function of the CCD camera exposure time *T* and it is related to the correlation time τ_C of the speckle, which is assumed to be inversely proportional to the speed of the scattering particles (Briers, 2001). A window of 5×5 pixels (0.3×0.3mm) was used to compute the speckle contrast images and the relative changes in blood flow were obtained with the following formula:

$$C = \frac{\sigma}{\langle I\rangle}, -\frac{2\Delta C}{C_0} \cong \frac{\Delta V}{V_0} \cong \frac{\Delta CBF}{CBF_0} \tag{5.2}$$

Since $\Delta v/v_0$ laser speckle imaging underestimates CBF by less than 5% (Luckl et al., 2010), in this work both quantities were assumed to be equal. Flow images then underwent the same spatial filtering as the hemoglobin images, and images from all three different contrasts were further resized to ¼ of the original size due to memory constraints.

5.4.6 Cerebral metabolic rate of oxygen

Changes in the cerebral metabolic rate of oxygen consumption ($CMRO_2$) were calculated from the images of changes in CBF, total hemoglobin (HbT) and HbR using the steady state relationship (M. Jones et al., 2001; Mayhew et al., 2000):

$$\frac{\Delta CMRO_2}{CMRO_{2,0}} = \frac{\left(1+\frac{\Delta CBF}{CBF_0}\right)\left(1+\gamma_R\frac{\Delta HbR}{HbR_0}\right)}{\left(1+\gamma_T\frac{\Delta HbT}{HbT_0}\right)} - 1 \tag{5.3}$$

A central hypothesis of this relation is the absence of transients with decoupled hemodynamic components. Here, since resting state networks were identified from data filtered between 0.009-0.08 Hz (see below), we hypothesized that for these networks, the relationship was maintained. The constants γ_R and γ_T where both assumed to be 1, which is within a physiologically plausible range (0.75–1.25) (M. Jones et al., 2001).

5.4.7 Functional connectivity

In this paper we followed the procedure outlined by (Brian R White et al., 2011)to produce seed-based correlation maps as a method for studying one aspect of functional connectivity; the steps are briefly described below.

Multimodal recording sessions (optical and electrical) of 15 minutes were carried out in resting-state conditions: Two sessions were performed before the injection of 4-AP and two more consecutive sessions were carried out ~5 minutes after the release of the epileptogenic compound in the somatosensory cortex, giving a total of 4 sessions per mouse. Time courses of every pixel were temporally band-pass filtered (zero phase-shift fourth-order Butterworth filter) at 0.009-0.08 Hz, according to previous functional connectivity studies (Bero et al., 2012; Brian R White et al., 2011). After temporal filtering, each pixel time trace was downsampled from 5 Hz to 1 Hz.

A global brain signal was created from the average of all the pixels time traces. In order to account for coherent variability common to all pixels, this global brain signal was regressed from each pixel time course, using a General Linear Model (GLM) from the package Statistical Parametrical Mapping (Karl J. Friston et al., 2006)(SPM8, www.fil.ion.ucl.ac.uk/spm) running on a MATLAB (The MathWorks, Natick, MA) platform.

All seeds were manually placed a priori using the coordinates corresponding to left and right frontal, cingulate, motor, somatosensory, cingulate and visual cortices (Brian R White et al., 2011), as shown on Figure 5-1B. Seed time-courses were computed as the mean time course of the pixels within a 3.5 pixel radius (0.2mm) from the seed locus. An example of seed time-trace during seizure are illustrated in Figure 5-1D. This seed is placed at the epileptic focus and its location is indicated with a dotted circle in Figure 5-1B. An increase in HbO_2 and a correspondent decrease in HbR is observed at the seizure onset.

With the unilateral application of 4-AP we expect bilateral differences between brain regions so the metric used to evaluate functional connectivity was a regional bilateral functional correlation, defined as the correlation between each seed time-course and its contralateral homologue, yielding six values for each mouse. The Pearson's coefficient r-values were converted to Fisher Z measures using $Z(r) = \frac{1}{2}\ln[(1+r)/(1-r)]$ before performing the random effect rank sum tests. Since the assumptions for normal distributions might not hold in this study, significance

was determined by the Wilcoxon rank sum test. P values were corrected for multiple comparisons using false discovery rate (FDR) adjustment. Adjusted values were considered significant at $p<0.05$.

5.5 Results

5.5.1 Identification of functional networks

Functional networks were identified prior to 4-AP injection and in agreement with previous literature (Brian R White et al., 2011) across mice for HbO_2 (see Figure 5-2 for representative maps of four sample mice) albeit with a stronger lateralization of some networks.

With multispectral acquisition, the same procedure was also performed for HbR and CBF estimated from speckle imaging, no significant change in spatial network organization was observed (data not shown). In one experiment we performed the network analysis using a higher frame rate and compared with a similar analysis performed by dropping camera frames to investigate the effect of acquisition frame rate. No significant difference was observed confirming that the chosen 5Hz acquisition rate was adequate (data not shown).

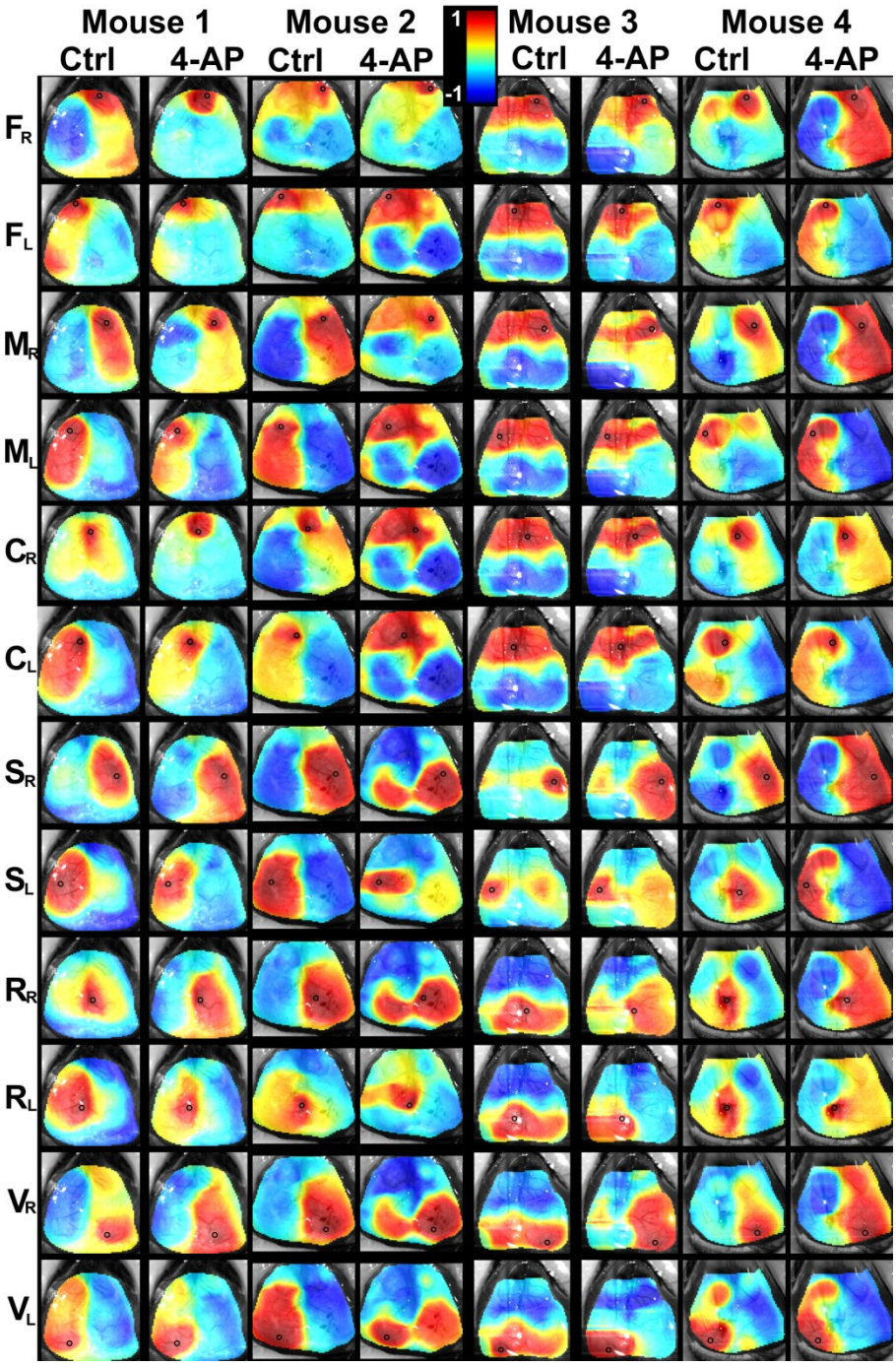

Figure 5-2: Seed-based HbO_2 correlation maps for four mice. One control session and one post-4-AP injection session are displayed for each mouse. (F: frontal cortex, M:motor cortex, C: cingulate cortex, S: somatosensory cortex R: retrosplenial cortex, V: visual cortex; subscripts L and R refer to left or right hemisphere, respectively). The scale for all correlation maps is from r = -1 to 1. Maps are shown overlaid on the anatomical image of the brain, acquired with green light. Seeds placement and sizes are indicated with black circles.

5.5.2 Changes in functional connectivity after injection of 4-AP

Out of 9 mice, 5 showed clear seizure-like activity (see Table 5.1 below) while 4 showed high intensity spiking activity. Seizure-like activity was characterized by fast rhythmic spiking activity of increasing amplitude and decreasing frequency, evolving into rhythmic spike and slow wave activity prior to gradual offset (see an example in Figure 5-1C), while spiking activity presents fewer than 10 spikes per burst (data not shown). All mice were combined in the analysis of this section. To assess the impact of acute seizures and epileptiform activity on resting state networks, resting state sessions acquired following injection of 4-AP were analyzed following the same methodology as above.

Correlations between homologous seeds were investigated and compared before and after injection of the neurotoxin. Data extracted from the HbO_2 time course showed a significant difference in retrosplenial seeds (Figure 5-3A). For HbR contrast there was no significant difference in any paired seeds time trace (Figure 5-3B), although a decrease in functional connectivity was seen on the somatosensory region, a trend also seen in flow and $CMRO_2$ data. Seeds of the cingulate, somatosensory and retrosplenial cortex saw significant changes when analyzed with CBF contrast (Figure 5-3C): a decreased bi-lateral functional connectivity was observed in the somatosensory seeds while increased connectivity was seen in the cingulate and retrosplenial regions.

To assess whether these hemodynamic changes were associated with metabolic consumption patterns, we computed $CMRO_2$ using steady state formulas given the low frequency fluctuations frequently documented in functional connectivity studies (B. B. Biswal et al., 2010; B. Biswal et al., 1995; Fox & Raichle, 2007; Greicius et al., 2003). Data shows no significant differences (Figure 5-3D). However there was a decrease in functional connectivity in the somatosensory and retrosplenial cortex, albeit not significant after FDR adjustment. All results were evaluated with a Wilcoxon rank sum test.

Functional networks were derived from low frequency filtered imaging data. We were also interested to measure correlation between raw signals, before and after seizures, to observe the degree of disruption in the whole signal prior to regression by the common signal (data not shown). Data show that all seeds are positively correlated, indicating the presence of a common signal to all the pixels time course during epileptic events, hence the need to regress a global

brain signal, obtained from the average time trace of all the pixels marked as belonging to the brain.

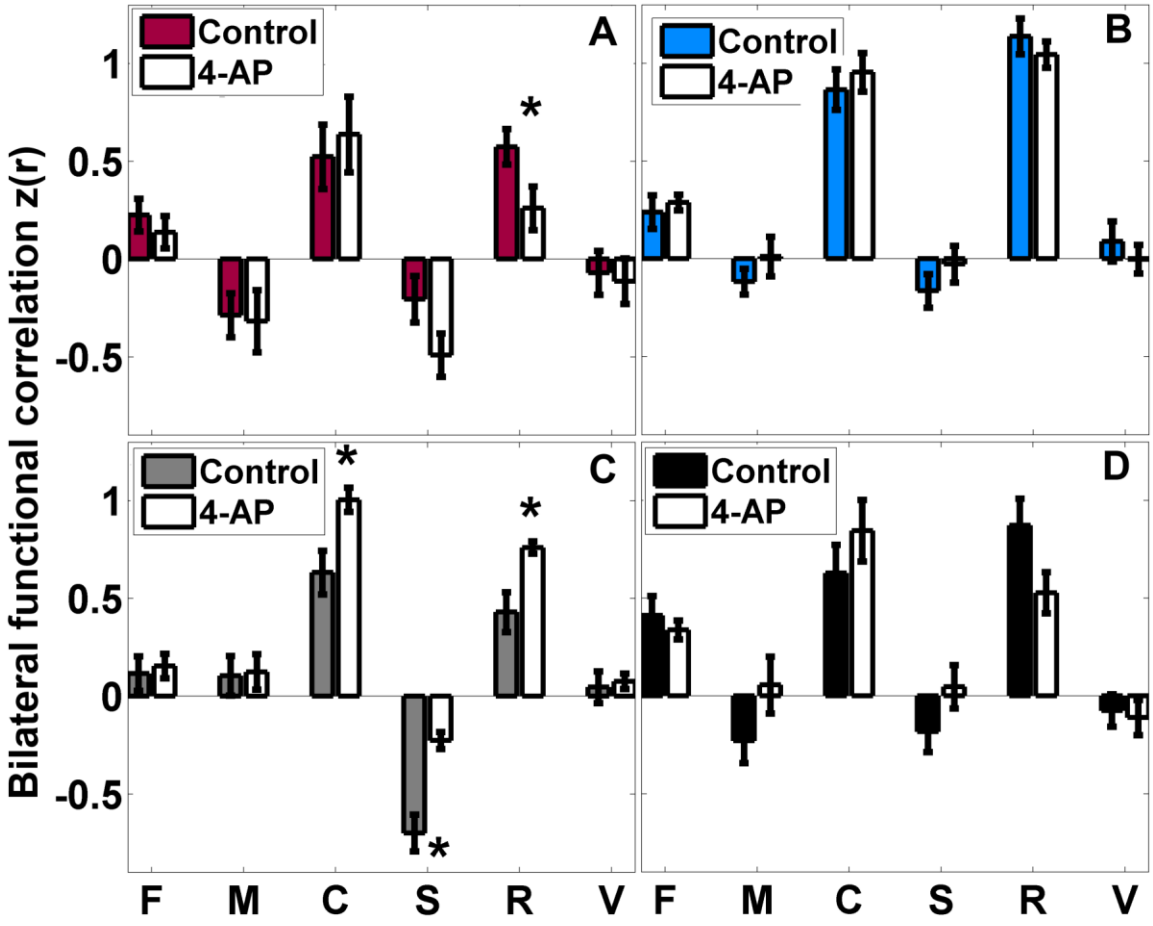

Figure 5-3: Regional bilateral functional correlation before and after the 4-AP injection, analysis done for every seed time-trace and its contralateral part. Contrasts shown: (A) HbO_2, (B) HbR (C) CBF and (D) $CMRO_2$. * $p<0.05$, FDR corrected. Standard error bars shown ($\sigma/\sqrt{N}$), with N=9.

5.5.3 Correlation between seizure duration and functional connectivity

Restricting the analysis to the mice showing clear seizure activity, we aimed to investigate whether seizure duration impacted network changes. To calculate changes of bilateral correlation we subtracted the bilateral correlation during control sessions, $z_0(r)$, from the bilateral correlation during the post 4-AP injection sessions, $z_{4AP}(r)$, and plotted this change versus the average seizure duration of the 4-AP sessions, as illustrated on Figure 5-4. Overall correlations between seizure duration and changes in bilateral correlations were moderate. For the somatosensory

cortex, where the toxin was injected, there was a positive correlation between the duration of the seizure and the changes in bilateral correlation. This same positive correlation was observed from the data extracted from the frontal cortex seeds. For other cortical regions, i.e. motor, cingulate, retrosplenial and visual a reverse effect was observed: the changes were negatively correlated with the seizure duration. For CBF contrast the correlation showed to be significant in the somatosensory (r^2=0.52) and retrosplenial (r^2=0.75) regions. HbR contrast had a significant correlation for retrosplenial seeds (r^2=0.50), while HbO_2 displayed a moderate (not significant) correlation for the motor seeds (r^2=0.41). The average length of seizures per subject was 68.7 ± 51 s. All recording sessions were 863 seconds long. Table 5.1 provides the duration of seizure-like activity for every recording session, the percentage of the recording session that belongs to seizure-like activity and the average duration of seizures per subject.

Table 5.1: Seizure data [a]

Subject ID	Seizure duration (s)		Percentage duration in seizure state (%)		Average seizure duration (s)
	Session 1	*Session 2*	*Session 1*	*Session 2*	*Both sessions*
1	**45, 43, 33, 32**	**35, 32, 27**	**5.2, 4.9, 3.8, 3.7**	**4, 3.7, 3.1**	**35.3**
3	**27, 33, 34**	**-**	**2.8, 3.4, 3.5**	**-**	**31.3**
4	**114**	**71, 112**	**13.2**	**8.2, 12.9**	**99**
7	**38, 30, 30**	**33, 32**	**4.4, 3.4, 3.4**	**3.8, 3.7**	**32.6**
9	**130**	**161**	**15**	**18.6**	**145.5**

[a] The first column provides the duration (in seconds) of seizure-like activity for every recording session, multiple numbers indicate multiple seizures recorded; the second column shows the percentage of the recording session that belongs to seizure-like activity; finally the last column indicates the average duration of seizures per subject.

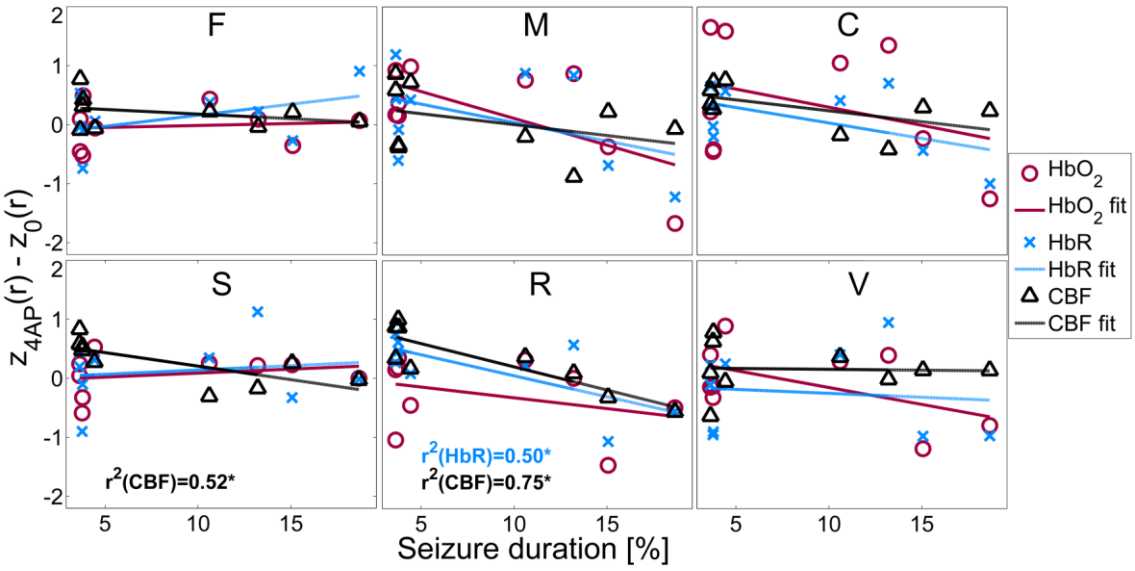

Figure 5-4: Changes in bilateral functional correlation plotted vs. seizure duration (expressed as a percentage of the recording session) for different cortical regions and different contrasts.

5.6 Discussion

In this work we investigated regional bilateral functional connectivity using a seed-based correlation analysis; functional connectivity was evaluated before and after the injection of epileptogenic 4-AP in the somatosensory cortex.

Using oxyhemoglobin contrast (HbO_2), significant differences in functional connectivity were found in the retrosplenial cortex. With deoxyhemoglobin (HbR) contrast, no seeds showed a statistically significant difference though most correlations decreased. In the case of relative blood flow contrast a significant difference was observed in the cingulate, somatosensory and retrosplenial regions. The only paired seeds to show a significant decrease of functional connectivity were in the somatosensory cortex, while the retrosplenial and cingulate exhibited an increase in functional correlation; we hypothesize this increase may be explained by the proximity of these last two regions to the superior sagittal sinus, so that their behavior is dominated by increased venous drainage at epileptic activity. For the estimated $CMRO_2$, no significant changes were found in functional connectivity measures.

Due to the proximity of cingulate and retrosplenial seeds to the site of 4-AP injection, the significant changes in the bilateral functional connectivity of these regions could be attributed to the proximity to the injection site, suggesting that the neurotoxin 4-AP might have propagated to

these regions. However, at the site of injection, homologous connectivity decreased suggesting a decoupling of hemispheric connections linking the somatosensory areas while at the cingulate and retrosplenial sites, connectivity increased. An explanation might be a potential compensatory role for nearby regions (increasing their connectivity) to compensate for a reduction in the somatosensory homologous synchronization. A similar phenomenon was observed in (Brown et al., 2009), where following stroke in the sensory cortex in mice, a functional reorganization in nearby areas was observed but after much longer periods (8 weeks). Another hypothesis is that hemodynamic changes observed here may reflect a local redistribution of blood flow associated with the high metabolic activity at the seizure location.

5.6.1 Acute seizure activity leads to both decrease and increase in functional connectivity

In the case of HbO_2 a significant decrease of functional connectivity was observed in retrosplenial cortex.; However the difference between control and post-4-AP injection were not significant in HbR networks. In blood flow contrast a significant increase of functional connectivity was observed in both cingulate and retrosplenial paired seeds, and there was a significant decrease for somatosensory cortex.

Previous literature using fMRI (C. Luo et al., 2012; Mankinen et al., 2012; Waites et al., 2006; Z. Wang et al., 2011), mostly documented reduced functional connectivity in several functional networks in epileptic patients measured at rest. While a clear distinction is required with current experiments which focused on resting state networks during acute epileptiform events, the picture emerging from this work indicates a complex interplay between the different components of the hemodynamic response leading to both increases and decreases in connectivity in our mouse model. While HbR, which closely correlates to BOLD-fMRI, saw a non-significant decrease in connectivity in most seeds (4/5), HbO_2 and CBF saw their bilateral correlations move in opposite directions in seeds closest to the injection site (somatosensory and retrosplenial, for which changes were significant). Hemodynamic component dependent correlation changes indicate a potential uncoupling of flow and metabolism, even in low frequency networks.

These observations suggest that using a single modality, e.g. fMRI BOLD, to investigate resting state network in epilepsy may remain limited without controlling for flow or oxygenation.

Whether the observed changes are due to changes in physiology (however no significant change was observed on our ECG), high metabolic demand at the seizure location or neural activity remains to be investigated. Further work with a chronic model investigating networks outside of epileptic periods may help reveal more coherent changes across hemodynamic components.

5.6.2 Correlation between electrophysiological activity and resting state correlations

Since electrophysiology was measured simultaneously, we could investigate the effect of seizure duration on pair wise network correlations. Our results showed a dependence of the changes in bilateral functional correlations on seizure duration but remained mitigated due the low values of r^2 obtained in this analysis. Whether these changes are also present in sub-acute conditions, during simple spiking events, and the cause for network changes observed in patients remain to be studied. Our results are further limited by the fact that electrophysiology was measured in the somatosensory cortex; it may be that similar activity measured at other seeds may lead to a different outcome. Keeping the skull intact apart from the injection site allowed studying an almost intact cortex but the absence of multiple LFP recording sites implied that the spatial dependence of the LFP response remained a potentially confounding variable that was not investigated.

5.6.3 Metabolic consumption reflect hemodynamic changes

$CMRO_2$ is potentially the closest marker to neuronal activity. Here we hypothesized that the steady-state relation between hemodynamic signals to estimate $CMRO_2$ held for the resting state networks due to their low frequency support. Assuming this hypothesis to be valid and comparing network correlation changes obtained by $CMRO_2$, our analysis displayed changes that followed similar trends as changes in HbR, except for the visual and frontal seeds where small differences were observed. This observation may in turn support HbR weighted fMRI-BOLD as a proxy for resting state network in epilepsy despite the known physiological confounds and hemodynamic network uncoupling displayed here.

5.7 Conclusion

Our original aim was to investigate the potential of OIS to study epileptic networks. Combining OIS with laser speckle imaging allows for simultaneous imaging of changes in HbO_2, HbR, CBF and potentially $CMRO_2$, providing a good set of hemodynamic data for functional connectivity studies during acute seizures. In our work, following 4-AP injection in the somatosensory cortex of mice, we observed significant changes in networks derived from spatial seeds near the injection site. Changes were not uniform across hemodynamic components signaling a complex picture with a potential decoupling of flow and metabolism within the low frequency networks. This study thus supports the need for a more extensive investigation and characterization of epileptic networks encompassing more than one hemodynamic measurement.

There are several limitations to be mentioned; first and foremost our results were obtained during acute epileptiform events in a relatively small sample size. They cannot therefore be directly compared with connectivity studies in humans typically obtained during rest periods devoid of acute epileptic events. Thus care must be taken when interpreting the current results since several physiological factors may be confounding the observed neuronal activity. Further work will aim to investigate larger populations of chronic animal models of epilepsy in conditions that are closer to ongoing human resting state studies.

5.8 Acknowledgments

This research was supported by NSERC Discovery grant to F. Lesage. E. Guevara acknowledges financial support from Mexican National Science and Technology Council (CONACYT) through scholarship No. 304501. The authors wish to thank Tri Truong Van for his assistance in animal preparation and Mingrui Zhao for advice with 4-AP injections.

5.9 References

Bero, A. W., Bauer, A. Q., Stewart, F. R., White, B. R., Cirrito, J. R., Raichle, M. E., … Holtzman, D. M. (2012). Bidirectional Relationship between Functional Connectivity and Amyloid-β Deposition in Mouse Brain. *The Journal of Neuroscience*, *32*(13), 4334–4340.

Bettus, G., Ranjeva, J.-P., Wendling, F., Bénar, C. G., Confort-Gouny, S., Régis, J., … Guye, M. (2011). Interictal Functional Connectivity of Human Epileptic Networks Assessed by Intracerebral EEG and BOLD Signal Fluctuations. *PLoS ONE*, *6*(5), e20071.

Biswal, B. B., Mennes, M., Zuo, X.-N., Gohel, S., Kelly, C., Smith, S. M., … Colcombe, S. (2010). Toward discovery science of human brain function. *Proceedings of the National Academy of Sciences*, *107*(10), 4734–4739.

Biswal, B., Yetkin, F. Z., Haughton, V. M., & Hyde, J. S. (1995). Functional connectivity in the motor cortex of resting human brain using echo-planar MRI. *Magnetic resonance in medicine: official journal of the Society of Magnetic Resonance in Medicine / Society of Magnetic Resonance in Medicine*, *34*(4), 537–541.

Boas, D. A., & Dunn, A. K. (2010). Laser speckle contrast imaging in biomedical optics. *Journal of Biomedical Optics*, *15*(1), 011109.

Briers, J. D. (2001). Laser Doppler, speckle and related techniques for blood perfusion mapping and imaging. *Physiological Measurement*, *22*(4), R35–R66.

Brieu, N., Beaumont, E., Dubeau, S., Cohen-Adad, J., & Lesage, F. (2010). Characterization of the hemodynamic response in the rat lumbar spinal cord using intrinsic optical imaging and laser speckle. *Journal of Neuroscience Methods*, *191*(2), 151–157.

Brown, C. E., Aminoltejari, K., Erb, H., Winship, I. R., & Murphy, T. H. (2009). In Vivo Voltage-Sensitive Dye Imaging in Adult Mice Reveals That Somatosensory Maps Lost to Stroke Are Replaced over Weeks by New Structural and Functional Circuits with Prolonged Modes of Activation within Both the Peri-Infarct Zone and Distant Sites. *The Journal of Neuroscience*, *29*(6), 1719–1734.

Delpy, D. T., Cope, M., Zee, P. van der, Arridge, S., Wray, S., & Wyatt, J. (1988). Estimation of optical pathlength through tissue from direct time of flight measurement. *Physics in Medicine and Biology*, *33*(12), 1433–1442.

Dubeau, S., Ferland, G., Gaudreau, P., Beaumont, E., & Lesage, F. (2011). Cerebrovascular hemodynamic correlates of aging in the Lou/c rat: A model of healthy aging. *NeuroImage*, *56*(4), 1892–1901.

Dunn, A. K., Bolay, H., Moskowitz, M. A., & Boas, D. A. (2001). Dynamic Imaging of Cerebral Blood Flow Using Laser Speckle. *J Cereb Blood Flow Metab*, *21*(3), 195–201.

Dunn, A. K., Devor, A., Bolay, H., Andermann, M. L., Moskowitz, M. A., Dale, A. M., & Boas, D. A. (2003). Simultaneous imaging of total cerebral hemoglobin concentration, oxygenation, and blood flow during functional activation. *Optics Letters*, *28*(1), 28–30.

Dunn, A. K., Devor, A., Dale, A. M., & Boas, D. A. (2005). Spatial extent of oxygen metabolism and hemodynamic changes during functional activation of the rat somatosensory cortex. *NeuroImage*, *27*(2), 279–290.

Fabene, P. F., Weiczner, R., Marzola, P., Nicolato, E., Calderan, L., Andrioli, A., … Sbarbati, A. (2006). Structural and functional MRI following 4-aminopyridine-induced seizures: a comparative imaging and anatomical study. *Neurobiology of disease*, *21*(1), 80–89.

Fox, M. D., & Raichle, M. E. (2007). Spontaneous fluctuations in brain activity observed with functional magnetic resonance imaging. *Nature Reviews Neuroscience*, *8*(9), 700–711.

Frings, L., Schulze-Bonhage, A., Spreer, J., & Wagner, K. (2009). Remote effects of hippocampal damage on default network connectivity in the human brain. *Journal of neurology*, *256*(12), 2021–2029.

Friston, K. J., Ashburner, J. T., Kiebel, S. J., Nichols, T. E., & Penny, W. D. (2006). *Statistical Parametric Mapping: The Analysis of Functional Brain Images* (1st ed.). Great Britain: Academic Press.

Gallagher, A., Lassonde, M., Bastien, D., Vannasing, P., Lesage, F., Grova, C., … Nguyen, D. K. (2008). Non-invasive pre-surgical investigation of a 10 year-old epileptic boy using simultaneous EEG-NIRS. *Seizure: the journal of the British Epilepsy Association*, *17*(6), 576–582.

Gibbs, F. A., Gibbs, E. L., & Lennox, W. G. (1937). Epilepsy: A Paroxysmal Cerebral Dysrhythmia. *Brain*, *60*(4), 377–388.

Gotman, J., Grova, C., Bagshaw, A., Kobayashi, E., Aghakhani, Y., & Dubeau, F. (2005). Generalized epileptic discharges show thalamocortical activation and suspension of the default state of the brain. *Proceedings of the National Academy of Sciences of the United States of America*, *102*(42), 15236–15240.

Greicius, M. D., Krasnow, B., Reiss, A. L., & Menon, V. (2003). Functional connectivity in the resting brain: a network analysis of the default mode hypothesis. *Proceedings of the National Academy of Sciences of the United States of America*, *100*(1), 253–258.

Jones, M., Berwick, J., Johnston, D., & Mayhew, J. (2001). Concurrent optical imaging spectroscopy and laser-Doppler flowmetry: the relationship between blood flow, oxygenation, and volume in rodent barrel cortex. *NeuroImage*, *13*(6 Pt 1), 1002–1015.

Kandel, E. R., Schwartz, J. H., & Jessell, T. M. (1991). *Principles of neural science* (3rd ed.). New York: Elsevier.

Kohl, M., Lindauer, U., Royl, G., Kuhl, M., Gold, L., Villringer, A., & Dirnagl, U. (2000). Physical model for the spectroscopic analysis of cortical intrinsic optical signals. *Physics in Medicine and Biology*, *45*(12), 3749–3764.

Liao, W., Zhang, Z., Pan, Z., Mantini, D., Ding, J., Duan, X., … Chen, H. (2011). Default mode network abnormalities in mesial temporal lobe epilepsy: a study combining fMRI and DTI. *Human brain mapping*, *32*(6), 883–895.

Luckl, J., Baker, W., Sun, Z.-H., Durduran, T., Yodh, A. G., & Greenberg, J. H. (2010). The biological effect of contralateral forepaw stimulation in rat focal cerebral ischemia: a multispectral optical imaging study. *Frontiers in Neuroenergetics*, *2*, pii: 19.

Luo, C., Qiu, C., Guo, Z., Fang, J., Li, Q., Lei, X., … Yao, D. (2012). Disrupted Functional Brain Connectivity in Partial Epilepsy: A Resting-State fMRI Study. *PLoS ONE*, *7*(1), e28196.

Mankinen, K., Jalovaara, P., Paakki, J.-J., Harila, M., Rytky, S., Tervonen, O., … Kiviniemi, V. (2012). Connectivity disruptions in resting-state functional brain networks in children with temporal lobe epilepsy. *Epilepsy Research*, *100*(1–2), 168–178.

Mayhew, J., Johnston, D., Berwick, J., Jones, M., Coffey, P., & Zheng, Y. (2000). Spectroscopic Analysis of Neural Activity in Brain: Increased Oxygen Consumption Following Activation of Barrel Cortex. *NeuroImage*, *12*(6), 664–675.

Moldestad, O., Karlsen, P., Molden, S., & Storm, J. F. (2009). Tracheotomy improves experiment success rate in mice during urethane anesthesia and stereotaxic surgery. *Journal of neuroscience methods*, *176*(2), 57–62.

Morrell, F., & deToledo-Morrell, L. (1999). From mirror focus to secondary epileptogenesis in man: an historical review. *Advances in neurology*, *81*, 11–23.

Nguyen, D. K., Tremblay, J., Pouliot, P., Vannasing, P., Florea, O., Carmant, L., … Lassonde, M. (2012). Non-invasive continuous EEG-fNIRS recording of temporal lobe seizures. *Epilepsy research*, *99*(1-2), 112–126.

Prahl, S. (1999). *Optical Absorption of Hemoglobin*. Retrieved October 8, 2009, from http://omlc.ogi.edu/spectra/hemoglobin/

Voges, N., Blanchard, S., Wendling, F., David, O., Benali, H., Papadopoulo, T., … Bénar, C. (2012). Modeling of the neurovascular coupling in epileptic discharges. *Brain topography*, *25*(2), 136–156.

Waites, A. B., Briellmann, R. S., Saling, M. M., Abbott, D. F., & Jackson, G. D. (2006). Functional connectivity networks are disrupted in left temporal lobe epilepsy. *Annals of neurology*, *59*(2), 335–343.

Wang, Z., Lu, G., Zhang, Z., Zhong, Y., Jiao, Q., Zhang, Z., … Liu, Y. (2011). Altered resting state networks in epileptic patients with generalized tonic-clonic seizures. *Brain research*, *1374*, 134–141.

White, B. R., Bauer, A. Q., Snyder, A. Z., Schlaggar, B. L., Lee, J.-M., & Culver, J. P. (2011). Imaging of functional connectivity in the mouse brain. *PloS one*, *6*(1), e16322.

Zhang, Z., Lu, G., Zhong, Y., Tan, Q., Yang, Z., Liao, W., … Liu, Y. (2009). Impaired attention network in temporal lobe epilepsy: a resting FMRI study. *Neuroscience letters*, *458*(3), 97–101.

Zhao, M., Ma, H., Suh, M., & Schwartz, T. H. (2009). Spatiotemporal Dynamics of Perfusion and Oximetry during Ictal Discharges in the Rat Neocortex. *The Journal of Neuroscience*, *29*(9), 2814–2823.

Zhao, M., Nguyen, J., Ma, H., Nishimura, N., Schaffer, C. B., & Schwartz, T. H. (2011). Preictal and ictal neurovascular and metabolic coupling surrounding a seizure focus. *The Journal of neuroscience: the official journal of the Society for Neuroscience*, *31*(37), 13292–13300.

Zhao, M., Suh, M., Ma, H., Perry, C., Geneslaw, A., & Schwartz, T. H. (2007). Focal increases in perfusion and decreases in hemoglobin oxygenation precede seizure onset in spontaneous human epilepsy. *Epilepsia*, *48*(11), 2059–2067.

CHAPTER 6 ARTICLE 2: OPTICAL IMAGING OF RESTING-STATE FUNCTIONAL CONNECTIVITY IN A NOVEL ARTERIAL STIFFNESS MODEL

Edgar Guevara[1,2], Nataliya Sadekova[3], Hélène Girouard[3], Frédéric Lesage[1,2]

6.1 Presentation of the article

This article (Guevara, Sadekova, Girouard, & Lesage, 2013) was published in Biomedical Optics Express. In this work we assessed the impact of unilateral carotid stiffness in the resting-state networks. A decreasing trend of bilateral correlation strength was found in $CMRO_2$ measures, the trend was more evident in the motor and cingulate areas of the cortex. Graph theory results suggest a loss of connectivity of the overall functional networks.

6.2 Abstract

This study aims to assess the impact of unilateral increases in carotid stiffness on cortical functional connectivity measures in the resting state. Using a novel animal model of induced arterial stiffness combined with optical intrinsic signals and laser speckle imaging, resting state functional networks derived from hemodynamic signals are investigated for their modulation by isolated changes in stiffness of the right common carotid artery. By means of seed-based analysis, results showed a decreasing trend of homologous correlation in the motor and cingulate cortices. Furthermore, a graph analysis indicated a randomization of the cortex functional networks, suggesting a loss of connectivity, more specifically in the motor cortex lateral to the treated carotid, which however did not translate in differentiated metabolic activity.

[1] Department of Electrical Engineering, École Polytechnique de Montréal, Canada

[2] Montreal Heart Institute, Montréal, Canada

[3] Department of Pharmacology, Faculty of Medicine, Université de Montréal, Montréal, Canada

6.3 Introduction

Arterial hypertension is a non-communicable disease with a prevalence between 25% and 30% of the world adult population (World Health Organization, 2012) and is a risk factor in early brain aging, the development of cognitive dysfunctions and dementias. Cognitive deficits, including non-amnesic mild cognitive impairment (Roberts et al., 2010), have also been associated with coronary heart diseases (CHD) (Aronson et al., 1990; Breteler, Claus, Grobbee, & Hofman, 1994; Singh-Manoux, Britton, & Marmot, 2003). Hardening of the arteries has been identified as a risk factor in the development of cardiovascular disease (CVD) and may play a role in the development of such deficits. Arterial stiffness has been shown to be a predictor of cognitive decline and dementia (Pase et al., 2012). Basic cognitive functions such as attention and memory are also adversely affected by aging (Glisky, 2007), a process accelerated by risk factors for CVD.

Anatomic and functional brain imaging are actively used to investigate such changes to brain function. Imaging correlates of aging and age-induced cognitive deficits include a decrease in connectivity and efficiency of functional brain networks (J. Sun et al., 2011), smaller brain volume and weight (Anderton, 2002; Iadecola, 2010) and a reduction in cerebral blood flow (CBF) (R S Marshall et al., 2001; Randolph S Marshall & Lazar, 2011) related to endothelial dysfunction (Bolduc et al., 2012; Faraci, 2011). While the above investigations suggest a potential for functional brain imaging techniques in the clinical setting, they remain hampered by interpretation difficulties. A key step forward is to understand the impact of systemic physiology and vascular hardening and/or stenosis on functional imaging brain signals derived from hemodynamics.

While functional MRI (fMRI) studies used in basic research to explore brain organization have focused on the brain's response to a task; the complexities of task design, the duration of multiple trials, interpretation and statistical analysis have limited their use in extensive clinical studies. Resting-state networks (RSN) with fMRI eases the participation of the patient, and reduce the number of behavioral variables implicit in task-based paradigms, yielding a set of basic networks that can be reliably imaged in human subjects (Fox & Raichle, 2007; Greicius et al., 2003; Gusnard et al., 2001; van den Heuvel & Hulshoff Pol, 2010). The application of RSN mapping with fMRI to diverse neuroscience research areas has revealed new insights in the organization of

both healthy (Buckner, Andrews-Hanna, & Schacter, 2008; Cole, Smith, & Beckmann, 2010) and diseased brain, such as Alzheimer's (Gili et al., 2011; Greicius et al., 2004; Y. He et al., 2009; van den Heuvel & Hulshoff Pol, 2010). RSNs have unraveled potential mechanisms of the brain in several areas, but the concrete meaning of the underlying processes and their interpretation remain to be resolved. Characterizing RSNs in the presence of vascular disease is a first step to establish RSN techniques in this context and may explain the scarcity of RSN studies in vascular pathology. Both increases and decreases in functional connectivity in vascular cognitive impairment were found by Sun et al. (Y. Sun et al., 2011). Resting-state connectivity has been included in the RUN DMC study of cerebral small vessel disease (van Norden et al., 2011), a project recently begun. Recently, distinct patterns of RSN disruptions correlated with diminished cognitive performance in patients with carotid stenosis (Cheng et al., 2012).

The current work exploits the recent development of a controlled murine arterial stiffness model induced unilaterally by the application of calcium chloride ($CaCl_2$). In previous work (Sadekova et al., 2013), this model was shown to induce neuronal degeneration in the hippocampus. To further reveal the impact of carotid artery calcification and increased stiffness on the brain, blood flow pulsatility in small arteries was quantified in both hemispheres. Statistically significant changes in pulsatility were observed on the $CaCl_2$ group, suggesting that carotid stiffness has an impact on blood delivery but none were observed on baseline flow. This model, whereby one can study the isolated effect of unilateral carotid calcification on the brain, provides a unique opportunity to investigate the specific impact arterial hardening on resting state networks.

The current study aims to assess resting-state connectivity in this unilateral carotid stiffness murine model using multi-spectral intrinsic optical imaging. Using multiple illumination wavelengths, relative changes in HbO_2 and HbR can be estimated, while speckle imaging provides access to relative CBF. This then enables estimations of $CMRO_2$. Hence, due to access to distinct hemodynamic components, functional connectivity based on optical imaging of intrinsic signals (fcOIS) may provide additional information that complements resting-state studies with fMRI in the context of vascular disease.

6.4 Materials and methods

6.4.1 Animal model

A total of N=23 Male C57BL/6 mice (8 ± 0.2 weeks old, 23.6 ± 1.4 g weight, Charles River, Wilmington, MA), divided in two groups were used in this study. Animal carotids were exposed and submitted to a sham procedure (Group 1, N=11), where a sterile NaCl 0.9% solution was applied to the carotid or the calcification procedure (Group 2, N=12) with a 0.3M $CaCl_2$ solution applied. The Animal Research Ethics Committee of the Montreal Heart Institute approved all surgical procedures, which were performed according to the recommendations of the Canadian Council on Animal Care.

6.4.2 Application of calcium chloride

Applying calcium chloride periarterially developed carotid stiffness *in vivo*. Male C57BL/6 mice (8 ± 0.2 weeks old, 23.7 ± 1.6 g weight) were anaesthetized with isoflurane (5% for induction, 2% for maintenance) in oxygen (2 L/min for induction, 1.5 L/min for maintenance). The procedure required 45 minutes of anesthesia per animal and body temperature was controlled between 36 and 37 °C using a heating blanket (MouseSTAT, Kent Scientific, Torrington, CT). A midline incision was performed in the neck and the right common carotid artery (RCCA) was isolated, then a sterile cotton gaze soaked in either sterile NaCl 0.9% solution for the control group (N=11) or with a 0.3M $CaCl_2$ solution for the treated group (N=12) was applied to the carotid artery for twenty minutes. Afterwards the skin incision was closed with sutures and sealed with tissue adhesive (Vetbond, 3M, St. Paul, MN). Bupivacaine (Marcaine) (4mg/kg) and Carprofen (5 mg/kg) were administered subcutaneously (SC) to provide post-surgical local anesthesia. Furthermore, Carprofen (5 mg/kg SC) was injected every 24 hours for 48 hours and on the third day if deemed necessary. Infections were effectively prevented with the administration of trimethoprim-sulfamethoxazole (Tribrissen, 30 mg/kg SC) post-operatory and every 24 hours for 3 to 5 days. Animals were monitored twice a day during the first postoperative week and assessed for body weight, symptoms of local infection, discomfort or pain, behavior, and water and food consumption. Following this recovery period, mice were monitored daily. Optical imaging of intrinsic signals (OIS) was performed two weeks after the surgical procedure.

6.4.3 OIS Imaging

6.4.3.1 Animal preparation

Mice were anesthetized via intraperitoneal injections of urethane (2mg/g body weight) in a 10% (wt/vol) saline solution. Body temperature was maintained at 36.6±1.2°C with a feedback controlled heating blanket. A tracheotomy was done in order to avoid respiratory distress (Moldestad et al., 2009). Scalp was carefully removed prior to imaging.

Mice were placed on a stereotaxic apparatus and a subcutaneous electrocardiogram was recorded with a single lead ECG amplifier (amp-b01, emka TECHNOLOGIES, Paris). The amplified (1000× gain) and filtered signal (0.2-500 Hz) was sampled at 1 kHz. All vital signals were digitized by a data acquisition card (NI-USB 6353, National Instruments, Austin, TX) controlled by a custom made graphical user interface developed in LabView (National Instruments), which also controlled the image acquisition. To prevent drying of the exposed skull a custom chamber made of bone wax was adhered to the skull with ultrasound gel and filled with mineral oil.

6.4.3.2 Optical recording setup

OIS images were acquired with a 12-bit CCD camera (Pantera 1M60, DS-21-01M60-12E, Teledyne Dalsa, Waterloo, ON) with a pixel size on chip of 12μm and full resolution of 1024×1024 pixels. The setup used in this work is depicted in Figure 6-1a.

A custom-made interface controls the camera, records images and vital signs, while synchronizing acquisition and illumination. A Macro Lens (105mm f/2.8max, Sigma Corp., Ronkonkoma, NY) with small focal depth (350 μm) was used. Reflectance images of the brain were recorded with time-multiplexed illumination (525, 590, 625 nm) produced by 10W LEDs (LZ4-00MA00, Led Engin, San Diego, CA). Illumination for speckle imaging was provided by a 90 mW, 785 nm laser diode (L785P090, Thorlabs, Newton, NJ) and the camera aperture was adjusted to f/8, so that the pixel size and speckle size were matched. The four temporally multiplexed wavelengths led to a full-frame rate of 5 Hz. A 2×2 binning on camera was performed to allow continuous data streaming to the hard drive. The camera field of view (FOV) was set to ~10.1×10.7 mm in order to cover most of the convexity of the cortex; the image pixel size for the chosen FOV was approximately 33μm. Illumination was further adjusted so that no part of the brain was under- or over-saturated by any of the wavelengths. The exposure time of

the camera was set to 10 msec. The setup was mounted on an optic table with tuned damping (RS 2000, Newport, Irvine, CA) to avoid spurious signals from vibrations.

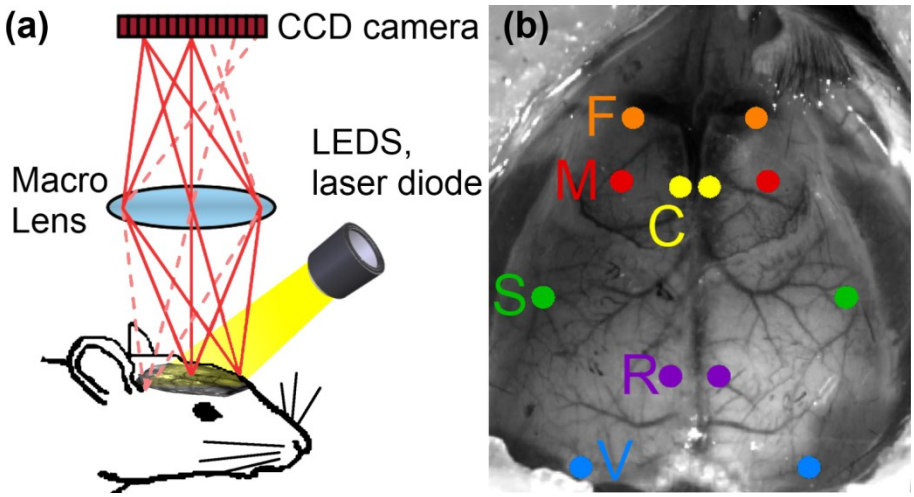

Figure 6-1: (a) Overview of the intrinsic signal optical imaging system. LEDs and laser diode are time-multiplexed and synchronized to the acquisition system so that each recorded image corresponds to either a single LED wavelength (525, 590, 625 nm) or to the laser illumination (785 nm). (b) Functional regions on the mouse cortex and seed placement and size, manually constructed from the work of Bero et al. (Bero et al., 2012). Abbreviations: F, frontal; M, motor; C, cingulate; S, somatosensory; R, retrosplenial; V, visual.

6.4.3.3 OIS processing

The analysis of spectroscopic images was based on previously published work (Dubeau et al., 2011; Dunn et al., 2003). In short reflectance images from each LED wavelength were recorded with the CCD camera and interpreted as changes in attenuation (optical density) $\Delta OD = \log(I_0/I)$, where I is the reflected light intensity and I_0 the incident light intensity. Relative changes in oxy- and deoxyhemoglobin were found using the modified Beer-Lambert law (Delpy et al., 1988) and a Moore-Penrose pseudoinverse:

$$\Delta OD(\lambda, t) = \sum_i \epsilon_i(\lambda)\, C_i(t) D(\lambda) \tag{6.1}$$

The differential path length factor, D(λ), was taken from (Dunn et al., 2005) and values out of the 560-610 nm range were extrapolated from (Kohl et al., 2000). Total hemoglobin baseline

concentration of 100 μM with 60% oxygen saturation was assumed (Dunn et al., 2005) for the spectroscopic analysis. The hemoglobin extinction coefficients were obtained from (Prahl, 1999) and the reflectance values were corrected for the spectral response of the CCD camera and convolved with the LEDs spectral power distribution (Brieu et al., 2010).

Images of each chromophore (HbO_2, HbR) were spatially smoothed with a Gaussian kernel of 11×11 pixels (~0.3×0.3mm) with a 5 pixel standard deviation (~0.15mm). An anatomical image was recorded with illumination at 525 nm to emphasize vasculature, and then the region corresponding to the brain was manually selected using a closed spline curve to create a brain mask. All further processing was performed only on those pixels belonging to the brain mask.

6.4.3.4 Speckle contrast imaging

In addition to imaging changes in hemoglobin concentrations, changes in cerebral blood flow (CBF) were also computed by laser speckle contrast imaging (Boas & Dunn, 2010; Dunn et al., 2001, 2005). Images of blood flow were obtained by measuring the spatial contrast of the speckle *C*, defined as the ratio of the standard deviation to the average intensity $\sigma/\langle I\rangle$ (Briers, 2001). A window of 5×5 pixels (0.15×0.15mm) was used to compute the speckle contrast images and the relative changes in blood flow were obtained with the following formula:

$$C = \frac{\sigma}{\langle I\rangle}, -\frac{2\Delta C}{C_0} \approx \frac{\Delta V}{V_0} \approx \frac{\Delta CBF}{CBF_0} \tag{6.2}$$

The quantity $\Delta v/v_0$ is not directly related to CBF, however laser speckle imaging underestimates CBF by less than 5% (Luckl et al., 2010), so both quantities were assumed to be equal in this work. Flow images then underwent the same spatial filtering as the hemoglobin images, and images from all three different contrasts were further resized to ½ of the original size due to memory constraints.

6.4.3.5 Cerebral metabolic rate of oxygen

Changes in the cerebral metabolic rate of oxygen consumption ($CMRO_2$) were calculated from the images of changes in CBF, total hemoglobin (HbT) and HbR using the steady state relationship (M. Jones et al., 2001; Mayhew et al., 2000):

$$\frac{\Delta CMRO_2}{CMRO_{2,0}} = \frac{\left(1 + \frac{\Delta CBF}{CBF_0}\right)\left(1 + \gamma_R \frac{\Delta HbR}{HbR_0}\right)}{\left(1 + \gamma_T \frac{\Delta HbT}{HbT_0}\right)} - 1 \quad (6.3)$$

A central hypothesis of this relation is the absence of transients with decoupled hemodynamic components. Here, since resting state networks were identified from data filtered between 0.009-0.08 Hz, we hypothesized that for these networks, the relationship was maintained. The constants γ_R and γ_T where both assumed to be 1, which is within a physiologically plausible range (0.75–1.25)(M. Jones et al., 2001).

6.4.4 Resting state network analysis

6.4.4.1 Seed based functional connectivity

Optical recording sessions of 15 minutes were carried out in resting-state conditions for the fcOIS analysis. Time courses of every pixel were temporally band-pass filtered (zero phase-shift fourth-order Butterworth IIR filter) at 0.009-0.08 Hz, according to previous functional connectivity studies in mice (Bero et al., 2012; Brian R White et al., 2011). After temporal filtering, each pixel time trace was downsampled from 5 Hz to 1 Hz.

A global brain signal was created from the average of all the pixels time traces. In order to account for coherent variability common to all pixels, this global brain signal was regressed from every pixel's time course, using a General Linear Model (GLM) from the package Statistical Parametrical Mapping (Karl J. Friston et al., 2006)(SPM8, www.fil.ion.ucl.ac.uk/spm) running on MATLAB (The MathWorks, Natick, MA).

All seeds were manually placed *a priori* using the coordinates corresponding to left and right frontal, cingulate, motor, somatosensory, cingulate and visual cortices, as shown on Figure 6-1b. Manual positioning of the seeds was done in order to avoid contributions from large vessels. Seed time-courses were computed as the mean time course of the pixels within a 7 pixel (~0.23mm) radius from the seed locus.

With the unilateral application of $CaCl_2$ we expect differences between bilateral brain regions so the metric used to evaluate functional connectivity was a regional bilateral functional correlation,

defined as the correlation between each seed time course and its contralateral homologue, yielding six values for each mouse. The Pearson's coefficient r values were converted to Fisher Z measures using $z(r) = \frac{1}{2}\ln[(1+r)/(1-r)]$ before performing the random effect t-tests. Statistical significance was evaluated using the Student's unpaired t-test. Values were considered significant at $p<0.05$, adjusted for false discovery rate (FDR).

6.4.4.2 Graph theoretical measures

Several graph theoretical measures were computed in addition to assess the potential impact of the carotid calcification on the topological properties of the brain networks. While these measures do not provide clear informative information about function, they yield indicators of network changes that may occur with arterial stiffness. The brain was modeled as a graph where the nodes (N) were associated with seeds and edges (K) were associated with the amplitude of functional connectivity *z(r)* among these seeds (Latora & Marchiori, 2001). Following the computation of seed-to-seed connectivity matrix, a threshold was applied to define the adjacency matrix characterizing the graph G. A cost threshold level of 0.3 was chosen at which the network exhibited small-world properties, characteristic of brain functional networks (Achard & Bullmore, 2007; Bassett & Bullmore, 2006).

Several properties of brain organization were investigated through the proxy of graph measures at seed level (Bassett & Bullmore, 2006; Whitfield-Gabrieli & Nieto-Castanon, 2012): 1) the degree, $k_n(G)$, defined as the number of edges that connect to a certain node n. 2) the cost $C_n(G)$, defined as the proportion of connected neighbors to a given seed. 3) The average path length $L_n(G)$ is defined as the average shortest-path distance from a node n to all other nodes in the graph, 4) the global efficiency $E_n^{global}(G)$, which is the average inverse shortest-path distance from node n to all other vertices in the graph. 5) the clustering coefficient $CC_n(G)$, defined as the probability that the neighbors of this node are also connected to each other. 6) the local efficiency $E_n^{local}(G)$, defined as the average global efficiency across all neighbors of node n. Finally, 7) the betweenness centrality $CB_n(G)$ of a particular node n is the proportion of all shortest-paths in a network that pass through this node.

Averaging seed-level measures across all nodes within the network generated measures reflecting the global integration in the network. These summary network-level measures were entered in a

second-level general linear model to compare functional connectivity patterns between the control (NaCl) and the $CaCl_2$ groups. Statistical significance was determined by a Student's unpaired t-test ($p<0.05$) with false discovery rate (FDR) correction. All the graph theoretical measures were performed with the CONN functional connectivity toolbox (Whitfield-Gabrieli & Nieto-Castanon, 2012).

6.5 Results

No signs of infection at the incision site, weight loss, or discomfort were observed during daily inspections throughout the post-operatory period. Two animals of the $CaCl_2$ group deceased prior to the imaging session, possibly due to incorrect positioning of the tracheotomy tube, which hampered normal breathing. One more animal of the same group was not included in the analysis due to poor quality data caused by unwanted saturation outside the region of interest, which in turn saturated a whole line of the CCD camera. The final sample size used for all analyses was N=9 for $CaCl_2$ group and N=11 for NaCl (control) group.

6.5.1 Seed-based functional connectivity

Average seed-based correlation maps across animals for HbO_2 are depicted in Figure 6-2. The first two columns belong to the control (NaCl) group, while the last two columns are from the $CaCl_2$ group. Every row contains maps generated from a seed located in a different cortical region, first using the seed located in the left hemisphere and then its contralateral homologue. The $CaCl_2$ group showed a greater spatial extent of high positively correlated pixels, when compared to the NaCl group ($CaCl_2$ = 7.6% ± 3.6% vs. NaCl = 5.14% ± 1.63%, p=0.0278) with the spatial extent defined as the percentage of pixels showing a correlation coefficient greater than 0.5. Representative fc maps of other contrasts are shown in Figure 6-5.

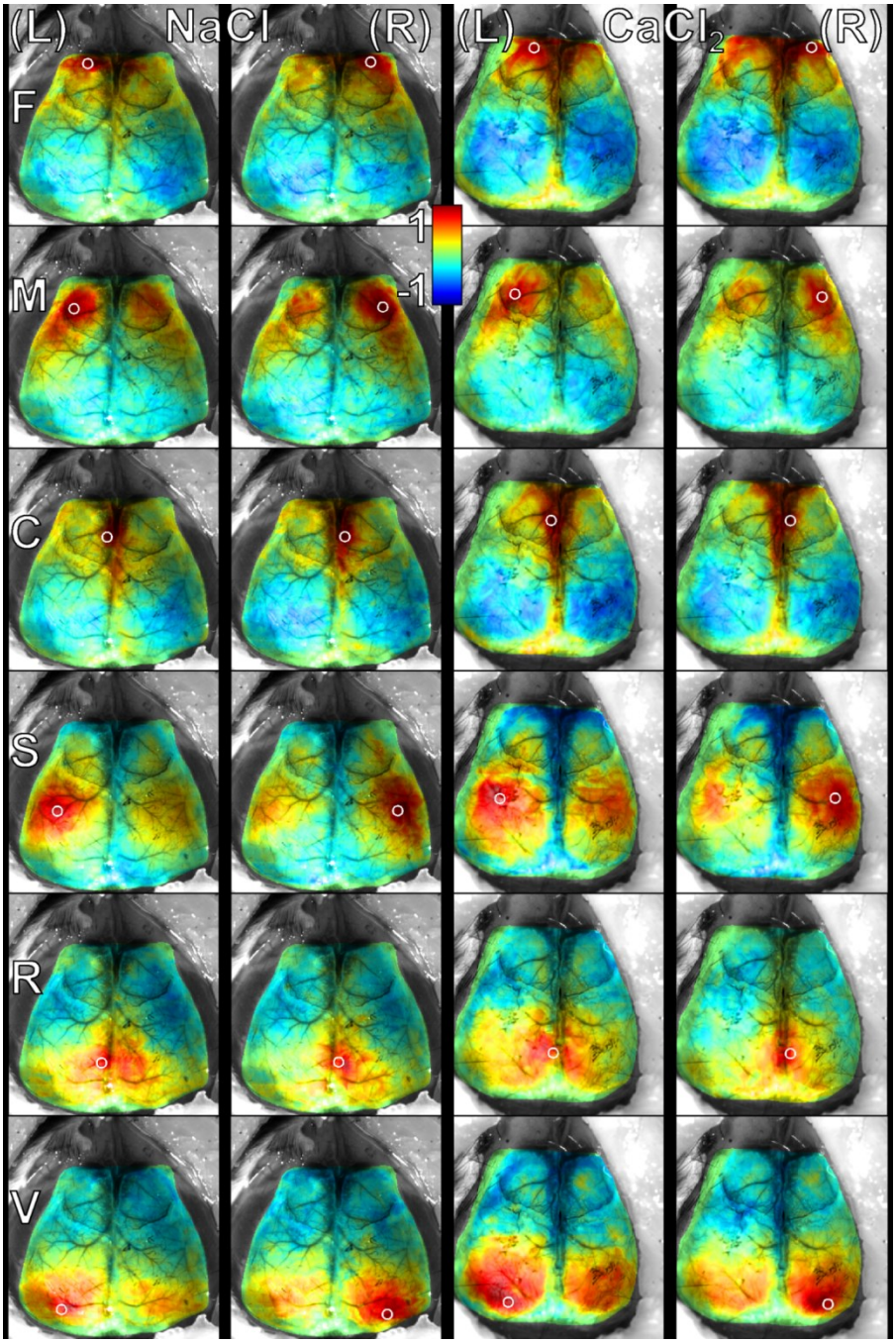

Figure 6-2: Average seed-based correlation maps. Images were manually aligned through an affine registration using ImageJ`s plugin TurboReg (Thevenaz, Ruttimann, & Unser, 1998). HbO_2 contrast is shown. The scale for all correlation maps is $-1 \leq r \leq 1$. Maps are shown overlaid on the anatomical image of one of the mice for reference (λ=525 nm). White circles denote seed position and size. Abbreviations: F: frontal cortex, M: motor cortex, C: cingulate cortex, S: somatosensory cortex R: retrosplenial cortex, V: visual cortex, (L) left seed, (R) right seed.

HbO_2 contrast Figure 6-3a data displayed mostly non-significant changes of bilateral functional correlation *z(r)* in $CaCl_2$ mice when compared to controls. A decrease was seen in the seeds of the frontal, motor and retrosplenial cortex, while an increase was noted in the cingulate, somatosensory and visual regions. HbR (Figure 6-3b) data showed diminished *z(r)* in all regions except in the visual cortex where it increased, albeit not significantly. CBF (Figure 6-3c) data showed overall a smaller *z(r)* values in all cortical regions. This might be explained by a greater variance in CBF seeds time traces associated with a noisier recording of the speckle signal. With this contrast the seeds that showed a smaller *z(r)* in the $CaCl_2$ mice were located in the motor, cingulate and somatosensory regions of the cortex. Frontal, retrosplenial and visual cortex seeds showed a slightly larger *z(r)* in the $CaCl_2$ group, when compared to NaCl mice. $CMRO_2$ (Figure 6-3d) data showed a general trend of decreased functional connectivity *z(r)* in the mice that underwent $CaCl_2$ procedure, except in frontal cortex seeds. Decreased connectivity showed a trend in the motor (p=0.1241) and cingulate (p=0.1241) regions.

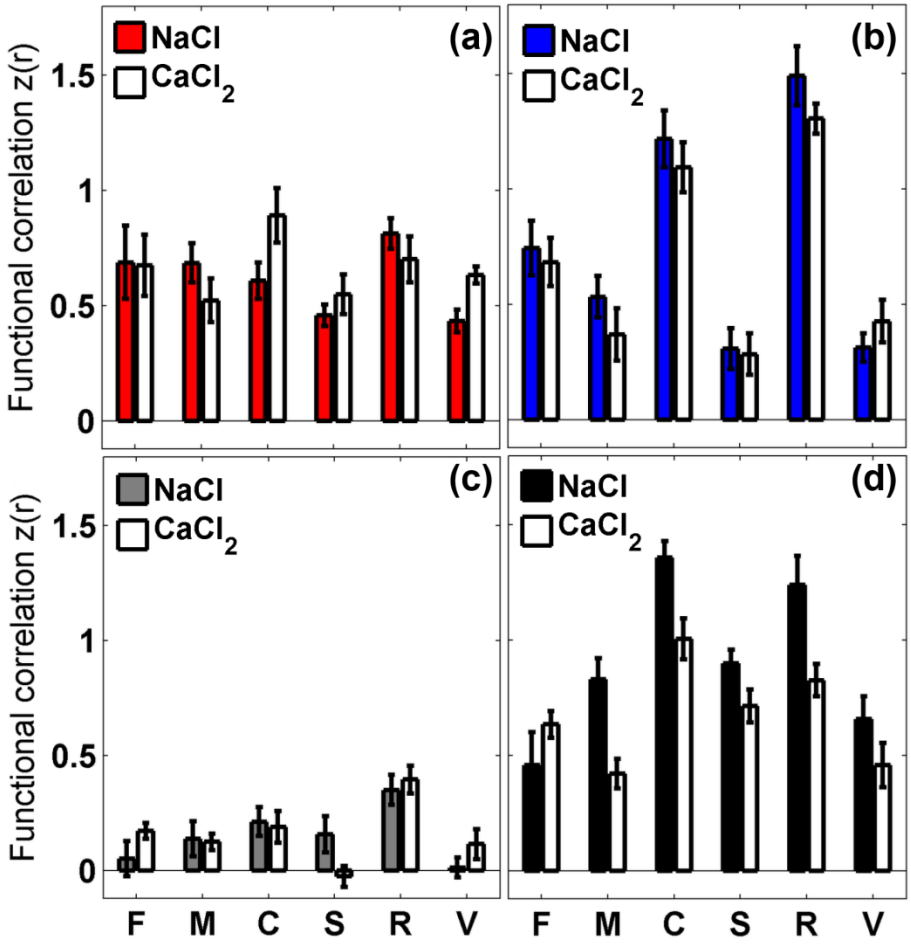

Figure 6-3: Regional bilateral functional correlation, comparison performed between control NaCl and treatment group $CaCl_2$; analysis done for every seed time-trace and its contralateral part. Contrasts shown: (a) HbO_2, (b) HbR (c) CBF and (d) $CMRO_2$. Standard error bars shown (F: frontal cortex, M: motor cortex, C: cingulate cortex, S: somatosensory cortex R: retrosplenial cortex, V: visual cortex).

To further explore the robustness of observed bilateral functional connectivity, a second analysis was performed, where data points that were more than 3 standard deviations away from the mean were considered outliers and excluded (Pukelsheim, 1994). Results obtained after outlier removal are shown in Figure 6-6, results remain very similar to the full data set, with HbO_2 data for visual cortex and $CMRO_2$ data in motor and cingulate regions showing the same trends.

6.5.2 Graph Theoretical measures

In HbO_2 measures, we found significant differences in the global network measures in the betweenness centrality and average path length, which were both higher for the NaCl group. When looking at the topological properties of each seed we found differences (although not significant when FDR corrected) in global, local efficiency, betweenness centrality, average path length and clustering coefficient.

Table 6.1: Summary of significant results from second-level analysis using graph theoretical measures [a].

	ROI level					Network level			
	HbO_2	HbR	CBF	$CMRO_2$		HbO_2	HbR	CBF	$CMRO_2$
$\boldsymbol{E_n^{global}(G)}$	M_R		M_L,F_L,M_R		$\boldsymbol{E^{global}(G)}$			*	
$\boldsymbol{E_n^{local}(G)}$	F_R		M_R, R_L, V_R		$\boldsymbol{E^{local}(G)}$			*	
$\boldsymbol{CB_n(G)}$	M_L		**M_R***		$\boldsymbol{CB(G)}$	*		*	
$\boldsymbol{C_n(G)}$		M_L		C_L	$\boldsymbol{C(G)}$				
$\boldsymbol{L_n(G)}$	S_R,S_L,F_R, F_L,C_L	S_L	F_R,V_R		$\boldsymbol{L(G)}$	*		*	
$\boldsymbol{CC_n(G)}$	F_R		***M_R***,R_L,V_R		$\boldsymbol{CC(G)}$			*	
$\boldsymbol{k_n(G)}$		M_L		C_L	$\boldsymbol{k(G)}$				

[a]Subscripts indicate hemisphere (Left/Right). Increase in the $CaCl_2$ group with respect to NaCl group is shown in red font, while decrease is shown in cursive blue font. Bold font and * indicate FDR-corrected p values at a 0.05 significance level. Measurements abbreviations: global

efficiency $\boldsymbol{E_n^{global}(G)}$, local efficiency $\boldsymbol{E_n^{local}(G)}$, betweenness centrality$\boldsymbol{CB_n(G)}$, cost $\boldsymbol{C_n(G)}$ $C_n(G)$, average path length $\boldsymbol{L_n(G)}$, clustering coefficient $\boldsymbol{CC_n(G)}$ and degree $\boldsymbol{k_n(G)}E_n^{global}(G)$. Regions abbreviations: F: frontal cortex, M: motor cortex, C: cingulate cortex, S: somatosensory cortex R: retrosplenial cortex, V: visual cortex $CC_n(G)$

At the network-level there were no significant differences in HbR measures, but at ROI level the left motor seed showed significant (not FDR-corrected) differences in cost and degree. Also the left somatosensory seed showed increased average pathlength.

Graph analysis based on CBF data showed significant increase in the global efficiency, betweenness centrality and average pathlength; significant decreases were found in local efficiency and clustering coefficients. At seed level there was a significant increased betweenness centrality and clustering coefficient for the right motor seed. Some differences were also found at seed level, although not significant when FDR corrected in global and local efficiency, average path length and clustering coefficient.

Using $CMRO_2$ estimates increased clustering and degree were found to be significant (not FDR-corrected) in the left cingulate seed; although no significant differences were found with $CMRO_2$ measures at network level.

The results above were based on binarized networks. Extending these results, Figure 6-4 reports results for weighted networks, displaying the average strength of connections for both groups, with node sizes proportional to their betweenness centrality $CB_n(G)$, a measure of the relative importance of a seed in the network. Few evident changes in the overall connectivity can be inferred from visual inspection of hemoglobin and CBF networks alone. However, the connectivity changes in $CMRO_2$ are more evident: a large number of nodes are anticorrelated in the $CaCl_2$ group and also a larger number of edges survived the applied threshold. $CMRO_2$ data also displays more anticorrelated nodes in the $CaCl_2$ group when compared to the control group.

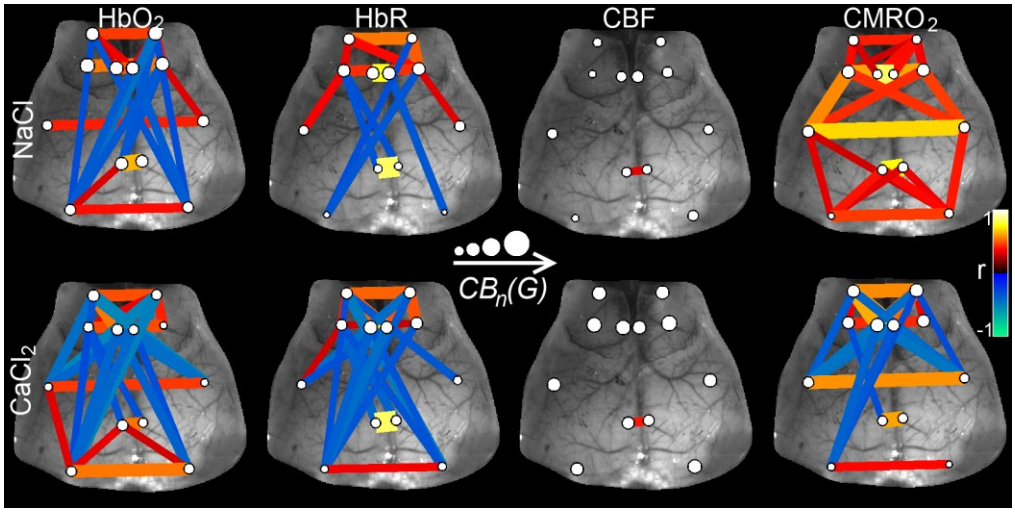

Figure 6-4: Functional connectivity diagrams for NaCl (top row) and $CaCl_2$ (bottom row) subjects. Edge thicknesses depend on the seed-to-seed average correlation coefficients, only edges with $|r|>0.3$ are shown. Node sizes are proportional to betweenness centrality $CB_n(G)$ of each seed. Positive correlations are depicted in warm colors. Negative correlations are depicted in cool colors.

6.6 Discussion

The goal of this work was to investigate the impact of a controlled unilateral carotid stiffness on resting state networks in anesthetized mice. While an increasing number of studies suggest that arterial stiffness is a risk factor predictive of ensuing cognitive dysfunction with age, its role in modulating functional hemodynamic imaging remain difficult to assess, mainly due to a lack of animal model in the past to isolate its effect. Blood flow coming from the carotids feeds the circle of Willis and typically represents 70% of the total cerebral perfusion. Amongst regions selected for our analysis, we expect that the occipital cortex (visual) as well as part of the temporal and parietal cortices to receive diminished output from the affected carotid when compared to others.

6.6.1 Hemodynamic changes

The observed changes of correlation maps spatial extent reflect a spatial reorganization of the hemodynamic-derived functional connectivity within the cortex. For individual seeds, significant larger spatial areas of contra-lateral coherent hemodynamic fluctuations were observed in the $CaCl_2$ group. We can speculate that this mechanism originates in the physiological response to

the modified pulse wave from the rigidified carotid to the circle of Willis, potentially inducing a global response from resistance arteries. In a separate study (in-progress) we observed changes in flow mediated dilation and myogenic tone in pressurized isolated arteries subject to different levels of pulsatility, supporting this mechanism as a vascular modulator of connectivity changes independent of metabolism.

Focusing on the seed location and correlation amplitude rather than the correlation extent, results from HbO_2, HbR and CBF measures show that compared to the NaCl group, the $CaCl_2$ group had decreased bilateral correlation values within the motor cortex but increased bilateral correlations within the visual cortex. In other seeds, depending on the hemodynamic component and spatial location, changes in bilateral correlations going in both directions (increase and decrease) suggest interplay between systemic hemodynamic changes when blood supply is unilaterally manipulated and loss of neuronal synchrony from neural degeneration in the hippocampus previously observed in this model. Overall results from evaluations of the bilateral synchrony underline the importance of careful interpretation when using a single hemodynamic signal as a proxy for neural changes is situations where blood supply is compromised.

6.6.2 $CMRO_2$

Amongst important findings, $CMRO_2$ functional connectivity changes did not always correspond to changes observed in the other contrasts. In fact, when looking at homologous correlations, $CMRO_2$ results were different in 50% of the analyzed seeds, with respect to CBF, HbO_2 and HbR changes. $CMRO_2$ indicated a decreasing trend of functional connectivity in the $CaCl_2$ group that was more evident in the motor and cingulate regions. Since $CMRO_2$ potentially displays increased independence to vascular changes and provides a metabolic measure expected to closely match neural activity, observed changes may better reflect hippocampal neurodegeneration observed previously in this model. Using fcOIS based on hemoglobin absorption only we would not be able to discern the vascular response from the underlying metabolic activity, hence the need for a more complete set of hemodynamic parameters. These results further support that care must be taken when interpreting functional connectivity studies with techniques that solely rely on hemodynamics.

6.6.3 Graph theoretical measures

When looking at seed level, RCCA stiffness proved to have the most impact on network measures in the right frontal cortex, in both HbO_2 and CBF measures. Local efficiency and clustering coefficient, both measures of network robustness were significantly higher in the NaCl group, potentially indicating loss of network efficiency due to the application of $CaCl_2$. The decrease in whole cortex average clustering coefficient can be interpreted as a reflection of the randomization of the functional networks with arterial stiffness; this randomization is particularly remarkable in the right motor cortex. Betweenness centrality was higher in the $CaCl_2$ group suggesting a more central hub role of the motor right regions in the general network structure. The non-significant differences in cost and degree in left motor seed (HbR) suggest that this node became more disconnected from the global network, with fewer neighbors in the $CaCl_2$ group. Cost and degree were also reduced in left cingulate seed in $CMRO_2$ measures, but these changes were not reflected at a global level.

Visual inspection of the weighted functional networks (Figure 6-4) indicate a reorganization of the $CMRO_2$ networks, but due to the lack of a single formulation for weighted network measurements (Saramäki, Kivelä, Onnela, Kaski, & Kertész, 2007) their full characterization remains complex.

6.6.4 Impact for BOLD-fMRI

Mapping resting-state networks provides an approach to assess brain function in populations where task-based fMRI scanning is challenging. The BOLD-fMRI signal arises from the magnetic properties of HbR, is dependent on local blood volume, flow and deoxygenation and is weighted towards venous vasculature. Our results show that investigating network connectivity solely based on HbR signals indeed showed decreased connectivity between homologous regions but these changes were not significant, weaker and only partially coherent with observations using $CMRO_2$. Globally, at the network level, HbR signals displayed small changes where compared to flow and $CMRO_2$. Overall, these results suggest that BOLD-fMRI signals may potentially be modulated by the rigidification of arterial vasculature and benefit from combined flow and calibration measures in studies investigating resting state networks in populations affected by arterial stiffness.

6.7 Conclusion

Using a new carotid calcification murine model, we were able for the first time to investigate the isolated effect of unilateral carotid stiffness on resting state networks. It is difficult to make a direct comparison of our results to disease in humans and even other animal models, since our novel model is specific to study the role of carotid stiffness, independently of confounding variables, such as systemic changes in blood pressure, high levels of circulating lipids present in other models; or other factors leading to arterial stiffness in humans such as aging or atherosclerosis. Using multispectral fcOIS, our results show network modifications associated with the procedure and a potential uncoupling between hemodynamic measures (HbO_2, HbR and CBF) and metabolism ($CMRO_2$). While confounds remain due to the fact that the procedure leads to both neural degeneration in the hippocampus and lateral vascular alterations due to carotid rigidification, both of which will affect resting state networks, they underline the importance of calibration of brain images in the presence of arterial remodeling.

6.8 Acknowledgments

The work described in this article was supported by NSERC Discovery Grant to F. Lesage and CONACYT scholarship No. 304501 to E. Guevara. The authors cordially thank Marc-Antoine Gillis for his assistance with animal preparation and Natacha Duquette for laboratory animal monitoring.

6.9 References

Achard, S., & Bullmore, E. (2007). Efficiency and Cost of Economical Brain Functional Networks. PLoS Comput Biol, 3(2), e17. doi:10.1371/journal.pcbi.0030017

Anderton, B. H. (2002). Ageing of the brain. Mechanisms of Ageing and Development, 123(7), 811–817. doi:10.1016/S0047-6374(01)00426-2

Aronson, M. K., Ooi, W. L., Morgenstern, H., Hafner, A., Masur, D., Crystal, H., … Katzman, R. (1990). Women, myocardial infarction, and dementia in the very old. Neurology, 40(7), 1102–1106.

Bassett, D. S., & Bullmore, E. (2006). Small-world brain networks. The Neuroscientist: a review journal bringing neurobiology, neurology and psychiatry, 12(6), 512–523. doi:10.1177/1073858406293182

Bero, A. W., Bauer, A. Q., Stewart, F. R., White, B. R., Cirrito, J. R., Raichle, M. E., … Holtzman, D. M. (2012). Bidirectional Relationship between Functional Connectivity and Amyloid-β Deposition in Mouse Brain. The Journal of Neuroscience, 32(13), 4334–4340. doi:10.1523/JNEUROSCI.5845-11.2012

Boas, D. A., & Dunn, A. K. (2010). Laser speckle contrast imaging in biomedical optics. Journal of Biomedical Optics, 15(1), 011109. doi:10.1117/1.3285504

Bolduc, V., Baraghis, E., Duquette, N., Thorin-Trescases, N., Lambert, J., Lesage, F., & Thorin, E. (2012). Catechin prevents severe dyslipidemia-associated changes in wall biomechanics of cerebral arteries in LDLr-/-:hApoB+/+ mice and improves cerebral blood flow. American journal of physiology. Heart and circulatory physiology, 302(6), H1330–1339. doi:10.1152/ajpheart.01044.2011

Breteler, M. M., Claus, J. J., Grobbee, D. E., & Hofman, A. (1994). Cardiovascular disease and distribution of cognitive function in elderly people: the Rotterdam Study. BMJ (Clinical research ed.), 308(6944), 1604–1608.

Briers, J. D. (2001). Laser Doppler, speckle and related techniques for blood perfusion mapping and imaging. Physiological Measurement, 22(4), R35–R66. doi:10.1088/0967-3334/22/4/201

Brieu, N., Beaumont, E., Dubeau, S., Cohen-Adad, J., & Lesage, F. (2010). Characterization of the hemodynamic response in the rat lumbar spinal cord using intrinsic optical imaging and laser speckle. Journal of Neuroscience Methods, 191(2), 151–157. doi:10.1016/j.jneumeth.2010.06.012

Buckner, R. L., Andrews-Hanna, J. R., & Schacter, D. L. (2008). The brain's default network: anatomy, function, and relevance to disease. Annals of the New York Academy of Sciences, 1124, 1–38. doi:10.1196/annals.1440.011

Cheng, H.-L., Lin, C.-J., Soong, B.-W., Wang, P.-N., Chang, F.-C., Wu, Y.-T., … Lee, I.-H. (2012). Impairments in cognitive function and brain connectivity in severe asymptomatic carotid

stenosis. Stroke; a journal of cerebral circulation, 43(10), 2567–2573. doi:10.1161/STROKEAHA.111.645614

Cole, D. M., Smith, S. M., & Beckmann, C. F. (2010). Advances and pitfalls in the analysis and interpretation of resting-state FMRI data. Frontiers in systems neuroscience, 4, 8. doi:10.3389/fnsys.2010.00008

Delpy, D. T., Cope, M., Zee, P. van der, Arridge, S., Wray, S., & Wyatt, J. (1988). Estimation of optical pathlength through tissue from direct time of flight measurement. Physics in Medicine and Biology, 33(12), 1433–1442. doi:10.1088/0031-9155/33/12/008

Dubeau, S., Ferland, G., Gaudreau, P., Beaumont, E., & Lesage, F. (2011). Cerebrovascular hemodynamic correlates of aging in the Lou/c rat: A model of healthy aging. NeuroImage, 56(4), 1892–1901. doi:10.1016/j.neuroimage.2011.03.076

Dunn, A. K., Bolay, H., Moskowitz, M. A., & Boas, D. A. (2001). Dynamic Imaging of Cerebral Blood Flow Using Laser Speckle. J Cereb Blood Flow Metab, 21(3), 195–201. doi:10.1097/00004647-200103000-00002

Dunn, A. K., Devor, A., Bolay, H., Andermann, M. L., Moskowitz, M. A., Dale, A. M., & Boas, D. A. (2003). Simultaneous imaging of total cerebral hemoglobin concentration, oxygenation, and blood flow during functional activation. Optics Letters, 28(1), 28–30. doi:10.1364/OL.28.000028

Dunn, A. K., Devor, A., Dale, A. M., & Boas, D. A. (2005). Spatial extent of oxygen metabolism and hemodynamic changes during functional activation of the rat somatosensory cortex. NeuroImage, 27(2), 279–290. doi:10.1016/j.neuroimage.2005.04.024

Faraci, F. M. (2011). Protecting against vascular disease in brain. American journal of physiology. Heart and circulatory physiology, 300(5), H1566–1582. doi:10.1152/ajpheart.01310.2010

Fox, M. D., & Raichle, M. E. (2007). Spontaneous fluctuations in brain activity observed with functional magnetic resonance imaging. Nature Reviews Neuroscience, 8(9), 700–711. doi:10.1038/nrn2201

Friston, K. J., Ashburner, J. T., Kiebel, S. J., Nichols, T. E., & Penny, W. D. (2006). Statistical Parametric Mapping: The Analysis of Functional Brain Images (1st ed.). Great Britain: Academic Press. Retrieved from http://www.fil.ion.ucl.ac.uk/spm/

Gili, T., Cercignani, M., Serra, L., Perri, R., Giove, F., Maraviglia, B., … Bozzali, M. (2011). Regional brain atrophy and functional disconnection across Alzheimer's disease evolution. Journal of neurology, neurosurgery, and psychiatry, 82(1), 58–66. doi:10.1136/jnnp.2009.199935

Glisky, E. L. (2007). Changes in Cognitive Function in Human Aging. In D. Riddle (Ed.), Brain Aging: Models, Methods, and Mechanisms. Boca Raton, USA: CRC Press. Retrieved from http://www.ncbi.nlm.nih.gov/books/NBK3885/

Greicius, M. D., Krasnow, B., Reiss, A. L., & Menon, V. (2003). Functional connectivity in the resting brain: a network analysis of the default mode hypothesis. Proceedings of the National Academy of Sciences of the United States of America, 100(1), 253–258. doi:10.1073/pnas.0135058100

Greicius, M. D., Srivastava, G., Reiss, A. L., & Menon, V. (2004). Default-mode network activity distinguishes Alzheimer's disease from healthy aging: evidence from functional MRI. Proceedings of the National Academy of Sciences of the United States of America, 101(13), 4637–4642. doi:10.1073/pnas.0308627101

Gusnard, D. A., Raichle, M. E., & Raichle, M. E. (2001). Searching for a baseline: functional imaging and the resting human brain. Nature reviews. Neuroscience, 2(10), 685–694. doi:10.1038/35094500

He, Y., Chen, Z., Gong, G., & Evans, A. (2009). Neuronal networks in Alzheimer's disease. The Neuroscientist: a review journal bringing neurobiology, neurology and psychiatry, 15(4), 333–350. doi:10.1177/1073858409334423

Iadecola, C. (2010). The overlap between neurodegenerative and vascular factors in the pathogenesis of dementia. Acta neuropathologica, 120(3), 287–296. doi:10.1007/s00401-010-0718-6

Jones, M., Berwick, J., Johnston, D., & Mayhew, J. (2001). Concurrent optical imaging spectroscopy and laser-Doppler flowmetry: the relationship between blood flow, oxygenation,

and volume in rodent barrel cortex. NeuroImage, 13(6 Pt 1), 1002–1015. doi:10.1006/nimg.2001.0808

Kohl, M., Lindauer, U., Royl, G., Kuhl, M., Gold, L., Villringer, A., & Dirnagl, U. (2000). Physical model for the spectroscopic analysis of cortical intrinsic optical signals. Physics in Medicine and Biology, 45(12), 3749–3764.

Latora, V., & Marchiori, M. (2001). Efficient Behavior of Small-World Networks. Physical Review Letters, 87(19), 198701. doi:10.1103/PhysRevLett.87.198701

Luckl, J., Baker, W., Sun, Z.-H., Durduran, T., Yodh, A. G., & Greenberg, J. H. (2010). The biological effect of contralateral forepaw stimulation in rat focal cerebral ischemia: a multispectral optical imaging study. Frontiers in Neuroenergetics, 2, pii: 19. doi:10.3389/fnene.2010.00019

Marshall, R S, Lazar, R. M., Pile-Spellman, J., Young, W. L., Duong, D. H., Joshi, S., & Ostapkovich, N. (2001). Recovery of brain function during induced cerebral hypoperfusion. Brain: a journal of neurology, 124(Pt 6), 1208–1217.

Marshall, Randolph S, & Lazar, R. M. (2011). Pumps, aqueducts, and drought management: vascular physiology in vascular cognitive impairment. Stroke; a journal of cerebral circulation, 42(1), 221–226. doi:10.1161/STROKEAHA.110.595645

Mayhew, J., Johnston, D., Berwick, J., Jones, M., Coffey, P., & Zheng, Y. (2000). Spectroscopic Analysis of Neural Activity in Brain: Increased Oxygen Consumption Following Activation of Barrel Cortex. NeuroImage, 12(6), 664–675. doi:10.1006/nimg.2000.0656

Moldestad, O., Karlsen, P., Molden, S., & Storm, J. F. (2009). Tracheotomy improves experiment success rate in mice during urethane anesthesia and stereotaxic surgery. Journal of neuroscience methods, 176(2), 57–62. doi:10.1016/j.jneumeth.2008.08.015

Pase, M. P., Herbert, A., Grima, N. A., Pipingas, A., & O'Rourke, M. F. (2012). Arterial stiffness as a cause of cognitive decline and dementia: a systematic review and meta-analysis. Internal medicine journal, 42(7), 808–815. doi:10.1111/j.1445-5994.2011.02645.x

Prahl, S. (1999). Optical Absorption of Hemoglobin. Retrieved October 8, 2009, from http://omlc.ogi.edu/spectra/hemoglobin/

Pukelsheim, F. (1994). The Three Sigma Rule. The American Statistician, 48(2), 88. doi:10.2307/2684253

Roberts, R. O., Knopman, D. S., Geda, Y. E., Cha, R. H., Roger, V. L., & Petersen, R. C. (2010). Coronary heart disease is associated with non-amnestic mild cognitive impairment. Neurobiology of aging, 31(11), 1894–1902. doi:10.1016/j.neurobiolaging.2008.10.018

Sadekova, N., Vallerand, D., Guevara, E., Lesage, F., & Girouard, H. (In Press). Carotid calcification in mice: a new model to study the effects of arterial stiffness on the brain. Journal of the American Heart Association.

Saramäki, J., Kivelä, M., Onnela, J.-P., Kaski, K., & Kertész, J. (2007). Generalizations of the clustering coefficient to weighted complex networks. Physical Review E, 75(2), 027105. doi:10.1103/PhysRevE.75.027105

Singh-Manoux, A., Britton, A. R., & Marmot, M. (2003). Vascular disease and cognitive function: evidence from the Whitehall II Study. Journal of the American Geriatrics Society, 51(10), 1445–1450.

Sun, J., Tong, S., & Yang, G.-Y. (2011). Reorganization of Brain Networks in Aging and Age-related Diseases. Aging and Disease, 3(2), 181–193.

Sun, Y., Qin, L., Zhou, Y., Xu, Q., Qian, L., Tao, J., & Xu, J. (2011). Abnormal functional connectivity in patients with vascular cognitive impairment, no dementia: a resting-state functional magnetic resonance imaging study. Behavioural brain research, 223(2), 388–394. doi:10.1016/j.bbr.2011.05.006

Thevenaz, P., Ruttimann, U. E., & Unser, M. (1998). A pyramid approach to subpixel registration based on intensity. IEEE Transactions on Image Processing, 7(1), 27–41. doi:10.1109/83.650848

Van den Heuvel, M. P., & Hulshoff Pol, H. E. (2010). Exploring the brain network: A review on resting-state fMRI functional connectivity. European Neuropsychopharmacology, 20(8), 519–534. doi:10.1016/j.euroneuro.2010.03.008

Van Norden, A. G., de Laat, K. F., Gons, R. A., van Uden, I. W., van Dijk, E. J., van Oudheusden, L. J., … de Leeuw, F.-E. (2011). Causes and consequences of cerebral small vessel disease. The RUN DMC study: a prospective cohort study. Study rationale and protocol. BMC neurology, 11, 29. doi:10.1186/1471-2377-11-29

White, B. R., Bauer, A. Q., Snyder, A. Z., Schlaggar, B. L., Lee, J.-M., & Culver, J. P. (2011). Imaging of functional connectivity in the mouse brain. PloS one, 6(1), e16322. doi:10.1371/journal.pone.0016322

Whitfield-Gabrieli, S., & Nieto-Castanon, A. (2012). Conn: a functional connectivity toolbox for correlated and anticorrelated brain networks. Brain connectivity, 2(3), 125–141. doi:10.1089/brain.2012.0073

World Health Organization. (2012). World Health Statistics 2012. Geneva, Switzerland: WHO Press. Retrieved from http://www.who.int/healthinfo/EN_WHS2012_Full.pdf

6.10 Supplemental Figures

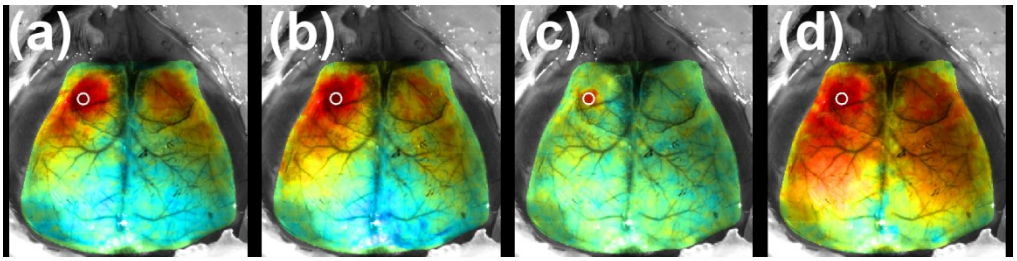

Figure 6-5: Representative fc maps for all contrasts for a given seed (M_L) (a)HbO_2 (b)HbR (c) CBF (d) $CMRO_2$.

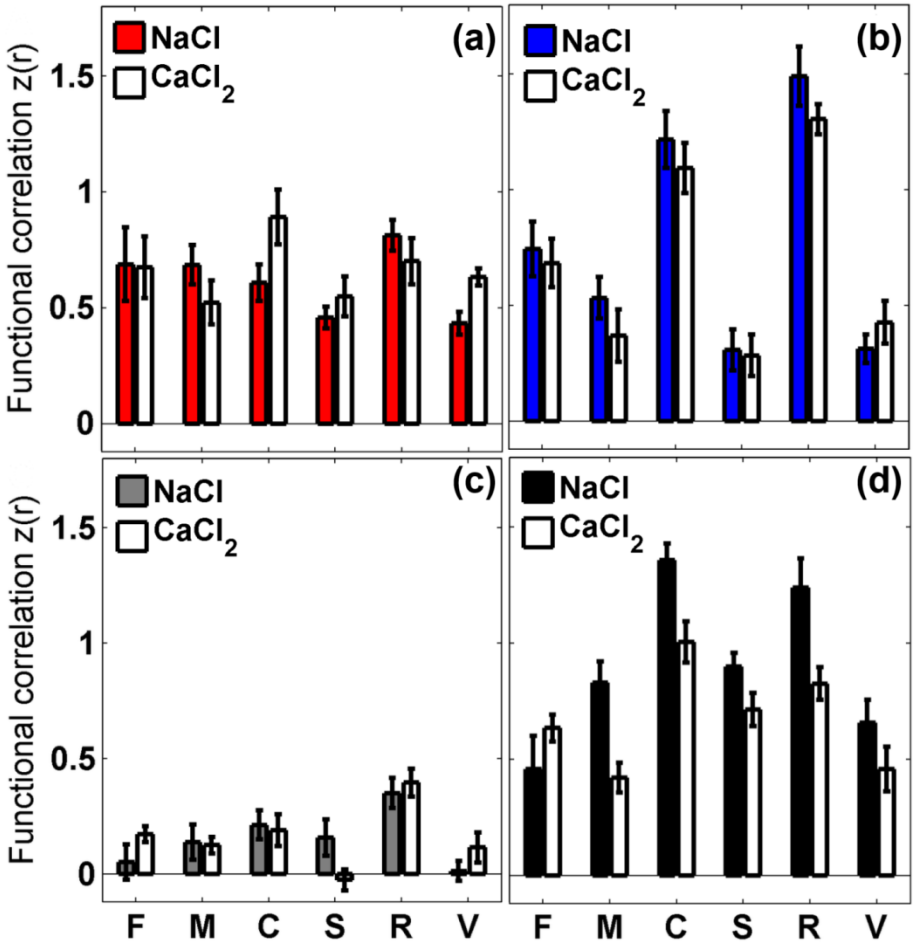

Figure 6-6: Regional bilateral functional connectivity, comparison performed between control NaCl and treatment group $CaCl_2$; analysis done for every seed time-trace and its contralateral part. Data points that were more than 3 standard deviations away from the mean were considered outliers and consequently removed. Contrasts shown: (a) HbO_2, (b) HbR (c) CBF and (d) $CMRO_2$. Standard error bars shown ($\sigma/\sqrt{N}$), with N=19. (F: frontal cortex, M: motor cortex, C: cingulate cortex, S: somatosensory cortex R: retrosplenial cortex, V: visual cortex).

CHAPTER 7 ARTICLE 3: IMAGING OF AN INFLAMMATORY INJURY IN THE NEWBORN RAT BRAIN WITH PHOTOACOUSTIC TOMOGRAPHY

Edgar Guevara[1,2], Romain Berti[1,2], Irène Londono[3], Ningshi Xie[3], Pierre Bellec[4], Frédéric Lesage[1,2] and Gregory A. Lodygensky[2,3]

7.1 Presentation of the article

In this work (Guevara, Berti, et al., 2013) we applied PAT to assess SO_2 and connectivity changes in the newborn rat brain, in a model of white matter injury. The reduced SO_2 measured in vivo was partly explained by histological evaluation of microvasculature. Homologous functional connectivity was not differentiated in the injured group, as compared to shams, this result may be explained by the short time between the injury and the imaging session. The article was recently accepted for publication in the *PLOS ONE* journal.

7.2 Abstract

Background: The precise assessment of cerebral saturation changes during an inflammatory injury in the developing brain, such as seen in periventricular leukomalacia, is not well defined. This study investigated the impact of inflammation on locoregional cerebral oxygen saturation in a newborn rodent model using photoacoustic imaging. Methods: 1 mg/kg of lipopolysaccharide (LPS) diluted in saline or saline alone was injected under ultrasound guidance directly in the corpus callosum of P3 rat pups. Coronal photoacoustic images were carried out 24h after LPS exposure. Locoregional oxygen saturation (SO_2) and resting state connectivity were assessed in the cortex and the corpus callosum. Microvasculature was then evaluated on cryosection slices by

[1] Department of Electrical Engineering, École Polytechnique de Montréal, Canada

[2] Montreal Heart Institute, Montréal, Canada

[3] Sainte-Justine University Hospital and Research Center, Department of Pediatrics, Université de Montréal, Canada

[4] Geriatric Institute Research Center, Université de Montréal, Canada

lectin histochemistry. Results: Significant reduction of SO_2 was found in the corpus callosum and in the cortex ipsilateral to the injection site. Seed-based functional connectivity analysis showed that bilateral connectivity was not affected by LPS exposure. Changes in locoregional oxygen saturation were accompanied by a significant reduction in the average length of microvessels in the left cortex but no differences were observed in the corpus callosum. Conclusion: Inflammation in the developing brain induces marked reduction of locoregional oxygen saturation, predominantly in the white matter not explained by microvascular degeneration. The ability to examine regional saturation offers a new way to monitor injury and understand physiological disturbance non-invasively.

7.3 Introduction

Periventricular leukomalacia (PVL) stands as a predominant cause of cerebral palsy and significant neurodevelopmental impairment in premature infants (Blumenthal, 2004). The primary physiopathological mechanism was thought to be secondary to hemodynamic instability in a pressure passive immature cerebral circulation weakening the watershed areas of the white matter composed of pre-oligodendrocytes highly vulnerable to free radicals (Blumenthal, 2004). Only recent epidemiological studies have shown an association between inflammation and white matter injury (Dammann, Kuban, & Leviton, 2002; Dammann & Leviton, 2004; Hagberg, Mallard, & Jacobsson, 2005). Yet it is not clear if inflammation induces hemodynamic changes in the developing white matter. An intravenous dose of LPS sufficient to cause hypotension also affected O_2 delivery to white matter (Dalitz, Harding, Rees, & Cock, 2003). Yet an experiment conducted in fetal sheep showed that small intravenous doses of LPS not sufficient to produce hypoxemia and systemic hypotension still triggered significant white matter injury (Duncan et al., 2006). To date, little is known regarding local changes in oxygen delivery with LPS induced inflammation. In rodents, one of the most robust and reproducible post-natal models consists in an injection of LPS into the corpus callosum. It replicates every aspect of periventricular leukomalacia including astrogliosis, microglial reaction, pre-oligodendrocyte cell loss, necrosis, apoptosis, hypomyelination (Cai, Pang, Lin, & Rhodes, 2003; Pang, Cai, & Rhodes, 2003), hippocampal atrophy (K.-C. Wang et al., 2013) and behavioral hallmarks of PVL (Choi et al., 2011). Recent characterization of the model by magnetic resonance imaging (MRI) has shown striking similarities with what is seen in preterm infants with ongoing injury such as a reduction

of the apparent diffusion coefficient in the white matter, increased T2 relaxation time constant, measurable ventricular dilation and increased radial diffusivity (Lodygensky et al., 2010).

The regional changes seen in white matter injury of the preterm infants have been described using near-infrared spectroscopy (NIRS). This well-established bedside technique is limited by the absence of depth resolved information where for instance the presence of sub-dural hematoma or scalp edema seen in newborns might lead to inaccurate results. Moreover the technique cannot differentiate the cortex from the white matter or saturation extracted from the venous circulation. Although partial depth information can be obtained by using tomographic reconstruction methods (Boas et al., 2001; O'Leary, Boas, Chance, & Yodh, 1995), they remain limited. Photoacoustic imaging is a depth-sensitive, non-invasive technique that combines the intrinsic contrast capabilities of optical imaging with the advantage of high spatial resolution of ultrasound (L. V. Wang & Hu, 2012),(Xiang et al., 2012). By illuminating tissue using a short laser pulse, a transient thermoelastic expansion occurs, generating an ultrasonic pressure wave detected by an ultrasound transducer (X. Wang et al., 2003). Using more than one wavelength and spectroscopic information on hemoglobin, it has the potential to determine the locoregional oxygen saturation. In mouse pups, recent data shows that just 24 hours of hypoxic ischemic injury was sufficient to induce a 40% reduction of cerebrovascular density (Honoré et al., 2013). In this study, we sought to evaluate changes in locoregional oxygen saturation 24h after LPS exposure, at the peak of the inflammatory injury, and determine if any changes detected in vivo would correlate with modification of the microvascular skeleton of the cortex and the white matter.

Several functional imaging studies in the developing brain have been successful in identifying a physiological response to external tasks (A. P. Born et al., 2000; P. Born et al., 1998; Seghier, Lazeyras, & Huppi, 2006). Despite the success of this approach requiring a complex setup, attention has shifted to brain mapping in resting conditions (Smyser, Snyder, & Neil, 2011), an approach more suitable in neonates, where task-based functional magnetic resonance imaging (fMRI) scanning is challenging. Resting-state functional imaging (rsMRI) simplifies the experimental design, making longitudinal studies feasible in infants (Doria et al., 2010; Smyser et al., 2010, 2011).

Since the discovery of spatially remote areas connected by spontaneous low frequency in the temporal domain with coherent fluctuations in the BOLD signal (<0.1 Hz) (Biswal, Yetkin,

Haughton, & Hyde, 1995), a number of resting-state functional connectivity studies have been performed in infants (Church et al., 2009; Damaraju et al., 2010; Doria et al., 2010; Fransson et al., 2007; Liu, Flax, Guise, Sukul, & Benasich, 2008; Smyser et al., 2010); although infants presenting PVL were excluded from those studies (Damaraju et al., 2010; Fransson et al., 2007). Recently, Smyser et al. have specifically characterized the dramatic effect of white matter injury in the preterm infant on resting state activity at term equivalent (Smyser et al., 2013). Thus, early detection of the functional connectivity changes induced by PVL could reveal itself as a non-invasive tool to monitor newborns at risk and eventually identify the ones requiring neuroprotective therapy. Still performing routine MRI in unstable extreme preterm infants is challenging. Having depth sensitive data on resting state connectivity using a non-invasive technique that could be performed at bedside would be immensely useful, which is why we explored the potential of photoacoustic imaging to detect functional connectivity.

The objective of this study was to determine the impact of inflammation on the corpus callosum and the cortex both known to be affected by inflammation. Moreover the possibility of assessing resting-state functional connectivity using PAT imaging in immature rat pups was examined.

7.4 Materials and Methods

7.4.1 Ethics statement

All surgical procedures performed according to the recommendations of the Canadian Council on Animal Care, were approved by the Animal Research Ethics Committee of the Montreal Heart Institute and by the Institutional Committee for Animal Care in Research of the CHU Sainte-Justine Research Center. All the procedures were performed under isoflurane anesthesia, and all efforts were made to minimize suffering.

7.4.2 Neonatal inflammatory injury

Nineteen postnatal day 3 (P3) Sprague-Dawley rat pups from four litters were used in this study (9.8 ± 0.3 g weight, Charles River, Wilmington, MA); the rat pups were given *ad libitum* access to food and water. P3 rat pups are equivalent to very premature human infants between 24 and 28 weeks gestation (Sizonenko et al., 2003). In this work, we followed the same animal procedure as

in previous studies (Lodygensky et al., 2010) which was outlined by the group of Cai (Cai, Pang, Lin, & Rhodes, 2003; Pang, Cai, & Rhodes, 2003) and briefly described below.

P3 rat pups (n=19) were randomized to two experimental groups: LPS (n=11; n_{male}=6, n_{female}=5) and NaCl (sham n=8; n_{male} =7, n_{female} =1). Pups were injected under ultrasound guidance using the Vevo LAZR micro-ultrasound system (FUJIFILM VisualSonics Inc., Toronto, ON, Canada) with LPS (1 mg/kg) suspension (E. Coli, serotype 055:B5, Sigma St Louis, MO) in 0.5 µL of sterile saline or with the same volume of sterile saline alone for the sham group. The injection was placed in the corpus callosum at the level equivalent to P-7, c9 (Ramachandra & Subramanian, 2011), depicted in Figure 1-1A. Injections were made with a micropipette mounted on a microprocessor-controlled injector (Micro4 from World Precision Instruments) at a rate of 100nL/min. All the injections were performed under isoflurane anesthesia, and all efforts were made to minimize suffering. All animals survived the injection. 24 hours later animals were imaged as described in the following sub-section.

7.4.3 PAT imaging

The rat pups were secured in a custom-designed stereotaxic neonatal frame and placed on an imaging station; monitoring of the respiration and body temperature were done using the 1025L monitoring system (SA Instruments Inc., Stony Brook, NY). The Vevo LAZR photoacoustic imaging system was used to acquire all images with the LZ250 ultrasound probe at a central frequency of 21 MHz. The chosen coronal B-scan was located at the injection site. The acquisition time was 1.4 s per B-scan, with a field of view (FOV) of 13 mm width × 18 mm depth (512 A-lines, 416 samples) using a 256-element array transducer that provides 75µm axial resolution. A time-series of B-scans were acquired in resting-state conditions for a 5-minute period. Functional photoacoustic imaging was performed at two wavelengths (λ_1=750 nm and λ_2=850 nm) with pulse energy output of approximately 18 mJ/cm^2. Total hemoglobin (HbT) and oxygen saturation (SO_2) weighted images were internally computed from the raw data according to the procedure described in detail in refs. (Ephrat et al., 2012; X. Wang, Xie, Ku, Wang, & Stoica, 2006):

$$HbT = \frac{\mu_a(\lambda_1)\Delta\epsilon_{HbR}(\lambda_2) - \mu_a(\lambda_2)\Delta\epsilon_{HbR}(\lambda_1)}{\epsilon_{HbR}(\lambda_1)\epsilon_{HbO_2}(\lambda_2) - \epsilon_{HbR}(\lambda_2)\epsilon_{HbO_2}(\lambda_1)} \quad (7.1)$$

$$SO_2 = \frac{\mu_a(\lambda_2)\epsilon_{HbR}(\lambda_1) - \mu_a(\lambda_1)\epsilon_{HbR}(\lambda_2)}{\mu_a(\lambda_1)\Delta\epsilon_{HbR}(\lambda_2) - \mu_a(\lambda_2)\Delta\epsilon_{HbR}(\lambda_1)} \quad (7.2)$$

where μ_a was the estimated effective absorption coefficient (cm^{-1}); ϵ_{HbO_2} and ϵ_{HbR} are the known molar extinction coefficients ($cm^{-1}M^{-1}$) of oxy- and deoxygenated hemoglobin respectively; and $\Delta\epsilon_{HbR} = \epsilon_{HbO_2} - \epsilon_{HbR}$. Once the effective absorption coefficients were estimated, HbT and SO_2 could be calculated. Values of oxy- and deoxygenated hemoglobin (HbO_2 and HbR respectively) were computed using the following equations:

$$\begin{cases} HbO_2 = SO_2 HbT \\ HbR = (1 - SO_2)HbT \end{cases} \quad (7.3)$$

One session of five minutes was recorded for every animal. The same recording session was used to assess both locoregional cortical saturation and functional connectivity. Locoregional cortical saturation was computed as the mean SO_2 values during resting-state after removing frames contaminated with excessive motion (See Scrubbing technique below). Average locoregional saturation values in corpus callosum were computed over a $1 \times 0.5 mm^2$ rectangle; locoregional SO_2 in the cortex was calculated over a closed spline that encircled the region of interest, either the left or right cortex, as shown on Figure 7-1B.

7.4.4 Seed-based functional connectivity analysis

First, all functional images (PAT) within each scan were realigned to the first image to reduce the impact of motion artifacts. Images of each contrast were spatially smoothed with a Gaussian kernel of FWHM=0.2 mm. Imaging of the anatomy was performed by an ultrasonic B-scan simultaneously recorded, from which the region corresponding to brain was manually selected using a closed spline curve to create a brain mask. All further processing was performed only on those pixels belonging to the brain mask. The image time series were temporally band-pass filtered (zero phase-shift fourth-order Butterworth filter) at 0.009-0.08 Hz, according to previous functional connectivity studies (Guevara, Pouliot, et al., 2013; Jonckers et al., 2011; Brian R White et al., 2011; F. Zhao et al., 2008). In order to account for spurious variability, several

nuisance variables were regressed from each pixel time course including (a) The signal averaged over the lateral ventricles (LV), (b) the signal averaged over a region in the deep white matter and (c) three parameters obtained by rigid body motion correction (translation along X and Y axes and rotation around those same axes). Regression of the aforementioned parameters was performed simultaneously using a General Linear Model (GLM) from the package Statistical Parametrical Mapping (Karl J. Friston et al., 2006) (SPM8, www.fil.ion.ucl.ac.uk/spm) running on a MATLAB (The MathWorks, Natick, MA) platform. In previous studies, the global brain signal, created from the average of all the pixels time traces, was found to introduce artificial anticorrelations (Murphy, Birn, Handwerker, Jones, & Bandettini, 2009), even though a neural basis for such anticorrelations is probable (Fox et al., 2009), it was not included as a regressor in this study.

All seeds were placed a priori on the rat brain using anatomical definitions from the Ramachandra atlas with complementary information from the Paxinos atlas (Paxinos & Watson, 2007; Ramachandra & Subramanian, 2011), as shown on Figure 7-1B. Seed time-courses were computed as the mean time course of the pixels within a 0.5 mm radius from the seed locus. Several seed radii were explored (from 0.1 to 0.5 mm), only limited by anatomical specificity; the largest radius was chosen because of stronger values in bilateral correlations.

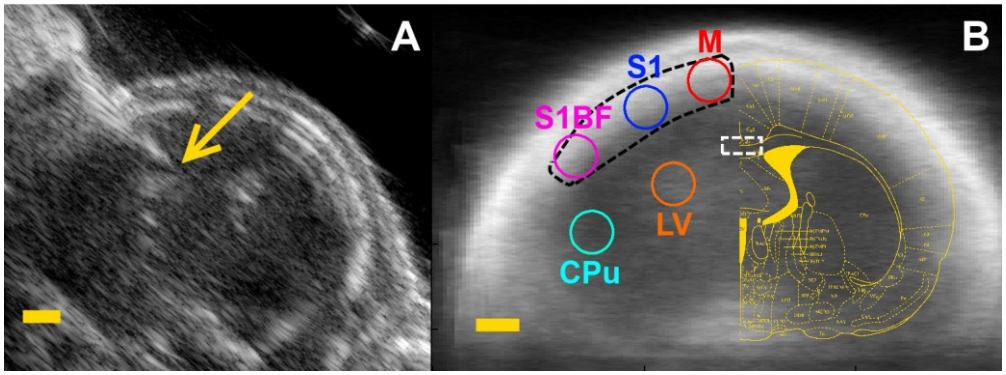

Figure 7-1: (A) Arrow marks injection site. (B) Seeds placement, overlaid a coronal B-scan, averaged over 11 individual B-scans. Abbreviations: M, motor cortex; S1, primary somatosensory cortex; S1BF, barrel field primary somatosensory cortex; LV, Lateral ventricle; CPu, Caudate putamen. Black dotted line indicates Left Cortex ROI used for locoregional SO_2 measurement. White dotted rectangle indicates ROI used for local SO_2 measurement in corpus callosum. Scale bar: 1mm.

7.4.5 Scrubbing

Movement during scanning influences the quality of PAT data. Head motion causes spurious changes in photoacoustic signal intensity. After frame realignment and motion parameters regression, a technique called "scrubbing" was applied to remove measures distorted by unwanted movement (Power, Barnes, Snyder, Schlaggar, & Petersen, 2012). Scrubbing relies on two measures to flag frames contaminated by excessive motion: framewise displacement (FD) and DVARS (D stands for temporal derivative and VARS standing for RMS variance over pixels) (Smyser et al., 2010).

FD represents instantaneous head motion and is an empirical measurement computed from the motion parameters; in equation (7.4) $\Delta d_{ix} = d_{ix} - d_{(i-1)x}$ represents the derivative of translation along x and the same for the other rigid-motion parameter; the rotational displacement $|\Delta\alpha_i|$ was converted from radians to mm by calculating arc length on a circle of radius 4.05 mm, which was approximately the mean distance from the cortex to the center of the head in P4 rats.

$$FD_i = |\Delta d_{ix}| + |\Delta d_{iy}| + |\Delta \alpha_i| \tag{7.4}$$

DVARS was computed as the RMS of the derivative of the global brain signal; this measure represents how much the intensity of a brain image changed in comparison to the previous frame.

$$DVARS(\Delta I)_i = \sqrt{\langle [\Delta I_i(\vec{x})]^2 \rangle} = \sqrt{\langle [I_i(\vec{x}) - I_{i-1}(\vec{x})]^2 \rangle} \tag{7.5}$$

In equation (7.5) $I_i(x)$ represents the image intensity at pixel *x* on frame *i*. A threshold is applied on FD and DVARS measures, and those frames over the threshold were flagged. After carefully reviewing the plots of the whole population, values of FD>0.001mm and DVARS>3000 were chosen to represent levels above the norm in unmoving pups. A minimum of 80% of each session (~4 minutes) of utilizable PAT data was further required for inclusion in the results below. Non-flagged frames were then concatenated to perform bilateral correlation analysis. No harmful effects have previously been found with the use of discontinuous functional data in previous seed-based resting-state studies (Power et al., 2012; Van Dijk, Sabuncu, & Buckner, 2012). Figure 7-6 shows an example of flagging the frames of suspect quality.

With the unilateral LPS injection we investigated bilateral differences between brain regions so the metric used to evaluate functional connectivity was a regional bilateral functional correlation, defined as the correlation between each seed time-course and its contralateral homologue, yielding six values for each rat pup. The Pearson's coefficient r-values were converted to Fisher Z measures using $Z(r) = \frac{1}{2}\ln[(1+r)/(1-r)]$ before performing the population-level inferences.

7.4.6 Histology

LPS and NaCl-injected brains were fixed after PAT imaging by transcardiac saline perfusion followed by 4% paraformaldehyde. The whole brains were kept at in paraformaldehyde 4°C and transferred to 30% sucrose after twenty-four hours. Cryosections (50µm) were obtained and kept in cryoprotectant solution at -20°C.

7.4.7 Lectin Staining and Vessel Counting

Four consecutive brain slices were chosen from each brain, spanning the injection site for staining and analysis with tetramethylrhodamine isothiocyanate (TRITC)-conjugated lectin to characterise microvasculature (Sirinyan et al., 2006; Zhu et al., 2005). The sections were pre-incubated at room temperature in 1% Triton X-100/PBS for 30 minutes, followed a 2-hour incubation in the same solution with TRITC–conjugated lectin from Griffonia simplicifolia (1:100; Sigma-Aldrich). Brain sections were subsequently subjected to three 10-minute washes with PBS and mounted on microscope slides. Sections were assessed using fluorescent microscopy (20x, Leica DMR with Retiga 1300 Qimaging Camera), and the microvascular skeleton was analyzed by AngioTool (Zudaire, Gambardella, Kurcz, & Vermeren, 2011). This approach was employed rather than a standard quantification of vessel surface. Indeed vessel thickness appearance was modified by the presence of macrophages also stained by lectin in the brains exposed to LPS. Twenty-eight images were taken for each brain covering three regions of interest (left cortex, right cortex and corpus callosum). Each image was then individually processed and analyzed using AngioTool to calculate the total and average skeleton lengths of microvessels in the regions of interests.

7.4.8 Statistical analysis

Statistical significance in imaging and in microvasculature morphometry measures was evaluated using Wilcoxon-Mann-Whitney test. Since histology and locoregional SO_2 measures were performed over only a few *a priori* planned regions, correcting for multiple comparisons was not done, according to recommendations from the literature (Rothman, 1990; Saville, 1990). For seed based connectivity, a false discovery rate (FDR) multiple comparisons test was applied (Benjamini & Hochberg, 1995). FDR-adjusted p-values were then considered significant at $p<0.05$. In order to find out if gender was a confounding factor, a Fisher's exact mid-P method was used (Thorvaldsen, Flå, & Willassen, 2010). All data are presented as mean ± standard error of the mean (SEM).

7.5 Results

7.5.1 Locoregional cortical saturation

After removal of four animals due to excessive motion (these animals were not included in the population description above) average SO_2 was measured both on the left cortex (unilateral to LPS injection), the corpus callosum (cc) and on the right cortex. An example of SO_2 weighted image is depicted in Figure 7-2A. Average SO_2 values measured on the left cortex and the corpus callosum significantly decreased in LPS, when compared to sham controls, as shown on Figure 7-2B; more specifically, mean SO_2 in the left cortex changed from 53.3% in the NaCl group to 49.4% in the LPS group ($p=0.0203$). In the corpus callosum, mean SO_2decreased from 50.1% in the NaCl group to 40.4% in the LPS group ($p=0.0002$). Figure 7-2B also shows no significant SO_2 differences ($p=0.2060$) on the right cortex (contralateral to the injection site). The association between gender and locoregional SO_2 values was not statistically significant ($p=0.1089$).

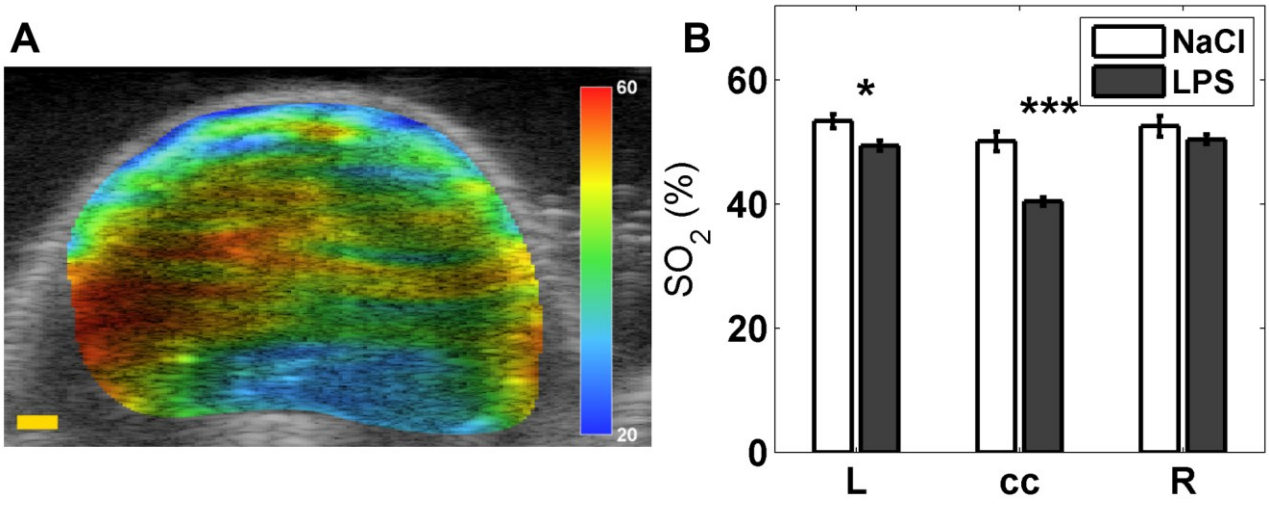

Figure 7-2: Locoregional cortical saturation (SO_2%) (A) Average SO_2 weighted PAT image, scale bar: 1mm (B)SO_2 Comparison performed between LPS group (N=11), and NaCl (sham) group (N=8). SO_2 showed significant decrease in the LPS group compared to NaCl group in left cortex (L) and corpus callosum (cc). The hemisphere contralateral (R) to injection showed no difference. *P<0.05, ***P<0.001.

7.5.2 Microvascular quantification

We analyzed changes in vessel lengths in rat pup brains post LPS injection using lectin fluorescent staining due to its sensitivity in detecting microvessels (Zhu et al., 2005). We found that the average length of microvessels in the left cortex of the LPS injected brains were greatly reduced compared with the saline injected brains (p=0.0093 ; Figure 7-3). We found no statistical difference in microvessel length in the right cortex and in the corpus callosum. Moreover, the average microvessels length in the left cortex was positively correlated with locoregional SO_2 values measured with PAT imaging, as shown in Figure 7-4.

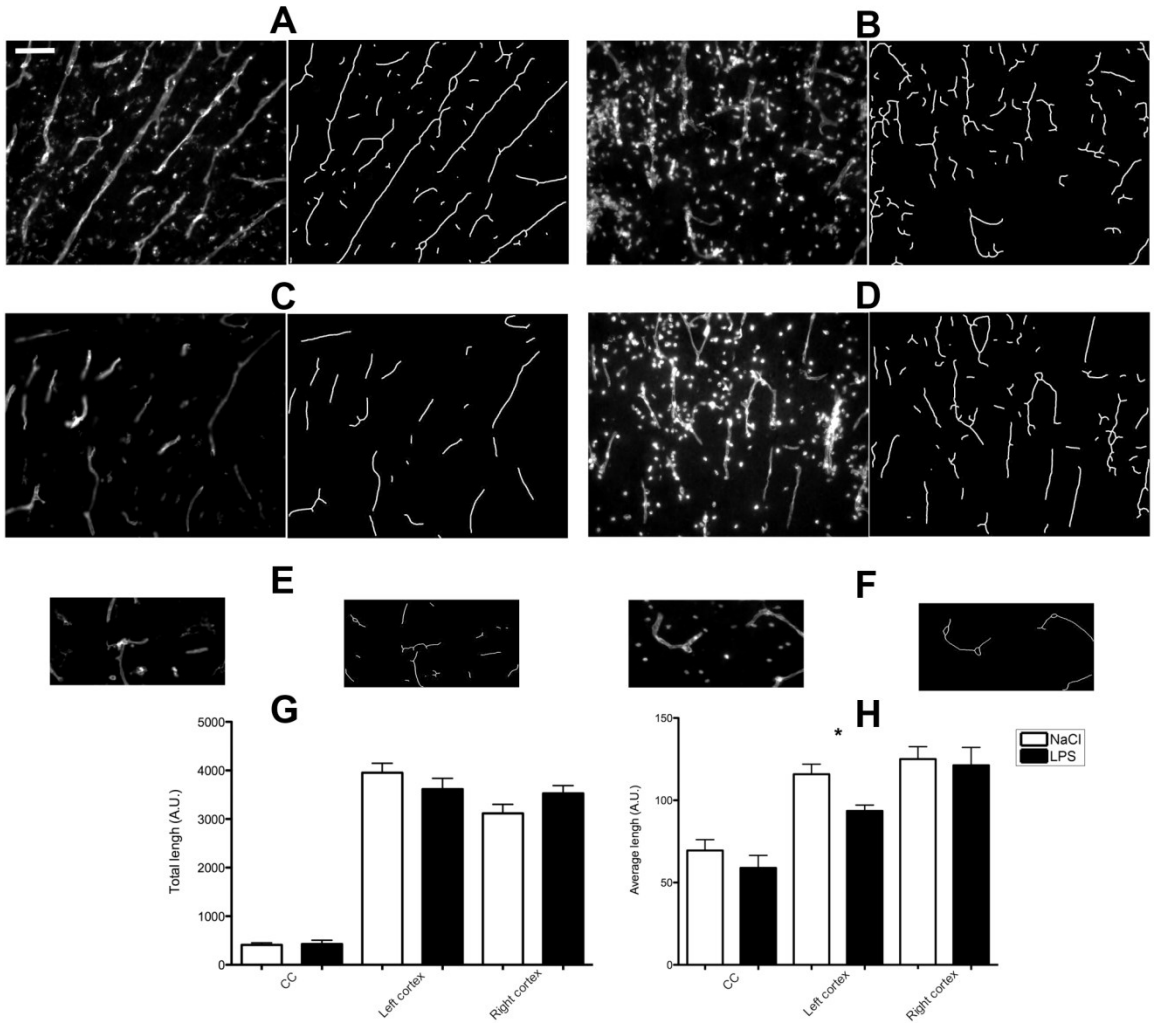

Figure 7-3: TRITC-conjugated lectin staining of brain sections 24h after LPS or saline injection with the associated microvascular skeleton extracted with Angio Tool. A= left cortex; sham, B=left cortex; LPS, C= right cortex; sham, D = right cortex; LPS, E = corpus callosum; sham, F = corpus callosum; LPS. The average microvessel length in the left cortex of brains injected with LPS (B) is greatly reduced compared to brains injected with saline (A). Bar graphs of total microvessel length (G) and average microvessel length (H) in rat brain sections over the cortex and corpus callosum using the skeleton technique with AngioTool. Note the significant decrease in average microvessel length on the left cortex in brains injected with LPS (* $p = 0.0093$). Scale bar =100 μm.

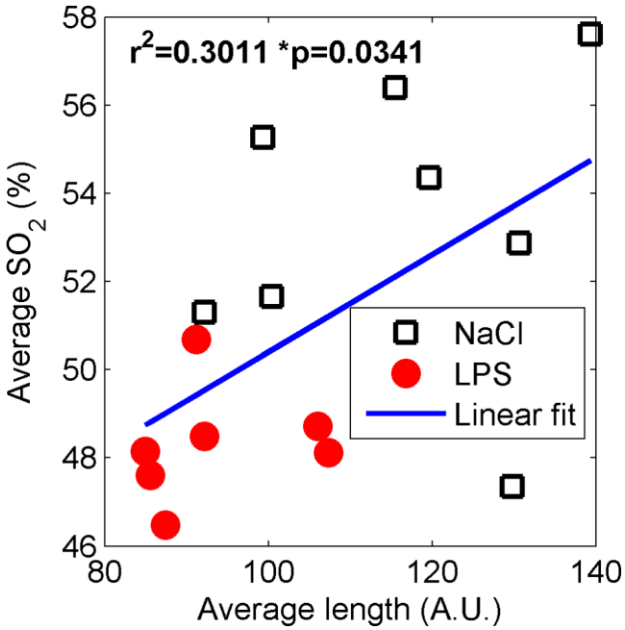

Figure 7-4: In the cortex ipsilateral to the LPS injection locoregional SO_2 measures are positively correlated with average vessel length.

7.5.3 Seed-based functional connectivity

After scrubbing, a total of four scans were removed from the study due to excessive motion; (the same animals removed for computing locoregional SO_2). The results displayed in Figure 7-5 show bilateral fc values getting smaller in seed pairs located farther from the top of the head. There was no statistical difference between both groups in all contrasts (SO_2, HbT, HbO_2 and HbR) though some displayed a consistent trend towards increased connectivity in the LPS group (HbT).

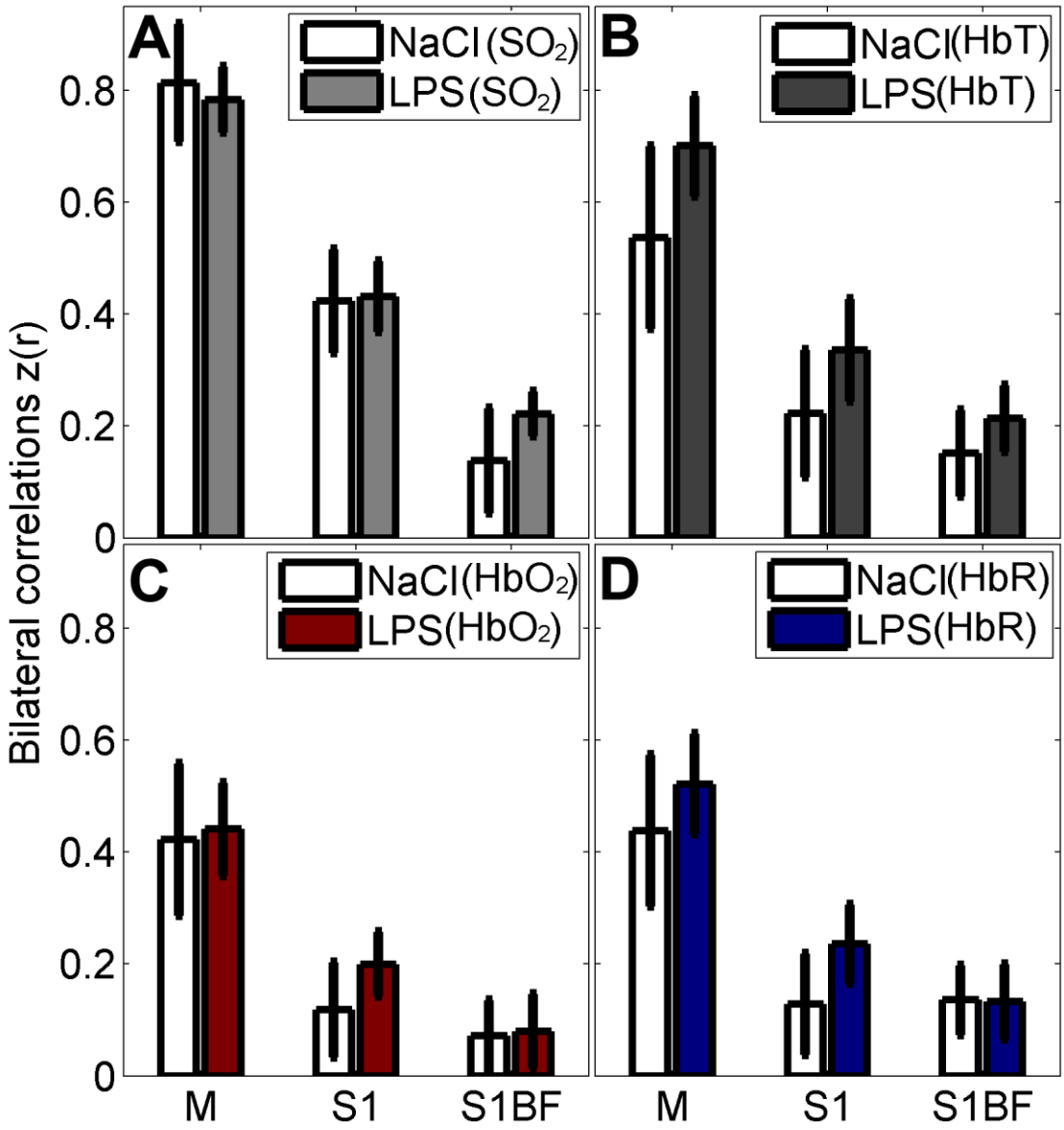

Figure 7-5: Regional bilateral functional correlation, comparison performed between LPS group (N=11), and NaCl (sham) group (N=8); analysis done for every seed time-trace and its contralateral part. Contrasts shown: (A) SO_2, (B) HbT (C) HbO_2 and (D) HbR. Abbreviations: (M, motor cortex; S1, primary somatosensory cortex; S1BF, barrel field primary somatosensory cortex).

7.6 Discussion

7.6.1 Locoregional cortical saturation

Locoregional SO_2 in both corpus callosum and on the cortex ipsilateral to the injection site were lower in the injured group, as compared to the sham group. This result coincides with lower regional cerebral tissue oxygen saturation found in preterm infants with transient PVL (Verhagen, Keating, ter Horst, Martijn, & Bos, 2009). To understand if there was any anatomic substrate for these findings we studied the impact of LPS on microvasculature and found that only the left cortical average microvascular length at the site of injection was reduced. This reduction in average length can be explained by the fragmentation of the microvasculature, as a possible result of the endotoxin ability to damage vascular endothelium (Clawson, Hartmann, & Vernier, 1966; Young, Yagel, & Towfighi, 1983). When assessing the impact of inflammation on the cortex we found a significant correlation between non-invasive PAT measures and histological assessments that explained 30% of the changes between cerebral microvascularisation rarefaction and reduction of saturation. This suggests that meso-scale measures of SO_2, are only partly explained by visible microscopic changes. This reduction in regional saturation especially in the corpus callosum potentially contributes to the white matter injury seen in this model with, apoptosis, necrosis hypomyelination and white matter loss (Cai et al., 2003). The corpus callosum, which had the most significant reduction in saturation, had no measurable change in microvascular content. This might be a reflection of upstream effect of LPS on vascular resistance not evaluated by lectin staining. This underlines the importance of including measures *in vivo* of actual physiological changes not always identified by histology.

Furthermore, these findings support the use of PAT as a non-invasive tool to study PVL animal models; due to its non-invasive and contrast agent-free nature, PAT could be applied to longitudinal studies.

7.6.2 Seed-based functional connectivity

When measuring bi-lateral seed connectivity, there was a strong correlation between the motor ROIs and less so in the S1 and S1BF ROIs and measured correlation values were similar that published in previous studies (Kannurpatti et al., 2008; F. Zhao et al., 2008). Comparing groups, we observed no significant difference on resting state activity following LPS exposure. This

might be explained by the young age of animals and the short interval between LPS exposure and PAT imaging. Previous studies have shown the presence of resting-state networks in preterm infants (from 29 weeks of gestation) (Doria et al., 2010), however the bilateral correlation values in motor and somatosensory cortices were weaker and more variable in the earlier weeks. The marked reduction of resting state activity in preterm infants white matter injury was described at term equivalent (Smyser et al., 2013). Little is known of acute modifications with injury in these infants. Our results thus show that while oxygen saturation is modified with injury between hemispheres, investigating the synchronicity of temporal fluctuations yielded no observable changes. One hypothesis is that the reduction of resting state activity in this population might lead to a large variability of measures across the population. A second hypothesis, which may combine with the first, is that the SNR of PAT imaging was not high enough to measure these small fluctuations homogenously in the brain. Indeed we found a reduction in bilateral correlations in the seeds located farther from the top of the skull attributed to lower SNR values in regions located further from the probe. We believe that resting state evaluation might be limited in these regions due to technical reasons. In future work, we will confirm these findings with rsMRI or invasive optical imaging based on intrinsic signals and laser speckle contrast imaging.

7.7 Conclusions

The results of this exploratory work reveal lower locoregional SO_2 values in LPS group, showing decreased values in the corpus callosum and in the left cortex, ipsilateral to the injection site. Our findings support the use of PAT as a completely non-invasive tool to assess average oxygenation values *in vivo* in the newborn brain.

7.8 Acknowledgements

Research reported in this publication was supported by start-up grant from the Canadian Institutes of Health Research - Institute of Human Development, Child and Youth Health (IHDCYH) #126-790. E. Guevara was supported in part by CONACYT scholarship No. 304501. The authors would like to express their gratitude to the laboratory of Dr. Sylvain Chemtob for the fruitful discussions and advice regarding microvascular quantification. The authors also wish to thank Andrew Needles from Visual Sonics for his technical assistance.

7.9 Author contributions

Conceived and designed the experiments: EG FL GAL. Performed the experiments: EG RB IL NX GAL. Analyzed the data: EG RB IL NX GAL. Contributed reagents/materials/analysis tools: EG RB IL PB. Wrote the paper: EG IL FL GAL.

7.10 References

Benjamini, Y., & Hochberg, Y. (1995). Controlling the false discovery rate: a practical and powerful approach to multiple testing. *Journal of the Royal Statistical Society. Series B. Methodological*, *57*(1), 289–300.

Biswal, B., Yetkin, F. Z., Haughton, V. M., & Hyde, J. S. (1995). Functional connectivity in the motor cortex of resting human brain using echo-planar MRI. *Magnetic resonance in medicine: official journal of the Society of Magnetic Resonance in Medicine / Society of Magnetic Resonance in Medicine*, *34*(4), 537–541.

Blumenthal, I. (2004). Periventricular leucomalacia: a review. *European journal of pediatrics*, *163*(8), 435–442. doi:10.1007/s00431-004-1477-y

Boas, D. A., Gaudette, T., Strangman, G., Cheng, X., Marota, J. J., & Mandeville, J. B. (2001). The accuracy of near infrared spectroscopy and imaging during focal changes in cerebral hemodynamics. *NeuroImage*, *13*(1), 76–90. doi:10.1006/nimg.2000.0674

Born, A. P., Miranda, M. J., Rostrup, E., Toft, P. B., Peitersen, B., Larsson, H. B., & Lou, H. C. (2000). Functional magnetic resonance imaging of the normal and abnormal visual system in early life. *Neuropediatrics*, *31*(1), 24–32. doi:10.1055/s-2000-15402

Born, P., Leth, H., Miranda, M. J., Rostrup, E., Stensgaard, A., Peitersen, B., … Lou, H. C. (1998). Visual activation in infants and young children studied by functional magnetic resonance imaging. *Pediatric research*, *44*(4), 578–583. doi:10.1203/00006450-199810000-00018

Cai, Z., Pang, Y., Lin, S., & Rhodes, P. G. (2003). Differential roles of tumor necrosis factor-alpha and interleukin-1 beta in lipopolysaccharide-induced brain injury in the neonatal rat. *Brain research*, *975*(1-2), 37–47.

Choi, E.-K., Park, D., Kim, T. K., Lee, S. H., Bae, D.-K., Yang, G., … Kim, Y.-B. (2011). Animal models of periventricular leukomalacia. *Laboratory animal research*, *27*(2), 77–84. doi:10.5625/lar.2011.27.2.77

Church, J. A., Fair, D. A., Dosenbach, N. U. F., Cohen, A. L., Miezin, F. M., Petersen, S. E., & Schlaggar, B. L. (2009). Control networks in paediatric Tourette syndrome show immature and anomalous patterns of functional connectivity. *Brain: a journal of neurology*, *132*(Pt 1), 225–238. doi:10.1093/brain/awn223

Clawson, C. C., Hartmann, J. F., & Vernier, R. L. (1966). Electron microscopy of the effect of gram-negative endotoxin on the blood-brain barrier. *The Journal of comparative neurology*, *127*(2), 183–198. doi:10.1002/cne.901270204

Dalitz, P., Harding, R., Rees, S. M., & Cock, M. L. (2003). Prolonged reductions in placental blood flow and cerebral oxygen delivery in preterm fetal sheep exposed to endotoxin: possible factors in white matter injury after acute infection. *Journal of the Society for Gynecologic Investigation*, *10*(5), 283–290.

Damaraju, E., Phillips, J. R., Lowe, J. R., Ohls, R., Calhoun, V. D., & Caprihan, A. (2010). Resting-state functional connectivity differences in premature children. *Frontiers in systems neuroscience*, *4*. doi:10.3389/fnsys.2010.00023

Dammann, O., Kuban, K. C. K., & Leviton, A. (2002). Perinatal infection, fetal inflammatory response, white matter damage, and cognitive limitations in children born preterm. *Mental Retardation and Developmental Disabilities Research Reviews*, *8*(1), 46–50. doi:10.1002/mrdd.10005

Dammann, O., & Leviton, A. (2004). Inflammatory brain damage in preterm newborns—dry numbers, wet lab, and causal inferences. *Early Human Development*, *79*(1), 1–15. doi:10.1016/j.earlhumdev.2004.04.009

Doria, V., Beckmann, C. F., Arichi, T., Merchant, N., Groppo, M., Turkheimer, F. E., … Edwards, A. D. (2010). Emergence of resting state networks in the preterm human brain. *Proceedings of the National Academy of Sciences*, *107*(46), 20015–20020. doi:10.1073/pnas.1007921107

Duncan, J. R., Cock, M. L., Suzuki, K., Scheerlinck, J.-P. Y., Harding, R., & Rees, S. M. (2006). Chronic endotoxin exposure causes brain injury in the ovine fetus in the absence of hypoxemia. *Journal of the Society for Gynecologic Investigation*, *13*(2), 87–96. doi:10.1016/j.jsgi.2005.12.003

Ephrat, P., Needles, A., Bilan, C., Trujillo, A., Theodoropoulos, C., Hirson, D., & Foster, S. (2012). *Photoacoustic Imaging of Murine Tumors Using the Vevo® 2100 Micro-Ultrasound System* (White Paper No. Ver 1.0) (p. 14). Toronto, ON, Canada: VisualSonics Inc. Retrieved from http://www.visualsonics.com/online-file-request.php?f=media&p=WP_2100_Cb_Photoacoustic_Imaging_ver1.0.pdf

Fox, M. D., Zhang, D., Snyder, A. Z., & Raichle, M. E. (2009). The Global Signal and Observed Anticorrelated Resting State Brain Networks. *Journal of Neurophysiology*, *101*(6), 3270–3283. doi:10.1152/jn.90777.2008

Fransson, P., Skiöld, B., Horsch, S., Nordell, A., Blennow, M., Lagercrantz, H., & Aden, U. (2007). Resting-state networks in the infant brain. *Proceedings of the National Academy of Sciences of the United States of America*, *104*(39), 15531–15536. doi:10.1073/pnas.0704380104

Friston, K. J., Ashburner, J. T., Kiebel, S. J., Nichols, T. E., & Penny, W. D. (2006). *Statistical Parametric Mapping: The Analysis of Functional Brain Images* (1st ed.). Great Britain: Academic Press. Retrieved from http://www.fil.ion.ucl.ac.uk/spm/

Guevara, E., Pouliot, P., Nguyen, D. K., & Lesage, F. (2013). Optical imaging of acute epileptic networks in mice. *Journal of Biomedical Optics*, *18*(7), 076021–076021. doi:10.1117/1.JBO.18.7.076021

Hagberg, H., Mallard, C., & Jacobsson, B. (2005). Role of cytokines in preterm labour and brain injury. *BJOG: An International Journal of Obstetrics & Gynaecology*, *112*, 16–18. doi:10.1111/j.1471-0528.2005.00578.x

Honoré, J.-C., Kooli, A., Hamel, D., Alquier, T., Rivera, J.-C., Quiniou, C., … Chemtob, S. (2013). Fatty acid receptor Gpr40 mediates neuromicrovascular degeneration induced by transarachidonic acids in rodents. *Arteriosclerosis, thrombosis, and vascular biology*, *33*(5), 954–961. doi:10.1161/ATVBAHA.112.300943

Jonckers, E., Van Audekerke, J., De Visscher, G., Van der Linden, A., & Verhoye, M. (2011). Functional Connectivity fMRI of the Rodent Brain: Comparison of Functional Connectivity Networks in Rat and Mouse. *PLoS ONE*, *6*(4), e18876. doi:10.1371/journal.pone.0018876

Kannurpatti, S. S., Biswal, B. B., Kim, Y. R., & Rosen, B. R. (2008). Spatio-temporal characteristics of low-frequency BOLD signal fluctuations in isoflurane-anesthetized rat brain. *NeuroImage*, *40*(4), 1738–1747. doi:10.1016/j.neuroimage.2007.05.061

Liu, W.-C., Flax, J. F., Guise, K. G., Sukul, V., & Benasich, A. A. (2008). Functional connectivity of the sensorimotor area in naturally sleeping infants. *Brain research*, *1223*, 42–49. doi:10.1016/j.brainres.2008.05.054

Lodygensky, G. A., West, T., Stump, M., Holtzman, D. M., Inder, T. E., & Neil, J. J. (2010). In vivo MRI analysis of an inflammatory injury in the developing brain. *Brain, Behavior, and Immunity*, *24*(5), 759–767. doi:10.1016/j.bbi.2009.11.005

Murphy, K., Birn, R. M., Handwerker, D. A., Jones, T. B., & Bandettini, P. A. (2009). The impact of global signal regression on resting state correlations: Are anti-correlated networks introduced? *NeuroImage*, *44*(3), 893–905. doi:10.1016/j.neuroimage.2008.09.036

O'Leary, M. A., Boas, D. A., Chance, B., & Yodh, A. G. (1995). Experimental images of heterogeneous turbid media by frequency-domain diffusing-photon tomography. *Optics Letters*, *20*(5), 426–428. doi:10.1364/OL.20.000426

Pang, Y., Cai, Z., & Rhodes, P. G. (2003). Disturbance of oligodendrocyte development, hypomyelination and white matter injury in the neonatal rat brain after intracerebral injection of lipopolysaccharide. *Brain research. Developmental brain research*, *140*(2), 205–214.

Paxinos, G., & Watson, C. (2007). *The rat brain in stereotaxic coordinates* (6th ed.). London, UK: Academic Press.

Power, J. D., Barnes, K. A., Snyder, A. Z., Schlaggar, B. L., & Petersen, S. E. (2012). Spurious but systematic correlations in functional connectivity MRI networks arise from subject motion. *NeuroImage*, *59*(3), 2142–2154. doi:10.1016/j.neuroimage.2011.10.018

Ramachandra, R., & Subramanian, T. (2011). *Atlas of the Neonatal Rat Brain* (1st ed.). CRC Press.

Rothman, K. J. (1990). No adjustments are needed for multiple comparisons. *Epidemiology (Cambridge, Mass.)*, *1*(1), 43–46.

Saville, D. J. (1990). Multiple Comparison Procedures: The Practical Solution. *The American Statistician*, *44*(2), 174. doi:10.2307/2684163

Seghier, M. L., Lazeyras, F., & Huppi, P. S. (2006). Functional MRI of the newborn. *Seminars in fetal & neonatal medicine*, *11*(6), 479–488. doi:10.1016/j.siny.2006.07.007

Sirinyan, M., Sennlaub, F., Dorfman, A., Sapieha, P., Gobeil, F., Jr, Hardy, P., … Chemtob, S. (2006). Hyperoxic exposure leads to nitrative stress and ensuing microvascular degeneration and diminished brain mass and function in the immature subject. *Stroke; a journal of cerebral circulation*, *37*(11), 2807–2815. doi:10.1161/01.STR.0000245082.19294.ff

Sizonenko, S. V., Sirimanne, E., Mayall, Y., Gluckman, P. D., Inder, T., & Williams, C. (2003). Selective cortical alteration after hypoxic-ischemic injury in the very immature rat brain. *Pediatric research*, *54*(2), 263–269. doi:10.1203/01.PDR.0000072517.01207.87

Smyser, C. D., Inder, T. E., Shimony, J. S., Hill, J. E., Degnan, A. J., Snyder, A. Z., & Neil, J. J. (2010). Longitudinal analysis of neural network development in preterm infants. *Cerebral cortex (New York, N.Y.: 1991)*, *20*(12), 2852–2862. doi:10.1093/cercor/bhq035

Smyser, C. D., Snyder, A. Z., & Neil, J. J. (2011). Functional Connectivity MRI in Infants: Exploration of the Functional Organization of the Developing Brain. *NeuroImage*, *56*(3), 1437–1452. doi:10.1016/j.neuroimage.2011.02.073

Smyser, C. D., Snyder, A. Z., Shimony, J. S., Blazey, T. M., Inder, T. E., & Neil, J. J. (2013). Effects of white matter injury on resting state FMRI measures in prematurely born infants. *PloS one*, *8*(7), e68098. doi:10.1371/journal.pone.0068098

Thorvaldsen, S., Flå, T., & Willassen, N. P. (2010). DeltaProt: a software toolbox for comparative genomics. *BMC Bioinformatics*, *11*(1), 573. doi:10.1186/1471-2105-11-573

Van Dijk, K. R. A., Sabuncu, M. R., & Buckner, R. L. (2012). The influence of head motion on intrinsic functional connectivity MRI. *NeuroImage*, *59*(1), 431–438. doi:10.1016/j.neuroimage.2011.07.044

Verhagen, E. A., Keating, P., ter Horst, H. J., Martijn, A., & Bos, A. F. (2009). Cerebral oxygen saturation and extraction in preterm infants with transient periventricular echodensities. *Pediatrics*, *124*(1), 294–301. doi:10.1542/peds.2008-2057

Wang, K.-C., Fan, L.-W., Kaizaki, A., Pang, Y., Cai, Z., & Tien, L.-T. (2013). Neonatal lipopolysaccharide exposure induces long-lasting learning impairment, less anxiety-like response and hippocampal injury in adult rats. *Neuroscience*, *234*, 146–157. doi:10.1016/j.neuroscience.2012.12.049

Wang, L. V., & Hu, S. (2012). Photoacoustic Tomography: In Vivo Imaging from Organelles to Organs. *Science*, *335*(6075), 1458–1462. doi:10.1126/science.1216210

Wang, X., Pang, Y., Ku, G., Xie, X., Stoica, G., & Wang, L. V. (2003). Noninvasive laser-induced photoacoustic tomography for structural and functional in vivo imaging of the brain. *Nature Biotechnology*, *21*(7), 803–806. doi:10.1038/nbt839

Wang, X., Xie, X., Ku, G., Wang, L. V., & Stoica, G. (2006). Noninvasive imaging of hemoglobin concentration and oxygenation in the rat brain using high-resolution photoacoustic tomography. *Journal of biomedical optics*, *11*(2), 024015. doi:10.1117/1.2192804

White, B. R., Bauer, A. Q., Snyder, A. Z., Schlaggar, B. L., Lee, J.-M., & Culver, J. P. (2011). Imaging of functional connectivity in the mouse brain. *PloS one*, *6*(1), e16322. doi:10.1371/journal.pone.0016322

Xiang, L., Ji, L., Zhang, T., Wang, B., Yang, J., Zhang, Q., … Jiang, H. (2012). Noninvasive real time tomographic imaging of epileptic foci and networks. *NeuroImage*, *66C*, 240–248. doi:10.1016/j.neuroimage.2012.10.077

Young, R. S. K., Yagel, S. K., & Towfighi, J. (1983). Systemic and Neuropathologic Effects of E. coli Endotoxin in Neonatal Dogs. *Pediatric Research*, *17*(5), 349–353. doi:10.1203/00006450-198305000-00008

Zhao, F., Zhao, T., Zhou, L., Wu, Q., & Hu, X. (2008). BOLD study of stimulation-induced neural activity and resting-state connectivity in medetomidine-sedated rat. *NeuroImage*, *39*(1), 248–260. doi:10.1016/j.neuroimage.2007.07.063

Zhu, Y., Lee, C., Shen, F., Du, R., Young, W. L., & Yang, G.-Y. (2005). Angiopoietin-2 facilitates vascular endothelial growth factor-induced angiogenesis in the mature mouse brain.

Stroke; a journal of cerebral circulation, *36*(7), 1533–1537. doi:10.1161/01.STR.0000170712.46106.2e

Zudaire, E., Gambardella, L., Kurcz, C., & Vermeren, S. (2011). A computational tool for quantitative analysis of vascular networks. *PloS one*, *6*(11), e27385. doi:10.1371/journal.pone.0027385

7.11 Supplemental figures

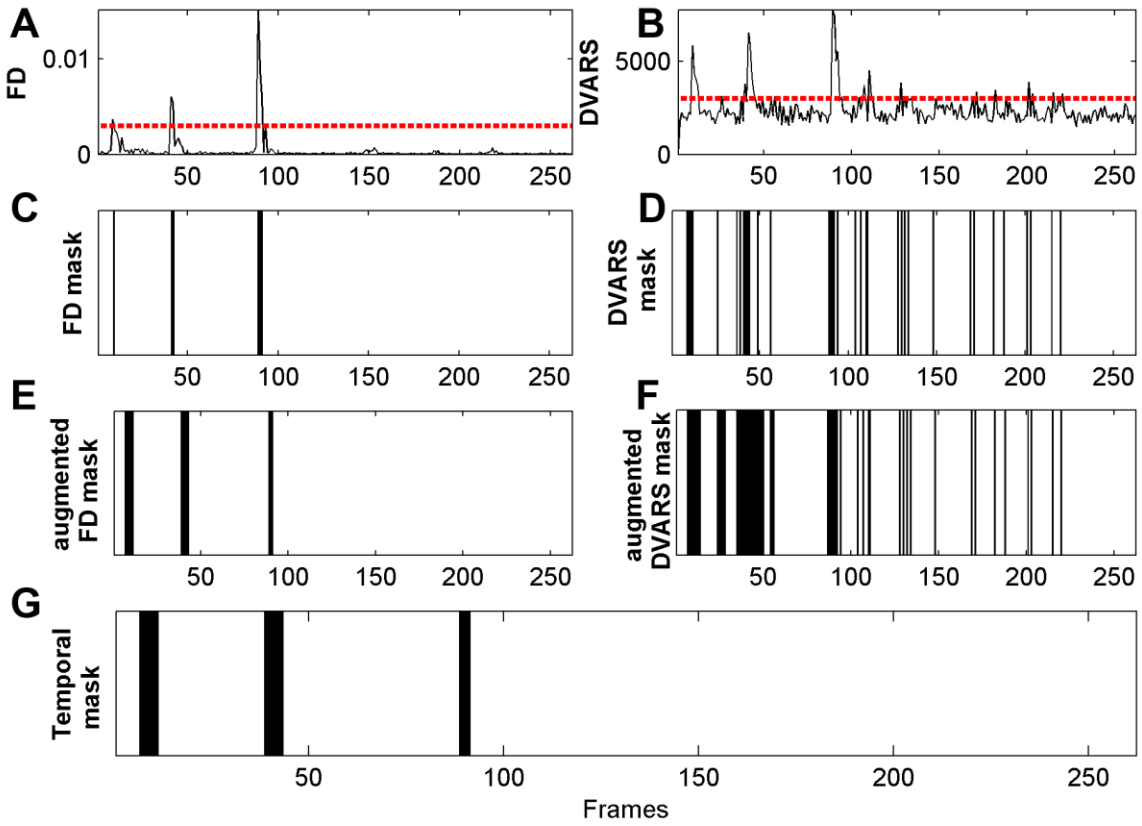

Figure 7-6: Framewise indices of data quality, the dotted line in insets A and B represents the threshold to signal suspect frames: (A) Framewise displacement (FD) of head position and (B) DVARS measure. All frames surpassing the threshold in FD and DVARS time courses are flagged, generating a temporal mask: (C)Frames flagged as having a FD>0.001mm and (D)Frames flagged as having a DVARS>3000. These temporal masks are augmented by also marking 1 frame back and 2 frames forward to accommodate temporal smoothing of PAT data: (E)Augmented FD mask and (F) Augmented DVARS mask. (G) Temporal mask comprised of the intersection of E and F.

CHAPTER 8 GENERAL DISCUSSION

Functional connectivity in resting state has been used as an investigative diagnostic tool for over a decade; it has been carried out with a variety of techniques either for direct or indirect assessment of neural activity. The numerous theoretical and empirical advantages of this modality make it a strong candidate as a diagnostic tool. Hence our motivation to explore functional connectivity in a more controlled environment, such as rodent models of neurological and cardiovascular conditions. Nevertheless, functional connectivity has not reached its maturity level to be applied in clinical studies, due to a number of reasons.

In this work, correlated fluctuations of hemodynamic signals between brain regions have been interpreted as a marker of functional connectivity. The presented results suggest that the resting-state patterns have spatial characteristics that qualitatively resemble activation patterns and functional zones delineated in the literature (Fonoff et al., 2009; Watson, Paxinos, & Puelles, 2011). Although direct recordings of neural activity suggest that these oscillations arise from underlying spontaneous neural activity, we have to keep in mind several confounding factors, from instrument noise to motion and physiological fluctuations. These results do not imply that the resting-state spatial patterns are of neuronal origin, they may be related to local changes in physiology, such as the vasculature. Further studies are required to characterize the influence of physiological processes to the functional connectivity findings.

8.1 Article 1

In the study presented in CHAPTER 5 an animal model of epilepsy was used to investigate if induced seizure activity alters regional resting-state connectivity. Epileptic seizures were induced by the unilateral injection of 4-AP on the somatosensory cortex. A combination of optical intrinsic signal imaging and laser speckle imaging was used to monitor cerebral oxygenation and blood flow. These measures were also combined to investigate changes in cerebral metabolism. Overall the methodology aims to be an integral approach, as the combination of the two optical techniques provides a more complete picture of the hemodynamic and metabolic responses to epilepsy than could be achieved with fMRI, which is most sensitive to changes in HbR.

The results indicate that the changes in HbO_2, HbR and CBF connectivity are quite different, suggesting a decoupling of metabolism and hemodynamics. This finding appeals to be of interest

to the neuroimaging community considering the growing interest in using resting-state fMRI in epilepsy research.

8.1.1 Regional bilateral functional connectivity is disrupted after the injection of a focal epileptogenic agent.

Bilateral functional connectivity was diminished in some contrasts and augmented in others, also depending on the observed region. This lack of consistency can be explained in part by several confounding factors that cannot be left out of the analysis. First, the variability in the injection of 4-AP: although the injection site was carefully chosen, there is inherent variability in the exact position and depth due to the manual positioning. Furthermore, diffusion of the injected volume will vary due to tortuosity of the brain tissue in each mouse (Nicholson, 1985). These limitations may explain the fact that only five out of nine mice presented seizure-like activity.

A second drawback was the heterogeneity of the correlation maps, due mostly to the position of the tungsten electrode after the injection. Nevertheless, this extraneous object provides precious information about the underlying neural activity, allowing us to confirm the type of epileptiform activity.

8.1.2 Changes in functional connectivity correlate with seizure duration.

Our hypothesis stated that the longer the seizure duration the more disrupted connectivity. Strong correlations were not found in all regions or in all contrasts because of large variability between the animals, and the relatively few mice who presented clear seizure-like activity (five out of nine). However two of the six explored cortical zones did show a significant correlation in agreement with our hypothesis: 1) The somatosensory cortex, where connectivity decrease correlated with seizure duration, in the case of CBF contrast and 2) the retrosplenial region, where the connectivity decrease was also correlated with seizure duration, in both HbR and CBF contrasts. The results in somatosensory cortex are mainly explained by the unilateral injection of the neurotoxin precisely on the left cortex. However the interpretation of the results in the retrosplenial region remains difficult, due to the close proximity of the sagittal sinus to the seeds, there is a large contribution from vascular components to the measurements.

8.2 Article 2

This article is included in CHAPTER 6, the objective of this work was to use functional connectivity methods to investigate connectivity changes induced by a novel carotid stiffness murine model.

8.2.1 Uncoupling is shown between hemodynamic measures and metabolic activity in bilateral functional correlations.

The lack of consistency in the results suggested an uncoupling between HbO_2, HbR, CBF and $CMRO_2$ bilateral correlations. In a previous work (Sadekova et al., 2013) we found that the side of the brain corresponding to the calcified carotid artery showed a significant increase in flow pulsatility after the application of $CaCl_2$. There was also evidence of neural degeneration in the hippocampus. Therefore, a vascular component independent of metabolism and localized neural degeneration potentially affecting connectivity may explain why different contrasts go in different directions.

8.2.2 Resting state functional networks derived from hemodynamic signals are disrupted following a unilateral carotid artery calcification.

The motor zone ipsilateral to the calcified carotid was the most affected. In this particular node, a measure of influence, betweenness centrality coefficient $CB_n(G)$ was increased in the $CaCl_2$ group, while a measure of segregation clustering coefficient $CC_n(G)$ was decreased. The increased relative importance of this node may be explained by the increased pulsatility in the middle cerebral artery of the same hemisphere. The most evident change was present in the measures derived from $CMRO_2$, where negative edges were found in the $CaCl_2$ group, unlike the positive connections in the control group. Whether this disruption has a neural origin (neural degeneration in the hippocampus) or a vascular origin (increased ipsilateral pulsatility) remains an open question.

8.3 Article 3

The last work, presented in CHAPTER 7 aimed to use resting-state photoacoustic tomography (PAT) imaging to assess the impact of an acute inflammatory injury in the neonatal rat brain.

8.3.1 Local SO_2 values are significantly lower in the injured group, as compared to sham controls.

The regional cerebral tissue SO_2 significantly decreased in the corpus callosum (LPS injection site) and in the left cortex (ipsilateral to the injection locus), however this reduction was no fully explained by histological evidence. Lectin immunochemistry showed fragmented vessels only on the left cortex but not on the corpus callosum. This finding may support the need of PAT imaging as complementary information to histological analyses; however there are some factors that might explain the lack of consistency. First, the spatial differences between the analyzed ROIs in vivo and the portion of tissue examined *ex vivo*; even with anatomical markers (such as the position of the lateral ventricles) the extent of tissue slices may not be an exact correspondence to the chosen ROIs, explaining thus the mismatch. Second, the poor vascularization of the corpus callosum may hamper the technique to quantify microvasculature. Finally, since not all brains were processed for histology, the smaller size of the sample for lectin analysis is another clear limitation.

8.3.2 Bilateral functional connectivity decreases significantly in pups with inflammatory brain injury.

No differences were found in the injured group as compared to shams. This may be explained by the absence of resting-state networks in very premature pups or the presence of intact RSNs even in the absence of corpus callosum. However, instrument noise is clearly one of the limitations of the technique. Even after the removal of several confounding factors no differences were found in connectivity between groups. The large amount of within-group variability did not allow the extraction of meaningful results. The use of PAT as a noninvasive, depth-sensitive technology is better suited to extract information averaged over large voxel regions with multiple measures, in order to minimize the effect of noise.

CONCLUSION AND RECOMMENDATIONS

In this thesis a variety of functional connectivity techniques with optical imaging has been applied to study the effects of diseases in the rodent brain. The results suggest that there is a reorganization of the resting-state networks in murine models of epilepsy and arterial stiffness; furthermore, the changes are not consistent across all contrasts, suggesting a potential uncoupling of the hemodynamic parameters and metabolic activity. Finally, functional connectivity using photoacoustics was not affected by the presence of a white matter injury in the newborn brain.

Limitations of the proposed works

Imaging sampling frequency

Removal of physiological confounds is only possible with short enough sampling period (Cordes et al., 2001). In the adult mouse, respiratory frequency-related components (~2Hz under urethane anesthesia) will not artificially appear because of our sufficient sampling rate ($f_s/2$ = 2.5 Hz). However cardiac frequencies (8.3 – 10Hz) will be aliased into the lower frequency range (Suckow, Danneman, & Brayton, 2001).

In the newborn rat, cardiac rate varies between 4 – 6 Hz (Smotherman, Robinson, Ronca, Alberts, & Hepper, 1991) and respiratory frequency is around 2.5 – 2.8 Hz (Kroon et al., 2011; Pendlebury et al., 2008); due to the low sampling rate ($f_s/2$ = 0.45 Hz) of the PAT system we expect these signals to be heavily aliased into the lower frequencies.

Even with adequate sampling rate, there are low-frequency physiological variations that cannot be removed by frequency filtering; such is the case of arterial CO_2 concentration and blood pressure variations which are in the same frequency range as the resting-state fluctuations.

Temporal filtering

The choice of cut-off frequencies of the band-pass filter (0.009 – 0.08 Hz) may not be optimal for the animal models, even though they were chosen from the existing literature in rodent models (Bero et al., 2012; Guilfoyle et al., 2013; Jonckers et al., 2011; Li et al., 2012; Brian R White et al., 2011). However the higher frequencies cannot always be considered to contain only noise; recent studies have shown that useful resting-state neural information is present at 0.2 or even 0.5 Hz (Feinberg et al., 2010; Smith et al., 2013).

Time scale

The optical techniques were used to image the co-variation of hemodynamic activity in distant regions, focused on the slow fluctuations between 12.5 and 111 seconds. Conversely, it is commonly accepted that electrophysiological oscillations can be distinguished within five time-scales, ranging from milliseconds to around one second (Ganzetti & Mantini, 2013). Although power of gamma frequency has been shown to correlate with hemodynamic signal, while remaining spatially coherent (B. J. He et al., 2008). An important step towards a better understanding of functional imaging RSNs should involve evidence from electrophysiological and hemodynamic studies. Multimodal imaging has been used to investigate correlates between neuronal and hemodynamic signals in the brain (B. J. He et al., 2008; Nir et al., 2008; Shmuel et al., 2006).

Head motion

Although movement of the adult mouse is perfectly restrained by the use of a stereotactic frame and urethane anesthesia, this not the case of the newborn rat. Light isoflurane anesthesia together with an imperfect fixation frame allows motion artifacts. It is important to note that the absence of teeth and incomplete ossification of the skull in newborn rats represent a challenge to motion-restriction apparatus.

Removing physiological confounds: When are nuisance regressors one too many?

In this work we have chosen to regress one or more signals, either the average signal from all brain pixels, the deeper white matter, the lateral ventricles or three rigid-body motion parameters. There remains the question if some signal of interest has been removed. This is not the case for white matter, lateral ventricle or motion parameters, since they are not expected to contain any variance of interest. Nevertheless, the case of the global brain signal is different. It has been shown that global signal regression introduces artificial anti-correlation where there was none (Murphy et al., 2009; Weissenbacher et al., 2009), but some studies show that a neural basis for these anticorrelations is probable (Chai, Castañón, Ongür, & Whitfield-Gabrieli, 2012; Fox et al., 2009). The use of global signal regression is still open to debate and depends on further investigations (Smith et al., 2013), however it is not recommended by some recent studies (Murphy, Birn, & Bandettini, 2013).

Noisy measurements

The main proof of resting-state networks unraveled by seed-based fc analyses is the similarity of correlation maps to specific functional areas delineated in the cortex. When looking at HbO_2 and HbR data this similarity is very evident, but it is not the case for all the contrasts. Fc maps obtained from CBF measures do not show a striking resemblance to definite functional areas, in fact due to spatio-temporal noise only the pixels around the seed are strongly correlated; this issue makes CBF maps of sub-optimal quality and therefore the derived $CMRO_2$ data. In the opinion of the author this drawback may limit the use of LSCI as a tool for functional connectivity studies.

Effects of anesthesia in resting-state networks

Resting-state networks in the rodent have been unraveled under different anesthetic agents, suggesting that coherent spontaneous fluctuations in the brain transcend the state of consciousness. Medetomidine hydrochloride has been shown to give consistent results in functional connectivity studies in rodents (Pawela et al., 2008; F. Zhao et al., 2008), as well as Ketamine/Xylazine (Bero et al., 2012; Brian R White et al., 2011), chloral hydrate/urethane (Li et al., 2012) and isoflurane (Guilfoyle et al., 2013). A recent study showed a significant decrease in connectivity strength in the anesthetized rat brain (Liang, King, & Zhang, 2012), although the topological features on the whole-brain were well maintained. Nevertheless, all anesthetics alter cerebral blood flow and metabolism and their impact in functional connectivity is not yet fully understood.

Future improvements

Increase imaging sampling rate

In order to mitigate or even suppress aliasing of respiratory and cardiac frequencies, improvements on the OIS/LSCI setup could be made; since frame rate was mainly limited by the speed of data streaming to disk the most straightforward improvement would be switching to a computer with faster bus frequency and saving data to a solid-state disk. In theory, the maximal frame rate of the system could be achieved ($f_s/2 = 10Hz$), thus suppressing aliasing.

Optimizing CBF measures

Accurate estimation of speckle contrast depends on a variety of parameters, speckle size, window size, integration time and camera noise. In this work, the effect of window size on the speckle

images was tested for different window sizes, from 5 to 11 pixels, in close agreement with the optimal size (7×7 pixels) found in the literature (Boas & Dunn, 2010). The actual size of the window had a negligible effect in the final correlation maps. The camera aperture was chosen to match the speckle size with pixel size, but a test could be made to empirically choose the best aperture. In a particular experimental setup the speckle contrast is measured as a function of the camera aperture, then the optimal aperture is chosen where the speckle contrast is maximum. The integration time was also chosen to be close to the decorrelation time in rodents (S. Yuan, Devor, Boas, & Dunn, 2005), but a test to determine of the optimal integration time yielding the highest speckle contrast should be performed. A similar test can be run to find the optimal camera gain.

Limiting newborn head motion

Given the light condition of anesthesia in newborn rats, involuntary head motion remains an issue; a redesigned frame that would effectively impede motion while being harmless to the pup would be an important improvement on the experimental conditions.

Additional cleanup techniques

The removal of physiological confounds can be possible by their simultaneous recording and by following standard regression techniques. Currently the OIS/LSCI system allows recording several variables (ECG, temperature, blood pressure), which could be eventually included as nuisance regressors, a method akin to those used in fMRI (Birn, Diamond, Smith, & Bandettini, 2006). The addition of a synchronized physiological monitoring device to the PAT system would also enable the inclusion of this cleanup technique.

Reduce spatial variability in seeds placement

Although manual placement of the seeds for each subject has advantages, e.g. to avoid large vessels it can be cumbersome and introduce variability to our studies. The addition of a pre-processing stage where all the images would be aligned to an atlas would simplify the individual placement of the seeds, and eliminate the variability due to placement differences in the seeds. Another option would be to acquire an activation dataset along with the resting-state data. Then, place the seeds at the coordinates of the highest activated pixels cluster. This latter option would make a less arbitrary choice for seeds positioning.

Exploring different functional connectivity techniques

Seed-based functional connectivity, despite its relative ease of implementation and interpretation, also possesses several drawbacks, such as the dependence on the *a priori* definitions of seeds. Although the widely applied ICA technique shows similar results to seed-based functional connectivity (Van Dijk et al., 2010), it has some advantages and is worth of exploration. Data-driven techniques such as ICA may be less affected by the physiological confounds, even when these physiological frequencies become aliased into the low-frequency range of the resting state fluctuations (Beckmann et al., 2005).

REFERENCES

Aarabi, A., Wallois, F., & Grebe, R. (2008). Does spatiotemporal synchronization of EEG change prior to absence seizures? *Brain Research*, *1188*, 207–221. doi:10.1016/j.brainres.2007.10.048

Abdelnour, F., Genovese, C., & Huppert, T. (2010). Hierarchical Bayesian regularization of reconstructions for diffuse optical tomography using multiple priors. *Biomedical Optics Express*, *1*(4), 1084–1103. doi:10.1364/BOE.1.001084

Achard, S., & Bullmore, E. (2007). Efficiency and Cost of Economical Brain Functional Networks. *PLoS Comput Biol*, *3*(2), e17. doi:10.1371/journal.pcbi.0030017

Alavi, A., Dann, R., Chawluk, J., Alavi, J., Kushner, M., & Reivich, M. (1986). Positron emission tomography imaging of regional cerebral glucose metabolism. *Seminars in Nuclear Medicine*, *16*(1), 2–34.

Anderton, B. H. (2002). Ageing of the brain. *Mechanisms of Ageing and Development*, *123*(7), 811–817. doi:10.1016/S0047-6374(01)00426-2

Anthonisse, J. M. (1971). *The Rush In A Directed Graph* (CWI Technical Report No. Stichting Mathematisch Centrum. Mathematische Besliskunde-BN 9/71) (pp. 1 – 10). Stichting Mathematisch Centrum. Retrieved from http://oai.cwi.nl/oai/asset/9791/9791A.pdf

Aronson, M. K., Ooi, W. L., Morgenstern, H., Hafner, A., Masur, D., Crystal, H., … Katzman, R. (1990). Women, myocardial infarction, and dementia in the very old. *Neurology*, *40*(7), 1102–1106.

Arridge, S. R., & Hebden, J. C. (1997). Optical imaging in medicine: II. Modelling and reconstruction. *Physics in Medicine and Biology*, *42*(5), 841–854. doi:10.1088/0031-9155/42/5/008

Baraghis, E., Bolduc, V., Lefebvre, J., Srinivasan, V. J., Boudoux, C., Thorin, E., & Lesage, F. (2011). Measurement of cerebral microvascular compliance in a model of atherosclerosis with optical coherence tomography. *Biomedical Optics Express*, *2*(11), 3079–3093. doi:10.1364/BOE.2.003079

Bassett, D. S., & Bullmore, E. (2006). Small-world brain networks. *The Neuroscientist: A Review Journal Bringing Neurobiology, Neurology and Psychiatry*, *12*(6), 512–523. doi:10.1177/1073858406293182

Beaumont, E., Brieu, N., Dubeau, S., & Lesage, F. (2008a). Alteration of the neuronal and vascular response in the lumbar spinal cord 4 weeks after a T10 transection in rat. In *International 38th anual meeting for the Society of Neuroscience (SNF)*. Washington, USA.

Beaumont, E., Brieu, N., Dubeau, S., & Lesage, F. (2008b). Characterization of the hemodynamic and metabolic response in the in-vivo rat lumbar spinal cord by intrinsic imaging. In *3rd National spinal cord injury conference*. Toronto, Canada.

Beaumont, E., Guevara, E., Dubeau, S., Lesage, F., Nagai, M., & Popovic, M. R. (2013). Functional electrical stimulation post spinal cord injury improves locomotion and increases afferent input into the central nervous system in rats. *Journal of Spinal Cord Medicine*. doi:http://dx.doi.org/10.1179/2045772313Y.0000000117

Beckmann, C. F., DeLuca, M., Devlin, J. T., & Smith, S. M. (2005). Investigations into resting-state connectivity using independent component analysis. *Philosophical Transactions of the Royal Society B: Biological Sciences*, *360*(1457), 1001–1013. doi:10.1098/rstb.2005.1634

Belanger, S., Abran, M., Intes, X., Casanova, C., & Lesage, F. (2010). Real-time diffuse optical tomography based on structured illumination. *Journal of Biomedical Optics*, *15*(1), 016006–7. doi:10.1117/1.3290818

Belliveau, J. W., Kennedy, D. N., Jr, McKinstry, R. C., Buchbinder, B. R., Weisskoff, R. M., Cohen, M. S., … Rosen, B. R. (1991). Functional mapping of the human visual cortex by magnetic resonance imaging. *Science (New York, N.Y.)*, *254*(5032), 716–719.

Benjamini, Y., & Hochberg, Y. (1995). Controlling the false discovery rate: a practical and powerful approach to multiple testing. *Journal of the Royal Statistical Society. Series B. Methodological*, *57*(1), 289–300.

Benveniste, H., & Blackband, S. (2002). MR microscopy and high resolution small animal MRI: applications in neuroscience research. *Progress in Neurobiology*, *67*(5), 393–420.

Bero, A. W., Bauer, A. Q., Stewart, F. R., White, B. R., Cirrito, J. R., Raichle, M. E., … Holtzman, D. M. (2012). Bidirectional Relationship between Functional Connectivity and Amyloid-β Deposition in Mouse Brain. *The Journal of Neuroscience*, *32*(13), 4334–4340. doi:10.1523/JNEUROSCI.5845-11.2012

Bettus, G., Ranjeva, J.-P., Wendling, F., Bénar, C. G., Confort-Gouny, S., Régis, J., … Guye, M. (2011). Interictal Functional Connectivity of Human Epileptic Networks Assessed by

Intracerebral EEG and BOLD Signal Fluctuations. *PLoS ONE*, *6*(5), e20071. doi:10.1371/journal.pone.0020071

Bettus, G., Wendling, F., Guye, M., Valton, L., Régis, J., Chauvel, P., & Bartolomei, F. (2008). Enhanced EEG functional connectivity in mesial temporal lobe epilepsy. *Epilepsy Research*, *81*(1), 58–68. doi:10.1016/j.eplepsyres.2008.04.020

Bevilacqua, F., Piguet, D., Marquet, P., Gross, J. D., Tromberg, B. J., & Depeursinge, C. (1999). In Vivo Local Determination of Tissue Optical Properties: Applications to Human Brain. *Appl. Opt.*, *38*(22), 4939–4950.

Bifone, A., Gozzi, A., & Schwarz, A. J. (2010). Functional connectivity in the rat brain: a complex network approach. *Magnetic Resonance Imaging*, *28*(8), 1200–1209. doi:10.1016/j.mri.2010.07.001

Birn, R. M., Diamond, J. B., Smith, M. A., & Bandettini, P. A. (2006). Separating respiratory-variation-related fluctuations from neuronal-activity-related fluctuations in fMRI. *NeuroImage*, *31*(4), 1536–1548. doi:10.1016/j.neuroimage.2006.02.048

Biswal, B. B., & Kannurpatti, S. S. (2009). Resting-state functional connectivity in animal models: modulations by exsanguination. *Methods in Molecular Biology (Clifton, N.J.)*, *489*, 255–274. doi:10.1007/978-1-59745-543-5_12

Biswal, B. B., Mennes, M., Zuo, X.-N., Gohel, S., Kelly, C., Smith, S. M., … Milham, M. P. (2010). Toward discovery science of human brain function. *Proceedings of the National Academy of Sciences*, *107*(10), 4734–4739. doi:10.1073/pnas.0911855107

Biswal, B., Yetkin, F. Z., Haughton, V. M., & Hyde, J. S. (1995). Functional connectivity in the motor cortex of resting human brain using echo-planar MRI. *Magnetic Resonance in*

Medicine: Official Journal of the Society of Magnetic Resonance in Medicine / Society of Magnetic Resonance in Medicine, *34*(4), 537–541.

Boas, D. A., Culver, J., Stott, J., & Dunn, A. (2002). Three dimensional Monte Carlo code for photon migration through complex heterogeneous media including the adult human head. *Optics Express*, *10*(3), 159–170.

Boas, D. A., & Dunn, A. K. (2010). Laser speckle contrast imaging in biomedical optics. *Journal of Biomedical Optics*, *15*(1), 011109. doi:10.1117/1.3285504

Bolduc, V., Baraghis, E., Duquette, N., Thorin-Trescases, N., Lambert, J., Lesage, F., & Thorin, E. (2012). Catechin prevents severe dyslipidemia-associated changes in wall biomechanics of cerebral arteries in LDLr-/-:hApoB+/+ mice and improves cerebral blood flow. *American Journal of Physiology. Heart and Circulatory Physiology*, *302*(6), H1330–1339. doi:10.1152/ajpheart.01044.2011

Bonner, R., & Nossal, R. (1981). Model for laser Doppler measurements of blood flow in tissue. *Applied Optics*, *20*(12), 2097–2107. doi:10.1364/AO.20.002097

Bonvento, G., Charbonné, R., Corrèze, J. L., Borredon, J., Seylaz, J., & Lacombe, P. (1994). Is alpha-chloralose plus halothane induction a suitable anesthetic regimen for cerebrovascular research? *Brain Research*, *665*(2), 213–221.

Bouma, B. E., Tearney, G. J., Vakoc, B. J., & Yun, S. H. (2008). Optical Frequency Domain Imaging. In P. D. W. Drexler & P. D. J. G. Fujimoto (Eds.), *Optical Coherence Tomography* (pp. 209–237). Springer Berlin Heidelberg. Retrieved from http://link.springer.com/chapter/10.1007/978-3-540-77550-8_7

Bressler, S. L., Ding, M., & Yang, W. (1999). Investigation of cooperative cortical dynamics by multivariate autoregressive modeling of event-related local field potentials. *Neurocomputing*, *26*, 625–631.

Breteler, M. M., Claus, J. J., Grobbee, D. E., & Hofman, A. (1994). Cardiovascular disease and distribution of cognitive function in elderly people: the Rotterdam Study. *BMJ (Clinical Research Ed.)*, *308*(6944), 1604–1608.

Brezinski, M. E. (2006). *Optical Coherence Tomography: Principles and Applications* (1st ed.). London, UK: Academic Press.

Briers, J. D. (2001). Laser Doppler, speckle and related techniques for blood perfusion mapping and imaging. *Physiological Measurement*, *22*(4), R35–R66. doi:10.1088/0967-3334/22/4/201

Briers, J. D., & Webster, S. (1995). Quasi real-time digital version of single-exposure speckle photography for full-field monitoring of velocity or flow fields. *Optics Communications*, *116*(1–3), 36–42. doi:10.1016/0030-4018(95)00042-7

Brieu, N., Beaumont, E., Dubeau, S., Cohen-Adad, J., & Lesage, F. (2010). Characterization of the hemodynamic response in the rat lumbar spinal cord using intrinsic optical imaging and laser speckle. *Journal of Neuroscience Methods*, *191*(2), 151–157. doi:10.1016/j.jneumeth.2010.06.012

Brieu, N., Beaumont, E., & Lesage, F. (2008). Intrinsic optical imaging of the rat lumbar spinal cord. In *OSA Biomed*.

Brookes, M. J., Hale, J. R., Zumer, J. M., Stevenson, C. M., Francis, S. T., Barnes, G. R., … Nagarajan, S. S. (2011). Measuring functional connectivity using MEG: methodology and

comparison with fcMRI. *NeuroImage*, *56*(3), 1082–1104. doi:10.1016/j.neuroimage.2011.02.054

Bruehl, C., Hagemann, G., & Witte, O. W. (1998). Uncoupling of blood flow and metabolism in focal epilepsy. *Epilepsia*, *39*(12), 1235–1242.

Buckner, R. L., Andrews-Hanna, J. R., & Schacter, D. L. (2008). The brain's default network: anatomy, function, and relevance to disease. *Annals of the New York Academy of Sciences*, *1124*, 1–38. doi:10.1196/annals.1440.011

Burgess, S. A., Baohong, Y., Radosevich, A. J., Bouchard, M. B., & Hillman, E. M. C. (2007). High-resolution 3D imaging of tissue. In *Lasers and Electro-Optics Society, 2007. LEOS 2007. The 20th Annual Meeting of the IEEE* (pp. 5–6). doi:10.1109/LEOS.2007.4382246

Buxton, R B. (2001). The elusive initial dip. *NeuroImage*, *13*(6 Pt 1), 953–958. doi:10.1006/nimg.2001.0814

Buxton, Richard B., Uludag, K., Dubowitz, D. J., & Liu, T. T. (2004). Modeling the hemodynamic response to brain activation. *NeuroImage*, *23*(Supplement 1), S220–S233. doi:10.1016/j.neuroimage.2004.07.013

Cai, Z., Pang, Y., Lin, S., & Rhodes, P. G. (2003). Differential roles of tumor necrosis factor-alpha and interleukin-1 beta in lipopolysaccharide-induced brain injury in the neonatal rat. *Brain Research*, *975*(1-2), 37–47.

Cang, J., Kalatsky, V. A., Löwel, S., & Stryker, M. P. (2005). Optical Imaging of the Intrinsic Signal as a Measure of Cortical Plasticity in the Mouse. *Visual Neuroscience*, *22*(05), 685–691. doi:10.1017/S0952523805225178

Cauli, B., Tong, X.-K., Rancillac, A., Serluca, N., Lambolez, B., Rossier, J., & Hamel, E. (2004). Cortical GABA interneurons in neurovascular coupling: relays for subcortical vasoactive pathways. *The Journal of Neuroscience: The Official Journal of the Society for Neuroscience*, *24*(41), 8940–8949. doi:10.1523/JNEUROSCI.3065-04.2004

Chai, X. J., Castañón, A. N., Ongür, D., & Whitfield-Gabrieli, S. (2012). Anticorrelations in resting state networks without global signal regression. *NeuroImage*, *59*(2), 1420–1428. doi:10.1016/j.neuroimage.2011.08.048

Chen, J. J., & Pike, G. B. (2009). Origins of the BOLD post-stimulus undershoot. *NeuroImage*, *46*(3), 559–568. doi:10.1016/j.neuroimage.2009.03.015

Cheng, H.-L., Lin, C.-J., Soong, B.-W., Wang, P.-N., Chang, F.-C., Wu, Y.-T., … Lee, I.-H. (2012). Impairments in cognitive function and brain connectivity in severe asymptomatic carotid stenosis. *Stroke; a Journal of Cerebral Circulation*, *43*(10), 2567–2573. doi:10.1161/STROKEAHA.111.645614

Church, J. A., Fair, D. A., Dosenbach, N. U. F., Cohen, A. L., Miezin, F. M., Petersen, S. E., & Schlaggar, B. L. (2009). Control networks in paediatric Tourette syndrome show immature and anomalous patterns of functional connectivity. *Brain: A Journal of Neurology*, *132*(Pt 1), 225–238. doi:10.1093/brain/awn223

Clawson, C. C., Hartmann, J. F., & Vernier, R. L. (1966). Electron microscopy of the effect of gram-negative endotoxin on the blood-brain barrier. *The Journal of Comparative Neurology*, *127*(2), 183–198. doi:10.1002/cne.901270204

Cohen, D. (1972). Magnetoencephalography: detection of the brain's electrical activity with a superconducting magnetometer. *Science (New York, N.Y.)*, *175*(4022), 664–666.

Cole, D. M., Smith, S. M., & Beckmann, C. F. (2010). Advances and pitfalls in the analysis and interpretation of resting-state FMRI data. *Frontiers in Systems Neuroscience*, *4*, 8. doi:10.3389/fnsys.2010.00008

Cordes, D., Haughton, V., Carew, J. D., Arfanakis, K., & Maravilla, K. (2002). Hierarchical clustering to measure connectivity in fMRI resting-state data. *Magnetic Resonance Imaging*, *20*(4), 305–317.

Cordes, D., Haughton, V. M., Arfanakis, K., Carew, J. D., Turski, P. A., Moritz, C. H., … Meyerand, M. E. (2001). Frequencies contributing to functional connectivity in the cerebral cortex in "resting-state" data. *AJNR. American Journal of Neuroradiology*, *22*(7), 1326–1333.

Cox, S. B., Woolsey, T. A., & Rovainen, C. M. (1993). Localized dynamic changes in cortical blood flow with whisker stimulation corresponds to matched vascular and neuronal architecture of rat barrels. *Journal of Cerebral Blood Flow and Metabolism: Official Journal of the International Society of Cerebral Blood Flow and Metabolism*, *13*(6), 899–913. doi:10.1038/jcbfm.1993.113

Culver, J. P., Choe, R., Holboke, M. J., Zubkov, L., Durduran, T., Slemp, A., … Yodh, A. G. (2003). Three-dimensional diffuse optical tomography in the parallel plane transmission geometry: Evaluation of a hybrid frequency domain/continuous wave clinical system for breast imaging. *Medical Physics*, *30*(2), 235–247. doi:10.1118/1.1534109

Damaraju, E., Phillips, J. R., Lowe, J. R., Ohls, R., Calhoun, V. D., & Caprihan, A. (2010). Resting-state functional connectivity differences in premature children. *Frontiers in Systems Neuroscience*, *4*. doi:10.3389/fnsys.2010.00023

Damoiseaux, J. S., Beckmann, C. F., Arigita, E. J. S., Barkhof, F., Scheltens, P., Stam, C. J., … Rombouts, S. A. R. B. (2008). Reduced resting-state brain activity in the "default network" in normal aging. *Cerebral Cortex (New York, N.Y.: 1991)*, *18*(8), 1856–1864. doi:10.1093/cercor/bhm207

Damoiseaux, J. S., Rombouts, S. a. R. B., Barkhof, F., Scheltens, P., Stam, C. J., Smith, S. M., & Beckmann, C. F. (2006). Consistent resting-state networks across healthy subjects. *Proceedings of the National Academy of Sciences*, *103*(37), 13848–13853. doi:10.1073/pnas.0601417103

De Luca, M., Beckmann, C. F., De Stefano, N., Matthews, P. M., & Smith, S. M. (2006). fMRI resting state networks define distinct modes of long-distance interactions in the human brain. *NeuroImage*, *29*(4), 1359–1367. doi:10.1016/j.neuroimage.2005.08.035

Deco, G., & Corbetta, M. (2011). The dynamical balance of the brain at rest. *The Neuroscientist: A Review Journal Bringing Neurobiology, Neurology and Psychiatry*, *17*(1), 107–123. doi:10.1177/1073858409354384

Delpy, D. T., Cope, M., Zee, P. van der, Arridge, S., Wray, S., & Wyatt, J. (1988). Estimation of optical pathlength through tissue from direct time of flight measurement. *Physics in Medicine and Biology*, *33*(12), 1433–1442. doi:10.1088/0031-9155/33/12/008

Devor, A., Dunn, A. K., Andermann, M. L., Ulbert, I., Boas, D. A., & Dale, A. M. (2003). Coupling of total hemoglobin concentration, oxygenation, and neural activity in rat somatosensory cortex. *Neuron*, *39*(2), 353–359.

Dharmarajan, S., & Schuster, D. P. (2012, December 20). Molecular Imaging of Pulmonary Gene Expression with Positron Emission Tomography. other. Retrieved April 21, 2013, from http://www.atsjournals.org/doi/full/10.1513/pats.200507-068DS

Ding, M., Bressler, S. L., Yang, W., & Liang, H. (2000). Short-window spectral analysis of cortical event-related potentials by adaptive multivariate autoregressive modeling: data preprocessing, model validation, and variability assessment. *Biological Cybernetics*, *83*(1), 35–45.

Doria, V., Beckmann, C. F., Arichi, T., Merchant, N., Groppo, M., Turkheimer, F. E., … Edwards, A. D. (2010). Emergence of resting state networks in the preterm human brain. *Proceedings of the National Academy of Sciences*, *107*(46), 20015–20020. doi:10.1073/pnas.1007921107

Douw, L, de Groot, M., van Dellen, E., Aronica, E., Heimans, J. J., Klein, M., … Hillebrand, A. (2013). Local MEG networks: The missing link between protein expression and epilepsy in glioma patients? *NeuroImage*, *75C*, 203–211. doi:10.1016/j.neuroimage.2013.02.067

Douw, Linda, de Groot, M., van Dellen, E., Heimans, J. J., Ronner, H. E., Stam, C. J., & Reijneveld, J. C. (2010). "Functional Connectivity" Is a Sensitive Predictor of Epilepsy Diagnosis after the First Seizure. *PLoS ONE*, *5*(5), e10839. doi:10.1371/journal.pone.0010839

Draper, B. A., Baek, K., Bartlett, M. S., & Beveridge, J. R. (2003). Recognizing faces with PCA and ICA. *Computer Vision and Image Understanding*, *91*(1–2), 115–137. doi:10.1016/S1077-3142(03)00077-8

Drexler, W., & Fujimoto, J. G. (Eds.). (2008). *Optical Coherence Tomography Technology and Applications*. Berlin: Springer. Retrieved from http://www.springerlink.com/content/978-3-540-77549-2#section=229022&page=1

Dubeau, S., Ferland, G., Gaudreau, P., Beaumont, E., & Lesage, F. (2011). Cerebrovascular hemodynamic correlates of aging in the Lou/c rat: A model of healthy aging. *NeuroImage*, *56*(4), 1892–1901. doi:10.1016/j.neuroimage.2011.03.076

Duncan, D. D., & Kirkpatrick, S. J. (2008). Can laser speckle flowmetry be made a quantitative tool? *Journal of the Optical Society of America. A, Optics, Image Science, and Vision*, *25*(8), 2088–2094.

Dunn, A. K., Bolay, H., Moskowitz, M. A., & Boas, D. A. (2001). Dynamic Imaging of Cerebral Blood Flow Using Laser Speckle. *J Cereb Blood Flow Metab*, *21*(3), 195–201. doi:10.1097/00004647-200103000-00002

Dunn, A. K., Devor, A., Bolay, H., Andermann, M. L., Moskowitz, M. A., Dale, A. M., & Boas, D. A. (2003). Simultaneous imaging of total cerebral hemoglobin concentration, oxygenation, and blood flow during functional activation. *Optics Letters*, *28*(1), 28–30. doi:10.1364/OL.28.000028

Dunn, A. K., Devor, A., Dale, A. M., & Boas, D. A. (2005). Spatial extent of oxygen metabolism and hemodynamic changes during functional activation of the rat somatosensory cortex. *NeuroImage*, *27*(2), 279–290. doi:10.1016/j.neuroimage.2005.04.024

Elwell, C. E., Springett, R., Hillman, E., & Delpy, D. T. (1999). Oscillations in cerebral haemodynamics. Implications for functional activation studies. *Advances in Experimental Medicine and Biology*, *471*, 57–65.

Ephrat, P., Needles, A., Bilan, C., Trujillo, A., Theodoropoulos, C., Hirson, D., & Foster, S. (2012). *Photoacoustic Imaging of Murine Tumors Using the Vevo® 2100 Micro-Ultrasound System* (White Paper No. Ver 1.0) (p. 14). Toronto, ON, Canada: VisualSonics Inc. Retrieved from http://www.visualsonics.com/online-file-request.php?f=media&p=WP_2100_Cb_Photoacoustic_Imaging_ver1.0.pdf

Euler, L. (1741). Solutio problematis ad geometriam situs pertinentis. *Commentarii academiae scientiarum Petropolitanae*, *8*, 128–140.

European Commission Workshop. (2010). Of mice and men – are mice relevant models for human disease? In *European Commission workshop*. London, UK.

Fabene, P. F., Weiczner, R., Marzola, P., Nicolato, E., Calderan, L., Andrioli, A., … Sbarbati, A. (2006). Structural and functional MRI following 4-aminopyridine-induced seizures: a comparative imaging and anatomical study. *Neurobiology of Disease*, *21*(1), 80–89. doi:10.1016/j.nbd.2005.06.013

Fair, D. A., Cohen, A. L., Dosenbach, N. U. F., Church, J. A., Miezin, F. M., Barch, D. M., … Schlaggar, B. L. (2008). The maturing architecture of the brain's default network. *Proceedings of the National Academy of Sciences of the United States of America*, *105*(10), 4028–4032. doi:10.1073/pnas.0800376105

Fair, D. A., Dosenbach, N. U. F., Church, J. A., Cohen, A. L., Brahmbhatt, S., Miezin, F. M., … Schlaggar, B. L. (2007). Development of distinct control networks through segregation and integration. *Proceedings of the National Academy of Sciences of the United States of America*, *104*(33), 13507–13512. doi:10.1073/pnas.0705843104

Faraci, F. M. (2011). Protecting against vascular disease in brain. *American Journal of Physiology. Heart and Circulatory Physiology*, *300*(5), H1566–1582. doi:10.1152/ajpheart.01310.2010

Feinberg, D. A., Moeller, S., Smith, S. M., Auerbach, E., Ramanna, S., Gunther, M., … Yacoub, E. (2010). Multiplexed echo planar imaging for sub-second whole brain FMRI and fast diffusion imaging. *PloS One*, *5*(12), e15710. doi:10.1371/journal.pone.0015710

Fercher, A. F., Hitzenberger, C. K., Kamp, G., & El-Zaiat, S. Y. (1995). Measurement of intraocular distances by backscattering spectral interferometry. *Optics Communications*, *117*(1–2), 43–48. doi:10.1016/0030-4018(95)00119-S

Fonoff, E. T., Pereira, J. F., Jr, Camargo, L. V., Dale, C. S., Pagano, R. L., Ballester, G., & Teixeira, M. J. (2009). Functional mapping of the motor cortex of the rat using transdural electrical stimulation. *Behavioural Brain Research*, *202*(1), 138–141. doi:10.1016/j.bbr.2009.03.018

Fox, M. D., & Raichle, M. E. (2007). Spontaneous fluctuations in brain activity observed with functional magnetic resonance imaging. *Nature Reviews Neuroscience*, *8*(9), 700–711. doi:10.1038/nrn2201

Fox, M. D., Snyder, A. Z., Zacks, J. M., & Raichle, M. E. (2006). Coherent spontaneous activity accounts for trial-to-trial variability in human evoked brain responses. *Nature Neuroscience*, *9*(1), 23–25. doi:10.1038/nn1616

Fox, M. D., Zhang, D., Snyder, A. Z., & Raichle, M. E. (2009). The Global Signal and Observed Anticorrelated Resting State Brain Networks. *Journal of Neurophysiology*, *101*(6), 3270–3283. doi:10.1152/jn.90777.2008

Fransson, P., Skiöld, B., Horsch, S., Nordell, A., Blennow, M., Lagercrantz, H., & Aden, U. (2007). Resting-state networks in the infant brain. *Proceedings of the National Academy of Sciences of the United States of America*, *104*(39), 15531–15536. doi:10.1073/pnas.0704380104

Freeman, L. C. (1977). A Set of Measures of Centrality Based on Betweenness. *Sociometry*, *40*(1), 35. doi:10.2307/3033543

Frings, L., Schulze-Bonhage, A., Spreer, J., & Wagner, K. (2009). Remote effects of hippocampal damage on default network connectivity in the human brain. *Journal of Neurology*, *256*(12), 2021–2029. doi:10.1007/s00415-009-5233-0

Friston, K J, Frith, C. D., Liddle, P. F., & Frackowiak, R. S. (1993). Functional connectivity: the principal-component analysis of large (PET) data sets. *Journal of Cerebral Blood Flow and Metabolism: Official Journal of the International Society of Cerebral Blood Flow and Metabolism*, *13*(1), 5–14. doi:10.1038/jcbfm.1993.4

Friston, Karl J. (2011). Functional and effective connectivity: a review. *Brain Connectivity*, *1*(1), 13–36. doi:10.1089/brain.2011.0008

Friston, Karl J., Ashburner, J. T., Kiebel, S. J., Nichols, T. E., & Penny, W. D. (2006). *Statistical Parametric Mapping: The Analysis of Functional Brain Images* (1st ed.). Great Britain: Academic Press. Retrieved from http://www.fil.ion.ucl.ac.uk/spm/

Frostig, R. D., Lieke, E. E., Ts'o, D. Y., & Grinvald, A. (1990). Cortical functional architecture and local coupling between neuronal activity and the microcirculation revealed by in vivo high-resolution optical imaging of intrinsic signals. *Proc Natl Acad Sci U S A*, *87*(16), 6082–6.

Fujimoto, J. G., Pitris, C., Boppart, S. A., & Brezinski, M. E. (2000). Optical Coherence Tomography: An Emerging Technology for Biomedical Imaging and Optical Biopsy. *Neoplasia*, *2*(1-2), 9–25.

Gallagher, A., Lassonde, M., Bastien, D., Vannasing, P., Lesage, F., Grova, C., … Nguyen, D. K. (2008). Non-invasive pre-surgical investigation of a 10 year-old epileptic boy using simultaneous EEG-NIRS. *Seizure: The Journal of the British Epilepsy Association*, *17*(6), 576–582. doi:10.1016/j.seizure.2008.01.009

Ganzetti, M., & Mantini, D. (2013). Functional connectivity and oscillatory neuronal activity in the resting human brain. *Neuroscience*, *240*, 297–309. doi:10.1016/j.neuroscience.2013.02.032

Gelikonov, V. M., Kasatkina, I. V., & Shilyagin, P. A. (2010). Suppression of image artifacts in the spectral-domain optical coherence tomography. *Radiophysics and Quantum Electronics*, *52*(11), 810–821. doi:10.1007/s11141-010-9188-x

Ghafoori-Shiraz, H., & Okoshi, T. (1985). Optical-fiber diagnosis using optical-frequency-domain reflectometry. *Optics Letters*, *10*(3), 160–162.

Ghafoori-Shiraz, H., & Okoshi, T. (1986). Fault location in optical fibers using optical frequency domain reflectometry. *Lightwave Technology, Journal of*, *4*(3), 316 – 322. doi:10.1109/JLT.1986.1074720

Gibbs, F. A., Gibbs, E. L., & Lennox, W. G. (1937). Epilepsy: A Paroxysmal Cerebral Dysrhythmia. *Brain*, *60*(4), 377–388. doi:10.1093/brain/60.4.377

Gili, T., Cercignani, M., Serra, L., Perri, R., Giove, F., Maraviglia, B., … Bozzali, M. (2011). Regional brain atrophy and functional disconnection across Alzheimer's disease

evolution. *Journal of Neurology, Neurosurgery, and Psychiatry*, *82*(1), 58–66. doi:10.1136/jnnp.2009.199935

Glisky, E. L. (2007). Changes in Cognitive Function in Human Aging. In D. Riddle (Ed.), *Brain Aging: Models, Methods, and Mechanisms*. Boca Raton, USA: CRC Press. Retrieved from http://www.ncbi.nlm.nih.gov/books/NBK3885/

Gonçalves, M. S., & Hall, D. A. (2003). Connectivity analysis with structural equation modelling: an example of the effects of voxel selection. *NeuroImage*, *20*(3), 1455–1467.

Gotman, J., Grova, C., Bagshaw, A., Kobayashi, E., Aghakhani, Y., & Dubeau, F. (2005). Generalized epileptic discharges show thalamocortical activation and suspension of the default state of the brain. *Proceedings of the National Academy of Sciences of the United States of America*, *102*(42), 15236–15240. doi:10.1073/pnas.0504935102

Granger, C. W. (1969). Investigating causal relations by econometric models and cross-spectral methods. *Econometrica: Journal of the Econometric Society*, *37*(3), 424–438.

Green, J. B., Sora, E., Bialy, Y., Ricamato, A., & Thatcher, R. W. (1998). Cortical sensorimotor reorganization after spinal cord injury: an electroencephalographic study. *Neurology*, *50*(4), 1115–1121.

Greicius, M. D., Flores, B. H., Menon, V., Glover, G. H., Solvason, H. B., Kenna, H., … Schatzberg, A. F. (2007). Resting-state functional connectivity in major depression: abnormally increased contributions from subgenual cingulate cortex and thalamus. *Biological Psychiatry*, *62*(5), 429–437. doi:10.1016/j.biopsych.2006.09.020

Greicius, M. D., Krasnow, B., Reiss, A. L., & Menon, V. (2003). Functional connectivity in the resting brain: a network analysis of the default mode hypothesis. *Proceedings of the*

National Academy of Sciences of the United States of America, *100*(1), 253–258. doi:10.1073/pnas.0135058100

Greicius, M. D., Srivastava, G., Reiss, A. L., & Menon, V. (2004). Default-mode network activity distinguishes Alzheimer's disease from healthy aging: evidence from functional MRI. *Proceedings of the National Academy of Sciences of the United States of America*, *101*(13), 4637–4642. doi:10.1073/pnas.0308627101

Grinvald, A., Lieke, E., Frostig, R. D., Gilbert, C. D., & Wiesel, T. N. (1986). Functional architecture of cortex revealed by optical imaging of intrinsic signals. *Nature*, *324*(6095), 361–364. doi:10.1038/324361a0

Grubb, R. L., Jr, Raichle, M. E., Eichling, J. O., & Ter-Pogossian, M. M. (1974). The effects of changes in PaCO2 on cerebral blood volume, blood flow, and vascular mean transit time. *Stroke; a Journal of Cerebral Circulation*, *5*(5), 630–639.

Guevara, E., Abran, M., Belanger, S., Ouakli, N., & Lesage, F. (2010). Comparison of the performance of two depth-resolved optical imaging systems: laminar optical tomography and spatially modulated imaging. In A. P. Wax & V. Backman (Eds.), *Biomedical Applications of Light Scattering IV* (Vol. 7573, pp. 757317–10). San Francisco, California, USA: SPIE. doi:10.1117/12.841886

Guevara, E., Berti, R., Londono, I., Xie, N., Bellec, P., Lesage, F., & Lodygensky, G. A. (2013). Imaging of an inflammatory injury in the newborn rat brain with photoacoustic tomography. *Submitted to PLOS ONE*.

Guevara, E., Pouliot, P., Nguyen, D. K., & Lesage, F. (2013). Optical imaging of acute epileptic networks in mice. *Journal of Biomedical Optics*, *18*(7), 076021–076021. doi:10.1117/1.JBO.18.7.076021

Guevara, E., Sadekova, N., Girouard, H., & Lesage, F. (2013). Optical imaging of resting-state functional connectivity in a novel arterial stiffness model. *Biomedical Optics Express*, *4*(11), 2332–2346. doi:10.1364/BOE.4.002332

Guilfoyle, D. N., Gerum, S. V., Sanchez, J. L., Balla, A., Sershen, H., Javitt, D. C., & Hoptman, M. J. (2013). Functional connectivity fMRI in mouse brain at 7T using isoflurane. *Journal of Neuroscience Methods*, *214*(2), 144–148. doi:10.1016/j.jneumeth.2013.01.019

Gusnard, D. A., Raichle, M. E., & Raichle, M. E. (2001). Searching for a baseline: functional imaging and the resting human brain. *Nature Reviews. Neuroscience*, *2*(10), 685–694. doi:10.1038/35094500

Häusler, G., & Lindner, M. W. (1998). "Coherence radar" and "spectral radar"-new tools for dermatological diagnosis. *Journal of Biomedical Optics*, *3*(1), 21–31. doi:10.1117/1.429899

He, B. J., Snyder, A. Z., Zempel, J. M., Smyth, M. D., & Raichle, M. E. (2008). Electrophysiological correlates of the brain's intrinsic large-scale functional architecture. *Proceedings of the National Academy of Sciences*, *105*(41), 16039–16044. doi:10.1073/pnas.0807010105

He, Y., Chen, Z., Gong, G., & Evans, A. (2009). Neuronal networks in Alzheimer's disease. *The Neuroscientist: A Review Journal Bringing Neurobiology, Neurology and Psychiatry*, *15*(4), 333–350. doi:10.1177/1073858409334423

Hillman, E. M. C. (2007). Optical brain imaging in vivo: techniques and applications from animal to man. *Journal of Biomedical Optics*, *12*(5), 051402.

Hillman, E. M. C., Boas, D. A., Dale, A. M., & Dunn, A. K. (2004). Laminar optical tomography: Demonstration of millimeter-scale depth-resolved imaging in turbid media. *Opt. Lett.*, *29*(14), 1650–2. doi:10.1364/ol.29.001650

Hillman, E. M. C., Bouchard, M., Devor, A., Crespigny, A. de, & Boas, D. A. (2006). Functional optical imaging of brain activation: a multi-scale, multi-modality approach. In *Life Science Systems and Applications Workshop, 2006. IEEE/NLM* (pp. 1–2). Bethesda, MD. doi:10.1109/LSSA.2006.250368

Hillman, E. M. C., & Burgess, S. A. (2008). Sub-millimeter resolution 3D optical imaging of living tissue using laminar optical tomography. *Laser & Photonics Review*, *3*(1-2), 159–179. doi:10.1002/lpor.200810031

Hillman, E. M. C., Devor, A., Bouchard, M. B., Dunn, A. K., Krauss, G. W., Skoch, J., … Boas, D. A. (2007). Depth-resolved optical imaging and microscopy of vascular compartment dynamics during somatosensory stimulation. *NeuroImage*, *35*(1), 89–104.

Hillman, Elizabeth M. C. (2006). Laminar optical tomography: high-resolution 3D functional imaging of superficial tissues. In *Proceedings of SPIE* (Vol. 6143, p. 61431M–61431M–14). San Diego, CA, USA. doi:10.1117/12.655876

Hinkley, L. B. N., Owen, J. P., Fisher, M., Findlay, A. M., Vinogradov, S., & Nagarajan, S. S. (2010). Cognitive Impairments in Schizophrenia as Assessed Through Activation and Connectivity Measures of Magnetoencephalography (MEG) Data. *Frontiers in Human Neuroscience*, *3*, 73. doi:10.3389/neuro.09.073.2009

Horstmann, M.-T., Bialonski, S., Noennig, N., Mai, H., Prusseit, J., Wellmer, J., … Lehnertz, K. (2010). State dependent properties of epileptic brain networks: comparative graph-theoretical analyses of simultaneously recorded EEG and MEG. *Clinical Neurophysiology: Official Journal of the International Federation of Clinical Neurophysiology*, *121*(2), 172–185. doi:10.1016/j.clinph.2009.10.013

Huang, D., Swanson, E. A., Lin, C. P., Schuman, J. S., Stinson, W. G., Chang, W., … Fujimoto, J. G. (1991). Optical coherence tomography. *Science*, *254*(5035), 1178–1181. doi:10.1126/science.1957169

Hubel, D. H., & Wiesel, T. N. (1962). Receptive fields, binocular interaction and functional architecture in the cat's visual cortex. *The Journal of Physiology*, *160*(1), 106–154.2.

Hutchison, R. M., Mirsattari, S. M., Jones, C. K., Gati, J. S., & Leung, L. S. (2010). Functional Networks in the Anesthetized Rat Brain Revealed by Independent Component Analysis of Resting-State fMRI. *Journal of Neurophysiology*, *103*(6), 3398–3406. doi:10.1152/jn.00141.2010

Iadecola, C. (2004). Neurovascular regulation in the normal brain and in Alzheimer's disease. *Nature Reviews Neuroscience*, *5*(5), 347–360. doi:10.1038/nrn1387

Iadecola, C. (2010). The overlap between neurodegenerative and vascular factors in the pathogenesis of dementia. *Acta Neuropathologica*, *120*(3), 287–296. doi:10.1007/s00401-010-0718-6

Jonckers, E., Van Audekerke, J., De Visscher, G., Van der Linden, A., & Verhoye, M. (2011). Functional Connectivity fMRI of the Rodent Brain: Comparison of Functional

Connectivity Networks in Rat and Mouse. *PLoS ONE*, *6*(4), e18876. doi:10.1371/journal.pone.0018876

Jones, M., Berwick, J., Johnston, D., & Mayhew, J. (2001). Concurrent optical imaging spectroscopy and laser-Doppler flowmetry: the relationship between blood flow, oxygenation, and volume in rodent barrel cortex. *NeuroImage*, *13*(6 Pt 1), 1002–1015. doi:10.1006/nimg.2001.0808

Jones, P. B., Shin, H. K., Boas, D. A., Hyman, B. T., Moskowitz, M. A., Ayata, C., & Dunn, A. K. (2008). Simultaneous multispectral reflectance imaging and laser speckle flowmetry of cerebral blood flow and oxygen metabolism in focal cerebral ischemia. *Journal of Biomedical Optics*, *13*(4), 044007. doi:10.1117/1.2950312

Kalthoff, D., Seehafer, J. U., Po, C., Wiedermann, D., & Hoehn, M. (2011). Functional connectivity in the rat at 11.7T: Impact of physiological noise in resting state fMRI. *NeuroImage*, *54*(4), 2828–2839. doi:10.1016/j.neuroimage.2010.10.053

Kandel, E. R., Schwartz, J. H., & Jessell, T. M. (1991). *Principles of neural science* (3rd ed.). New York: Elsevier.

Kannurpatti, S. S., Biswal, B. B., Kim, Y. R., & Rosen, B. R. (2008). Spatio-temporal characteristics of low-frequency BOLD signal fluctuations in isoflurane-anesthetized rat brain. *NeuroImage*, *40*(4), 1738–1747. doi:10.1016/j.neuroimage.2007.05.061

Kim, A. D., & Schotland, J. C. (2006). Self-consistent scattering theory for the radiative transport equation. *J. Opt. Soc. Am. A*, *23*(3), 596–602. doi:10.1364/JOSAA.23.000596

Kohl, M., Lindauer, U., Royl, G., Kuhl, M., Gold, L., Villringer, A., & Dirnagl, U. (2000). Physical model for the spectroscopic analysis of cortical intrinsic optical signals. *Physics in Medicine and Biology*, *45*(12), 3749–3764.

Kroon, A. A., Wang, J., Kavanagh, B., Huang, Z., Kuliszewski, M., van Goudoever, J. B., & Post, M. (2011). Prolonged Mechanical Ventilation Induces Cell Cycle Arrest in Newborn Rat Lung. *PLoS ONE*, *6*(2), e16910. doi:10.1371/journal.pone.0016910

Kwong, K. K., Belliveau, J. W., Chesler, D. A., Goldberg, I. E., Weisskoff, R. M., Poncelet, B. P., … Turner, R. (1992). Dynamic magnetic resonance imaging of human brain activity during primary sensory stimulation. *Proceedings of the National Academy of Sciences of the United States of America*, *89*(12), 5675–5679.

La Iglesia-Vaya, M. de, Molina-Mateo, J., Jose, M., S., A., & Marti-Bonmati, L. (2013). Brain Connections – Resting State fMRI Functional Connectivity. In K. Fountas (Ed.), *Novel Frontiers of Advanced Neuroimaging*. InTech. Retrieved from http://www.intechopen.com/books/novel-frontiers-of-advanced-neuroimaging/brain-connections-resting-state-fmri-functional-connectivity

Latora, V., & Marchiori, M. (2001). Efficient Behavior of Small-World Networks. *Physical Review Letters*, *87*(19), 198701. doi:10.1103/PhysRevLett.87.198701

Lawrie, S. M., Buechel, C., Whalley, H. C., Frith, C. D., Friston, K. J., & Johnstone, E. C. (2002). Reduced frontotemporal functional connectivity in schizophrenia associated with auditory hallucinations. *Biological Psychiatry*, *51*(12), 1008–1011.

Le, T. T., Yue, S., & Cheng, J.-X. (2010). Shedding new light on lipid biology with coherent anti-Stokes Raman scattering microscopy. *Journal of Lipid Research*, *51*(11), 3091–3102. doi:10.1194/jlr.R008730

Leitgeb, R., Wojtkowski, M., Kowalczyk, A., Hitzenberger, C. K., Sticker, M., & Fercher, A. F. (2000). Spectral measurement of absorption by spectroscopic frequency-domain optical coherence tomography. *Optics Letters*, *25*(11), 820–822.

Lesage, F., Brieu, N., Dubeau, S., & Beaumont, E. (2009). Optical imaging of vascular and metabolic responses in the lumbar spinal cord after T10 transection in rats. *Neuroscience Letters*, *454*(1), 105–109. doi:10.1016/j.neulet.2009.02.060

Lexer, F., Hitzenberger, C. K., Fercher, A. F., & Kulhavy, M. (1997). Wavelength-tuning interferometry of intraocular distances. *Appl. Opt.*, *36*(25), 6548–6553. doi:10.1364/AO.36.006548

Li, B., Zhou, F., Luo, Q., & Li, P. (2012). Altered resting-state functional connectivity after cortical spreading depression in mice. *NeuroImage*, *63*(3), 1171–1177. doi:10.1016/j.neuroimage.2012.08.024

Liang, Z., King, J., & Zhang, N. (2012). Intrinsic organization of the anesthetized brain. *The Journal of Neuroscience: The Official Journal of the Society for Neuroscience*, *32*(30), 10183–10191. doi:10.1523/JNEUROSCI.1020-12.2012

Liao, C. H., Worsley, K. J., Poline, J.-B., Aston, J. A. D., Duncan, G. H., & Evans, A. C. (2002). Estimating the delay of the fMRI response. *NeuroImage*, *16*(3 Pt 1), 593–606.

Liao, S. M., Ferradal, S. L., White, B. R., Gregg, N., Inder, T. E., & Culver, J. P. (2012). High-density diffuse optical tomography of term infant visual cortex in the nursery. *Journal of Biomedical Optics*, *17*(8), 0814141–0814147. doi:10.1117/1.JBO.17.8.081414

Liao, W., Zhang, Z., Pan, Z., Mantini, D., Ding, J., Duan, X., … Chen, H. (2011). Default mode network abnormalities in mesial temporal lobe epilepsy: a study combining fMRI and DTI. *Human Brain Mapping*, *32*(6), 883–895. doi:10.1002/hbm.21076

Liu, B., & Brezinski, M. E. (2007). Theoretical and practical considerations on detection performance of time domain, Fourier domain, and swept source optical coherence tomography. *Journal of Biomedical Optics*, *12*(4), 044007. doi:10.1117/1.2753410

Liu, W.-C., Flax, J. F., Guise, K. G., Sukul, V., & Benasich, A. A. (2008). Functional connectivity of the sensorimotor area in naturally sleeping infants. *Brain Research*, *1223*, 42–49. doi:10.1016/j.brainres.2008.05.054

Liu, Y., Liang, M., Zhou, Y., He, Y., Hao, Y., Song, M., … Jiang, T. (2008). Disrupted small-world networks in schizophrenia. *Brain: A Journal of Neurology*, *131*(Pt 4), 945–961. doi:10.1093/brain/awn018

Liu, Z., Fukunaga, M., de Zwart, J. A., & Duyn, J. H. (2010). Large-scale spontaneous fluctuations and correlations in brain electrical activity observed with magnetoencephalography. *NeuroImage*, *51*(1), 102–111. doi:10.1016/j.neuroimage.2010.01.092

Lodygensky, G. A., West, T., Stump, M., Holtzman, D. M., Inder, T. E., & Neil, J. J. (2010). In vivo MRI analysis of an inflammatory injury in the developing brain. *Brain, Behavior, and Immunity*, *24*(5), 759–767. doi:10.1016/j.bbi.2009.11.005

Lowe, M. J., Dzemidzic, M., Lurito, J. T., Mathews, V. P., & Phillips, M. D. (2000). Correlations in low-frequency BOLD fluctuations reflect cortico-cortical connections. *NeuroImage*, *12*(5), 582–587. doi:10.1006/nimg.2000.0654

Lu, C.-M., Zhang, Y.-J., Biswal, B. B., Zang, Y.-F., Peng, D.-L., & Zhu, C.-Z. (2010). Use of fNIRS to assess resting state functional connectivity. *Journal of Neuroscience Methods*, *186*(2), 242–249. doi:10.1016/j.jneumeth.2009.11.010

Luckl, J., Baker, W., Sun, Z.-H., Durduran, T., Yodh, A. G., & Greenberg, J. H. (2010). The biological effect of contralateral forepaw stimulation in rat focal cerebral ischemia: a multispectral optical imaging study. *Frontiers in Neuroenergetics*, *2*, pii: 19. doi:10.3389/fnene.2010.00019

Luo, C., Qiu, C., Guo, Z., Fang, J., Li, Q., Lei, X., … Yao, D. (2012). Disrupted Functional Brain Connectivity in Partial Epilepsy: A Resting-State fMRI Study. *PLoS ONE*, *7*(1), e28196. doi:10.1371/journal.pone.0028196

Luo, W., Li, P., Chen, S., Zeng, S., & Luo, Q. (2007). Differentiating hemodynamic responses in rat primary somatosensory cortex during non-noxious and noxious electrical stimulation by optical imaging. *Brain Research*, *1133*(1), 67–77. doi:10.1016/j.brainres.2006.09.111

Magill, P. J., Pogosyan, A., Sharott, A., Csicsvari, J., Bolam, J. P., & Brown, P. (2006). Changes in Functional Connectivity within the Rat Striatopallidal Axis during Global Brain Activation In Vivo. *The Journal of Neuroscience*, *26*(23), 6318–6329. doi:10.1523/JNEUROSCI.0620-06.2006

Magnuson, M., Majeed, W., & Keilholz, S. D. (2010). Functional connectivity in blood oxygenation level-dependent and cerebral blood volume-weighted resting state functional

magnetic resonance imaging in the rat brain. *Journal of Magnetic Resonance Imaging: JMRI*, *32*(3), 584–592. doi:10.1002/jmri.22295

Malonek, D., & Grinvald, A. (1996). Interactions Between Electrical Activity and Cortical Microcirculation Revealed by Imaging Spectroscopy: Implications for Functional Brain Mapping. *Science*, *272*(5261), 551–554. doi:10.1126/science.272.5261.551

Mankinen, K., Jalovaara, P., Paakki, J.-J., Harila, M., Rytky, S., Tervonen, O., … Kiviniemi, V. (2012). Connectivity disruptions in resting-state functional brain networks in children with temporal lobe epilepsy. *Epilepsy Research*, *100*(1–2), 168–178. doi:10.1016/j.eplepsyres.2012.02.010

Margulies, D. S., Böttger, J., Long, X., Lv, Y., Kelly, C., Schäfer, A., … Villringer, A. (2010). Resting developments: a review of fMRI post-processing methodologies for spontaneous brain activity. *Magma (New York, N.Y.)*, *23*(5-6), 289–307. doi:10.1007/s10334-010-0228-5

Marshall, R S, Lazar, R. M., Pile-Spellman, J., Young, W. L., Duong, D. H., Joshi, S., & Ostapkovich, N. (2001). Recovery of brain function during induced cerebral hypoperfusion. *Brain: A Journal of Neurology*, *124*(Pt 6), 1208–1217.

Marshall, Randolph S, & Lazar, R. M. (2011). Pumps, aqueducts, and drought management: vascular physiology in vascular cognitive impairment. *Stroke; a Journal of Cerebral Circulation*, *42*(1), 221–226. doi:10.1161/STROKEAHA.110.595645

Mayhew, J., Johnston, D., Berwick, J., Jones, M., Coffey, P., & Zheng, Y. (2000). Spectroscopic Analysis of Neural Activity in Brain: Increased Oxygen Consumption Following Activation of Barrel Cortex. *NeuroImage*, *12*(6), 664–675. doi:10.1006/nimg.2000.0656

McKeown, M. J., Hansen, L. K., & Sejnowsk, T. J. (2003). Independent component analysis of functional MRI: what is signal and what is noise? *Current Opinion in Neurobiology*, *13*(5), 620–629. doi:10.1016/j.conb.2003.09.012

Mesquita, R. C., Franceschini, M. A., & Boas, D. A. (2010). Resting state functional connectivity of the whole head with near-infrared spectroscopy. *Biomedical Optics Express*, *1*(1), 324–336. doi:10.1364/BOE.1.000324

Moeller, S., Nallasamy, N., Tsao, D. Y., & Freiwald, W. A. (2009). Functional connectivity of the macaque brain across stimulus and arousal states. *The Journal of Neuroscience: The Official Journal of the Society for Neuroscience*, *29*(18), 5897–5909. doi:10.1523/JNEUROSCI.0220-09.2009

Moldestad, O., Karlsen, P., Molden, S., & Storm, J. F. (2009). Tracheotomy improves experiment success rate in mice during urethane anesthesia and stereotaxic surgery. *Journal of Neuroscience Methods*, *176*(2), 57–62. doi:10.1016/j.jneumeth.2008.08.015

Mormann, F., Kreuz, T., Andrzejak, R. G., David, P., Lehnertz, K., & Elger, C. E. (2003). Epileptic seizures are preceded by a decrease in synchronization. *Epilepsy Research*, *53*(3), 173–185.

Morrell, F., & deToledo-Morrell, L. (1999). From mirror focus to secondary epileptogenesis in man: an historical review. *Advances in Neurology*, *81*, 11–23.

Mosso, A. (1884). Applicazione della bilancia allo studio della circolazione sanguigna dell'uomo. *Atti Della R Acad Lincei Mem Cl Sci Fis Mat Nat*, *19*, 531–543.

Murphy, K., Birn, R. M., & Bandettini, P. A. (2013). Resting-state fMRI confounds and cleanup. *NeuroImage*, *80*, 349–359. doi:10.1016/j.neuroimage.2013.04.001

Murphy, K., Birn, R. M., Handwerker, D. A., Jones, T. B., & Bandettini, P. A. (2009). The impact of global signal regression on resting state correlations: Are anti-correlated networks introduced? *NeuroImage*, *44*(3), 893–905. doi:10.1016/j.neuroimage.2008.09.036

Nguyen, D. K., Tremblay, J., Pouliot, P., Vannasing, P., Florea, O., Carmant, L., … Lassonde, M. (2012). Non-invasive continuous EEG-fNIRS recording of temporal lobe seizures. *Epilepsy Research*, *99*(1-2), 112–126. doi:10.1016/j.eplepsyres.2011.10.035

Nicholson, C. (1985). Diffusion from an injected volume of a substance in brain tissue with arbitrary volume fraction and tortuosity. *Brain Research*, *333*(2), 325–329.

Nir, Y., Mukamel, R., Dinstein, I., Privman, E., Harel, M., Fisch, L., … Malach, R. (2008). Interhemispheric correlations of slow spontaneous neuronal fluctuations revealed in human sensory cortex. *Nature Neuroscience*, *11*(9), 1100–1108.

Niu, H., Khadka, S., Tian, F., Lin, Z.-J., Lu, C., Zhu, C., & Liu, H. (2011). Resting-state functional connectivity assessed with two diffuse optical tomographic systems. *Journal of Biomedical Optics*, *16*(4), 046006. doi:10.1117/1.3561687

Obrig, H., Neufang, M., Wenzel, R., Kohl, M., Steinbrink, J., Einhäupl, K., & Villringer, A. (2000). Spontaneous low frequency oscillations of cerebral hemodynamics and metabolism in human adults. *NeuroImage*, *12*(6), 623–639. doi:10.1006/nimg.2000.0657

Ogawa, S., Lee, T. M., Kay, A. R., & Tank, D. W. (1990). Brain magnetic resonance imaging with contrast dependent on blood oxygenation. *Proceedings of the National Academy of Sciences of the United States of America*, *87*(24), 9868–9872.

Ogawa, S., Tank, D. W., Menon, R., Ellermann, J. M., Kim, S. G., Merkle, H., & Ugurbil, K. (1992). Intrinsic signal changes accompanying sensory stimulation: functional brain mapping with magnetic resonance imaging. *Proceedings of the National Academy of Sciences of the United States of America*, *89*(13), 5951–5955.

Oppenheim, A. V., Schafer, R. W., & Buck, J. R. (1999). *Discrete-time signal processing* (2nd ed.). Upper Saddler River, NJ: Prentice Hall. Retrieved from http://www.amazon.ca/Discrete-Time-Signal-Processing-Alan-Oppenheim/dp/0137549202

Ouakli, N., Guevara, E., Dubeau, S., Beaumont, E., & Lesage, F. (2010). Laminar optical tomography of the hemodynamic response in the lumbar spinal cord of rats. *Optics Express*, *18*(10), 10068–10077. doi:10.1364/OE.18.010068

Pang, Y., Cai, Z., & Rhodes, P. G. (2003). Disturbance of oligodendrocyte development, hypomyelination and white matter injury in the neonatal rat brain after intracerebral injection of lipopolysaccharide. *Brain Research. Developmental Brain Research*, *140*(2), 205–214.

Pase, M. P., Herbert, A., Grima, N. A., Pipingas, A., & O'Rourke, M. F. (2012). Arterial stiffness as a cause of cognitive decline and dementia: a systematic review and meta-analysis. *Internal Medicine Journal*, *42*(7), 808–815. doi:10.1111/j.1445-5994.2011.02645.x

Pasquale, F. de, Penna, S. D., Snyder, A. Z., Lewis, C., Mantini, D., Marzetti, L., … Corbetta, M. (2010). Temporal dynamics of spontaneous MEG activity in brain networks. *Proceedings of the National Academy of Sciences*, *107*(13), 6040–6045. doi:10.1073/pnas.0913863107

Pawela, C. P., Biswal, B. B., Cho, Y. R., Kao, D. S., Li, R., Jones, S. R., … Hyde, J. S. (2008). Resting-state functional connectivity of the rat brain. *Magnetic Resonance in Medicine: Official Journal of the Society of Magnetic Resonance in Medicine / Society of Magnetic Resonance in Medicine*, *59*(5), 1021–1029. doi:10.1002/mrm.21524

Pawela, C. P., Biswal, B. B., Hudetz, A. G., Li, R., Jones, S. R., Cho, Y. R., … Hyde, J. S. (2010). Interhemispheric neuroplasticity following limb deafferentation detected by resting-state functional connectivity magnetic resonance imaging (fcMRI) and functional magnetic resonance imaging (fMRI). *NeuroImage*, *49*(3), 2467–2478. doi:10.1016/j.neuroimage.2009.09.054

Pawela, C. P., Biswal, B. B., Hudetz, A. G., Schulte, M. L., Li, R., Jones, S. R., … Hyde, J. S. (2009). A protocol for use of medetomidine anesthesia in rats for extended studies using task-induced BOLD contrast and resting-state functional connectivity. *NeuroImage*, *46*(4), 1137–1147. doi:10.1016/j.neuroimage.2009.03.004

Paxinos, G., & Watson, C. (2007). *The rat brain in stereotaxic coordinates* (6th ed.). London, UK: Academic Press.

Peltier, S. J., Polk, T. A., & Noll, D. C. (2003). Detecting low-frequency functional connectivity in fMRI using a self-organizing map (SOM) algorithm. *Human Brain Mapping*, *20*(4), 220–226. doi:10.1002/hbm.10144

Pendlebury, J. D., Wilson, R. J. A., Bano, S., Lumb, K. J., Schneider, J. M., & Hasan, S. U. (2008). Respiratory Control in Neonatal Rats Exposed to Prenatal Cigarette Smoke. *American Journal of Respiratory and Critical Care Medicine*, *177*(11), 1255–1261. doi:10.1164/rccm.200711-1739OC

Petrella, J. R. (2011). Use of Graph Theory to Evaluate Brain Networks: A Clinical Tool for a Small World? *Radiology*, *259*(2), 317–320. doi:10.1148/radiol.11110380

Petzold, G. C., & Murthy, V. N. (2011). Role of astrocytes in neurovascular coupling. *Neuron*, *71*(5), 782–797. doi:10.1016/j.neuron.2011.08.009

Ponten, S. C., Bartolomei, F., & Stam, C. J. (2007). Small-world networks and epilepsy: graph theoretical analysis of intracerebrally recorded mesial temporal lobe seizures. *Clinical Neurophysiology: Official Journal of the International Federation of Clinical Neurophysiology*, *118*(4), 918–927. doi:10.1016/j.clinph.2006.12.002

Pouliot, P., Tremblay, J., Robert, M., Vannasing, P., Lepore, F., Lassonde, M., … Lesage, F. (2012). Nonlinear hemodynamic responses in human epilepsy: a multimodal analysis with fNIRS-EEG and fMRI-EEG. *Journal of Neuroscience Methods*, *204*(2), 326–340. doi:10.1016/j.jneumeth.2011.11.016

Power, J. D., Barnes, K. A., Snyder, A. Z., Schlaggar, B. L., & Petersen, S. E. (2012). Spurious but systematic correlations in functional connectivity MRI networks arise from subject motion. *NeuroImage*, *59*(3), 2142–2154. doi:10.1016/j.neuroimage.2011.10.018

Prahl, S. (1999). Optical Absorption of Hemoglobin. Retrieved October 8, 2009, from http://omlc.ogi.edu/spectra/hemoglobin/

Prince, J. L., & Links, J. (2005). *Medical Imaging Signals and Systems* (1st ed.). Upper Saddle River, NJ: Prentice Hall.

Pukelsheim, F. (1994). The Three Sigma Rule. *The American Statistician*, *48*(2), 88. doi:10.2307/2684253

Raichle, M. E. (1998). Behind the scenes of functional brain imaging: A historical and physiological perspective. *Proceedings of the National Academy of Sciences*, *95*(3), 765–772.

Raichle, M. E. (2010). Two views of brain function. *Trends in Cognitive Sciences*, *14*(4), 180–190. doi:10.1016/j.tics.2010.01.008

Raichle, M. E. (2011). The Restless Brain. *Brain Connectivity*, *1*(1), 3–12. doi:10.1089/brain.2011.0019

Raichle, M. E., MacLeod, A. M., Snyder, A. Z., Powers, W. J., Gusnard, D. A., & Shulman, G. L. (2001). A default mode of brain function. *Proceedings of the National Academy of Sciences*, *98*(2), 676–682. doi:10.1073/pnas.98.2.676

Ramachandra, R., & Subramanian, T. (2011). *Atlas of the Neonatal Rat Brain* (1st ed.). CRC Press.

Ren, H., Sun, T., MacDonald, D. J., Cobb, M. J., & Li, X. (2006). Real-time in vivo blood-flow imaging by moving-scatterer-sensitive spectral-domain optical Doppler tomography. *Optics Letters*, *31*(7), 927–929. doi:10.1364/OL.31.000927

Righi, M., Barcaro, U., Starita, A., Karakonstantaki, E., & Micheloyannis, S. (2008). Detection of signs of brain dysfunction in epileptic children by recognition of transient changes in the correlation of seizure-free EEG. *Brain Topography*, *21*(1), 43–51. doi:10.1007/s10548-008-0057-2

Roberts, R. O., Knopman, D. S., Geda, Y. E., Cha, R. H., Roger, V. L., & Petersen, R. C. (2010). Coronary heart disease is associated with non-amnestic mild cognitive impairment. *Neurobiology of Aging*, *31*(11), 1894–1902. doi:10.1016/j.neurobiolaging.2008.10.018

Rombouts, S. A. R. B., Damoiseaux, J. S., Goekoop, R., Barkhof, F., Scheltens, P., Smith, S. M., & Beckmann, C. F. (2009). Model-free group analysis shows altered BOLD FMRI networks in dementia. *Human Brain Mapping*, *30*(1), 256–266. doi:10.1002/hbm.20505

Rothman, K. J. (1990). No adjustments are needed for multiple comparisons. *Epidemiology (Cambridge, Mass.)*, *1*(1), 43–46.

Saad, Z. S., DeYoe, E. A., & Ropella, K. M. (2003). Estimation of FMRI response delays. *NeuroImage*, *18*(2), 494–504.

Saad, Z. S., Ropella, K. M., DeYoe, E. A., & Bandettini, P. A. (2003). The spatial extent of the BOLD response. *NeuroImage*, *19*(1), 132–144.

Sadekova, N., Vallerand, D., Guevara, E., Lesage, F., & Girouard, H. (2013). Carotid calcification in mice: a new model to study the effects of arterial stiffness on the brain. *Journal of the American Heart Association*, *2*(3), e000224. doi:10.1161/JAHA.113.000224

Salvador, R., Martínez, A., Pomarol-Clotet, E., Sarró, S., Suckling, J., & Bullmore, E. (2007). Frequency based mutual information measures between clusters of brain regions in functional magnetic resonance imaging. *NeuroImage*, *35*(1), 83–88. doi:10.1016/j.neuroimage.2006.12.001

Sandrone, S., Bacigaluppi, M., Galloni, M. R., Cappa, S. F., Moro, A., Catani, M., … Martino, G. (2013). Weighing brain activity with the balance: Angelo Mosso's original manuscripts come to light. *Brain: A Journal of Neurology*. doi:10.1093/brain/awt091

Sanz-Arigita, E. J., Schoonheim, M. M., Damoiseaux, J. S., Rombouts, S. A. R. B., Maris, E., Barkhof, F., … Stam, C. J. (2010). Loss of "Small-World" Networks in Alzheimer's

Disease: Graph Analysis of fMRI Resting-State Functional Connectivity. *PLoS ONE*, *5*(11), e13788. doi:10.1371/journal.pone.0013788#pone.0013788-Watts1

Saramäki, J., Kivelä, M., Onnela, J.-P., Kaski, K., & Kertész, J. (2007). Generalizations of the clustering coefficient to weighted complex networks. *Physical Review E*, *75*(2), 027105. doi:10.1103/PhysRevE.75.027105

Sasai, S., Homae, F., Watanabe, H., & Taga, G. (2011). Frequency-specific functional connectivity in the brain during resting state revealed by NIRS. *NeuroImage*, *56*(1), 252–257. doi:10.1016/j.neuroimage.2010.12.075

Sasaki, S., Sato, K., Shinomiya, K., & Momose-Sato, Y. (2003). Postnatal changes in intrinsic optical responses to peripheral nerve stimulation in the in vivo rat spinal cord. *NeuroImage*, *20*(4), 2126–2134. doi:10.1016/j.neuroimage.2003.08.005

Sasaki, S., Yazawa, I., Miyakawa, N., Mochida, H., Shinomiya, K., Kamino, K., … Sato, K. (2002). Optical Imaging of Intrinsic Signals Induced by Peripheral Nerve Stimulation in the in Vivo Rat Spinal Cord. *NeuroImage*, *17*(3), 1240–1255. doi:10.1006/nimg.2002.1286

Saville, D. J. (1990). Multiple Comparison Procedures: The Practical Solution. *The American Statistician*, *44*(2), 174. doi:10.2307/2684163

Schindler, K., Leung, H., Elger, C. E., & Lehnertz, K. (2007). Assessing seizure dynamics by analysing the correlation structure of multichannel intracranial EEG. *Brain: A Journal of Neurology*, *130*(Pt 1), 65–77. doi:10.1093/brain/awl304

Schroeter, M. L., Schmiedel, O., & von Cramon, D. Y. (2004). Spontaneous low-frequency oscillations decline in the aging brain. *Journal of Cerebral Blood Flow and Metabolism:*

Official Journal of the International Society of Cerebral Blood Flow and Metabolism, *24*(10), 1183–1191. doi:10.1097/01.WCB.0000135231.90164.40

Shmuel, A., Augath, M., Oeltermann, A., & Logothetis, N. K. (2006). Negative functional MRI response correlates with decreases in neuronal activity in monkey visual area V1. *Nature Neuroscience*, *9*(4), 569–577. doi:10.1038/nn1675

Shmuel, A., & Leopold, D. A. (2008). Neuronal correlates of spontaneous fluctuations in fMRI signals in monkey visual cortex: Implications for functional connectivity at rest. *Human Brain Mapping*, *29*(7), 751–761. doi:10.1002/hbm.20580

Singh-Manoux, A., Britton, A. R., & Marmot, M. (2003). Vascular disease and cognitive function: evidence from the Whitehall II Study. *Journal of the American Geriatrics Society*, *51*(10), 1445–1450.

Sirinyan, M., Sennlaub, F., Dorfman, A., Sapieha, P., Gobeil, F., Jr, Hardy, P., … Chemtob, S. (2006). Hyperoxic exposure leads to nitrative stress and ensuing microvascular degeneration and diminished brain mass and function in the immature subject. *Stroke; a Journal of Cerebral Circulation*, *37*(11), 2807–2815. doi:10.1161/01.STR.0000245082.19294.ff

Sizonenko, S. V., Sirimanne, E., Mayall, Y., Gluckman, P. D., Inder, T., & Williams, C. (2003). Selective cortical alteration after hypoxic-ischemic injury in the very immature rat brain. *Pediatric Research*, *54*(2), 263–269. doi:10.1203/01.PDR.0000072517.01207.87

Smith, S. M., Beckmann, C. F., Andersson, J., Auerbach, E. J., Bijsterbosch, J., Douaud, G., … WU-Minn HCP Consortium. (2013). Resting-state fMRI in the Human Connectome Project. *NeuroImage*, *80*, 144–168. doi:10.1016/j.neuroimage.2013.05.039

Smotherman, W. P., Robinson, S. R., Ronca, A. E., Alberts, J. R., & Hepper, P. G. (1991). Heart rate response of the rat fetus and neonate to a chemosensory stimulus. *Physiology & Behavior*, *50*(1), 47–52.

Smyser, C. D., Inder, T. E., Shimony, J. S., Hill, J. E., Degnan, A. J., Snyder, A. Z., & Neil, J. J. (2010). Longitudinal analysis of neural network development in preterm infants. *Cerebral Cortex (New York, N.Y.: 1991)*, *20*(12), 2852–2862. doi:10.1093/cercor/bhq035

Smyser, C. D., Snyder, A. Z., Shimony, J. S., Blazey, T. M., Inder, T. E., & Neil, J. J. (2013). Effects of white matter injury on resting state FMRI measures in prematurely born infants. *PloS One*, *8*(7), e68098. doi:10.1371/journal.pone.0068098

Srinivasan, V. J., Sakadzić, S., Gorczynska, I., Ruvinskaya, S., Wu, W., Fujimoto, J. G., & Boas, D. A. (2010). Quantitative cerebral blood flow with optical coherence tomography. *Optics Express*, *18*(3), 2477–2494.

Stam, C. J., Jones, B. F., Nolte, G., Breakspear, M., & Scheltens, P. (2007). Small-World Networks and Functional Connectivity in Alzheimer's Disease. *Cerebral Cortex*, *17*(1), 92–99. doi:10.1093/cercor/bhj127

Stam, Cornelis J., & Reijneveld, J. C. (2007). Graph theoretical analysis of complex networks in the brain. *Nonlinear Biomedical Physics*, *1*(1), 3. doi:10.1186/1753-4631-1-3

Stevenson, I. H., & Körding, K. P. (2010). On the Similarity of Functional Connectivity between Neurons Estimated across Timescales. *PLoS ONE*, *5*(2), e9206. doi:10.1371/journal.pone.0009206

Suckow, M. A., Danneman, P., & Brayton, C. (2001). *The laboratory mouse*. Boca Raton, Fla.: CRC Press.

Sun, J., Tong, S., & Yang, G.-Y. (2011). Reorganization of Brain Networks in Aging and Age-related Diseases. *Aging and Disease*, *3*(2), 181–193.

Sun, Y., Qin, L., Zhou, Y., Xu, Q., Qian, L., Tao, J., & Xu, J. (2011). Abnormal functional connectivity in patients with vascular cognitive impairment, no dementia: a resting-state functional magnetic resonance imaging study. *Behavioural Brain Research*, *223*(2), 388–394. doi:10.1016/j.bbr.2011.05.006

Taga, G., Konishi, Y., Maki, A., Tachibana, T., Fujiwara, M., & Koizumi, H. (2000). Spontaneous oscillation of oxy- and deoxy- hemoglobin changes with a phase difference throughout the occipital cortex of newborn infants observed using non-invasive optical topography. *Neuroscience Letters*, *282*(1-2), 101–104.

Tearney, G. J., Brezinski, M. E., Bouma, B. E., Boppart, S. A., Pitris, C., Southern, J. F., & Fujimoto, J. G. (1997). In Vivo Endoscopic Optical Biopsy with Optical Coherence Tomography. *Science*, *276*(5321), 2037–2039. doi:10.1126/science.276.5321.2037

Teichert, T., Grinband, J., Hirsch, J., & Ferrera, V. P. (2010). Effects of heartbeat and respiration on macaque fMRI: implications for functional connectivity. *Neuropsychologia*, *48*(7), 1886–1894. doi:10.1016/j.neuropsychologia.2009.11.026

Thatcher RW, Krause PJ, & Hrybyk M. (1986). Cortico-cortical associations and EEG coherence: a two-compartmental model. *Electroencephalogr Clin Neurophysiol.*, *64*(2), 123–43.

Thevenaz, P., Ruttimann, U. E., & Unser, M. (1998). A pyramid approach to subpixel registration based on intensity. *IEEE Transactions on Image Processing*, *7*(1), 27–41. doi:10.1109/83.650848

Thorvaldsen, S., Flå, T., & Willassen, N. P. (2010). DeltaProt: a software toolbox for comparative genomics. *BMC Bioinformatics*, *11*(1), 573. doi:10.1186/1471-2105-11-573

Toronov, V., Franceschini, M. A., Filiaci, M., Fantini, S., Wolf, M., Michalos, A., & Gratton, E. (2000). Near-infrared study of fluctuations in cerebral hemodynamics during rest and motor stimulation: temporal analysis and spatial mapping. *Medical Physics*, *27*(4), 801–815.

Ts'o, D. Y., Frostig, R. D., Lieke, E. E., & Grinvald, A. (1990). Functional organization of primate visual cortex revealed by high resolution optical imaging. *Science*, *249*(4967), 417–420. doi:10.1126/science.2165630

Van den Heuvel, M. P., & Hulshoff Pol, H. E. (2010). Exploring the brain network: A review on resting-state fMRI functional connectivity. *European Neuropsychopharmacology*, *20*(8), 519–534. doi:10.1016/j.euroneuro.2010.03.008

Van Dijk, K. R. A., Hedden, T., Venkataraman, A., Evans, K. C., Lazar, S. W., & Buckner, R. L. (2010). Intrinsic Functional Connectivity As a Tool For Human Connectomics: Theory, Properties, and Optimization. *Journal of Neurophysiology*, *103*(1), 297–321. doi:10.1152/jn.00783.2009

Van Dijk, K. R. A., Sabuncu, M. R., & Buckner, R. L. (2012). The influence of head motion on intrinsic functional connectivity MRI. *NeuroImage*, *59*(1), 431–438. doi:10.1016/j.neuroimage.2011.07.044

Van Meer, M. P. A., van der Marel, K., Otte, W. M., Berkelbach van der Sprenkel, J. W., & Dijkhuizen, R. M. (2010). Correspondence between altered functional and structural connectivity in the contralesional sensorimotor cortex after unilateral stroke in rats: a

combined resting-state functional MRI and manganese-enhanced MRI study. *Journal of Cerebral Blood Flow and Metabolism: Official Journal of the International Society of Cerebral Blood Flow and Metabolism*, *30*(10), 1707–1711. doi:10.1038/jcbfm.2010.124

Van Norden, A. G., de Laat, K. F., Gons, R. A., van Uden, I. W., van Dijk, E. J., van Oudheusden, L. J., … de Leeuw, F.-E. (2011). Causes and consequences of cerebral small vessel disease. The RUN DMC study: a prospective cohort study. Study rationale and protocol. *BMC Neurology*, *11*, 29. doi:10.1186/1471-2377-11-29

Verhagen, E. A., Keating, P., ter Horst, H. J., Martijn, A., & Bos, A. F. (2009). Cerebral oxygen saturation and extraction in preterm infants with transient periventricular echodensities. *Pediatrics*, *124*(1), 294–301. doi:10.1542/peds.2008-2057

Vincent, J. L., Patel, G. H., Fox, M. D., Snyder, A. Z., Baker, J. T., Van Essen, D. C., … Raichle, M. E. (2007). Intrinsic functional architecture in the anaesthetized monkey brain. *Nature*, *447*(7140), 83–86. doi:10.1038/nature05758

Vogel, C. R. (2002). Computational methods for inverse problems (pp. 106–108). Philadelphia, PA: Society for Industrial and Applied Mathematics.

Voges, N., Blanchard, S., Wendling, F., David, O., Benali, H., Papadopoulo, T., … Bénar, C. (2012). Modeling of the neurovascular coupling in epileptic discharges. *Brain Topography*, *25*(2), 136–156. doi:10.1007/s10548-011-0190-1

Waites, A. B., Briellmann, R. S., Saling, M. M., Abbott, D. F., & Jackson, G. D. (2006). Functional connectivity networks are disrupted in left temporal lobe epilepsy. *Annals of Neurology*, *59*(2), 335–343. doi:10.1002/ana.20733

Wang, L. V., & Hu, S. (2012). Photoacoustic Tomography: In Vivo Imaging from Organelles to Organs. *Science*, *335*(6075), 1458–1462. doi:10.1126/science.1216210

Wang, L. V., & Wu, H.-I. (2007). *Biomedical Optics: Principles and Imaging*. New Jersey, USA: John Wiley & Sons.

Wang, X., Pang, Y., Ku, G., Xie, X., Stoica, G., & Wang, L. V. (2003). Noninvasive laser-induced photoacoustic tomography for structural and functional in vivo imaging of the brain. *Nature Biotechnology*, *21*(7), 803–806. doi:10.1038/nbt839

Wang, X., Xie, X., Ku, G., Wang, L. V., & Stoica, G. (2006). Noninvasive imaging of hemoglobin concentration and oxygenation in the rat brain using high-resolution photoacoustic tomography. *Journal of Biomedical Optics*, *11*(2), 024015. doi:10.1117/1.2192804

Wang, Z., Lu, G., Zhang, Z., Zhong, Y., Jiao, Q., Zhang, Z., … Liu, Y. (2011). Altered resting state networks in epileptic patients with generalized tonic-clonic seizures. *Brain Research*, *1374*, 134–141. doi:10.1016/j.brainres.2010.12.034

Watson, C., Paxinos, G., & Puelles, L. (2011). *The Mouse Nervous System*. Burlington: Elsevier Science. Retrieved from http://public.eblib.com/EBLPublic/PublicView.do?ptiID=787248

Weissenbacher, A., Kasess, C., Gerstl, F., Lanzenberger, R., Moser, E., & Windischberger, C. (2009). Correlations and anticorrelations in resting-state functional connectivity MRI: a quantitative comparison of preprocessing strategies. *NeuroImage*, *47*(4), 1408–1416. doi:10.1016/j.neuroimage.2009.05.005

Wendling, F., Hernandez, A., Bellanger, J.-J., Chauvel, P., & Bartolomei, F. (2005). Interictal to ictal transition in human temporal lobe epilepsy: insights from a computational model of

intracerebral EEG. *Journal of Clinical Neurophysiology: Official Publication of the American Electroencephalographic Society*, *22*(5), 343–356.

White, Brian R, Bauer, A. Q., Snyder, A. Z., Schlaggar, B. L., Lee, J.-M., & Culver, J. P. (2011). Imaging of functional connectivity in the mouse brain. *PloS One*, *6*(1), e16322. doi:10.1371/journal.pone.0016322

White, Brian R, Liao, S. M., Ferradal, S. L., Inder, T. E., & Culver, J. P. (2012). Bedside optical imaging of occipital resting-state functional connectivity in neonates. *NeuroImage*, *59*(3), 2529–2538. doi:10.1016/j.neuroimage.2011.08.094

White, Brian R., Snyder, A. Z., Cohen, A. L., Petersen, S. E., Raich-le, M. E., Schlaggar, B. L., & Culver, J. P. (2009). Resting-state functional connectivity in the human brain revealed with diffuse optical tomography. *NeuroImage*, *47*(1), 148–156. doi:10.1016/j.neuroimage.2009.03.058

White, Brian Richard. (2012). *Developing High-Density Diffuse Optical Tomography for Neuroimaging* (PhD dissertation). Washington University in St. Louis, United States -- Missouri. Retrieved from http://search.proquest.com/pqdtft/docview/926209544/abstract/13C78136FA421D025A1/1?accountid=40695

Whitfield-Gabrieli, S., & Nieto-Castanon, A. (2012). Conn: a functional connectivity toolbox for correlated and anticorrelated brain networks. *Brain Connectivity*, *2*(3), 125–141. doi:10.1089/brain.2012.0073

Whitfield-Gabrieli, S., Thermenos, H. W., Milanovic, S., Tsuang, M. T., Faraone, S. V., McCarley, R. W., … Seidman, L. J. (2009). Hyperactivity and hyperconnectivity of the

default network in schizophrenia and in first-degree relatives of persons with schizophrenia. *Proceedings of the National Academy of Sciences of the United States of America*, *106*(4), 1279–1284. doi:10.1073/pnas.0809141106

Willis, W. D., & Coggeshall, R. E. (1991). *Sensory mechanisms of the spinal cord* (2nd ed.). New York: Plenum Press.

Wojtkowski, M., Leitgeb, R., Kowalczyk, A., Bajraszewski, T., & Fercher, A. F. (2002). In vivo human retinal imaging by Fourier domain optical coherence tomography. *Journal of Biomedical Optics*, *7*(3), 457. doi:10.1117/1.1482379

Wojtkowski, M., Srinivasan, V., Ko, T., Fujimoto, J., Kowalczyk, A., & Duker, J. (2004). Ultrahigh-resolution, high-speed, Fourier domain optical coherence tomography and methods for dispersion compensation. *Optics Express*, *12*(11), 2404–2422. doi:10.1364/OPEX.12.002404

Wolf, U., Toronov, V., Choi, J. H., Gupta, R., Michalos, A., Gratton, E., & Wolf, M. (2011). Correlation of functional and resting state connectivity of cerebral oxy-, deoxy-, and total hemoglobin concentration changes measured by near-infrared spectrophotometry. *Journal of Biomedical Optics*, *16*(8). doi:10.1117/1.3615249

World Health Organization. (2006). *Neurological Disorders: Public Health Challenges*. Geneva, Switzerland: WHO Press. Retrieved from http://www.who.int/mental_health/publications/neurological_disorders_ph_challenges/en/

World Health Organization. (2012). *World Health Statistics 2012*. Geneva, Switzerland: WHO Press. Retrieved from http://www.who.int/healthinfo/EN_WHS2012_Full.pdf

Worsley, K. J., Chen, J.-I., Lerch, J., & Evans, A. C. (2005). Comparing functional connectivity via thresholding correlations and singular value decomposition. *Philosophical Transactions of the Royal Society B: Biological Sciences*, *360*(1457), 913–920. doi:10.1098/rstb.2005.1637

Xiang, L., Ji, L., Zhang, T., Wang, B., Yang, J., Zhang, Q., … Jiang, H. (2012). Noninvasive real time tomographic imaging of epileptic foci and networks. *NeuroImage*, *66C*, 240–248. doi:10.1016/j.neuroimage.2012.10.077

Yaroslavsky, A. N., Schulze, P. C., Yaroslavsky, I. V., Schober, R., Ulrich, F., & Schwarzmaier, H.-J. (2002). Optical properties of selected native and coagulated human brain tissues in vitro in the visible and near infrared spectral range. *Physics in Medicine and Biology*, *47*(12), 2059–2073. doi:10.1088/0031-9155/47/12/305

Young, R. S. K., Yagel, S. K., & Towfighi, J. (1983). Systemic and Neuropathologic Effects of E. coli Endotoxin in Neonatal Dogs. *Pediatric Research*, *17*(5), 349–353. doi:10.1203/00006450-198305000-00008

Yu, H., Schummers, J., & Sur, M. (2010). The Influence of Astrocyte Activation on Hemodynamic Signals for Functional Brain Imaging. In A. W. Roe (Ed.), *Imaging the Brain with Optical Methods* (pp. 45–64). Springer New York. Retrieved from http://link.springer.com/chapter/10.1007/978-1-4419-0452-2_3

Yuan, B., Burgess, S. A., Iranmahboob, A., Bouchard, M. B., Lehrer, N., Bordier, C., & Hillman, E. M. C. (2009). A system for high-resolution depth-resolved optical imaging of fluorescence and absorption contrast. *Review of Scientific Instruments*, *80*(4), 043706. doi:10.1063/1.3117204

Yuan, S., Devor, A., Boas, D. A., & Dunn, A. K. (2005). Determination of optimal exposure time for imaging of blood flow changes with laser speckle contrast imaging. *Applied Optics*, *44*(10), 1823–1830.

Zago, S., Lorusso, L., Ferrucci, R., & Priori, A. (2012). Functional Neuroimaging: A Historical Perspective. In P. Bright (Ed.), *Neuroimaging - Methods*. InTech. Retrieved from http://www.intechopen.com/books/neuroimaging-methods/the-origins-of-functional-neuroimaging-techniques

Zappe, A. C., Uludag, K., Oeltermann, A., Ugurbil, K., & Logothetis, N. K. (2008). The Influence of Moderate Hypercapnia on Neural Activity in the Anesthetized Nonhuman Primate. *Cereb. Cortex*, *18*(11), 2666–2673. doi:10.1093/cercor/bhn023

Zhang, H., Zhang, Y.-J., Lu, C.-M., Ma, S.-Y., Zang, Y.-F., & Zhu, C.-Z. (2010). Functional connectivity as revealed by independent component analysis of resting-state fNIRS measurements. *NeuroImage*, *51*(3), 1150–1161. doi:10.1016/j.neuroimage.2010.02.080

Zhang, Z., Lu, G., Zhong, Y., Tan, Q., Yang, Z., Liao, W., … Liu, Y. (2009). Impaired attention network in temporal lobe epilepsy: a resting FMRI study. *Neuroscience Letters*, *458*(3), 97–101. doi:10.1016/j.neulet.2009.04.040

Zhao, F., Zhao, T., Zhou, L., Wu, Q., & Hu, X. (2008). BOLD study of stimulation-induced neural activity and resting-state connectivity in medetomidine-sedated rat. *NeuroImage*, *39*(1), 248–260. doi:10.1016/j.neuroimage.2007.07.063

Zhao, M., Ma, H., Suh, M., & Schwartz, T. H. (2009). Spatiotemporal Dynamics of Perfusion and Oximetry during Ictal Discharges in the Rat Neocortex. *The Journal of Neuroscience*, *29*(9), 2814–2823. doi:10.1523/JNEUROSCI.4667-08.2009

Zhao, M., Nguyen, J., Ma, H., Nishimura, N., Schaffer, C. B., & Schwartz, T. H. (2011). Preictal and ictal neurovascular and metabolic coupling surrounding a seizure focus. *The Journal of Neuroscience: The Official Journal of the Society for Neuroscience*, *31*(37), 13292–13300. doi:10.1523/JNEUROSCI.2597-11.2011

Zhao, M., Suh, M., Ma, H., Perry, C., Geneslaw, A., & Schwartz, T. H. (2007). Focal increases in perfusion and decreases in hemoglobin oxygenation precede seizure onset in spontaneous human epilepsy. *Epilepsia*, *48*(11), 2059–2067. doi:10.1111/j.1528-1167.2007.01229.x

Zhu, Y., Lee, C., Shen, F., Du, R., Young, W. L., & Yang, G.-Y. (2005). Angiopoietin-2 facilitates vascular endothelial growth factor-induced angiogenesis in the mature mouse brain. *Stroke; a Journal of Cerebral Circulation*, *36*(7), 1533–1537. doi:10.1161/01.STR.0000170712.46106.2e

Zudaire, E., Gambardella, L., Kurcz, C., & Vermeren, S. (2011). A computational tool for quantitative analysis of vascular networks. *PloS One*, *6*(11), e27385. doi:10.1371/journal.pone.0027385

ANNEX 1 –MATLAB TOOLBOXES

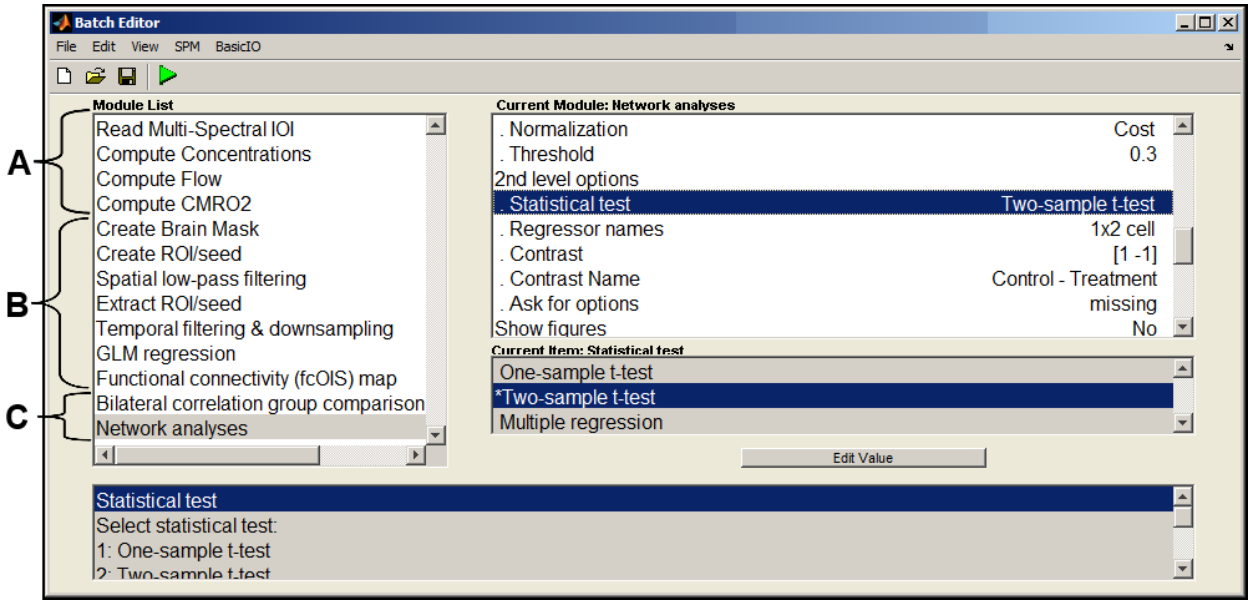

Figure A-1: Screenshots of an example of fcOIS toolbox running under SPM8. Configuration options for each individual module are shown on the right window. Module names are displayed on the left window: (A) Pre-processing stage (B) Analysis at subjects level (C) Analysis at group level. fcOIS toolbox is specifically conceived for batch processing of data. Its modules are executed automatically, one after another, with little user supervision. The processing pipeline is saved to a file, ensuring the reproducibility of the data analysis; this toolbox therefore allows users to concentrate on assessing the results.

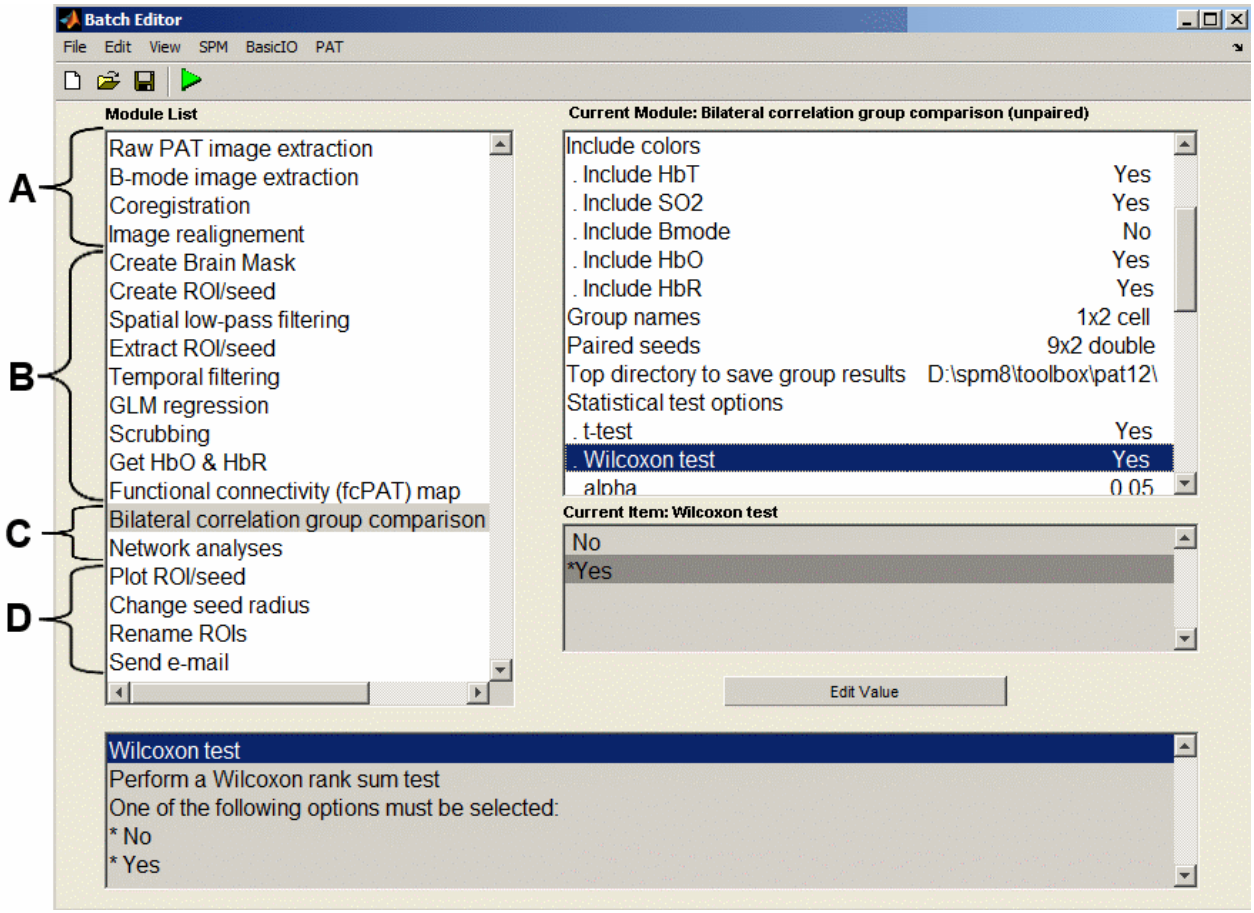

Figure A-2: Screenshots of an example of fcPAT toolbox running under SPM8. Configuration options for each individual module are shown on the right window. Module names are displayed on the left window: (A) Pre-processing stage (B) Analysis at subjects level (C) Analysis at group level (D) Miscellaneous options. For details refer to Figure A-1.